Structural investigation of Ge-Sb-Te thin films by aberration-corrected scanning transmission electron microscopy

Dissertation

zur Erlangung des akademischen Grades

Doktor der Ingenieurswissenschaften
(Dr. Ing.)

der Technischen Fakultät
der Christian-Albrechts-Universität zu Kiel

Ulrich Roß

Leipzig

2016

Vorsitz der Prüfungskommission: Prof. Gerhardt Schmidt

1. Referent: Prof. Dr. Lorenz Kienle

2. Koreferent: Prof. Dr. Dr. h.c. Bernd Rauschenbach

3. Koreferent: Prof. Dr. Oliver Eibl

Vorgelegt von: Dipl. Ing. Ulrich Roß

Datum der mündlichen Prüfung: 29.3.2017

„I have had my results for a long time: but I do not yet know how I am to arrive at them.”
(„Das Ergebnis habe ich schon, jetzt brauche ich nur noch den Weg, der zu ihm führt.“)

- Johann Carl Friedrich Gauß

Abstract

The work presented here details the structural characterization of Ge-Sb-Te (GST) thin films by aberration-corrected scanning transmission electron microscopy (STEM). GST materials are of eminent technological interest as phase change materials for their application in optical data storage and resistive memory devices. Despite the past and recent successes in translating empirical observations of the unique phase change material behaviour into useful concepts for applications, the underlying atomistic origin of the structural changes between amorphous glass, disordered metastable lattice and highly-ordered layered stable crystalline lattice and the accompanying property changes are not yet fully explored.

GST thin films produced by pulsed laser deposition (PLD) are subjected to a range of post-deposition annealing temperatures. The resulting amorphous, metastable crystalline and stable crystalline thin films are prepared for the transmission electron microscopy (TEM) cross-section study by focused ion beam methods. Very low ion-beam polishing energies under liquid nitrogen stage-cooling conditions result in excellent specimen quality and lamella thickness control, as was verified by electron energy-loss filtered imaging, high-resolution TEM imaging and Monte-Carlo simulation of the ion-beam induced effects. The resulting specimens are investigated using a range of TEM techniques, including nano-beam diffraction, STEM X-ray analysis, TEM diffraction contrast imaging and aberration-corrected high-angle annular dark-field (HAADF-) STEM imaging.

The experimental data is evaluated using image processing techniques as well as advanced methods, comparing individual atomic column scattering intensities with absorptive-potential multi-slice image simulations. Results reveal distorted octahedral motifs in the amorphous phase, pm-scale sublattice distortions and sublattice pre-ordering in the metastable crystalline phase, a distinct ordering of intrinsic vacancies into layers in a transition state to the stable crystalline phase, as well as chemical and structural disorder in the stable layered arrangement.

In addition, the PLD thin-film growth of GST layers at elevated substrate temperatures is investigated. The growth behaviour reveals a strong tendency towards (0001) texturing even on disordered interfaces, a distinct Te-rich surface passivation layer formation on Si(111) substrates, as well as the formation of a Van-der-Waals interface arrangement in the epitaxial growth regime at high deposition temperatures. Lastly 60° rotation twin domains, 3° rotation coincidence lattice domains and localized stacking transition defects are observed and characterized. The observation of defect structures and structural disorder in the layered phase in particular promises to be a valuable contribution, especially in the development of multi-layered phase change concepts.

List of abbreviations

Some common, recurring abbreviations are introduced for quick reference below:

PCM/iPCM	Phase Change Material / interfacial Phase Change Memory
GST	Ge-Sb-Te chalcogenide compounds
GST124	$Ge_1Sb_2Te_4$ composition
GST225	$Ge_2Sb_2Te_5$ composition
GST326	$Ge_3Sb_2Te_6$ composition

Experimentally determined GST compositions are sometimes subsequently referred to by the nearest stoichiometric $(GeTe)_{1-x}(Sb_2Te_3)_x$ composition even if a previously noted deviation remains.

PLD	Pulsed Laser Deposition
XRD	X-Ray Diffraction
MBE	Molecular Beam Epitaxy
STEM	Scanning Transmission Electron Microscopy
HAADF-	High Angle Annular Dark-Field (-STEM)
BF-	Bright-Field; can refer to bright-field imaging (-TEM) or scanning (-STEM)
ADF-	Annular Dark-Field; refers to Low- or Medium- Angle Annular Dark-Field depending on the detector (DF2 or DF4) and collection semi-angle given.
FT/FFT	Fourier Transformed / Fast Fourier Transformed; Fourier Transformed refers to spatial frequency space in general and 2D diffractogram in particular, while FFT refers to the specific Fast Fourier Transformation algorithm.
NBD	Nano-Beam Diffraction; scanning probe diffraction with very small beam convergence semi-angle (0.16 mrad).
SAED	Selected Area Electron Diffraction
VdW	Van-der-Waals; often used to denote the intrinsic vacancy gap in the trigonal phase, alternatively denoted VL (vacancy layer).

Table of contents

1. Introduction

1.1 Preface

All current studies on phase-change materials can be traced back to the description of novel material properties in chalcogenide materials by S. Ovshinsky in 1968[1]. While this initial work was already built around the ultra-fast (ns-) electrical switching of telluride compounds, characterising the distinct material states in terms of electrical resistance states, the topic lay somewhat dormant, with sporadic new results on the optical switching properties of amorphous semiconductors[2, 3]. In 1987, N. Yamada and colleagues published work on thin Telluride layers for optical data storage[4], which evolved to reveal the prominence of the $(GeTe)_{1-x} – (Sb_2Te_3)_x$ pseudobinary material system for optical data storage applications[5] due to its large optical reflectivity contrast and excellent optical switching properties.

The rapid reversible switching behaviour between structurally and functionally distinct states in chalcogenide tellurides has since lead to its use as the active layer material in re-writable optical disks (DVD-R)[6]. In addition, since approximately the turn of the millennium, the electronic properties of these materials have found renewed interest. As the scaling requirements of electronic memory components increase in order to achieve ever higher information densities, electronic charge storage devices such as NAND-Flash and dynamic random access memory approach their physical limitations. A number of potential technologies are being developed to replace current-generation solid-state memory devices, of which phase change materials (PCM) are among the most mature[7]. Prominent advantages of PCM are the non-volatility of the information storage and the scaling potential, while challenges include power consumption and access latency. Although some application-level products using phase change technology have already been realized by the large semiconductor manufacturers, the final market breakthrough still remains.

While the application of phase change materials has thus steadily advanced, the atomic origin of the fast switching mechanism and the pronounced property contrast has not been conclusively solved. Some selection criteria for the development of new PCMs have been proposed[8], however a better understanding of the structure-property relationship is required in order to improve the design of new materials. The following chapter will first establish what the characteristic phase change effect in Ge-Sb-Te based materials is, followed by an overview of relevant structural phases. As the investigation is centred on the experimental determination of structural features in thin films, the various classes of structural defects and their relevance to the material system are also shortly summarized.

1.2 The phase change effect

While the term “phase change material behaviour” has found its way into the standard repertoire of scientific literature, it may seem at first reading rather confusingly chosen. Any material can be regarded to undergo phase changes from one local minimum in the Gibbs free energy to another when acted upon by a change in temperature or pressure. Similarly, changes in the phase state of a material often bring with them drastic changes in properties. A liquid will usually act radically different from a solid or a gas. A mixture, in any phase state, may separate into constituents or multiple mixtures of different compositions and structures, each with its own set of physical properties. Furthermore many materials display metastable equilibria that may possess different properties than their absolute minimum energy configurations. In order for a material to be regarded as exhibiting phase change material behaviour, a very specific set of circumstances has to be observed[8-10].

The material needs to possess at least two solid structural phases at room temperature that are stable over intermediate timeframes. In order to be useful for phase change applications this timeframe is typically required to cover multiple years. The solid structural phases referred to are often an amorphous state with frozen disorder in the distribution of the constituent atoms and an ordered crystalline lattice arrangement. As such, the glass forming properties of the material are of critical importance[11, 12].

It also is required to exhibit a large contrast in at least one functional property upon transition from one solid phase state to another. The most common functional properties of interest are the optical behaviour as determined by the dielectric function[13] and the electrical conduction properties as dependent on the charge carrier density and density of states often described as an electronic band structure in the solid[14]. Increasingly attention is also being directed towards other physical properties such as changes in ferroelectric polarizability[15, 16], multiferroic behaviour[17] and anisotropic thermal conduction[18, 19].

Finally, it must be possible to induce the transition from one intermediate room temperature state to another on a nanosecond timescale. Therefore at least one state is constrained to a metastable equilibrium, while the kinetics of the phase transformation remain extraordinarily fast. In practice, many common phase change compounds display this fast transformation mechanism between the highly disordered amorphous state and an intermediate metastable phase, possessing an additional stable equilibrium structure that is only reached after extended annealing times at higher temperatures.

From these necessary characteristics, metastable solid phase, large property contrast and fast phase transformation, it becomes apparent that some extraordinary requirements are laid upon any phase change compound[20-22]. In particular, for the transformation process to be as fast as observed, only short-range movement of atomic positions can be required to dramatically change the electronic structure. Much work has been put into identifying the specific material characteristics that would help predict phase change behaviour[23, 24]. The most concrete evidence for a systematic composition – phase change property correlation, as well as the vast majority of known phase change materials themselves, was found in tellurium-rich chalcogenide compounds.

A schematic illustration of the phase change process in the example of Ge-Sb-Te (GST) compounds is shown in Figure 1.1 Starting from an amorphous disordered atomic arrangement; energy is supplied to the system thus increasing the temperature in the material. This energy transfer usually takes place by either supplying additional heat directly, via photon energy transfer to excited electronic states and subsequent relaxation in the case of optical switching[25], or by Joule heating through an electrical current[26, 27]. It is readily apparent that, rather elegantly, the energy transfer mechanism can be equally useful for a determination of the structural state thanks to the property contrast. Coherent light is used in optical switching to both induce the phase transformation and measure its optical reflectivity. A voltage can also be applied in electrical switching in order to measure the resistivity. In practice, due to geometrical constraints such as thermal cross-influence of cell elements and uneven crystallization in the cell active layer during direct Joule heating leading to the formation of crystalline filaments, current electrical memory designs favour a scheme wherein an additional bottom heating plug with low thermal conductivity is used to heat the active phase change layer[28].

During the initial short pulse of energy input, the temperature in the material remains below the melting point yet is sufficient to initiate the fast phase transformation process, i.e. surpasses the glass transition temperature for the timeframe of the pulse. Thus, after the SET pulse, the material has changed from a low reflectivity high resistance amorphous state to the high reflectivity low resistance metastable crystalline state. By applying an additional short pulse that is sufficient to heat the material above the melting point, and minimizing the time spent in the intermediate crystallization regime, the material can be brought back into the amorphous state in what amounts to a RESET action.

The particulars of the re-amorphization process, whether long-range order is completely broken or alternatively one sublattice is preferentially disordered, are still somewhat contentious and may depend on the specific profile of the power pulse used. Further background regarding the switching process and short-range order in the amorphous phase is given in section 1.3.4. In order to crystallize the stable configuration of the material, a much more prolonged annealing step has to be applied. The transition from metastable to stable crystalline configuration is accompanied by an additional smaller step in the reflectivity and conductivity. Simultaneously the thermal conductivity gradually increases, with larger jumps at the phase transformation steps, due to a further decrease in disorder-induced anharmonicity[29] and an increase of the electronic contribution with increasing conductivity consistent with the Wiedemann-Franz Law.

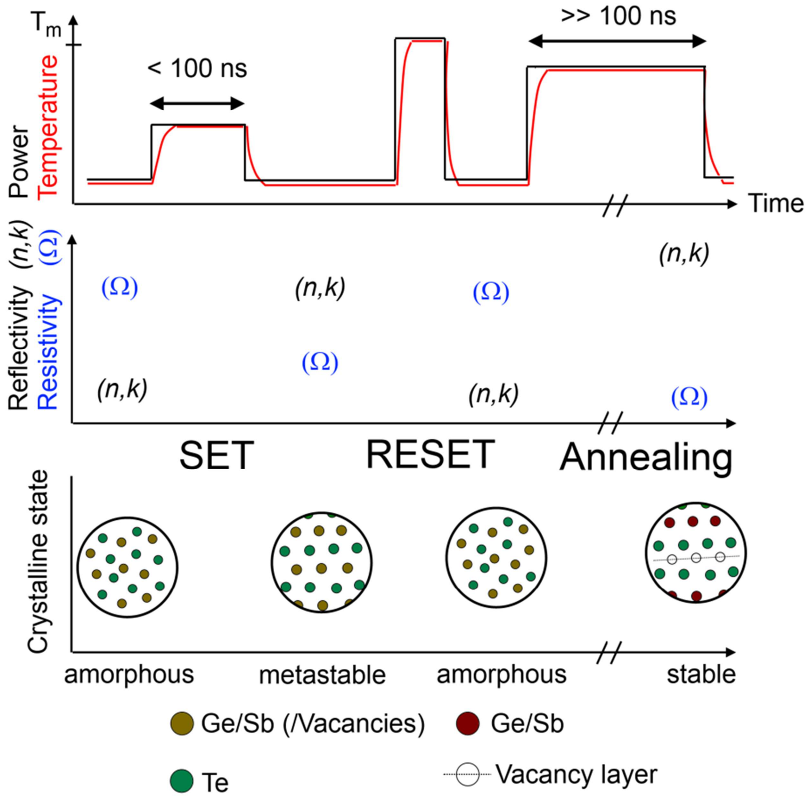

Fig. 1.1: Schematic phase change process in GST compounds, adapted from Ref. [30]. T_m denotes the melting point.

It can be readily seen that the local atomic arrangements in the lattice play a central part in the operation of a phase-change device. However not only are the functional properties coupled to the abrupt changes during fast phase transformation, but also influenced by further gradual changes in structural and chemical disorder in the lattice[31]. The following section thus introduces the current, continuously evolving knowledge about the distinct structural states.

1.3 Structure and properties

1.3.1 Ternary telluride chalcogenides: historical overview

All phase change compounds are thought to share common structural features that enable their functional phase-change behaviour. However, since the subject matter of this work are Ge-Sb-Te based chalcogenides which act as model systems for phase change behaviour, and as such have attracted a large repository of literature, this section will also focus on structure and properties of aforementioned GST compounds. It would nevertheless be neglectful not to mention competing material systems at least in passing. Figure 1.2 gives an overview of the most important known phase change compound compositions as well as some historical milestones in their applications. As indicated, the vast majority of compounds are based on tellurium anion chalcogenides, while the cations most commonly are comprised of group XIV and group XV elements. Further complicating is the fact that the phase change behaviour can be tuned by doping of a known phase change compound, most prominently with nitrogen or carbon up to single digit atomic percent[32, 33]. The most prominent phase change compositions are GeTe, $Sb_{70}Te_{30}$, $Ge_{15}Sb_{85}$, AgInSbTe (AIST) and the wide range of Ge-Sb-Te compositions from the GeTe – Sb_2Te_3 pseudobinary tieline.

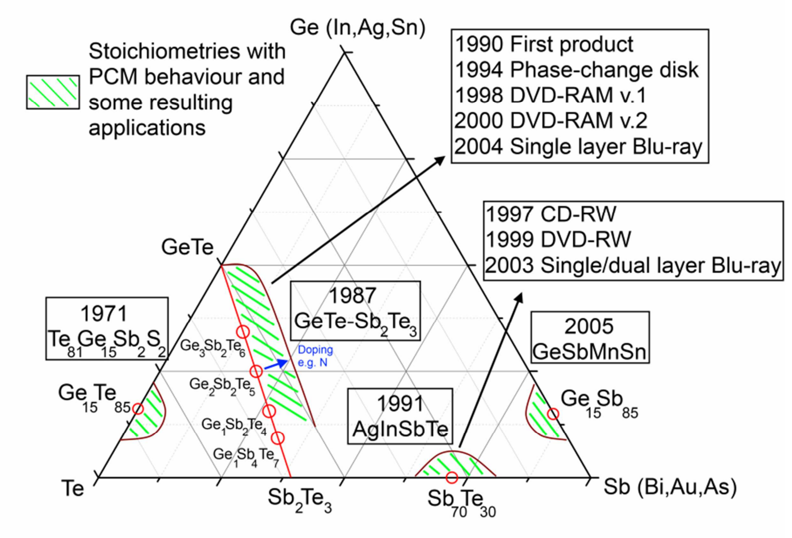

Fig.1.2: Phase change compounds in ternary telluride compounds, adapted from Ref. [9].

A literature-sourced[34] summary of stable phase compositions in the Ge-Sb-Te ternary system is shown in Table I, accompanied by the pseudobinary phase diagram of the GeTe – Sb_2Te_3 tieline shown in Figure 1.3 as well as the phase transformation temperatures from the as-prepared amorphous state during differential scanning calorimetry (DSC) measurements at 10 °C/min heating rates[5] in Figure 1.4. Both Sb_2Te_3 and GeTe occur in stable polytypes at different temperatures, however only the α-GeTe and β-GeTe phases possess a solubility of Sb significant enough to play a minor role in the pseudo-binary GeTe – Sb_2Te_3 system. Furthermore this literature source lists three stoichiometric phases of $(GeTe)_{1-x}$ – $(Sb_2Te_3)_x$, namely $GeSb_4Te_7$, $GeSb_2Te_4$ and $Ge_2Sb_2Te_5$. These are depicted as coexisting in mixed phases over wide composition ranges. Interestingly, more recent studies have found additional stoichiometric compositions of the $(GeTe)_{1-x}$ – $(Sb_2Te_3)_x$ type, most prominently $Ge_3Sb_2Te_6$[35] located in the A+α area of the phase diagram shown. The pseudobinary phase diagram in Figure 1.3 therefore is of rather historical value, however as a conclusive summary of all known stable and metastable phases is still somewhat lacking, it is sufficient to give a first impression of the complexity of the material system. Especially when regarding the phase transformation temperature diagram as measured during DSC in Figure 1.4, it becomes apparent that metastability plays a prominent role in the phase change behaviour of Ge-Sb-Te alloys. All stoichiometric compositions display an intermediate metastable crystallization from the frozen liquid into a cubic F m $\bar{3}$ m phase as well as a crystalline solid-solid phase transformation to the stable trigonal P $\bar{3}$ m 1 (denoted hexagonal in Figure 1.4) phase. The phase transition temperature rises with increasing GeTe content, as does the metastability range of the cubic phase. Thus, identifying what is and is not a stable configuration or mixture of stoichiometric phases has long posed a significant challenge.

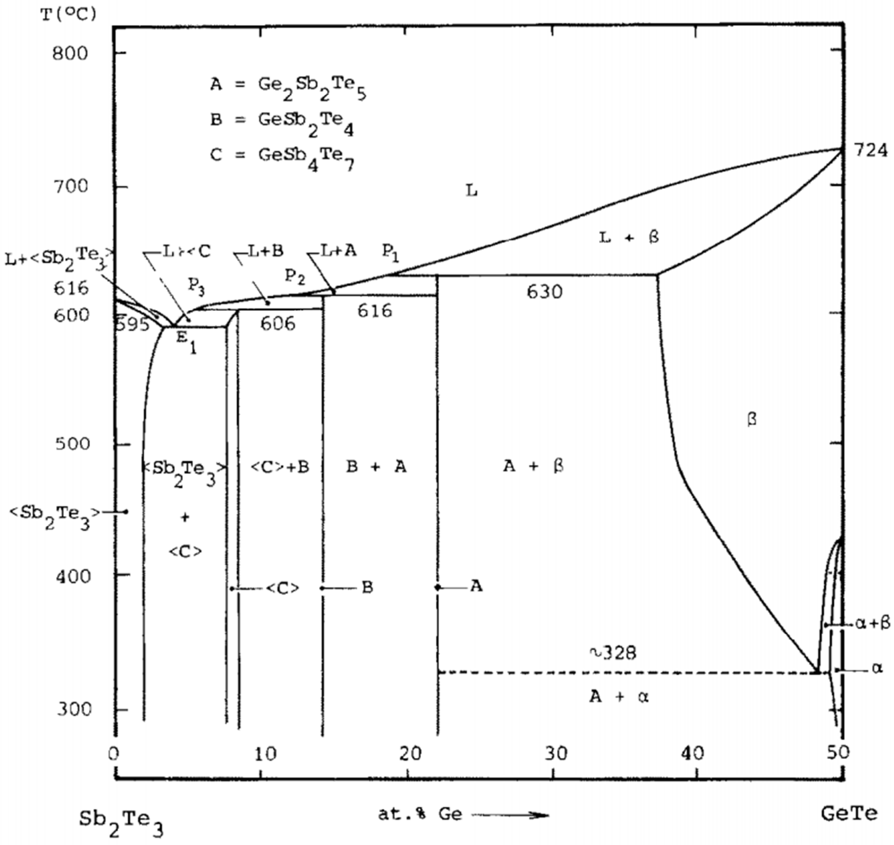

Fig. 1.3: Historical pseudobinary phase diagram of GeTe – Sb_2Te_3, accompanying Table I, from Ref. [36].

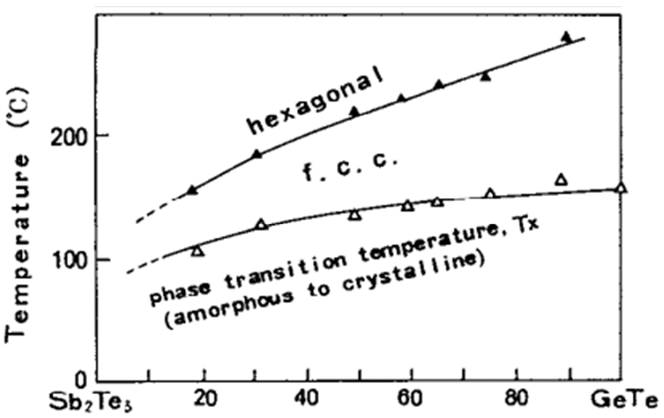

Fig. 1.4: Phase transformations in GeTe – Sb_2Te_3 compounds during DSC with 20 °C/min heating rate, first published in Ref. [5].

Tab. I: Stable phases in the ternary Ge-Sb-Te system, reproduced from Ref. [5].

Designation	Phase	Molar percent					
		Ge_{min}	Ge_{max}	Sb_{min}	Sb_{max}	Te_{min}	Te_{max}
L	Liquid solution	0	100	0	100	0	100
L'	"	0	50	0	40	50	100
L"	"	0	100	0	100	0	60
Ge	Ge	99.65	100	0	0.035	0	0.015
Sb	Sb	0	2.5	97.5	100	0	1.3
Te	Te	0	0.01	0	0.014	99.986	1
α	Sb_2Te_3	0	3.6	40.0	40.4	59.6	61.0
γ	$Sb_{1-x}Te_x$	0	8.0	40.4	51.0	41.1	49.0
δ	$Sb_{1-x}Te_x$	0	11.0	63.3	83.6	16.4	36.7
β^*	β-GeTe	39.5	49.8	0	11.5	50.2	53.3
α^*	α-GeTe	47.47	49.71	0	0.5	50.29	51.15
γ^*	γ-GeTe	47.52	49.12	0	0.5	50.88	51.24
A	$Ge_2Sb_2Te_5$	27.27	27.27	18.18	18.18	54.55	54.55
B	$GeSb_2Te_4$	14.28	14.28	28.56	28.56	57.16	57.16
C	$GeSb_4Te_7$	7.8	8.4	33.3	33.8	58.3	58.4

1.3.2 Structure of GeTe – Sb_2Te_3 compounds

In order to understand this crystallization behaviour it is useful to first regard the edge cases Sb_2Te_3 and GeTe. Sb_2Te_3 crystallizes into the rhombohedral R $\bar{3}$ m (H) phase that is strongly related to the trigonal symmetry of the stable GST configurations[37]. This phase displays some extraordinary properties. Due to its intrinsic weakly bonded Van-der-Waals (VdW) gap in the crystal structure, it is the simplest three-dimensional topological insulator known so far[38]. It also possesses excellent thermoelectric properties[39]. At increased pressures Sb_2Te_3 undergoes two phase transformations into monocline C 1 2/m 1 phases, thus losing its VdW-layered character, and subsequently into a highly disordered body-centred cubic I m $\bar{3}$ m phase[40]. The authors of the study even went so far as to speculate that Sb_2Te_3 may undergo a pressure transformation to topological superconducting akin to Bi_2Te_3[38]. While this pressure-induced phase transformation behaviour may seem unrelated at first glance since phase change material experiments and applications usually take place at ambient pressure, the pressure for the first rhombohedral – monocline transformation step at 9.3 GPa may be sufficiently low to allow pressure-induced phase transformations of local lattice fragments within strain fields of defects and interfaces in thin films.

GeTe possesses a metastable and a stable crystal structure, the transition between which is fluid[41]. At low temperatures it will crystallize into the rhombohedral (R 3 m) structure, with three long and three short Ge-Te bonds.

As the temperature increases this rhombohedral unit cell will be distorted in the cubic <111> direction until the crystal forms the NaCl-type F m $\bar{3}$ m lattice, in which the two cubic sublattices are fully occupied by Ge and Te respectively. One would therefore, in a naïve first assumption, expect a mixture of the two components to exhibit crystal structures that are characterized by competition of the two aforementioned structural patterns. On the one hand VdW layering, and on the other a metastable-stable transition from rhombohedral to cubic symmetry. However in reality, while VdW layering plays a prominent role in the stable structures of stoichiometric compositions, the metastable structure in $(GeTe)_{1-x}$ - $(Sb_2Te_3)_x$ compounds is generally described as a cubic NaCl-type structure with systematic distortion of the Ge/Sb octahedral sites similar to the off-centre shifts in rhombohedral GeTe[42]. Thus, the amorphous – metastable – stable transition path moves from disordered amorphous, to distorted cubic, to rhombohedral VdW layered (trigonal). Schematic models of crystalline Sb_2Te_3 and GeTe are shown in Figure 1.5.

In order to construct an ideal filled NaCl-type structure, exactly 50% anionic species (Te) and 50% cationic species (Ge,Sb) are required. In contrast, moving along the quasibinary tieline, replacing x amount of GeTe with Sb_2Te_3, only 2/3rds of every Ge cation are replaced by a Sb cation. The question arises how Ge, Sb and vacancies are distributed on the sublattice, and many resources have been expended to find a conclusive answer.

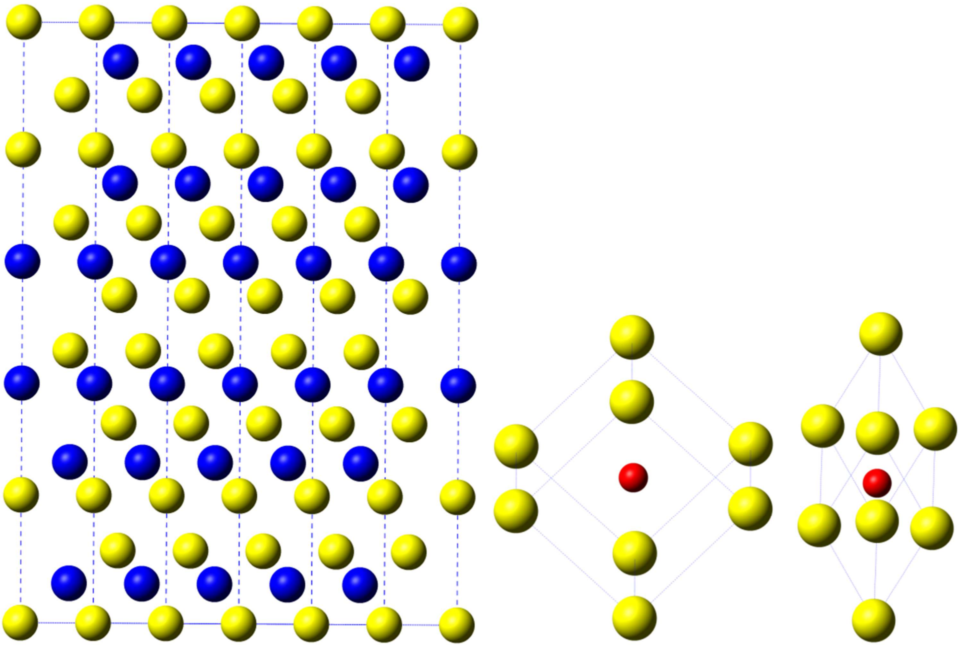

Fig. 1.5: Layered structure of Sb_2Te_3 (left) in [110] = $[11\bar{2}0]$ projection, cubic high-temperature structure of GeTe (centre) and rombohedral distortion of the cubic structure of GeTe at low crystallization temperatures (right) in $[2\bar{1}\bar{1}]$ projection. Te atoms are represented by yellow spheres, Ge by red spheres and Sb by blue spheres. The central Ge atom in the rhombohedral GeTe structure is displaced from the (1/2,1/2,1/2) position in [111] direction.

Most prominently, neutron diffraction and extended X-ray absorption fine structure are able to yield information on local arrangements in lattices. Based on such findings, the distorted nature of the octrahedral arrangements in the cubic lattice has been proposed[43] (see Figure 1.6). However, investigative methods to date have been unable to discern any chemical ordering on the sublattice, and thus the common structure model assumes uniform mixing according to stoichiometric concentrations. Theoretical studies on this matter are often based on density functional theory, and thus attempt to determine energy minima for specific short-range order configurations. Based on such models, ordering of the Ge, Sb and vacancy components into layers has been predicted[44]. Such studies need to be approached with a certain amount of scepticism, since naturally the lowest energy configuration of the metastable phase is the stable lattice configuration. Thus, reports on systematic ordering in the metastable phase can often be interpreted as describing the transformation path to the layered trigonal arrangement[45, 46]. The sublattice disorder represents a thermodynamic degree of freedom in the material system, and partial ordering can be used to explain the gradual property changes upon further phase transformation[47], as will also become apparent during the discussion in the experimental results section.

The ideal concentration of the intrinsic vacancies can be predicted depending on the relative concentration x of Sb_2Te_3 according to Ref. [48]:

$$N_{vac} = x/(1+2x)\,, 0 < x < 1 \tag{1.1}$$

The lattice models of common metastable and stable $(GeTe)_{1-x} - (Sb_2Te_3)_x$ compounds are illustrated in Figure 1.7. As the vacancy concentration changes in the metastable cubic phase, so too does the spacing of the intrinsic VdW gaps in the stable structures. When comparing vacancy concentration and trigonal structure it becomes apparent that one can be related to the other by moving all vacancies in the metastable state into a single Ge/Sb layer. The resulting unit cell after energy minimization is generally described as a P $\bar{3}$ m 1 trigonal lattice[49]. In further discussions of these structures, a sequence of Te and Ge/Sb layers bordered on both sides by a VdW gap will be referred to as a “building block” of the trigonal lattice due to the weak VdW interaction across the vacancy gap. The specific stacking order in stable trigonal lattices has been subject of much discussion, with various authors proposing e.g. for the $Ge_2Sb_2Te_5$ composition sequences such as Ge-Te-Sb-Te-v-Te-Sb-Te-Ge-Te-…[50] or the inverse Sb-Te-Ge-Te-v-Te-Ge-Te-Sb-Te…[51] (with v denoting a VdW vacancy gap). The best matches between experimental data and stacking models so far are those shown in Figure 1.7, and these share some common features for different compositions.

Most prominently, the layers retain some degree of random mixing on the Ge/Sb sites. The mixed Ge/Sb layer closest to the vacancy gap always exhibits the highest Sb concentration, e.g. Ge33:Sb66 for $Ge_2Sb_2Te_5$[52], Ge25:Sb75 for $GeSb_2Te_4$[53] and Ge36:Sb64 for $Ge_3Sb_2Te_6$[54]. Conversely, the Ge/Sb positions on the inside of the building blocks are rich in Ge, with concentrations ranging from Ge50:Sb50 to Ge77:Sb33.

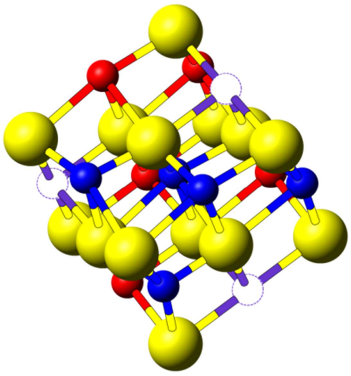

Fig. 1.6: Schematic model of cubic metastable $(GeTe)_{1-x}$-$(Sb_2Te_3)_x$ $0.1 < x < 1$ compounds. Yellow spheres indicate Te, while red, blue and magenta indicate the random distribution of Ge, Sb and intrinsic vacancies (not necessarily in the concentrations shown), respectively.

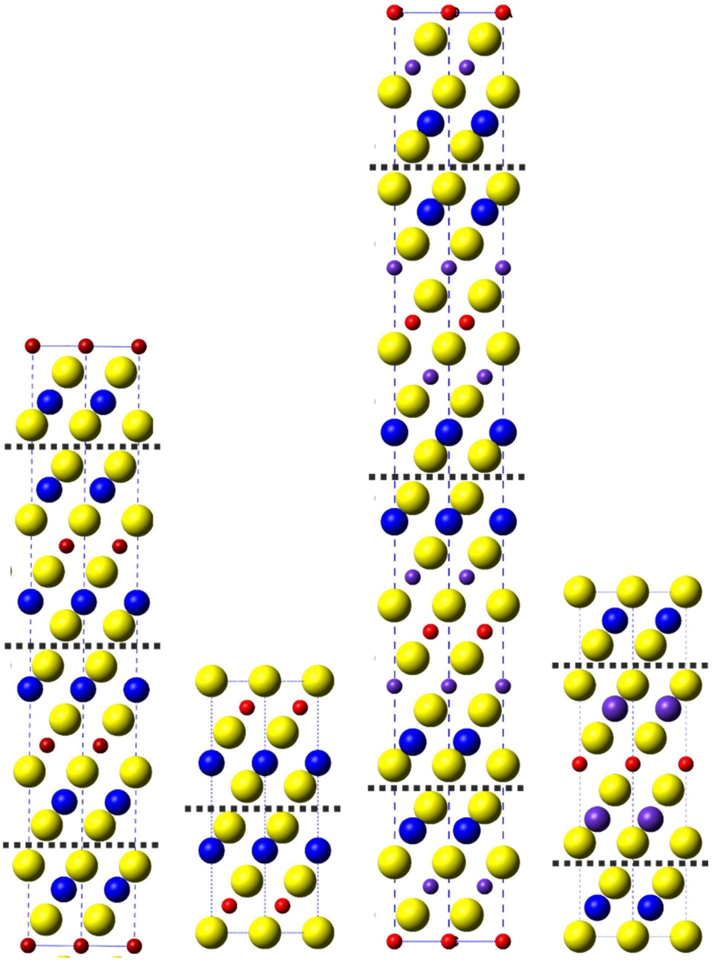

Fig. 1.7: Unit cell models of various stoichiometric GST compounds in the stable trigonal stacking, $[11\bar{2}0]$ projection. Left to right: $Ge_1Sb_2Te_4$, $Ge_2Sb_2Te_5$, $Ge_3Sb_2Te_6$ and $Ge_1Sb_4Te_7$. Yellow spheres indicate Te positions, while red, magenta and blue spheres indicate Ge/Sb positions of various mixed concentrations (see Table A.I for details). Dashed lines mark VdW gaps.

Meanwhile the positions of the individual Sb-rich columns are shifted towards the VdW gap, resulting in 3 long and 3 short bonds, while the Ge-rich positions are situated around the octahedral sites (centred if the unit cell is mirror symmetric at the Ge-rich plane, slightly off-centre if the mirror plane lies in a central pure Te plane). Purely phenomenologically, the Sb-Te-v-Te-Sb layer sequence therefore resembles a partial

Sb_2Te_3 building unit, and the Te-Ge-Te sequence resembles the cubic symmetry of a partial GeTe lattice fragment, all the while retaining significant amounts of “wrong” Ge and Sb content and pm-scale octahedral distortions. While this is surprising for a lowest-energy configuration of the lattice, no model to date has been able to propose an ordered arrangement of Ge and Sb within the same individual layer that sufficiently matches the experimental evidence. One of the greatest difficulties for atomistic simulations in Ge-Sb-Te phase change materials is a reliable expression of the sublattice disorder in the underlying model structures. Reported structural parameters from literature for various $(GeTe)_{1-x} – (Sb_2Te_3)_x$ compounds have been compiled in Appendix Table A.I. While the single-digit precision in concentrations on the Ge/Sb sites suggested therein may imply confidence in the idealized structural models, the wealth of literature studies shows the difficulty in determining exact distributions in stable configurations. One of the central questions discussed in this work was whether such structures could also be resolved and identified experimentally by electron microscopy methods in real crystal lattices[55].

Thus in summary, for e.g. $Ge_2Sb_2Te_5$ (x=0.333..) the expected intrinsic vacancy concentration in a NaCl-type structure is 20% and when replacing 20% of all Ge/Sb (111) layers in a cubic cell by regularly spaced vacancy layers, one arrives at a structure that is very similar to the trigonal stacking of $Ge_2Sb_2Te_5$. Three further differences remain, namely a small expansion of the lattice into the vacancy layer gap, a small off-centre shift of some Ge/Sb positions, and a preferential chemical ordering of Sb into the first Ge/Sb layers adjacent the vacancy gap. The lattice expansion can be viewed as an elastic relaxation into the vacancy gap. The Ge/Sb offsets from octahedral sites have been interpreted as a Peierls distortion of a linear bond chain[56] (see also section 1.3.5) resulting in 3+3 long and short bonds both in the metastable cubic arrangement and the Sb-rich layers of the trigonal structure, while the last is not fully explored yet, but possibly may be rooted in the electronic configuration at the VdW gap.

1.3.3 Glass formation in undercooled liquids

One complicating factor in the operation of a phase change device is that the amorphous structure as-deposited by the thin film deposition process may possess a characteristic short-range order selective to the deposition parameters, which in turn may differ from the configuration after re-amorphization[57]. In physical vapour deposition processes in particular, the target material may be deposited in small clusters mixed into the particle stream. A mass spectrometry study of the plasma composition in GST laser ablation plumes reported up to m/z = 629 mass over charge ratio clusters at very high laser fluences[58]. While not immediately comparable to the deposition conditions used for the thin films investigated in this work, this does illustrate that cluster ablation can play a role in the pulsed laser deposition of Ge-Sb-Te materials. Depending on the energetic conditions on the surface and the deposition rate, these clusters may get dissociated or rapidly buried beneath new impinging material, and the as-deposited structure can on the one hand possess crystalline seeds, or on the other hand be even more disordered than the re-amorphized structure (since depending on the power profile of the switching process cubic fragments may be retained). Thus, in real application scenarios, it is important to condition the material by applying multiple SET-RESET cycles before first application of the device. Similarly, for experimental and theoretical observations of the amorphous structure and fast amorphous to metastable transition under device conditions, the re-amorphized state usually described as a melt-quenched glass is predominantly taken into consideration.

In general, amorphous structures of phase change alloys are described in glass formation theory[59]. Glass formation is inherently kinetically driven, meaning that the observed timeframe and rates of structural changes in which a material presents glassy structure and behaviour is central to its classification as an amorphous glass. The most useful macroscopic property in this regard is the viscosity $\eta(T)$ of the material, relating the rate of deformation response dx/dt to a constant external stress τ at a given temperature T. For GST phase change compounds, the reduced glass transition temperature T_g/T_m, the temperature at which the viscosity surpasses 1 x 10^{12} Pa·s in a second order phase transformation during cooling, typically lies around 0.5 – 0.55.

Glass forming materials are empirically classified as either strong or fragile liquids. In strong glass forming liquids, the viscosity follows Arrhenius behaviour, i.e.:

$$\eta(T) \propto e^{\frac{E_a}{k_B T}} \tag{1.2}$$

where E_a denotes an activation energy and k_B the Boltzmann constant. In such liquids, overcoming the activation barrier for viscous deformation is thus purely driven by the Boltzmann statistic of thermal energies. This results in a high T_g (reduced T_g/T_m close to 1) and rigid glasses. In contrast, fragile liquids are described by a Tamann-Vogel-Fulcher (TVF) behaviour[60]:

$$\eta(T) = \eta_0 \, e^{\frac{A}{(T-T_0)}} \tag{1.3}$$

with η_0 denoting the saturation viscosity in the liquid and A, T_0 denoting constants. Another way to classify glass formers is by defining the fragility m of the undercooled liquid. Formally this is commonly introduced as the rate of change in the temperature dependence of the viscosity at the glass transition temperature[61]:

$$m = \frac{d}{d({}^{T_g}/_{T})} log_{10}(\eta(T)), T = T_g \tag{1.4}$$

Experimentally, fragilities have been observed to range from 20 for strong Arrhenius behaviour in classical glass formers like SiO_2 to 150 in fragile glass formers with TVF behaviour such as weakly VdW bonded organic liquids, cis/trans transitions and materials with large anharmonicity[62]. $Ge_2Sb_2Te_5$ and GeTe reportedly possess a fragility of m = 100 and 90, respectively[63, 64], and are thus classified as fragile glasses.

Radiation damage by knock-on displacement is usually characterized by the displacement energy threshold E_d, which in a disordered amorphous structure is not easily accessible but should be low in p-bond covalent networks of high fragility. Threshold values of the incident beam energy for knock-on displacement of e.g. carbon in graphite and diamond structure are 140 keV and 330 keV, respectively[65]. The maximum energy transfer to Ge (the lightest species present in the material) is ≈11.8 eV at 300 keV, and pure Ge possess a sputtering threshold energy between 115 and 181 keV at a sublimation energy of 3.86 eV, while Ref. [66] estimated that Ge in GST225 possesses a displacement energy (often used interchangeable with the sublimation energy) between 7 and 17.2 eV and a corresponding threshold energy between 200 and 400 keV. More exact values for the displacement energy in the specific phase and composition are not available, yet this does illustrate that under prolonged electron beam exposure at 300 keV amorphous GST can be able to form crystalline seeds. As the crystal growth of GST is dominated by the nucleation and growth in the bulk material[67] (Volmer-Weber model), these seeds can lead to rapid crystallization of amorphous samples if insufficient care is taken in limiting the electron beam dose.

1.3.4 Structural features of the amorphous-metastable switching

One of the major challenges in understanding the phase change mechanism is the experimental inaccessibility of local arrangements in amorphous structures. While coherent diffraction in crystalline solids allows fine probing of the average crystallographic symmetries, disordered amorphous structures by their very nature impede, but not entirely prohibit, this. Experimental studies therefore have typically relied on X-ray absorption effects[68] and vibrational properties[69, 70] (Raman spectroscopy), while theoretical approaches make use of computationally very intensive density functional (DFT) and molecular dynamics (MD) simulations[14, 71]. Both approaches have in common that they aim to characterize the structure primarily by means of interatomic distances and angles between the various atomic species.

Since the radial distribution is also accessible through TEM methods[72] (see experimental section 3.2), its basic concepts shall be shortly introduced. The pair distribution function (PDF) $g(r)$ in a model structure is the spherically averaged distribution of interatomic vectors $r_{i,,j}$ with ρ denoting the density:

$$g(r) = \frac{1}{\rho^2} \sum_{i} \sum_{j \neq i} \Delta r_i \Delta r_j - r \tag{1.5}$$

This can be restricted to specific atomic species a and b, e.g. Ge-Te or Sb-Te thus yielding the partial radial distribution function $g_{a,b}$ (RDF), from which the average local coordination between elements a and b $n_{a,b}$ can be extracted:

$$n_{a,b} = \int_0^{R_{min}} \rho_{a,b}(r) g_{a,b}(r) 4\pi r^2 \, dr \tag{1.6}$$

Note that the cutoff radius R_{min} can be critical. In the distorted rombohedral structure of GeTe for example, with short (2.8 A) and long (3.2 A) bonds around the Ge positions, any cutoff below 3.2 A will result in a tetrahedral coordination and layered structure while in practice this configuration is interpreted as an octahedral distorted arrangement in the cubic (rombohedrally distorted) framework[73, 74]. In amorphous structures this aspect is exacerbated since the RDF will possess less pronounced peaks at larger radii. The pair distribution function can be compared with diffraction experiments by Fourier-transformation of $g_{a,b}$ weighted by the relative concentration fraction and scattering form factor or coherent scattering length for X-ray and electron scattering or neutron scattering, respectively. This yields the structure factor $\phi(Q)$ in reciprocal (spatial frequency) space. Based on such investigations, some central features of amorphous phase change glasses have been identified. The most prominent aspect is the local octahedral coordination of Ge, Sb and Te.

The electron configuration of Ge, Sb and Te in the ground state is 3d10 4s2 4p2, 4d10 5s2 5p3 and 4d10 5s2 5p4, respectively. In the case of purely covalent bonding, the 8-N rule ("octet rule") aims to predict the expected coordination, where N is the number of valence (outer shell) electrons. According to this simple relation, Ge, Sb and Te would be expected to be 4-fold, 3-fold and 2-fold coordinated, respectively. In reality, aforementioned studies have determined coordination numbers e.g. for $Ge_2Sb_2Te_5$ of Ge 4.3, Sb 3.7 and Te 2.9 in the amorphous structures[75] and thus overcoordinated for a purely covalent glass network. Furthermore a significant amount of homopolar "wrong" Ge-Ge bonds has been discovered[68]. The tendency to form octahedral (3+3) coordinated glasses appears to be a central motif of phase change materials, with a systematic order parameter being the average number of valence electrons per atom which should not exceed 4.25[76]. As mentioned above, the differences between as-deposited (AD) and melt-quenched (MQ) amorphous GST can be significant, thus confounding a realistic description of the amorphous – metastable reversible phase transition.

The most notable difference between AD and MQ structures can be found in the reported fraction of homopolar pairs and tetrahedral coordinated Ge[77]. In AD-GST, 10% or more Ge-Ge pairs and up to 30% tetrahedral Ge (or up to 50% in GeTe) have been found by MD studies[57, 78]. The large scattering of reported values may be rooted in the different deposition methods used in experimental observations, as well as the large parameter space for MD calculations. The possible presence of large amounts of tetrahedral Ge has led to speculations about the so called umbrella-flip model of the phase change mechanism[79] (see Figure 1.8). In this hypothetical process, the Te sublattice of the cubic phase is essentially preserved in the amorphous phase bar small random distortions, while a significant portion of the Ge atoms on distorted octahedral sites break the 3 longer bonds and are thus displaced into tetrahedral positions. Such a process could occur without melting (extended bond-breaking) of the lattice. However, further corroborating evidence for this process is somewhat inconclusive, and the idea has subsequently fallen out of favour. In particular, the symmetric framework of the Te sublattice has not been identified elsewhere to the degree predicted outside the metastable cubic phase. The PDF of Te-Te distances in MQ-GST has been found to peak at the next-nearest neighbour around 4.16 Å[43], and rapidly diminishes until no further maxima are found above 10 Å. However it has also been noted that in the presence of intrinsic vacancies in the amorphous (long-range disordered) phase, distorted octahedral and tetrahedral sites may exhibit similar peaks in the RDF[80]. It may be possible that multiple phase transformation paths are valid depending on the initial structure and the thermal profile of the process i.e. the umbrella-flip model, the MQ approach with ring motifs, and the interfacial switching Ge layer-flip model in superlattices (see section 1.3.6).

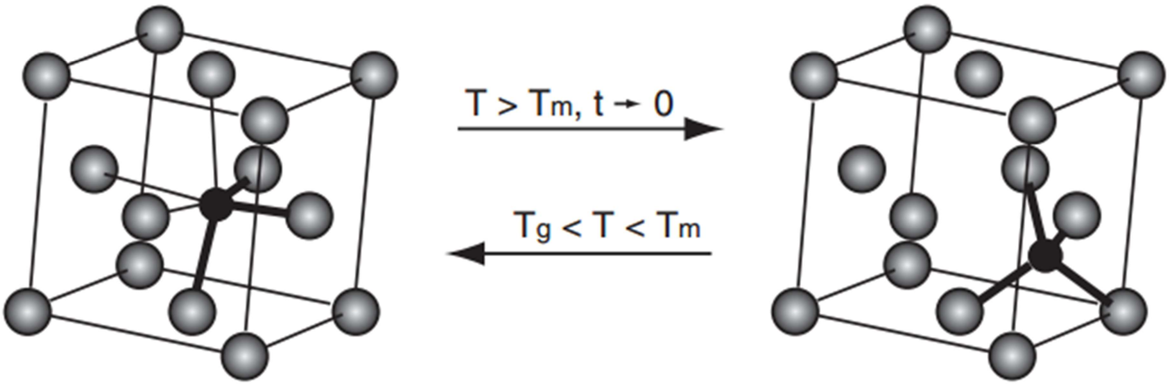

Fig. 1.8: The umbrella-flip process as proposed in Ref. [79]. Distorted octahedral Ge coordination (left) and tetrahedral coordination (right)

In the MQ approach, the central structural features in amorphous GST are alternating ring structures. Studies on the pair distribution function and bond angles in the MQ state of $Ge_2Sb_2Te_5$ have determined up to 80% of all Ge content situated in 4-member rings alternating A (Ge,Sb) and B (Te) species with close to 90° bond angles[81]. Such a “square” ring essentially resembles a fragment of the cubic metastable phase. The coordination of each member is then determined by the inclination of the fragment against its surrounding and the concentration of adjacent vacancies, but the bond angle implies a generally octahedral arrangement as expected. Larger rings of 6 and 8 members can be described as lattice fragments enclosing a substitutional vacancy, while the disordered arrangement of the fragments against each other can be regarded as enclosing interstitial sites. Thus, the reorientation of square ring fragments against each other to form the cubic lattice with intrinsic vacancies only requires movement over short distances. The central question then arises why the optical and electronic properties change so drastically with a small structural rearrangement. While this topic regularly sparks new discussion, the currently prevalent model is that of a resonant bonding network in the metastable phase[82].

1.3.5 Origin of the property contrast

The resonant bonding effect is described as pronounced delocalization of bonding p-electrons along a chain of octahedral coordinated positions along the three axes $p_{x,y,z}$ of nearest-neighbour orientation[83]. It thus favours a high-symmetry linear arrangement within the lattice. This linearity is counteracted by the Peierls instability effect[84], which posits that an alternating arrangement of long and short bonds is overall energetically more favourable than an equal charge delocalization (see Figure 1.9), and the resulting structure resembles a compromise between the two effects. The electrons in a resonant bonding chain possess a high polarizability due to the pronounced delocalization, resulting in the large optical contrast to the amorphous phase. The individual Peierls-distortion of the Ge/Sb sublattice positions is sufficient to have a systematic effect in e.g. the metastable rhombohedral distortion of the GeTe lattice. It can be seen that small rearrangements due to amorphization as well as intrinsic vacancies and vacancy clusters can break such a distorted linear chain, and the amorphous structure reverts to a predominantly covalent network. Defect disorder thus plays a significant role in the functional behaviour of PCMs.

Recently, a somewhat competing model of the switching process has been proposed that argues the partial sp^3 hybridization of Ge atoms on octahedral sites creating Ge sp^3 lone-pair (LP) nonbonding electrons[85]. It aims to explain the significant number of tetrahedral coordinations in the amorphous phase with the LP mediated formation of transient three-centre bonds of the homopolar Ge-Ge pairs during amorphization creating valence alternation pairs[86]. While the physics of this model are certainly much more involved than can be presented here, one aspect that deserves prominent mention is the importance of LP electrons in both the dynamics of the phase change process as well as their functional properties through the contribution of dative bonding LPs to the valence band near the edge of the band gap[87]. If this model can be refined and further experimentally tested, it may ultimately open up the possibility of designing phase change materials for specific applications from first principles.

Although the abrupt changes in properties at the phase transformation points are central to the functional characteristics of phase change materials, these also change gradually with continuously increasing temperature. In the amorphous phase, an increase in temperature also increases the free carrier concentration in accordance with the Fermi statistics in a p-type (hole) semiconductor[88]. The Fermi level is pinned by defect states (acceptor vacancies) inside the band gap, with a reported optical bandgap of about 0.6 – 0.9 eV for GST225. The continuous increase in conductivity in the cubic phase was attributed to an increase in free carrier mobility.

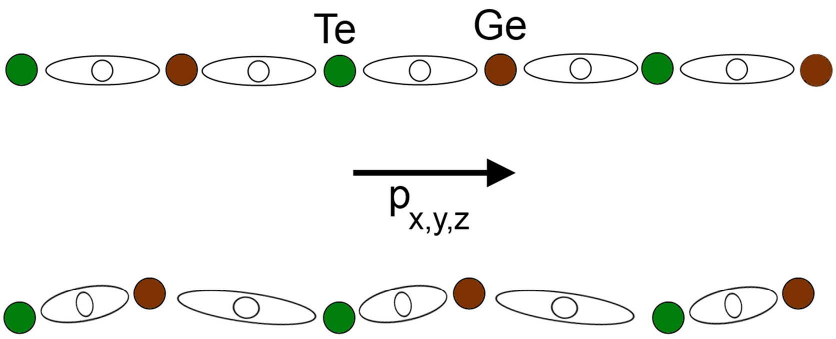

Fig. 1.9: Resonant bonding along one p-orbital chain in a 3D crystal (top) and splitting into long and short bonds due to Peierls instability (bottom).

Due to the high hole concentration of about 10^{20} cm^{-3}, the Fermi level was interpreted to lie at the edge of the valence band in a degenerate p-type semiconductor with a direct band gap of 0.5 eV[89] in the metastable crystalline phase. The hole mobility varies around 1 cm^2/Vs depending on the micro- and nanostructure. Grain boundaries and defect centres act as scattering sites for electronic conduction and as crystallites grow and become more uniform with crystallization time or temperature the impact of these on the overall mobility decreases. Investigation of various disordered structures have also been interpreted to lead to Anderson localization at vacancy sites and clusters of vacancies[90]. The layered ordering of vacancies and the partial chemical ordering of the Ge/Sb sublattice in the trigonal high-temperature phase is accompanied by a metal-insulator transition (MIT) which has been correlated to a reduction of these localized states[46]. Most notably this transition was described as to occur after the structural transition to the trigonal symmetry, simultaneous to the highly ordered vacancy layer formation. These additional property transitions have sparked ideas of multi-level resistance state memory designs[31]. Simulations of the electronic structure in layered GST depending on various stacking sequences have further indicated that an ordering of Te-Sb-Te-v-Te-Sb-Te leads to topological insulating behaviour while Te-Ge-Te-v-Te-Ge-Te leads to conducting interface states in isolated stacks of building blocks[91] (see also the speculation about a topological superconducting state mentioned before).

A full discussion of these phenomena goes beyond the scope of this work, in particular since these are still subject to ongoing research that may radically change the interpretation of the physical models. It is possible to speculate that the ordered arrangement of the Te lone-pair p-electrons at the VdW gaps, depending on the Sb concentration in the adjacent layer, is ultimately responsible for the MIT behaviour, and has strong implications for the anisotropic characteristics both in electronic conduction and thermal (phonon) scattering. The most concrete application of the functional properties in layered Ge-Sb-Te structures however is the interfacial switching effect that shall be briefly introduced next.

1.3.6 iPCM superlattices

The interfacial switching effect in superlattices of layered GST[92] is discussed separately in this subsection for two reasons. It describes a functional transformation within the lattice symmetry framework of the crystalline phases, and it has been first reported in the trigonal layered arrangement of the lattice. Accordingly it relies on the pre-existing chemical ordering of the Ge/Sb sublattice and can be expected to be particularly sensitive to defect structures. iPCM thin films consist of a superlattice alternating m Sb_2Te_3 and n GeTe layers in a VdW-layered arrangement[93]. Upon performing resistive heating plug assisted switching experiments on superlattices, similar to more conventional phase change memory cells, it was found that the energetic threshold for a change in resistance state was both lower (by almost half) than in an amorphous - metastable FCC cycle and more stable over 10^6 cycles. In addition a number of more esoteric effects such as multiferroic behaviour[94], giant magnetoresistance[95] and magneto-optical Kerr rotation[96] have been reported when directly applying electric or magnetic fields. These mark PCM superlattices as possible candidates for spintronic concepts[97]. The principle behind the interfacial switching effect is yet to be fully explored, but current ideas favour a layer switching model of the Ge planes, wherein a $(GeTe)_2$ block switches stacking order between Te-Ge-Te-Ge and Te-Ge-Ge-Te[98]. On the one hand, this meshes well with the functional significance of homopolar Ge-Ge pairs in the amorphous phase proposed elsewhere as mentioned before, however on the other hand direct observational evidence of a metastable Ge-Ge layered configuration still remains unsatisfactory[99]. While it has been confirmed that the superlattice orientation is conserved between cycles, it should be exceedingly difficult to entirely prevent intermixing of the layers during heating pulses[100]. Furthermore the exact nature of the layer switching process is not clear. Some proposals describe an abrupt flip of multiple Te and Ge positions[101], while alternatively one might imagine a continuous side-to-side movement of a stacking boundary within the affected layer (see experimental results sections 3.3.3 and 3.4 for such localized stacking defects in layered GST). It thus becomes clear that imaging the atomic structure by TEM and correlating the observed structures with the chemical ordering is exceedingly useful to gain further insight into such superlattices[102].

1.4 The role of structural defects in phase change materials

The prominent influence of lattice disorder on the functional properties of phase change materials has already been introduced above. Since this work deals with the structural features of real PCM lattices as observed by TEM, the various observable defect structures in crystalline lattices shall be briefly summarized.

1.4.1 Point defects

The smallest defect structures are those that only deal with displacements of single atoms from their expected positions in the lattice. Such point defects are generally classified as intrinsic or extrinsic, and can consist of interstitial atoms, additional vacancies or substitution of one atomic species with another. Intrinsic defects are those that arise from random thermal displacements of lattice constituents themselves in thermal equilibrium at non-zero temperatures. GST PCMs can possess an extraordinary large amount of intrinsic vacancies in the amorphous and metastable phase[103]. Since these are not related to interstitial atoms as in the generation of Frenkel pairs, and thus cannot recombine but rather aggregate to form the VdW gap in the trigonal arrangement, it is most useful to interpret them as an additional “virtual” component of the material system. Nevertheless, intrinsic vacancies break the resonant chains and thus increase anharmonicity[29], but also facilitate the fast amorphization cycle. The distribution of all three sublattice components Ge, Sb and vacancies falls under the heading of chemical disorder, and is thus not an exclusively statistical process but is mediated by the chemical environment of the sites.

While the concentration of intrinsic point defects c_{def} is governed by a thermal equilibrium, a more detailed description of the formation energy E_{form} i.e. $d(G)/d(c_{def})$ of intrinsic point defect pairs depends on the chemical and electronic properties of the displaced atom[104]:

$$E_{form} = E_{tot,defect} - E_{tot,bulk} - \sum_i n_i \mu_i + Q\left(E_F + E_{VB,bulk}\right) + \xi(Q) \qquad (1.7)$$

Here, $E_{tot,defect}$ denotes the total energy of the environment of a defect (i.e. a supercell containing the defect), $E_{tot,bulk}$ the total energy of an equivalent volume from the undisturbed lattice, n_i the change in number of i-th atomic species, μ_i its associated chemical potential, Q the charge state, E_F the Fermi energy, $E_{VB,bulk}$ the energy at the top of the valence band in the undisturbed lattice and $\xi(Q)$ an electrostatic correction term for the distribution of charged defects in the periodic lattice. It can thus be seen that the chemical potential, the charge state and the band structure all impact the intrinsic formation, as well as the exact arrangement in the chosen supercell from a partially disordered lattice.

Intrinsic interstitials are generated by displacement of constituent species into interstitial lattice sites. In a FCC framework of octahedral arrangements, the preferred interstitial sites are the tetrahedral positions at (1/4,1/4,1/4). However, in a lattice with intrinsic distortions, the distinction between tetrahedral interstitial and distorted octahedral arrangement near one or more vacancy becomes imprecise, and distorted tetrahedral sites near vacancy clusters may exhibit the same bond lengths as octahedral sites.

Extrinsic point defects can be generated through the in-diffusion of contaminants, predominantly oxygen from open surfaces. In addition, the energetic ion bombardment necessary to create sufficiently thin and uniform samples leads to ion implantation and defect generation[105]. These practical aspects are further discussed in Appendix B.

1.4.2 Line defects

Dislocations in crystals are grouped under the classification of line defects. Very generally speaking, they are introduced into the lattice due to additional lattice half-planes at the dislocation core. Arbitrary dislocations are described by the line vector L of the dislocation core, i.e. the view direction along the dislocation core, and the Burgers vector b that can be constructed by completing one circuit around the dislocation core, i.e. the amount and direction of deformation of the perfect lattice induced by the presence of the dislocation. The plane that is spanned by b and L is then the glide plane in which the dislocation can move without requiring interstitials or vacancies. Ideal dislocations possess Burgers vectors that are purely translation vectors of the lattice. The extreme case wherein dislocation line and Burgers vector are parallel describes a screw-type dislocation, while pure edge-type dislocations possess orthogonal line- and Burgers vector. Real structures will often possess dislocations that are mixed edge and screw type, or dislocation loops of edge and screw components that terminate on themselves. Dislocations necessarily terminate at defects, such as surfaces and interfaces (e.g. grain boundaries) or other dislocations, and can interact with each other both via the strain field in the lattice and by getting pinned in defect centres when crossing each other. The plastic deformation properties of materials are chiefly governed by the movement and interaction of dislocations. They can however also dissociate into partial dislocations with Burgers vectors that are not lattice translation vectors, such that the sum of partial dislocations results in an ideal dislocation. This is particularly important in crystals with a base of more than one component such as GST, since these can form complex stacking faults which are bordered by partial dislocations. If the Burgers vector of the partial dislocations is not parallel to the plane of the stacking fault it cannot glide along the planar defect unless diffusive motion of atoms is involved. In such a case the partial dislocations are effectively pinned unless they can interact with another set of defects. Such cases are also referred to as Frank partials or Frank dislocations. One relevant example of Frank partials in GST is the common case of a stacking fault by the addition of a close packed {111} layer of a FCC lattice. The most simple way to terminate such an extrinsic stacking fault within the bulk lattice is the formation of a partial edge-type dislocation with Burgers vector of the type a/3 <111> perpendicular to the plane of the stacking fault. An example of such a defect in GST can be seen in experimental results section 3.2.2.

Alternatively, partial dislocations can be mobile i.e. possess a burgers vector within the defect plane. Such partial pairs are commonly called Shockley partial dislocation pairs. Again describing the simple example of the FCC case, an intrinsic stacking fault can be formed by the displacement of a {111} layer along the easy slip direction <110>. Thus, a perfect edge-type dislocation with Burgers vector a/2 <110> (i.e. a lattice translation vector in the slip plane) can dissociate into a pair of Shockley partials by the formation of an intrinsic stacking fault that is bordered on both sides by partial dislocations with Burgers vector of the type a/6 <112> which still lie within the {111} defect plane. According to

Franks rule the elastic energy E_{el} of a dislocation is proportional to the square of the magnitude of its Burgers vector, where G is the shear modulus:

$$E_{el} \propto G * |b^2| \tag{1.8}$$

Thus, the formation of Shockley pairs is energetically favourable, and the resulting repellent interaction scales with the inverse of the distance i.e. the width of the stacking fault. A wealth of literature deals with the description of defects in solids, in general and for specific material systems[106-109]. TEM is a favoured method for dislocation analysis[110], since in e.g. the two-beam case they can result in strong contrast features.

1.4.3 Planar defects

Defects that describe the border between two lattice volumes of different orientation are regarded as planar defects. The most obvious planar defects are grain boundaries between similar grains and at interfaces. Between randomly oriented grains, grain boundary interfaces can contain amorphous disordered components as well as precipitates from extrinsic effects. In highly textured growth, neighbouring grains possess a preferential orientation that can result in energetically favourable coincidence site lattice (CSL) boundaries. The symmetry of the interface is described by the number of lattice points of the crystal lattice contained within the (two dimensional) unit cell of the coincidence lattice, Σ. A special case of coincidence lattice interfaces are twin boundaries, which in a FCC symmetry possess a CSL of $\Sigma = 3$. Rotation twins describe grain boundaries within a lattice plane across which the lattice is displaced by a fixed translation and rotation around the plane normal, but otherwise remains unchanged. As will be seen in results and discussion sections 3.3 and 3.4, the weak VdW interaction across the vacancy layer gaps in trigonal GST leads to an easy formation of rotation twin variants (see Figure 1.10). Twin variants often form when the grain is strained during growth, such as when the material undergoes a volume change during phase transformation (up to 7% in GST upon amorphous – metastable transition, but <2% during metastable – stable transformation) or due to small misorientations between neighbouring faceted grains energetically favouring small-angle grain boundaries. Twin planes can act as easy glide planes for partial dislocations and as scattering centres for phonons.

Stacking faults describe a defect in the stacking order e.g. the ABCABC… stacking of close packed {111} planes in FCC can contain either a missing layer (intrinsic stacking fault) resulting in an ABCAB_ABC… stacking, or an additional layer (extrinsic stacking fault) resulting in ABCAB_A_CABC… stacking. Such stacking faults are necessarily bordered by a dislocation or an interface. Similarly, in close-packed hexagonal HCP structures stacking faults can be intrinsic ABABACAC… (I_1) and ABABCACA… (I_2) or extrinsic as in ABABACBABA… stacking. In lattices with a complex multicomponent base such as GST however, lattice planes of either sublattice are not equivalent.

Consequently, a missing {111} layer of the Ge/Sb/v sublattice will be associated with an additional lattice distortion in the widening of the Te-Te faulty stacking distance. As introduced in section 1.3.2, the close stacking of Te-Te in e.g. Sb_2Te_3 only occurs in high-pressure modifications. A missing Te {111} plane would result in a close stacking of Ge/Sb-Ge/Sb, which appears not to be chemically stable, i.e. neither a close stacking of Ge/Sb-Ge/Sb nor a vacancy gap between two Ge/Sb layers is experimentally observed.

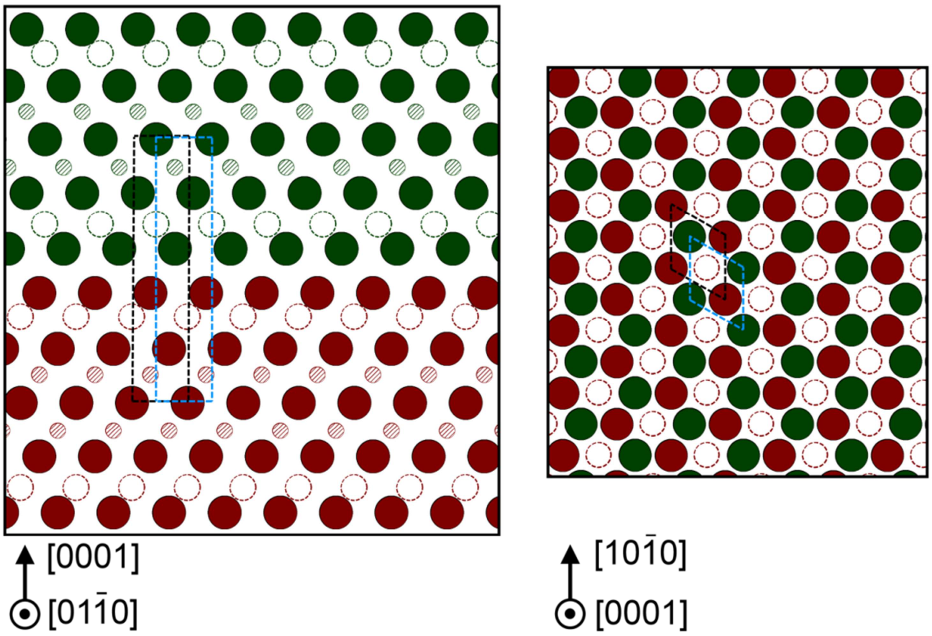

Fig. 1.10: 60° rotation twin boundary across a (0001) vacancy gap in trigonal GST, with a translation of <1/2,1/2,0,0>, seen in $[11\bar{2}0]$ projection of the lower half of the model (left), and in a three layer thick cut-out of the $[0001]$ projection (right). Dashed lines mark unit cells of the two twin variants, while filled, empty and dashed spheres correspond to Te, Sb-rich and Ge-rich sites, respectively.

1.4.4 Epitaxial interfaces

Epitaxial interfaces deserve special consideration since the final experimental subchapter of this work deals with the observation of oriented growth of GST on Si(111). An epitaxial interface describes a planar defect between a substrate material of fixed crystallographic orientation and another single-crystalline layer material above with a specific orientation relation. Homoepitaxy occurs if both materials are of the same composition, while heteroepitaxy describes the case wherein substrate and layer are of different compositions. Analogous to small angle grain boundaries and twins, it can be readily seen that two adjacent crystal planes of different composition (and potentially different symmetry) can form a CSL. The CSL is determined by the surface reconstruction of the substrate lattice. Often in material pairings of identical interface symmetry, the favoured configuration is a direct continuation of the substrate lattice. In either case, the layer material is affected by the misfit strain due to differences in lattice spacing. The accommodation of this strain in the thin film leads to the formation of misfit dislocations.

Epitaxial thin film growth can be divided into three categories. 2D Layer-by-layer growth of closed films (Frank-van der Merwe), layer-by-layer growth of separated crystallites and subsequent coalescence (Volmer-Weber) and island growth on top of a wetting layer (Stransky-Krastanov). While in-situ electron diffraction experiments (RHEED) can yield information on the growth behaviour close to in real time[111], each growth mode also leads to characteristic grain structures and strain effects visible in TEM. Frank-van-der-Merwe growth typically results in very uniform strained layers with misfit dislocations, while Volmer-Weber and Stransky-Krastanov growth are associated with multiple domain walls, oriented facets resulting in increased surface roughness, and strained or relaxed substrate interfaces, respectively. The peculiarity of the VdW layering in stable GST leads to a situation wherein the favourable interface configuration is that of a VdW gap close to the substrate. Due to the weak coupling across the gap, the CSL formation has a weaker impact on the lattice orientation in the layer material, and a 10% lattice mismatch Si(111)||GST(0001) of a straight continuation at the interface possesses a Σ9 CSL. Domains in Volmer-Weber and Stransky-Krastanov growth structures can however possess in-plane misorientations of multiple degrees. The resulting epitaxial interfaces are classed as Van-der-Waals or quasi Van-der-Waals epitaxy, when the layer material is either a purely 2D-layered structure such as graphene[112] or a quasi-2D layered structure such as Sb_2Te_3[113], respectively. In contrast, the surface topography resulting in misfit strain parallel to the surface normal possesses a strong influence on defect formation (see experimental results section 3.4). Epitaxial growth of the metastable phase is particularly difficult. In order to increase surface mobility, epitaxial thin film growth is enhanced by elevated substrate temperatures. The material therefore can often reach the stable configuration or an intermediate defect-rich state within the timeframe of the deposition process. Nevertheless, for a set of parameters at deposition temperatures close to 300 K, epitaxial growth of cubic GST is possible[114].

1.4.4 Voids and inclusions:

Lastly, clusters of vacancies or of foreign inclusions can be regarded as volumetric defects, whose border is described by planar defects. The particular relevance for GST can be found when regarding phase mixtures. A ready example is the volume fraction of unmodified amorphous GST in a direct Joule heating cell. Since the phase transformation occurs along the current path, typically only a filament of crystalline GST is formed within the matrix. Thus, when attempting to reset the cell to the entirely amorphous state, both the heat distribution in the conductive filament and the surrounding matrix has to be taken into account. However, the only role volumetric defects play in this work can be found in the formation of microvoids at the substrate interface after extended annealing times, foreign contaminants at grain boundaries, or phase mixtures.

2. Instrumentation and methods

2.1 Preface

The following chapter deals with a description of the experimental methods used to obtain the results of the electron microscopy study. As such, it is prefaced with a short description of the pulsed laser deposition (PLD) setup used in the thin film production. Since the thin-film characterization by X-ray diffraction (XRD) methods and scanning electron microscopy (SEM) formed the basis for a recent dissertation on the thin film deposition of GST that accompanied the TEM atomic structure investigation[115], these aspects can be referred to therein for further details.

The cross-section lamella preparation by focused ion beams is central to the acquisition of high quality TEM data. While the ion-beam method for TEM specimen preparation is in widespread use, the inherent instability of the phase-change materials poses particular challenges for the specimen preparation process. Relevant textbooks and publications on fundamentals of electron microscopy can be referenced where applicable[116-121].

The main focus of this section lies on the high-resolution STEM imaging and evaluation techniques by comparative image simulation used in the atomic structure investigation of disordered metastable and stable layered GST thin films.

2.2 Thin film deposition by pulsed laser method

The pulsed laser deposition was carried out in a custom ultra-high vacuum chamber (see Figure 2.1), operating at a base pressure of 4 x 10^{-8} mbar and a typical Ar auxiliary gas flow of 1 sccm resulting in a final chamber pressure of 4 x 10^{-5} mbar during deposition. The KrF excimer laser emitted 248 nm coherent light at 160 mJ total output in a 20 ns pulse, which was regulated down to 0.5 – 1 J/cm² on the target at 60° angle of incidence by defocusing the beam. The stoichiometric sintered $Ge_2Sb_2Te_5$ target possess an optical absorption coefficient of 10^6 cm^{-1} in the utilized wavelength regime (UV), and deposition rates up to 250 nm/min were possible at 100 Hz and 1 J/cm², although deposition rates for crystalline growth were chosen significantly lower. The substrate heater mount was calibrated by thermocouple measurements on various substrate materials (see Ref. [115]), however the effective surface temperatures during deposition can be expected to be higher than the nominal value due to surface heating from the plasma plume. This aspect is further discussed in the relevant subchapter (3.4), and details on specific parameters used as well as pre- and post-deposition treatment steps are given for each sample series.

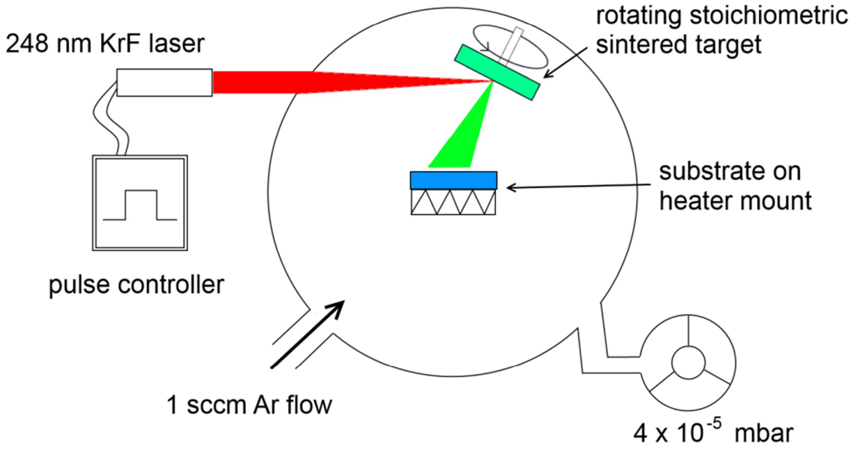

Fig. 2.1: A schematic view of the PLD process chamber for deposition of GST thin films.

2.3 Specimen preparation for TEM investigation

In order to resolve atomic structures in thin films with the best-possible resolution, special care must be taken in the cross-sectional lamella preparation[122]. In particular, the metastability of many of the structures investigated necessitates that the sample surface be protected from high incident Ga^+ ion currents by either depositing a surface protection layer in the PLD, or (additionally) depositing thick buffer layers of nanocrystalline Pt from metal-organic precursor inside the FIB, while the low-kV Ar^+ thinning process is carried out under constant liquid nitrogen cooling (-185 °C).

The FIB cut was carried out in a Zeiss Auriga Crossbeam Workstation FIB-SEM, using a high-current Ga^+ ion beam at 30 kV for cutting and at 5 kV for preliminary thinning at shallow angles (± 0.5 - 1.5°) down to a foil thickness of approximately 100 nm. The low-kV Ar^+ ion thinning was carried out on a Fishione Nanomill, each step consisting of 900 eV thinning and subsequently polishing at 300 – 500 eV at 10° glancing angle from both sides for 10 - 30 minutes each. The local thickness was then measured by energy-loss filtered imaging (EFTEM) thickness mapping using the log-ratio method[123] and, if required, the low-kV thinning repeated at adjusted parameters.

The implantation of ions and recoil displacements can be summarized in the mean displacements per atom (DPA), calculated by Monte-Carlo simulation (SRIM[124]). In Figure 2.2 it can be readily seen that at low energies and glancing angles, the DPA start out lower and rapidly fall off, with the significantly impacted zone ranging from 20 nm for 30 keV gallium ions at 1°, and even more at 90° direct incidence, to less than 2 nm for 300 eV argon ions at 10°. At bold angles to the surface, high-energy ions can penetrate the top layer and recoil cascades are projected forward so that the DPA curves, and thus the damage to crystalline structures, peak deeper inside the sample. Further details on the preparation procedure and possible ion-beam artefacts can be found in Ref. [122] as well as Appendix B.

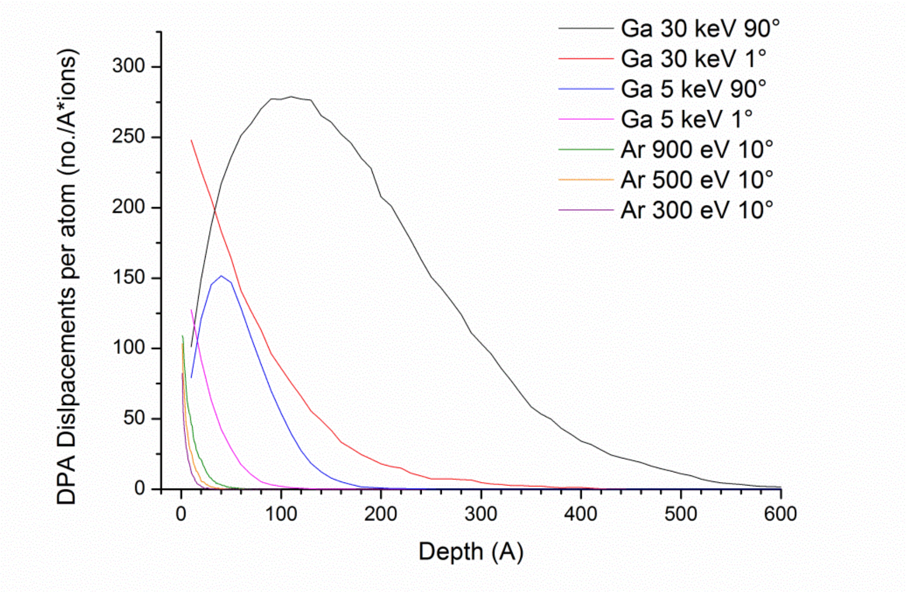

Fig. 2.2: Displacements per atom vs. depth from the surface for gallium and argon ions at various angles and energies, calculated from 50000 incident ions for each set of parameters.

2.5 STEM imaging and simulation

When describing the signal interpretation in a transmission electron microscope, the effects to consider can be divided into two larger subcategories, the interaction of the electron beam with the thin sample object, and the modulation and detection of the electron beam by the instrument. The electron – solid interaction determines the information encoded in the electrons and secondary particles exiting the sample. STEM images can be constructed from mass-thickness, diffraction and phase contrast, similar to the image formation in bright field (BF), diffraction contrast (DF) and high resolution (HRTEM) imaging, when collecting coherent directly transmitted and/or small-angle Bragg scattered electrons. A major advantage of STEM over TEM (alternatively conventional TEM or CTEM) is the ability to construct images from incoherent scattering into high angles. The image contrast in incoherent imaging largely depends on the atomic number Z^{ξ}, with reported ξ ranging from 1.5 – 2 but for the chosen experimental setup typically lying close to 1.8. However, for a quantitative view of the STEM information, a large number of possible scattering contributions have to be taken into account, and thus numerical models are used for computational image simulations in order to compare the STEM images to ideal model configurations. Instrument factors for a precise description of the probe forming system include the source size and energy spread inherent to the electron source, lens aberrations and the correction thereof, as well as detector characteristics such as linearity regime and noise. Furthermore the variable experimental parameters include beam forming apertures, lens defocus, objective aperture, parallel or convergent illumination determined by the condenser lenses and choice of camera length in the projection system.

The other strength of STEM lies in the ability to construct images from analytical detector data by sequential acquisition of EDX, EELS or similar information. The drawback however is that in order to acquire sufficient spectroscopic data, long measurement times can be necessary, which increase the electron beam damage to the sample. While for pure imaging purposes, electron beam damage in STEM is regarded as equal or less than in HRTEM, the high doses focused on a small area necessary for analytical STEM lead to sample heating, knock-on damage, contamination and electron beam evaporation.

It is typically assumed to be useful to relate the beam path and subsequent image formation in STEM to the image formation in classical TEM[125]. The principle of reciprocity (Figure 2.3) illustrates that bright field (BF-) STEM imaging can be considered the inverse geometry of HRTEM imaging. In the latter the condenser beam forming apertures and coils aim to create a coherent parallel beam from the idealized point source so that the electron wave exiting the sample is a plane wave, which is subsequently focused into the diffraction plane. In this case, the objective aperture determines the range of scattering vectors that interfere to form the high-resolution image on the image plane of the screen or CCD array.

In contrast, the STEM beam forming optics aim to focus the incident beam into a demagnified image of the source onto the sample. The range of scattering vectors used for image formation is then not solely determined by an aperture, but by the size and position of the detector plate (controlled by its physical dimensions and the camera length of the projection system) as well as the convergence angle of the incident probe. Effectively, one position in the image plane of conventional TEM corresponds to the demagnified electron source on one sample position in BF-STEM, attenuated by the phase and amplitude shifts along the beam path within the sample. The entire image plane in STEM is then formed by scanning the electron probe over the sample area. This also highlights the central difference between the two imaging modes. While the above described similarity is especially useful for a detector within the beam axis collecting a small range of scattering angles around the transmitted beam that is dominated by coherent contributions (BF-STEM), the introduction of annular plate detectors in STEM also allows for image formation only from selected higher scattering angles (annular dark field or ADF). In HRTEM this would require a disc-shaped objective aperture excluding the zero-order Laue zone (ZOLZ) from the image formation. The closest similar method in TEM may be the hollow cone illumination techniques in which a tilted beam is transmitted through the sample and the objective aperture is used to exclude the zero beam[126].

Particularly complicating factors in the description of STEM image formation and TEM analytics are the inelastic information also collected by the kinetic energy-insensitive detectors as well as the contrast reversal problem in coherent electron interference. Since the phase shifts that coherently scattered electrons experience are 2π-periodic, and furthermore multiple scattering has to be taken into account for samples of any realistic thickness (i.e. dynamical scattering theory[127, 128]), the interference in the overlap regions of the diffraction discs in convergent illumination can result in constructive or destructive interference when measuring the complex modulus of the total electron wave from an atomic column, collected on the detector plate. ABF and low-angle ADF images thus can exhibit contrast reversals with changing thickness, and the total scattering intensity is an amalgam of partial coherence effects (source size and stability, detector geometry), crystalline symmetry, structure factor, atomic scattering amplitude and local sample thickness as well as non-uniformity. The current development of segmented and/or pixelated STEM detectors promises to open up a closer utilization of the low-angle scattering distribution. Reports on the utilization of azimuthal resolution in STEM detectors[129] in order to detect defect strain fields, electrostatic fields in p-n junctions and even atomic ionicities by means of differential phase contrast STEM[130-132] illustrate that the development of novel STEM methods is far from concluded.

Inelastic losses are less sensitive to the collection angle than the elastically scattered electrons. The transfer of momentum to excitation processes in the sample such as phonons, plasmons, ionization events and valence band excitations results in a continuous distribution across the angular region of inelastically scattered electrons, peaked in forward direction. These form a diffuse background overlaid on the elastic Rutherford-scattered and transmitted signal. While for low collection angles and thin objects coherent elastic forward single-scattering dominates the total scattering intensity, exclusion of the ZOLZ in ADF geometry leads to a marked increase in the incoherent inelastic portion of the collected signal. In the context of the present work, one particularly important case of inelastic scattering is the thermal diffuse scattering (TDS) by very low energy electron - phonon interactions. These are the main contributors to the Kikuchi bands formed by diffuse multiple scattering and partial coherence. It was even shown that experimentally observed side-bands perpendicular to the main Kikuchi lines require correlated TDS phonons between nearest neighbouring atoms[133]. TDS contributions to the ADF intensity at a given radial scattering angle are thus not entirely insensitive to the azimuthal position on the detector, nor completely independent of the crystalline orientation. The second point also refers to the enhanced incoherent scattering resulting from the channelling of 1s Bloch states when the electron probe is located atop an atomic column in a low-index orientation[134, 135].

Nevertheless, when detecting the azimuthal sum of TDS contributions from a large range of scattering vectors on a circular high-angle scattering detector (HAADF), these are known to scale well with the average local atomic number and, as noted before, indeed dominate the high-angle scattering intensity so that a direct comparison between image intensity and chemical composition becomes possible[136, 137]. This is a central point for the work presented, since it allows a comparison between chemical composition in the mixed Ge/Sb/v sublattice of GST and the measured as well as simulated local image intensity in HAADF-STEM. Before this is discussed in further detail however, it is necessary to take a step back and consider the very basic formalism of STEM image formation, information transfer and instrument parameters.

In the following sections, the probe-forming system and image formation in STEM are summarized based on the wave-optics description by Nellist and Pennycook[117], followed by an overview of the different simulation approaches to annular dark field (ADF) and high-angle annular dark field (HAADF) imaging. The description of the semi-quantitative comparison between experimental and simulated HAADF-STEM images from FFT multislice simulations based on the algorithm and software developed by Ishizuka[138] is included in the chapter discussing the experimental results (see section 3.4).

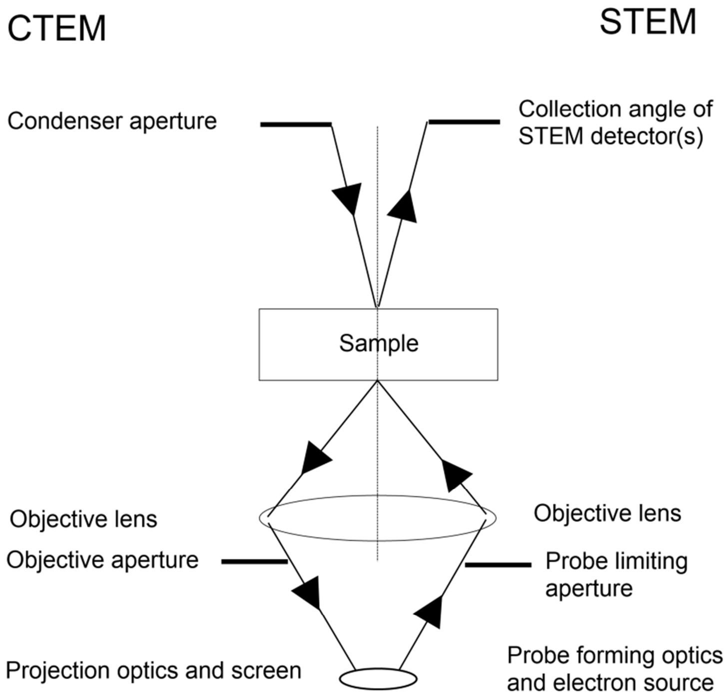

Fig. 2.3: The principle of reciprocity between the beam path in classical TEM and STEM.

2.5.1 STEM beam optics

The first step in order to describe the image formation in STEM is the mathematical construction of the probe forming optics. A coherent incident electron wave at the front focal plane is described by the lens transmission function T(K):

$$T(K) = A(K) * \exp(-i\chi(K)) \tag{2.1}$$

Here, the variable K is the transverse wave vector relative to the optical axis, A(K) the aperture function of the objective aperture, i.e. A(K) = 1 for 0<=K<=K_{max} and 0 elsewhere, and χ(K) the lens aberration function describing the phase shift induced by the lens imperfections. Often, the transverse wave vector K is substituted by the range of convergence angles of electrons collected by the objective lens, $\alpha = \lambda$K where λ is the relativistic wavelength of the electrons:

$$\lambda = \frac{h}{p} = \frac{hc}{\sqrt{E(2m_0c^2 + E)}} \tag{2.2}$$

Here, h denotes Planck's constant, c the vacuum speed of light, E the acceleration voltage and m_0 the resting mass of the electron. The shape of the focused electron probe P(R) on the sample is then the inverse Fourier transformed of 2.1:

$$P(R) = \int T(K) \exp(i2\pi\, K \cdot R)\, dK \tag{2.3}$$

where R is the position vector on the sample surface. The influence of the χ(K) aberration function cannot be overstated. The principles of electron lens aberrations and theoretical development of their correction were described in the 1940s and 1970s, respectively, by Scherzer[139, 140] and Rose[141], although the technical implementation and commercial availability were only achieved much more recently[142]. Even modern round electromagnetic lenses engineered specifically for microscope columns invariably change the shape of the electron beam and thus may reduce the achievable resolution. The contributions can be divided into the spherical aberration (Cs) and the chromatic aberration (Cc). In the case of the spherical aberration, the electron wave passing at different distances from the optical axis is deflected by the Lorentz force to varying degrees that do not result in a perfect focal point. Rather, those traveling further away are deflected more strongly than those closer to the beam axis (positive Cs), which results in optimal contrast transfer of spatial frequencies at underfocus conditions (Scherzer focus in HRTEM[143]). The chromatic aberration describes the deviation of the focal plane depending on the electron wavelength, as electrons of different energies are not deflected into a single focus crossover. The Schottky-emitter type X-FEG used in this work achieves a best primary beam energy distribution of about 0.8 eV, when measured from the primary peak width in the post-column magnetic sector energy filter (EELS). Instruments equipped with monochromators are able to reduce this value down to 0.1 to 0.2 eV[144, 145]. Both types of lens aberrations can be corrected by rather costly multipole correctors positioned before or after objective lens and sample for probe and image correction, respectively, with the chromatic aberration correction being at the forefront of the latest developments[146, 147].

When only a small range of K close to the optical axis needs to be considered, and assuming the probe forming lenses to be rotationally symmetric, the aberration function describes a phase error of the converging electron wave in reference to the ideal focusing wave path:

$$\chi = (\frac{2\pi}{\lambda})\delta \tag{2.4}$$

The δ in this term encompasses the absolute deviations of the electron beam through aberrations, depending on position (distance from the optical axis) and angle. Since the sample is situated close to the optical axis only angular deviations need to be considered, and δ can be expressed as an even power series of the aberration coefficients:

$$\chi(\alpha) = \frac{2\pi}{\lambda}\left(\frac{1}{2}C_1\alpha^2 + \frac{1}{4}C_3\alpha^4 + \frac{1}{6}C_5\alpha^6 + \cdots\right) \tag{2.5}$$

The coefficients C_i are referred to as the aberration coefficients of i-th order, where $-C_1 = \Delta f$ is the defocus value and $C_3 = C_s$ the third-order spherical aberration is often given as an overall indicator of the lens aberrations, since in uncorrected instruments the lower order aberrations dominate the contrast transfer (Scherzer's Theorem).

The description of the lens aberrations is further complicated by the treatment of higher-order aberrations. In order to correct the spherical aberration from a round lens, the beam is deflected through a series of multipoles, which invariably introduce aberrations that are not ideal spherical but rather possess a rotational symmetry of a certain order, i.e. 3-fold, 4-fold, 5-fold symmetric etc, and hence odd powers of α need to be included. Such aberrations may also arise from non-round imperfections in the lenses, commonly grouped under condenser astigmatism. In order to describe these in the aberration function, α can be rewritten as a complex angle $\omega = (\alpha_x + i\alpha_y)$, where α_x and α_y are karthesian directions of angular deviation from the ideal spherical wave. When describing an aberration of a certain order n, ω^n can then be expressed as $(\alpha_x + i\alpha_y)^n = \alpha^n \exp(in\phi)$, i.e. in terms of polar α and azimuthal ϕ angular deviation. The general expression of the aberration function is then[118]:

$$\chi(\alpha, \varphi) = \frac{2\pi}{\lambda}\sum_{m,n}\frac{1}{n+1}C_{nm}\alpha^{n+1}\cos(m(\varphi - \varphi_{nm})) \tag{2.6}$$

The sum and coefficients C_{nm} run over n = 1,2,3,… and m = 0,2,4,…,n+1 for odd n or m = 1,3,5,…,n+1 for even n. For ease of interpretation, the aberration coefficients are often rewritten and grouped according to their axial symmetry as $C_n = C_{n,0}$ the defocus (n=1) and n-th order spherical aberration (n odd), $A_n = C_{n,n+1}$ the (n+1)-fold astigmatism, $B_n = C_{(n/2)+1,(n/2)}$ the n-th order axial coma (n even), with higher order aberrations expanding to star-aberration, three-lobe aberration, rosette aberration and more.

While the treatment of lens aberrations may thus get arbitrarily complex, in practice during the experiments presented in this work, the Cs-corrector was used to manually correct up to third-order aberrations until C_1 and A_1 were less than 2 nm, B_2 and A_2 less than 50 nm, S_3 (third-order star aberration) and C_3 less than 500 nm, while the C_5 parameter was adjusted by the manufacturer to about 400 μm. This was done using the provided DCORR software, which records tilt-series plateaus from randomly oriented nanocrystalline or amorphous structures at under- and overfocus conditions in order to estimate the residual aberrations[148]. The ultimately achievable resolution of the STEM beam optics is determined by a trade-off between diffraction limit, source size, spherical aberration and chromatic aberration (see Figure 2.4, from Ref. [116]).

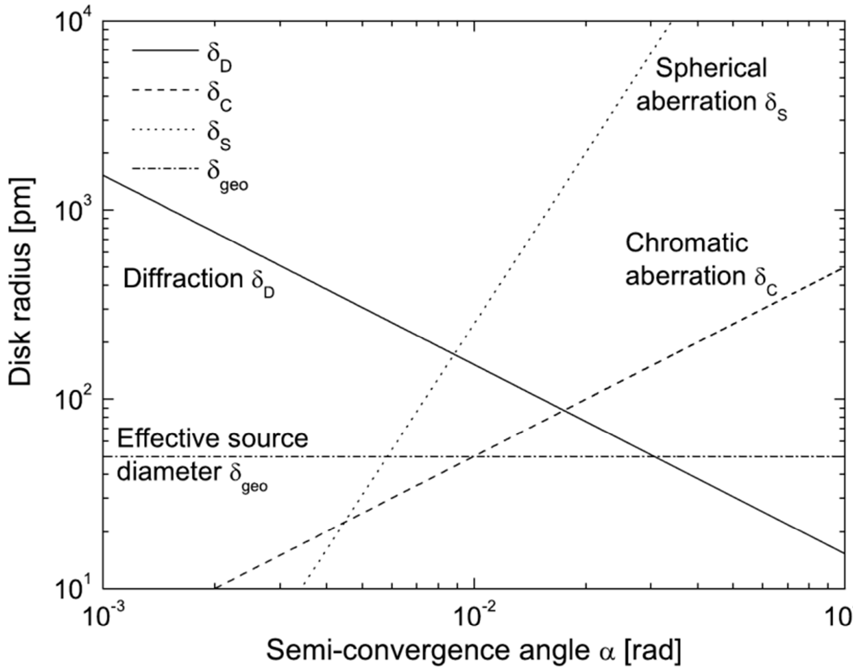

Fig. 2.4: STEM resolution limits to probe size, depending on probe-forming semiangle. Incoherent source size = 50 pm, C3 = Cc = 1 mm, ΔE = 1 eV, E_0 = 200 kV. Figure reproduced from Ref. [116].

The process of Fraunhofer diffraction at a circular aperture such as the objective aperture in STEM results in an Airy disc type focused pattern with a strong primary maximum and multiple weaker diffraction rings. The shape of the intensity distribution is described by the first order Bessel function of the first type, and the radius of the central maximum can be written as:

$$\delta_D \approx 0.61\frac{\lambda}{\alpha} \tag{2.7}$$

This gives a direct measure for the Rayleigh criterion, i.e. the minimum separation of two points in the focal plane that can be resolved if the convolution of both points with the point spread function (PSF) results in an overlap of the peak maximum of one point with the first minimum of the other. The source size refers not to the physical size of the luminescent tip of the electron emitter, but rather to the effective size of said emitter on the sample. Since scanning imaging and spectroscopy require a certain probe current in order to produce a signal, a limiting factor for the minimum effective source size is the gun brightness. For a high-brightness X-FEG Schottky type field emitter of the kind used in the Titan³ instrument, the gun lens and first condenser aperture limit the geometrical source spot so that only the central bright plateau is passed into the electron beam. The effective source radius is thus a function of the desired probe current I, brightness of the source B and probe convergence semiangle α:

$$d_g \approx \frac{0.199}{\alpha}\sqrt{I/_B} \tag{2.8}$$

The microscope specifications were measured to be 8.6 x 10^7 A/m²sradV brightness at 7.14 nA beam current and 7.8 x 10^7 A/m²sradV at 5.48 nA, using a 70 µm C2 aperture and parallel illumination. At typical experimental settings the beam current was limited to 100 pA or below for high-resolution work, and a rough estimate for the brightness would be the linear approximation 5.227 x 10^7 A/m²sradV at 25 mrad convergence semi-angle from the 70 µm C2 aperture. The corresponding geometric source size can (not very accurately) be estimated to be small (60 pm), yet gives a lower limit for the ultimately attainable resolution. The effect of the finite source size distribution S(R)[149] on the probe function P(R) can be described as a convolution with the intensity distribution of the electron probe (i.e. the absolute squared of the complex electron wave function):

$$P^*(R) = |P(R)|^2 \otimes S(R) \tag{2.9}$$

It thus results in an incoherent blurring of the electron probe, and hence even BF-STEM imaging of a theoretical ideal sample at 0K can only be considered partially coherent. Finally, in order to include the influence of the chromatic aberration, the effective probe function P*(R) needs to be further modified. The chromatic aberration coefficient C_c indicates the defocus spread $\Delta C_{1,0}$ along the beam direction due to a finite energy distribution around the acceleration voltage:

$$\Delta C_{1,0} = C_c \frac{\Delta E}{E_0} \tag{2.10}$$

The energy spread of the primary beam is in a first approximation Gaussian, as can be verified by recording the zero beam through the EELS spectrometer. In practice it is sufficient to replace the nominal defocus $C_{1,0}$ by the incremental effective defocus $C_{1,0} + \delta C_{1,0} = C_{1,0} + C_c\, \delta E/E_0$ in the aberration function $\chi(\omega,E)$. As a result, the probe intensity distribution can be weighted by the (Gaussian) shape of the energy distribution, $D(E,E_0)$:

$$P^*(R) = \int_{-\infty}^{\infty} [|P(R,E)|^2 \otimes S(R)]\, D(E,E_0) dE \tag{2.11}$$

The integration over the entire energy range in the presence of C_c thus results in a blurring of the electron probe both in lateral direction (R) and along the beam axis i.e. Δz.

It has been shown that, for a fixed C_5 and C_c, as is the case in the Titan³ instrument (C_5 = 0.4mm, C_c = 1.6 mm), the illumination semiangle and defocus can be optimized for either C_5 or C_c by allowing a maximum phase shift of $\pi/4$ within the radius of the beam forming aperture, and a minimum of 75% beam intensity in the primary peak[150, 151], and the resulting numerical estimates are:

$$\alpha_{C5} = \sqrt[6]{12 * \frac{\lambda}{C_5}} \approx 62\, mrad \quad C_1 = -1.3 \frac{\lambda}{\alpha_{c5}^2} \approx -0.6\, nm \qquad (2.12, 2.13)$$

$$\alpha_{Cc} = 1.2 \sqrt{\lambda \frac{E_0}{C_c \Delta E}} \approx 25.7\, mrad \qquad (2.14)$$

For comparison, the criteria for Scherzer conditions of a C_3-limited probe at 500 nm C_3 are $C_1 = -\sqrt{\lambda C_3} \approx$ -1 nm and $\alpha_{C3} = \sqrt[4]{4\lambda/c_3} \approx 63\, mrad$, i.e. at the recommended corrector settings $\alpha_{C3} \approx \alpha_{C5}$, yet the resolution limiting factors are C_c and ΔE.

If one assumes a ΔE of 1.1 eV (as is the maximal acceptable energy width for the Titan³ instrument used), the optimal α_{Cc} is reduced to ≈ 22 mrad. The experimentally chosen lens settings result in a convergence angle of 25 mrad for the intermediate 70 µm condenser aperture, which thus matches the optimal value for C_c quite well. The choice of the 50 µm condenser aperture then results in 20 mrad half-convergence angle at the same lens settings, reducing the diffuse contribution from C_c further, assuming an energy distribution slightly broader than the initially measured 0.8 eV, while sacrificing some intensity in the primary peak. Meanwhile, the diffraction limiting δ_D defined above measures 46 pm for 25 mrad and 60 pm for 20 mrad, and an even smaller convergence semiangle is not advisable in order to preserve sub-angstrom resolution. In practice, the aberrations, column adjustments and, to a much lesser degree, source characteristics are not constant between multiple days and multiple measurements, and it can be sufficient to verify the resolution of the microscope after adjustment by recording a well-known single-crystalline sample. Often, single crystal silicon substrates are readily available, and by measuring the maximum spatial frequencies in the Fourier transformed image it was regularly verified that a point resolution of at least 70 pm (i.e. the separation of atoms in the silicon dumbbells of [110] zone axis orientation) was reached.

2.5.2 STEM image formation

In order to create an image from the focused electron beam, the probe is scanned across the sample (R_0 ➔ $R-R_0$), and the detector situated in the diffraction plane of a convergent beam diffraction pattern records all electrons scattered into a specific range of transverse wave vectors. In a very rough first approach in line with the weak phase object approximation (WPOA), the sample can be treated as a thin (i.e. non-absorbing), multiplicative (single-scattering) linear transmission function φ(R). The wave exiting the sample at position R-R_0 can then be written as:

$$\Psi(R, R_0) = P^*(R - R_0)\phi(R) \tag{2.15}$$

The wave in the diffraction plane at transversal scattering vector K_f is then the Fourier transformed of above. The multiplication of transmission function and probe in the exit plane becomes a convolution in the diffraction plane.

$$\psi(K_f, R_0) = \int \phi\,(K_f - K)P^*(R_0)dK \tag{2.16}$$

Since the effective probe function was well-defined above, the further treatment of STEM contrast formation need only be concerned with the electron beam – sample interaction encoded in the transmission function of the object. It is, however, also important to first highlight the distinction between coherent and incoherent image formation. STEM detectors will effectively detect only the intensity of the wave on the detector plate, the magnitude squared $I_{Det.}(K_f) = |\psi(K_f)|^2$ integrated over the range of the detector aperture function (defined similarly to the objective aperture above).

Since the detector is a physical object with imperfections, the detector function is not a clean top-hat function. Rather, when discussing the angle-resolved distribution of scattered electrons, it needs to be weighted by the measured local detector sensitivity vs. scattering angle, and all experimental measurements need to be taken within the linear regime of the detector response.

If the detected wave is a coherent interference pattern of multiple scattered waves the image intensity will be dominated by the phase contrast, i.e. the phase relation between the interfering waves. In order for two scattered waves from neighbouring atoms to interfere on the STEM detector, however, there needs to exist a coherent phase relationship between the scattered waves. The interatomic spacing needs to be much smaller than the lateral coherence length. For this reason, the detector aperture function is said to impose a coherence envelope on the wave exiting the sample. The lateral coherence length $\Delta x \sim 0.16\frac{\lambda}{\theta_{max}}$ [118, 152] is a typical criterion for coherent or incoherent imaging, where θ_{max} is the largest acceptance angle of a circular plate aperture, or the smallest (inner) acceptance angle of an annular plate aperture. This is remarkably similar to the diffraction limit given in 2.7. Both formulations describe a numerical estimate of the value of the first order Bessel function of first kind (J_1) at a transversal length specified by the acceptance angle. The numerical coefficient 0.61 describes complete incoherence at the first zero of J_1, while the criterion for the coefficient of 0.16 is partial coherence with a maximum deviation of 0.88, meaning that the partial coherence parameter containing J_1 in Ref. [152](chapter 10) has fallen off to 88% of unity. This has some important implications:

- The finite size effect of aperture and source means that coherent imaging is only ever *partially coherent*. Phase changes of waves inside the coherence length are additive, and the projected intensity at K_f in coherent imaging is thus:

$$|\psi(K_f)|^2 = |\phi(K_f) \otimes P^*(K_f)|^2, \lambda \cdot K_f < \theta_{max} \tag{2.17}$$

- ADF imaging with large inner collection angles is predominantly *incoherent*, even though so far all electrons considered are elastically scattered. The projected intensity is then the convolution of intensities of probe and object transfer function:

$$|\psi(K_f)|^2 = |\phi(K_f)|^2 \otimes |P^*(K_f)|^2, \lambda \cdot K_f >> \theta_{max} \tag{2.18}$$

- Spatial coherence depending on collection angle oscillates as the higher order local maxima of J_1 enter the aperture. The rule of thumb is thus that $\theta_{max} < 0.16 \cdot \alpha$ for coherent imaging (bright field BF), or $\theta_{max} >> 0.16 \cdot \alpha$ for incoherent imaging (annular dark field ADF). At the here typically chosen experimental parameters (camera length CL = 73 mm, α = 25 mrad), only the inner 4 mrad of the BF detector (0 - 43.3 mrad) collect almost exclusively coherent information, which will nevertheless dominate the total intensity. The smallest dark field detector DF2 covering 10.1 – 105.3 mrad however still collects some partially coherent information, while the DF4 detector (19.1 – 106.5 mrad) and the high angle annular dark field (HAADF, 80 - 200 mrad) detectors collect mostly incoherent information. Since BF, DF2 and DF4 are mounted in series, simultaneous usage results in shadowing of the smaller outer angles by the larger inner ones, it is possible to record images from 10.1 – 19.1 mrad on DF2 (DF2 + DF4), and this range is also referred to as annular bright field (ABF), while the DF4 detector signal results in medium-angle ADF (MAADF) imaging. MAADF allows for enhanced image contrast of light elements, and is thus useful for the investigation of mixed light and heavy element materials such as GaN[153]. In this work, the focus lies on the HAADF image information since with the knowledge of the probe shape it is directly interpretable in terms of intercolumn distances at any sample thickness, and scattering intensities can be correlated to chemical composition.

2.5.3 Calculating scattering intensities in the incoherent regime

Incoherent imaging possesses some inherent advantages. For one, the attainable resolution is doubled (Rayleigh criterion). Additionally, since no phase reversals are present that could result in an inversion of image contrast, as they do in BF imaging, the images are much more readily interpretable over a range of sample thicknesses. A popular approximation for the image intensity depending on average atomic number of a column in zone axis is $I_{ADF} \approx Z^2$, which stems from the understanding that the atomic scattering cross-section for Rutherford scattering into a given solid angle scales with the square modulus of the atomic scattering factor, which itself contains the atomic number Z. The commonly used expression of the elastic atomic scattering factor for fast electrons at large angles is the well-known Mott formula:

$$f(\theta) = \frac{1}{2\pi^2 a_0}\left(\frac{Z - f_x(\theta)}{\theta^2}\right) \tag{2.19}$$

$$I_{ADF} \propto \frac{d\sigma(\theta)}{d\Omega} \propto |f(\theta)|^2 \tag{2.20}$$

Here, $\sigma(\theta)$ is the elastic scattering cross-section, Ω the scattering solid angle, $f(\theta)$ the atomic scattering factor, a_0 Bohr's atomic radius, Z the atomic number (the number of Protons in the core, since Rutherford scattering scales with the product $Z_1Z_2e^2$ of the charge of both particles, but the current considerations concern electron scattering $Z_1 = -1$) and $f_x(\theta)$ the x-ray scattering factor. In order to gain a quantitative understanding of the scattered intensity at high angles, matters are not quite as straight-forward. For one, the elastic scattering contribution needs to be expanded from the WPOA to include dynamical multiple scattering. The samples investigated in this work are purposefully prepared to a foil thickness of about 35 nm. This serves to reduce influences from preparation artefacts as well as electron beam damage, but in addition moves the incoherent contributions into the regime of linear thickness dependence as will be discussed further below.

If dynamical scattering is to be taken into account, the linear approximation used in equation 2.15 is no longer strictly valid. Elastic dynamical scattering from a lattice of point scattering centres can be described in the Bloch wave model[154]. Here, the scattering amplitude from a thick sample is given by the convolution of the instrument transmission function with the sum over Bloch states describing eigenstates of the electron wave function inside the sample, which themselves can be split into individual Fourier components. Since, as introduced above, the detector introduces a coherence envelope the resulting signal is still mostly incoherent, and the incident wave excites sharply peaked 1s Bloch states when placed along the atomic columns leading to enhanced channelling contrast.

In the next step, the idealized point lattice needs to be replaced by a realistic expression for the crystal scattering potential that includes both elastic and inelastic processes. The inelastic background due to plasmon and core-excitation losses is typically disregarded in the calculation of high-angle scattering intensities, and the focus lies on the much larger inelastic contributions from strongly localized phonon excitations, i.e. the thermally diffuse scattering TDS. The energy loss due to TDS phonons lies in the range of 0.2 eV, and therefore below the energy width of an un-monochromated primary beam. As a consequence, the inelasticity of the interaction is often disregarded, and only the incoherence in regards to single and multiple scattering is discussed when considering STEM image formation. In order to do so, the total scattering potential is constructed from a superposition of the individual atomic potentials, which themselves are split into a real (elastic) and imaginary (absorptive) component. Hence, this approach is also referred to as the “absorptive potential approach”. An excellent review of elastic and inelastic scattering form factors can be found in Ref. [155].

The method chosen for the calculation of high-angle scattering intensities in the here presented work was the FFT multislice formalism developed by Ishizuka[138]. It follows the absorptive potential approach, wherein the complex object scattering potential φ(R) in equation 2.15 is constructed from the inverse Fourier transformation of the Fourier components V_g, with g being the reciprocal periodicities in the crystal (unit cell) i.e. the vectors of the reciprocal lattice:

$$\phi(R) = FT^{-1} \sum_g V_g \tag{2.21}$$

Ishizuka constructs the Fourier components V_g from a summation over the complex atomic scattering form factors in the unit cell:

$$V_g = \frac{2\pi\hbar}{m_0} \frac{1}{\Omega} \sum_i f_i(s, B) \exp(-Bs^2) \exp(-2\pi i g r_i) \tag{2.22}$$

Here, m_0 denotes the electron mass at rest, Ω the unit cell volume, the sum runs over the atom positions i in the unit cell, $f_i(s, B)$ is the complex scattering form factor of atom i with a real (elastic) and imaginary (absorptive) component $f_i = f_i' + i f_i''$, s the scattering parameter with $s = g/2$ of the corresponding Bragg reflection, and r_i the mean position of atom i in the unit cell. The expression $\exp(-Bs^2)$ is often referred to as the Deby-Waller factor, which with the thermal displacement factor B is central to the discussion of TDS. The nomenclature here is often shortened to denote B or B_{iso} (for isotropic thermal displacements) as the Debye-Waller factor itself. Since the real part f_i' is the elastic form factor, and the summation in 2.21 runs over all Bragg beams, with the phase factor $\exp(-2\pi i g \cdot r)$, this formulation thus includes the incoherence contribution from TDS to the elastic scattering. Ishizuka notes that his approximation neglects spatial resolution of further scattered TDS electrons, which accounts for the formation of the Kikuchi lines, but argues that the influence is neglible since only the integrated intensity of the entire detector over a large angular range is of interest for the HAADF-STEM intensity. The temperature factor B is calculated from the mean square (time-averaged) amplitude (displacement) of the thermal vibrations:

$$B = 8\pi^2 \langle u^2 \rangle \tag{2.23}$$

In a first approximation these are usually assumed to be isotropic and independent (Einstein Model), which as has been already mentioned is not necessarily the real case. In particular, X-ray diffraction and absorption studies (EXAFS) often fit measured data points to numerical parameters for u_{iso} at different model symmetry sites, regardless of occupancy on mixed sites and nearest neighbour interactions. Furthermore, materials may undergo phonon mode softening as the experiment transitions the Debye temperature, and the temperature dependence of B is thus not straight-forward over the entire range. The mean-square displacements can, in principle, be extracted from the phonon dispersion, which can be measured by analytical fitting to inelastic X-ray or neutron scattering data, or calculated by ab-initio approaches. Peng[156] gives an example for an expression from isotropic thermal vibrations in a cubic lattice:

$$\langle u^2 \rangle = \sum_{j,m} \frac{\hbar}{\omega_{j.m}} \frac{|e(j,m)|^2}{M_k} \left[n_B \frac{\hbar \omega_{j,m}}{k_B T} + \frac{1}{2} \right] \tag{2.24}$$

Here, the double sum runs over all harmonic phonons j and lattice sites m of atomic species k. The $\omega_{j,m}$ denotes the frequency of the phonon mode, e(j,m) the eigenvector, M_k the mass of atom type k and n_B the Bose-Einstein occupation factor (i.e. the temperature dependence). A more general way to determine anisotropic thermal displacement parameters for ADF-STEM simulation was shown by Muller et. al. [133, 157], however it requires prior knowledge of the full dynamical matrix and therefore of all force constants between neighbouring sites. As available computational power and model algorithms improve, it may become desirable in the future to perform ab-initio DFT calculations of dynamical lattice parameters for each individual lattice model proposed. Software solutions such as the Greene-function based FEFF code are becoming increasingly accessible, and are already in use as well-known tools for e.g. EELS edge and EXAFS data simulation (and some attempts were made in the course of this work to calculate EELS edges for various arrangements of GST225, although the preliminary results indicated that differences were below the energy resolution threshold). However, the proper representation of sublattice disorder presents a significant hurdle in applying these principles to GST alloys. Recent reports on the role of the local chemical environment in the phase-change mechanism[85] highlight the importance of the local symmetry arrangements.

While this topic certainly warrants further investigation, one consequence of note that was also observed in the present work is that local lattice strain due to extended defect sites can result in a change in TDS intensity[158, 159]. It may be possible to draw an analogy here between strained bonds and a reduced effective crystal temperature, so that if one were to resolve the temperature dependence of the Debye-Waller factors for each site in the lattice (in a first approach in the harmonic approximation), one could relate this to the strain field in the lattice. This approach is however limited in its usefulness to HAADF contrast if the defect site additionally results in a strong tilt of the lattice columns out of zone axis for the electron beam, and such considerations are left to future research efforts.

For the purposes of correlating STEM image contrast with GST compositions in the experiments shown here, it is thus necessary to only regard quantitatively sections of lattice images that are well removed from defect sites. Since the layered structures of trigonal GST generally are assumed to possess weak coupling across the vacancy layers (therefore also referred to as Van-der-Waals gaps), defects that do not result in a strong distortion along the c-axis direction (i.e. do not cross the vacancy gap) do not influence a large area around the defect centre. However, as will become evident in the presentation of textured and epitaxial thin films in chapter 3.4, defect disorder in trigonal GST is most prominent in the local stacking of [0001] planes and the transitions thereof, and often the judgement of whether a subsection of a lattice image is far enough removed from the defect in order to be compared to equilibrium models is somewhat subjective.

The elastic scattering form factor in the real component of f_i in 2.22 can be extracted from tabulated values for known compounds or calculated from an analytical expression e.g. by Doyle and Turner[160]. However, this analytical expression is inaccurate at the high spatial frequencies ($s > 2$ Å^{-1}) corresponding to large scattering angles. The method chosen here for the selection of elastic form factors in high-angle TDS is the numerical expression from Ref. [161], which fits the model up to 6 Å^{-1} and focuses on modelling the asymptotic behaviour for large s more closely than Doyle and Turner:

$$f'(s) = s^{-2} \sum_{i=1}^{6} A_i [1 - \exp(-B_i s^2)] \tag{2.25}$$

The fitting parameters A_i are constrained as laid out by Weickenmeier and Kohl and B_i inserted as tabulated therein. This evaluation is performed automatically in the xHREM software implementation of Ishizuka, and elastic form factors are thus not explicitly shown further.

The absorptive form factor contained in the imaginary component of f_i in the absorptive potential is then calculated from the elastic form factor 2.25 and the Debye Waller factor following Ref. [162], i.e. for a Fourier component of the absorptive potential corresponding to a Bragg-scattering vector s = g, the elastic form factor is attenuated by the continuous spread into all scattering vectors s´ due to diffuse thermal scattering, scaling with the Debye-Waller factor and the path difference between s and s':

$$f_i''(s,B) = \frac{4\pi\hbar}{m_0 v} \int f_i'(|s'|) f_i'(|s - s'|) \times [1 - exp\{-2B(s'^2 - s \cdot s')\}] d^2 s' \tag{2.26}$$

In addition to the previously introduced notations, here v denotes the relativistic velocity of the electrons. The high-angle scattering absorptive potential V^{HA} from TDS is evaluated by performing the integration of the absorptive form factor over the detector area for all Bragg beams i.e. over $s \to k \triangleq \frac{2}{\lambda}(\theta_{inner} \to \theta_{outer})$ using the small-angle approximation.

$$V_g^{HA} = V_g(f''(s,k,B)) \tag{2.27}$$

With the detector size giving the integration range in 2.26:

$$f''(s,k,B) = \frac{4\pi\hbar}{m_0 v} \int_s^k \ldots \tag{2.28}$$

The integrated TDS intensity on the detector is then the magnitude squared of the wave exiting the sample of thickness Δz integrated over the lateral range R when the probe is positioned at R_0, which can be equated to the loss of electrons from the incident beam due to TDS over the entire sample thickness. In the multislice approach the sample is segmented into n thin additive slices along the beam direction, and the TDS intensity after n slices is given by:

$$I_n^{HA}(R_0) = \sum_{j=1}^{n} \frac{2}{\hbar v} \int \left|\Psi_j(R - R_0)\right|^2 \cdot V_j^{HA}(R - R_0) dR \tag{2.29}$$

Here, $\Psi_j(R)$ and $V_j^{HA}(R)$ are the complex incident electron wave function and projected absorptive high angle scattering potential after j slices in real-space, respectively. The distinct advantage of this method is that, since most calculations can occur in Fourier space, the fast Fourier transform algorithm (FFT) is applicable and simulations of large supercells can be done relatively quickly. It is however necessary to perform these for each new configuration of the lattice one wants to compare to experimental data. Furthermore, calculating and storing simulated images for arbitrary (within intervals) thickness values is impractical, and for a comparatively small number of samples it is sufficient to calculate simulated images at experimentally measured thicknesses, and compositions, each time anew. Of note regarding the Ishizuka approach is that, in addition to ignoring multiple scattering of TDS electrons as mentioned above, the calculated high—angle scattering intensity for small thicknesses < 10 nm strongly oscillates. An example of a simulated image from a GST model structure is given in the next section, while the comparison between experimental results and simulations is shown on in the results section(s).

2.5.4 Other approaches to image simulation

While other methods for STEM image simulation will not be discussed comprehensively, it is necessary to mention the two major alternative approaches to the FFT-multislice (MS) method, the Bloch-wave method and the frozen phonon approach. A comparative discussion of the three methods has been given by e.g. Ref. [163], and although there remain issues to be resolved especially regarding correlation of thermal vibrations, validity of the local approximation[164, 165] as well as modelling of incoherent and inelastic background signals, each method has been successfully applied to the quantitative reproduction of ADF images for appropriate case studies[166-168]. The FFT-multislice method occupies somewhat of a middle ground in the approaches to ADF image simulation.

In the Bloch-wave method, the wave function of the incident electron wave inside the periodic crystal potential is described by a superposition of three-dimensional Bloch-wave eigenstates within a unit cell, which is then replicated along the sample thickness[169]. The incoherence contribution from TDS is included by the formulation of an optical absorptive potential, in a manner identical to the one described in the previous section, which is then included in the excitation amplitudes in what is referred to as the mixed dynamic form factors (MDFF) by Ref. [163]. Solving the eigenstate equations for Bloch states requires strict periodic boundary conditions. The Bloch-wave method yields good results for the bright-field regime and intermediate angles, while the purely analytical matrix calculations can be performed very quickly for periodic unit cells. The frozen phonon (FP) approach on the other hand relies on the multislice propagation of the wave through a crystal potential, similarly to the FFT-MS method. However rather than defining an absorptive potential, in the FP method it is argued that, due to the high energies of the incident electrons, the interaction time for a single scattering process is much shorter than the vibration period of a thermal oscillation[170]. It follows that each electron effectively sees only a snapshot in time of the lattice configuration, where each atom is randomly displaced from its mean position. The probability for a specific displacement vector is given by the standard deviation of atomic positions <u>, which can be derived from the Debye-Waller factor. In what can be regarded as a Monte-Carlo approach, for a number of possible phonon configurations of the lattice with random displacements the elastic wave is then propagated through a multislice stack, and the results of multiple calculations incoherently averaged. This method is able to reproduce TDS scattering very well, and no distinction is made between elastic scattering and absorptive TDS. The resolution in reciprocal space is preserved, and it is thus able to accurately predict dynamical scattering of TDS electrons. Consequently the Kikuchi features can be resolved. The drawback of the method, in addition to the unknowns regarding accuracy of the thermal displacement model already mentioned, is that phase gratings between slices cannot be reused and, also since a number of iterations are required to generate randomness, the computation time required is significantly increased.

Since the FFT-MS method is able to predict the total amount of high-angle scattering from typical sample thicknesses reasonably well within the limitations of the models, the large majority of simulation results used in this work were created with the xHREM software. For selected cases, fast Bloch-wave calculations were performed using the STEM-SIM software[171], or detailed frozen phonon calculations using the COMPUTEM code provided in Ref. [118].

2.5.5 Examples of simulated STEM image intensities

As mentioned before, the best match between simulated STEM images and experimental results is found when each set of experimental parameters (microscope conditions) and sample characteristics (sample thickness, average composition, probable symmetry) is used to perform an image simulation for a proposed lattice model. As an example of the typical behaviour of STEM contrast based on the above described theory, the results of image simulations based on the GST 2:2:5 trigonal structure proposed by Ref. [52] that is slightly deficient in Ge content are given below. The structural model is given schematically in Figure 2.5, in $[01\bar{1}0]$ zone axis projection. The unit cell consists of alternating layers of Te and Ge/Sb/(v)acancies, stacked along the c-axis direction. Vacancies are concentrated in vacancy layers (VL) regularly spaced out by 9 Te/Ge/Sb layers. Mixed Ge/Sb layers contain different concentration ratios depending on the distance from the VL, as well as some residual intrinsic vacancies. The concentrations are $Ge_{60.4}Sb_{36.2}v_{3.4}$ for the mixed layers further away from the vacancy gap (Ge1), and inverted to $Ge_{33.7}Sb_{66.3}v_0$ for the mixed layers closer to the VL gap (Ge2). Ge1 positions are situated close to the octahedral centres between neighbouring Te layers, while Ge2 positions are strongly displaced resulting in a Ge2-Te bond splitting between long (Te2-Ge2 3.2 Å) and short (Ge2-Te3 2.9 Å) bonds. Isotropic thermal displacement parameters B_{iso}, and thus the standard deviation of atomic positions <u> for FP calculations, vary between symmetry sites, however for mixed Ge/Sb sites only one average displacement parameter is given per site (see Table II).

The displacement parameters given in the literature source, which were measured by Rietveld refinement of resonant X-ray diffraction data, are very large in comparison to many other inorganic compounds. In part this may be caused by the intrinsic disorder of the chemical distribution, as well as the residual vacancies. In particular for the Ge1 sites however, when one keeps in mind the resonant bonding characteristics in the metastable phase, this may indicate some form of directed oscillation along the p-chains, which brings the matter back to the need for an anisotropic description of displacements parameters that is specific to the atomic species in question as well as the next-nearest neighbour configuration (i.e. whether an octahedral Ge atom, past the first shell of Te neighbours, is surrounded by next-nearest Sb, Ge or vacancies, and whether there exists a preferred symmetric arrangement mediated by the electronic configuration of Te). Such a theoretical investigation may be the next step in understanding the structure – property relations in phase-change compounds, and efforts in this direction are underway[172, 173]. The work presented here instead focused on the atomic-resolution experimental observation of crystalline lattices depending on preparation and treatment conditions, in order to provide a framework of real existing GST lattices to compare theoretical models against.

Tab. II: Model parameters for image simulations. Lattice parameters a = b = 4.226 Å, c = 17.281 Å.

$Ge_{1.876}Sb_{2.039}Te_5$ according to Urban ICSD#188967, space group 164

Site	Occupancy	x	y	z	B_{iso} [Å²]	<u> [Å]
Te1	Te: 1	0	0	0	1.3738(5)	0.1319(1)
Ge1	Ge: 0.604	2/3	1/3	0.1063	2.2976(4)	0.1705(9)
Sb1	Sb: 0.362	2/3	1/3	0.1063	2.2976(4)	0.1705(9)
Te2	Te: 1	1/3	2/3	0.2045	1.3817(4)	0.1322(9)
Ge2	Ge: 0.337	0	0	0.3253	2.1239(4)	0.1640(1)
Sb2	Sb: 0.663	0	0	0.3253	2.1239(4)	0.1640(1)
Te3	Te: 1	2/3	1/3	0.4181	1.6896(8)	0.1462(9)

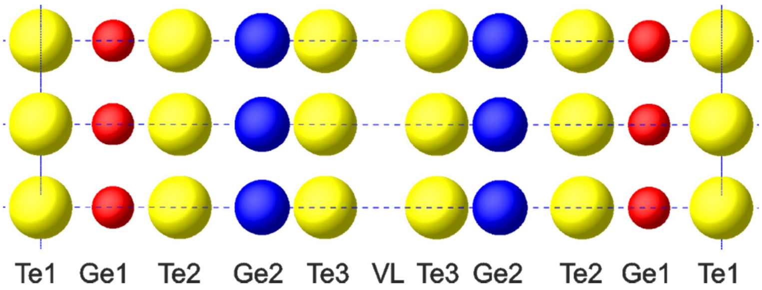

Fig. 2.5: Schematic mode unit celll of $Ge_2Sb_2Te_5$ in $[01\bar{1}0]$ projection, according to the Urban sequence as given in table II.

Figure 2.6 shows the resulting image of a FFT-multislice image simulation based on above described model and typical experimental parameters for HAADF-STEM imaging. The individual atomic columns as well as the vacancy gap are clearly resolved. Sub-angstrom displacements of Ge/Sb columns from the central octahedral position between pure Te layers can be measured and compared with experimental data. The image intensity within individual {0001} mixed layers correlates with the local composition. It is, however, important to point out that the image is based on the idealized unit cell, and experimental images can be expected to deviate near imperfections (as discussed before). In addition, the image intensity of an atomic column depends on the concentrations of its components (average Z), their combined average Debye-Waller factor, the shape (and locality) of the absorptive form factor, and the residual stray signal from neighbouring columns due to finite probe and dechanneling.

As a consequence of this, even though the Te columns are assumed to be completely filled, their image intensity contributions are not identical. Moreover since the mixed Ge/Sb/v sites occupy different symmetric arrangements and consequently also possess different Deby-Waller factors, they do not follow a simple Z^{ξ} intensity scaling either.

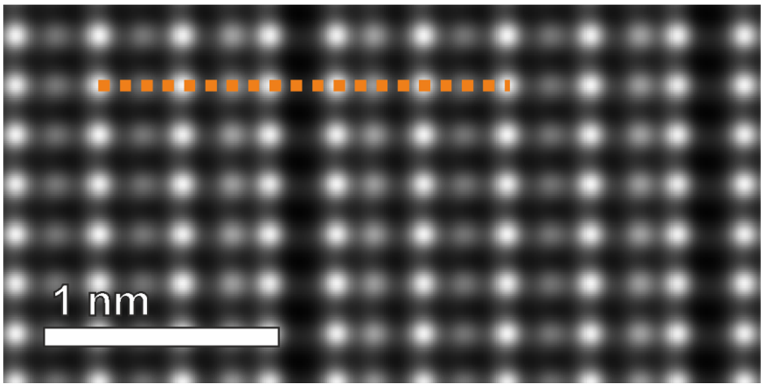

Fig. 2.6: FFT-multislice simulated HAADF-STEM image of trigonal GST using the Urban model shown in Figure 2.5. Thickness = 35 nm, defocus = 1.9 nm, C5 = 0.4 mm, Cc = 1.6 mm, C3 = 500 nm, α = 25 mrad, θ = 80 – 200 mrad. The dashed orange line indicates the position of the depth profiles in figures 2.7-2.9.

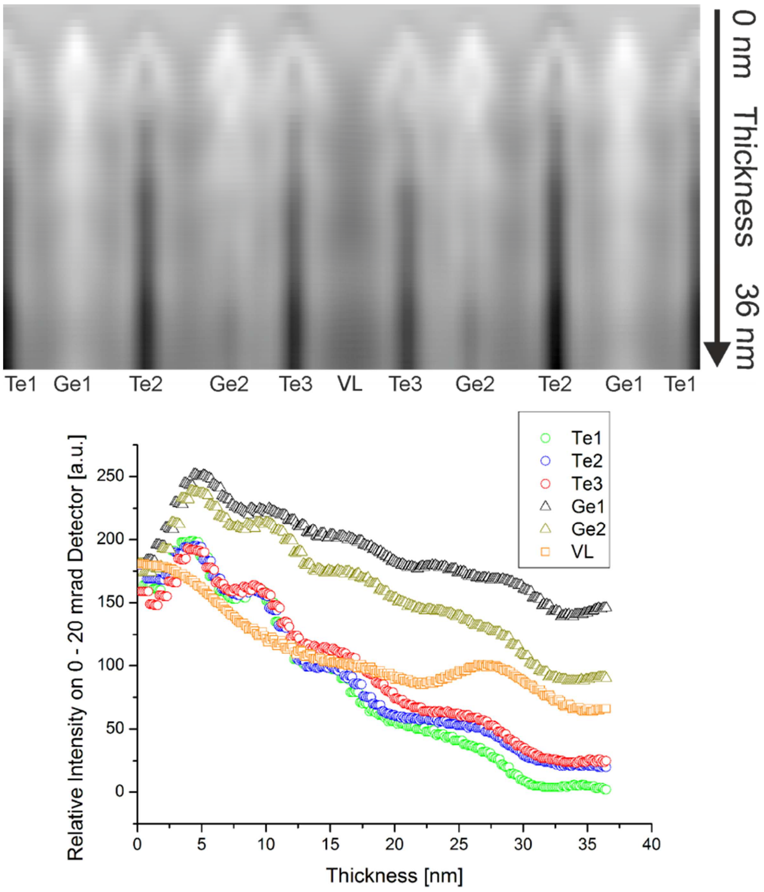

Fig. 2.7: FP simulated BF-STEM (0 - 20 mrad, 10 thermal configurations) depth-profile image of $Ge_2Sb_2Te_5$ lattice plane as indicated in Figure 2.6, across one unit cell in c-axis direction. Profiles below were extracted from individual column positions, measured along the depth axis.

The image intensity of a simulated line profile measurement as indicated in Figure 2.6, calculated with the frozen phonon method (n = 10) for the thickness range between 0 and 36 nm, is shown in figures 2.7-2.9. In the bright-field regime (Figure 2.7), the background intensity in-between atomic columns oscillates with thickness. Furthermore, while some columns appear dark on a bright background, others can appear bright on a darker background, and in general the intensities of atomic columns oscillate over the entire thickness regime. At some thicknesses, the contrast between atomic column and neighbouring background is inverted. In the graph shown, contrast between Te3 (red) and VL (orange) is inverted at around 3 nm and again at 17 nm. This serves to illustrate the difficulty in interpreting images that are dominate by coherent scattering.

In the ADF regime collecting all scattering information from 20 to 100 mrad (Figure 2.8), despite the stronger incoherent contributions, the simulated image intensities are still not directly interpretable by atomic columns. Rather, the image follows roughly the reverse trend of the BF information.

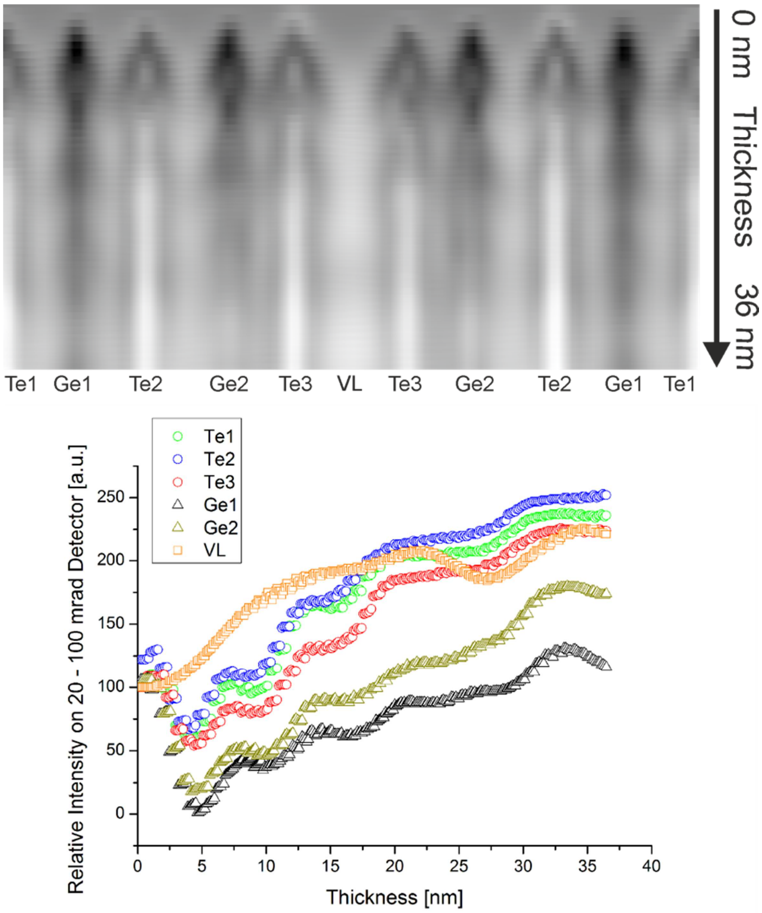

Fig. 2.8: FP simulated depth-profile image similar to Figure 2.7 calculated for ADF-STEM collection angles (20 – 100 mrad). Contrast inversions are still possible, and specific contrast features are not well localized on individual columns.

As was laid out above, when θ_{inner} includes the regime approximately between α and $3\cdot\alpha$, the scattering information includes partial coherence phenomena from higher-order local maxima of J_1. Only when the inner collection angle is opened beyond this regime does the image interpretation become more straight-forward. It is necessary to stress at this point that BF and ADF information still occupies an important role in the investigation of a-priori unknown samples. While the HAADF images yield excellent results for highly crystalline, well-oriented structures thanks to the confinement of the aberration-corrected probe to 1s- and 2s-like states along the zone axis columns, very light elements ($Z < 10$) sometimes result in hardly any HAADF-intensity at all, while these can be well visible under ADF conditions. Similarly, highly disordered structures such as amorphous or nanocrystalline thin films do not possess a strong HAADF scattering geometry, while these can be well visible under BF conditions. Although the accurate interpretation of the image contrast distribution in these cases is much less straight-forward, to the point where it may not be possible, it is often sufficient to show that amorphous components or light elements are present by comparing BF/ADF images with the corresponding HAADF information.

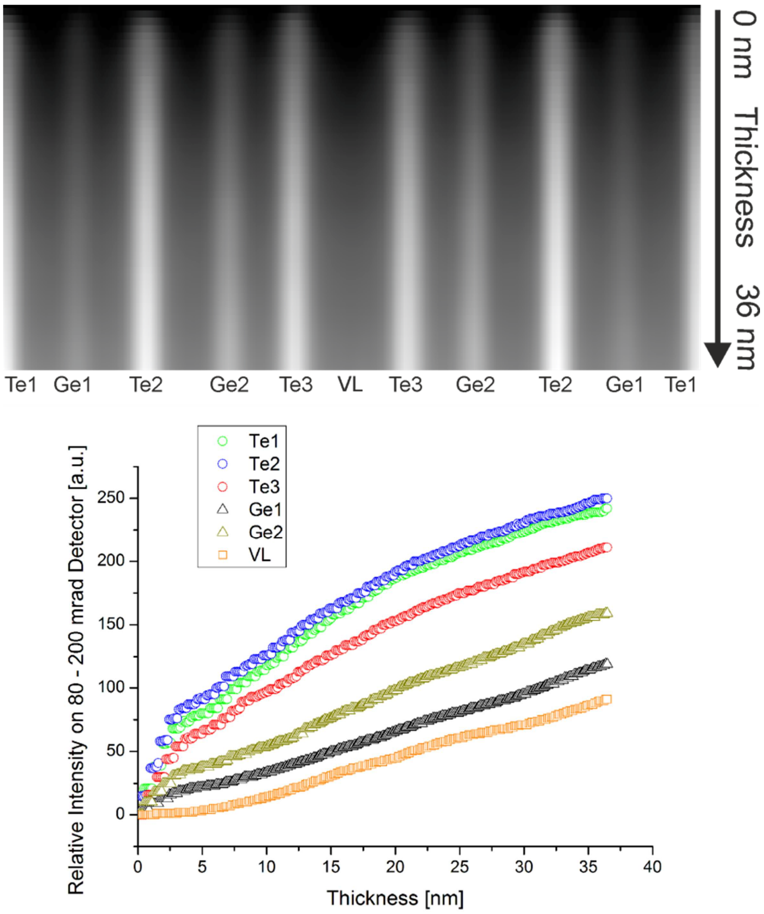

Fig. 2.9: FP simulated depth-profile image similar to figure 2.7, calculated for HAADF-STEM collection angles (80 – 200 mrad). The contrast behaviour approaches the linear regime, in particular at sample thicknesses above 20 nm, and individual columns are well resolved.

The simulated HAADF-STEM scattering intensity from 80 to 200 mrad is shown in Figure 2.9. It can be seen that atomic columns are well separated at all thicknesses, no contrast inversions take place, and the column intensities increase monotonically with thickness. Not shown here is that, as the thickness becomes very large, intensities converge towards the background, so that at sample thicknesses approximately $t > 1.5 \cdot \lambda_{\mathrm{MFP}}$ no image contrast can be observed. However it can also be seen that relative image intensities from different columns can rapidly change at very small sample thicknesses. In the thickness regime preferred in this work (30 – 35 nm), column intensities are largely linear. While this example thus illustrates that the chosen experimental conditions are well-suited for atomic resolution semi-quantitative STEM work, it is also made clear from the non-intuitive behaviour of relative intensities that each measurement needs to be regarded separately and compared to a probable best-fit model. Local symmetry and lattice distortions can be evaluated with sub-angstrom accuracy, when scan distortions are taken into account, while the possibility of residual vacancies and anisotropic effects of thermal displacements need to be taken into account when evaluating image intensities.

3. Experimental results and discussion

3.1 Preface

The experimental results presented here, as well as the discussion thereof, can be largely divided along the lines of the morphology and local atomic arrangements in the thin films depending on substrate and treatment. First it will be presented what information could be obtained by TEM methods from the as-deposited amorphous thin films. In the next step, the phase-change thin films were subjected to thermal treatment after deposition. The resulting metastable and trigonal crystalline structures are each discussed in separate subchapters. Lastly, thin films were deposited onto crystalline substrates at increased process temperatures.

While the main focus lies on the S/TEM imaging and diffraction information from the atomic arrangements, as well as the composition changes according to STEM-EDX, a short summary of the sample deposition conditions during PLD as well as the XRD information according to Ref. [115] is included in some subchapters. All FIB lamellae were prepared from regions excluding macroscopic deposition artefacts.

The results presented here have been, in part or in-depth, the subject of a number of peer-reviewed publications as well as conference contributions and presentations. Defect-rich metastable structures were described in [174], a close examination of the ex-situ annealed trigonal lattice is published in [55], the epitaxial crystalline deposition onto ionic crystals was presented in [114] and [175] , and the highly oriented and epitaxial growth on Si/SiOx and Si(111) was recently published in [176]. A full bibliography of all during the course of this dissertation published contributions can be found at the end of this work. It should also be mentioned that a large amount of publication activity currently takes place in the field of PCMs, regarding GST and layered superstructures[17, 46, 177, 178] as well as quantitative electron microscopy of GST atomic structures[102, 179, 180]. The research effort is certainly dynamic, however some reports can be conflicting, and various reported ordered layered structures require further testing against experimental evidence. STEM in particular is often used as a powerful method among other investigative tools for the determination of structure and properties. The work presented here may provide a nuanced view of the interpretation of STEM image information. Indeed, it can already be seen that such considerations are taken into account in the latest investigative reports on PCMs.

The aim of this chapter is thus not only to consider the observed structures separately, but to gain an understanding of the relationship between them which, hopefully, enables future efforts to target a specific crystalline growth behaviour by PLD, as well as helping to explore some of the highly anomalous properties of GST phase-change compounds that have produced such interest in this material for a variety of technical concepts. As such, each subchapter contains a discussion of the individual structures observed, in addition to a short section on summary and conclusions at the end of this work.

All S/TEM results shown were produced on the probe-Cs corrected Titan^3 G2 60-300 at an acceleration voltage of 300 kV. Unless otherwise indicated, high-resolution STEM images were acquired with a uniform set of parameters, using a C2 aperture / beam convergence semiangle of 25 mrad and STEM detectors covering 80 - 200 mrad (HAADF), 19.5 – 80 mrad (DF4), 9.5 – 19.5 mrad (DF2) and 0 – 9.5 mrad (BF). The corrector was tuned using the DCOR software until aberrations of less than 2 nm (A1,C1), 50 nm (A2,B2) and 500 nm (C3,A3,S3) were reached. All individual samples were iteratively thinned until a foil thickness of 50 nm or better was reached in EFTEM thickness maps.

3.2 Amorphous as-prepared GST thin film

The general PLD setup for the deposition of GST thin films has already been briefly introduced in chapter 2.2. As such, free parameters include the incident fluence of the laser on the target material, the pulse number, frequency and width, the ambient chamber pressure and auxiliary gas flow, the substrate composition and temperature. While the influence of various parameters is described in more detail in Ref. [115], a uniform set of parameters was used for the majority of the samples investigated in this work, and only the pulse number, substrate composition and temperature were adjusted for various experiments. The typical PLD parameters are listed in Table III.

Tab. III: PLD parameters and average compositions of target and as-deposited amorphous thin film from SEM-EDX and STEM-EDX, respectively. The residual difference to 100% can be attributed to small amounts of oxygen (0.5 – 3.5 at.%) at open surfaces. The standard deviations 1σ are derived from the widths of the deconvoluted peaks in the energy spectrum and the X-ray count statistic.

Laser fluence	Pulse No.	Frequency	Ar Partial pressure	Base pressure	Substrate temperature
0.8 J/cm²	4000 - 10000	1 - 10 Hz	4 x 10^{-5} mbar	4 x 10^{-8} mbar	RT - 280 °C

Composition PLD target [at.%]

Ge	1 σ (Ge)	Sb	1 σ (Sb)	Te	1 σ (Te)
23.41	0.88	23.97	1.13	52.44	2.55
Composition as-deposited amorphous [at.%]					
21.67	0.74	24.35	2.81	52.55	6.12
Ideal Composition GST 225					
22.2		22.2		55.5	

Since PLD ideally aims to provide a direct transfer of the target material composition onto the substrate, an EDX composition analysis of the nominally GST 225 target is also included. While there is a certain acceptable error in the composition measurements provided, in particular due to the X-ray emission peak overlap between Sb and Te L lines, as well as regarding the content of light elements such as oxygen, averaging over multiple measurements shows that the target may be slightly under-stoichiometric in Te. This is also seen in the resulting composition of amorphous as-deposited GST thin films. However, it is also evident that the Ge:Sb ratio has shifted slightly away from 1:1, although it is still far removed from the next preferred stoichiometry $Ge_{14.3}$: $Sb_{28.6}$ of trigonal GST124. In previous chapters it was introduced that the material system is resilient towards small off-stoichiometric compositions, mainly resulting in a small adjustment of the intrinsic vacancy concentration in the disordered and metastable phases. Contrary to the expectation for preferred $(GeTe)_{1-x}$ - $(Sb_2Te_3)_x$ stoichiometries, that each Ge cation is replaced by two thirds of a Sb cation (see introductory section 1.3.2), a shift from $(GeTe)_2$ – $(Sb_2Te_3)_1$ towards a real composition of $Ge_{1.95}Sb_{2.19}Te_{4.73}$ thus indicates that excess Sb needs to be incorporated. While the expected intrinsic vacancy sublattice concentration for $(GeTe)_{1-x}$ - $(Sb_2Te_3)_x$ with x = 0.36 corresponding to the experimentally determined Ge:Sb ratio would be 20.1 rel.% and thus hardly deviate from GST 225, the measured relative stoichiometric fraction of Te (4.73) is lower than that expected from $Ge_{1.95}$:$Sb_{2.19}$ since applying the 2/3rds rule for replacing Ge with Sb should result in a relative stoichiometric fraction of 5.235 for Te. In other terms, if an octahedral network of square alternating ABAB rings is constructed incorporating the entire Te content (52.55 at.%), and the mixed Ge/Sb positions are occupied by the 21.67 + 24.35 = 46.02 at.% of Ge/Sb, then the intrinsic vacancy concentration would be the difference 52.55 – 46.02 = 6.53 at.% or 13.06 rel.% of the mixed sublattice. Alternatively, it might be energetically preferable to incorporate the excess Sb in interstitial sites, which would result in 7 rel.% of Sb on tetrahedral positions.

In either case, at first glance this violates the 8-N rule for covalent bonding networks, meaning that Te species are over-coordinated. Somewhat contradictory, the density of an as-deposited (Ge and Te deficient) GST225 thin film was previously measured by XRR to be 5.6±0.1 g/cm³ and thus lower than typical for sputter-deposited amorphous GST225 thin films (5.88 g/cm³) or metastable cubic GST225 thin films (6.2 g/cm³). This would indicate that, rather than considering excess Sb which would increase the expected density, some Te positions may be left unoccupied. If the entire Ge/Sb content were situated in octahedral GeTe and Sb_2Te_3 arrangements, 5.65 at.% Te would be missing from the pseudo-lattice, or 11.3 rel.% of all Te positions. Since the missing mass of a Te vacancy is 127.6 g/mol, and a mixed Ge/Sb sublattice with 20.1 rel.% vacancies has an average mass per site of 77.8 g/mol, the average mass of all sites is 102.67 g/mol when Te sites are fully occupied, and 95.47 g/mol when incorporating Te vacancies, equating a decrease by about 7 %. A decrease of the density from the metastable cubic lattice by 7 % would result in an expected density of 5.76 g/cm³, and 5.46 g/cm³ for a 7% reduction from sputter-deposited amorphous GST, which indicates that some intrinsic Te vacancies may be a contributing factor but cannot be the only reason for the density observed. However several mitigating factors can be taken into account:

- The 8-N rule only aims to determine the expected coordination for entirely covalent bonding, while the exact local bonding characteristics in GST are still under discussion[85, 177] (partial hybridization).
- The concentration was measured from the amorphous as-deposited state, which can easily accommodate local inhomogeneities in structural motifs that do not need to conform to the octahedral arrangement. Furthermore, a semi-random arrangement of square rings inclined towards each other leads to an overall volume expansion, possibly explaining the low thin-film density observed.
- When taking into account the possible error in the EDX measurements (one standard deviation σ in table III), the ideal stoichiometric composition lies well within the scattering range of the experimental data. Furthermore, the target composition was measured by SEM-EDX of the entire surface information volume, thus necessarily applying ZAF (atomic number, absorption, fluorescence) correction. In contrast, the STEM-EDX evaluation from a thin film lamella using Cliff-Lorimer factors only factors in possible energy shifts and detector characteristics. Provided these were carried out appropriately the difference should be small, yet it is possible that a small systematic error was introduced. All further composition measurements shown were acquired by STEM-EDX under similar conditions, and thus should be comparable.
- During crystallization to the metastable and subsequently the stable layered phase, excess components may segregate into grain boundaries and structural defects. This possibility is discussed further during the presentation of the ex-situ annealed samples (chapter 3.2).

Nevertheless, the composition analysis highlights that off-stoichiometric effects are to be expected, and even low single-digit percent deviations in atomic concentrations may lead to a significant change in vacancy concentration relative to the ideal prediction. It is thus necessary to measure the composition of each sample before further discussing local features.

A surface survey of the as-deposited samples by SEM (Figure 3.1) confirms that the thin films present a smooth, closed surface. The surface roughness, previously measured by atomic force microscopy as 4 nm rms (root mean square), can be refined to 2 nm or less locally from bright-field TEM images of cross-section lamellae. A method for statistically comparable roughness evaluation applied to high-contrast interfaces is detailed in Appendix C.1. However, the samples also present spherical particles in the surface, which can be traced to the ejection of liquid droplets from the PLD target due to subsurface heating[181]. While this effect can be minimized by tuning the deposition parameters and geometry, for example by turning to off-axis deposition[182], it remains a challenge for the application scaling of PLD-produced thin films.

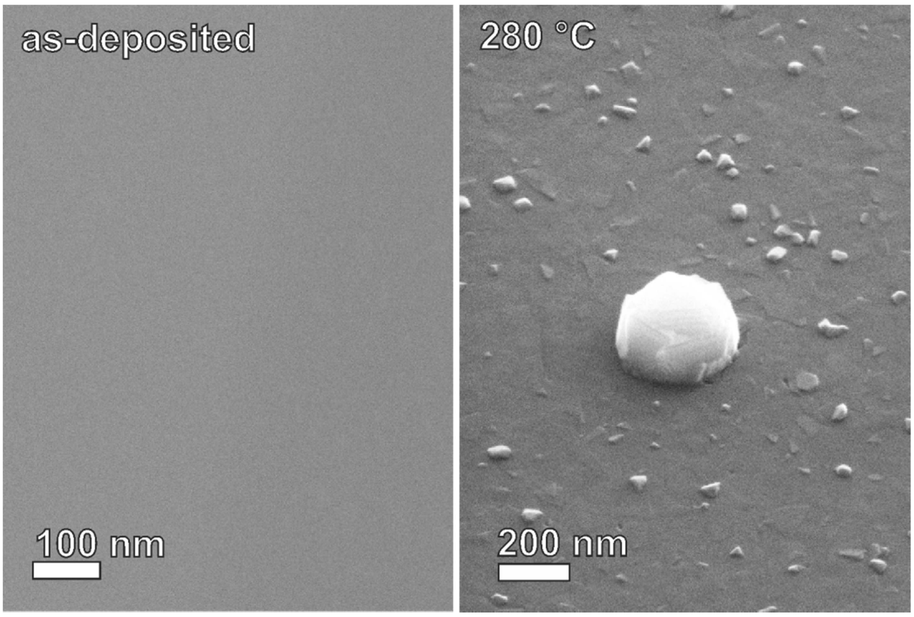

Fig. 3.1: SEM (20 kV, SE detector) overview of as-deposited amorphous GST (left), exhibiting a smooth surface, and of GST thin film deposited onto cleaned Si(111) at 280 °C (right, 45° tilt) for comparison, exhibiting some protrusions and surface facets in addition to the occasional always-present droplets (large spherical particle).

The particulate density (typically 10^4 cm^{-2} in a SEM surface view) is sufficiently low that thin film TEM samples, when prepared well-removed from individual droplets, can be interpreted in terms of planar thin film growth and structure. Another significant effect to be taken into account is surface oxidation and segregation during sample transfer and under FIB bombardment. STEM-EDX maps of an as-deposited sample cross-section are included in Appendix C.2. The surface amorphization due to kinetic transfer from the FIB beam is a well-known challenge in the TEM lamella preparation. In addition, preliminary EDX investigations of the as-deposited surface showed that the unprotected GST layer tends to react with ambient oxygen when exposed to air. The resulting surface layer typically measures 2-4 nm and is comprised predominantly of germanium and oxygen. While the possibility cannot be excluded that the FIB irradiation of the surface in the early steps of the FIB preparation enhances this surface modification, the presence of large amounts of oxygen indicates that the process does not occur inside the vacuum chamber. Furthermore, an open surface during post-deposition experiments such as thermal treatment or laser irradiation allows for the evaporation of volatile species, which can result in a drastically different thin film composition.

In order to prevent such effects in ex-situ crystallization experiments, a $LaAlO_x$ target was added to the deposition chamber, thus making it possible to deposit an amorphous protective surface layer immediately following the GST thin film deposition. As a result, even a very thin (2-10 nm) surface capping layer was sufficient to prevent further oxidation or out-diffusion even at high annealing temperatures (as shown in chapter 3.3).

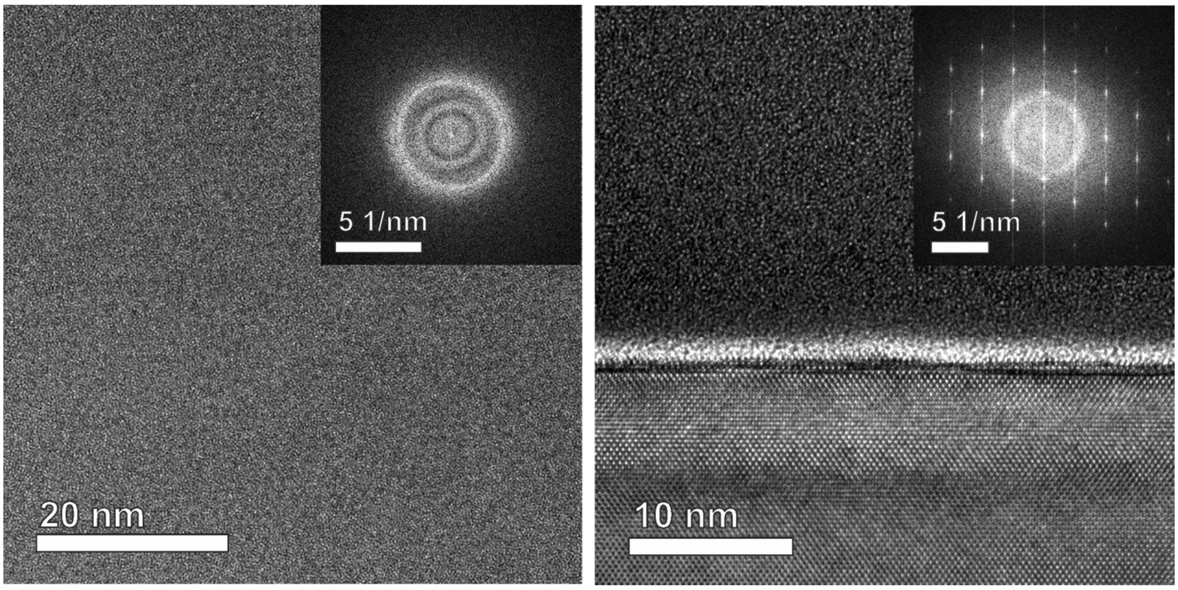

Fig. 3.2: HR-TEM images of as-deposited GST124 thin film (left) and as-deposited GST225 thin film – silicon substrate interface (right). The bright interface layer in right-hand panel stems from the SiOx native surface oxide. Insets show the corresponding HR-TEM images in spatial frequency space after Fourier transformation. While the inset on the left exhibits the influence of some objective astigmatism (elliptical distortion of the Thon rings[183]), and the inset on the right includes the strong point maxima from the Si[110] zone axis, the clearly discernible diffuse ring patterns illustrate the amorphous nature of the structures.

While conventional TEM imaging and Fourier analysis can provide a qualitative impression of the amorphous nature of the structure observed (Figure 3.2), a closer inspection of the diffraction information allows for a semi-quantitative view of the average local structure. The volume of evaluation can be narrowed by applying nanobeam diffraction (NBD) settings, effectively reducing the area of the beam spot to 3-5 nm diameter, and subsequently scanning over specific features of interest in the sample[72]. Selected area electron diffraction (SAED) is carried out under parallel illumination conditions using a circular aperture in the image plane in order to reduce the information area down to 100 nm diameter. Spread of diffraction features can thus be traced to either the random distribution of interatomic distances in the lattice structure or the imperfect information transfer of the objective lens. The convergence angle used in NBD (0.16 mrad) results in small diffraction disc features effectively blurring the diffraction plane.

One significant challenge for the RDF (radial distribution function) analysis from NBD is the limited signal intensity compared to the transmitted beam. Since the probed volume is intentionally reduced, weak features in the diffraction plane are often only visible when the CCD array is protected from the primary beam by the beam stop.

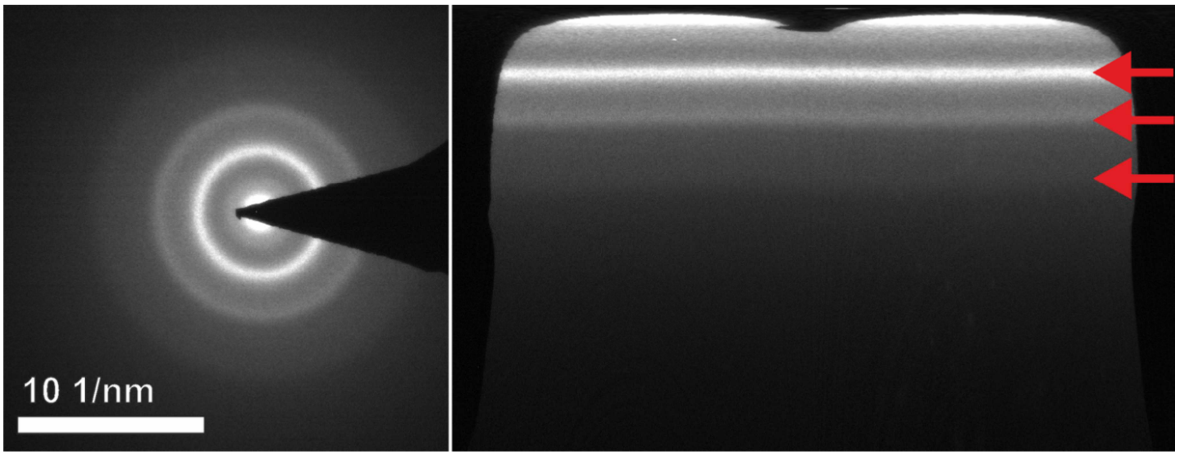

Fig. 3.3: SAED pattern of amorphous GST225 and corresponding azimuthal projection. Three diffuse diffraction bands are visible (red arrows) relating to preferred short-range order spatial frequencies.

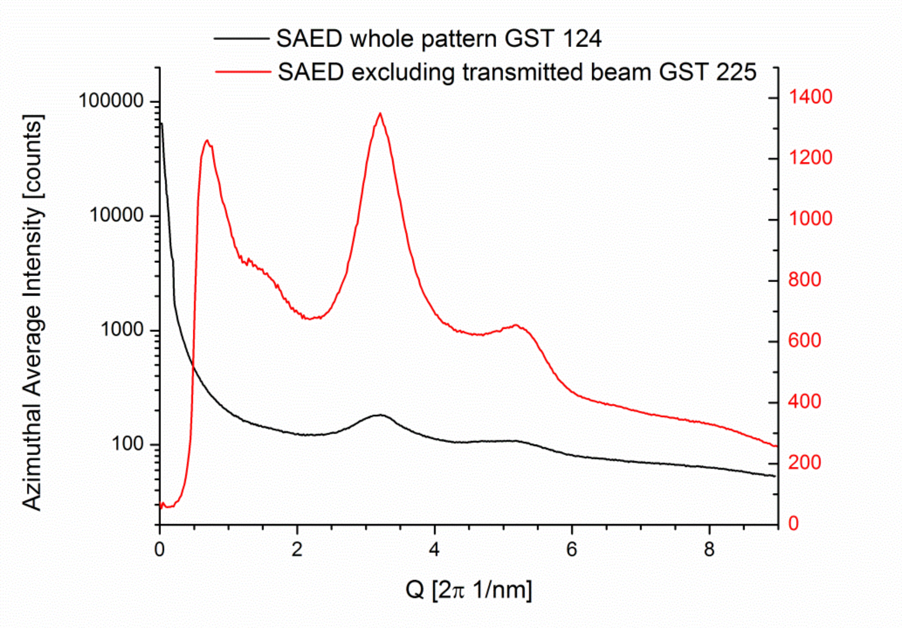

Fig. 3.4: I(Q) Azimuthal profiles of SAED diffraction patterns from amorphous GST124 and GST225. The pattern from GST124 was taken without a beam stop, and is thus plotted on the logarithmic scale (left). The pattern from GST225, shown in Figure 3.3, excludes the transmitted beam and can thus be plotted on a linear scale (right) revealing the pronounced diffuse peaks. One drawback of excluding the transmitted beam is, however, that the initial $N\langle f(Q)^2\rangle$ fit needs to be estimated from the noisy high-frequency region of the pattern, which often does not result in a good match around the relevant peaks.

The second step in the RDF analysis, after defining the centre of the pattern and azimuthal integration, is a fitting of the independent average scattering term $Nf^2(Q)$ to the baseline of the profile[184] in order to extract the structure factor $\phi(Q)$, where N is a fitting parameter from the volume probed and $\langle f(Q)\rangle$ is the average atomic scattering factor of all atomic species:

$$\Phi(Q) = \frac{I(Q) - N\langle f(Q)^2\rangle}{N\langle f(Q)^2\rangle} Q \qquad (3.1)$$

This is complicated by the exclusion of the transmitted beam, since the intensity distribution $I(Q)$no longer peaks at $Q = 0$. For small scattering parameters Q, $\phi(Q)$ and the ultimately resulting radial distribution function $J(r)$ and pair distribution function $g(r)$ from the inverse Fourier transformation of $\phi(Q)$ can thus vary strongly between measurements, depending on the best estimate for $N\langle f(Q)^2\rangle$ and other fitting parameters (such as the dampening function used to reduce the noise influence of the high-frequency region). Nevertheless, the RDF analysis is a useful tool in the presence of short-range ordering such as in amorphous GST. While the exact behaviour of $g(r)$ may vary, the positions of the first and second nearest neighbour peaks can typically be resolved, and be used to estimate bond angles and coordination.

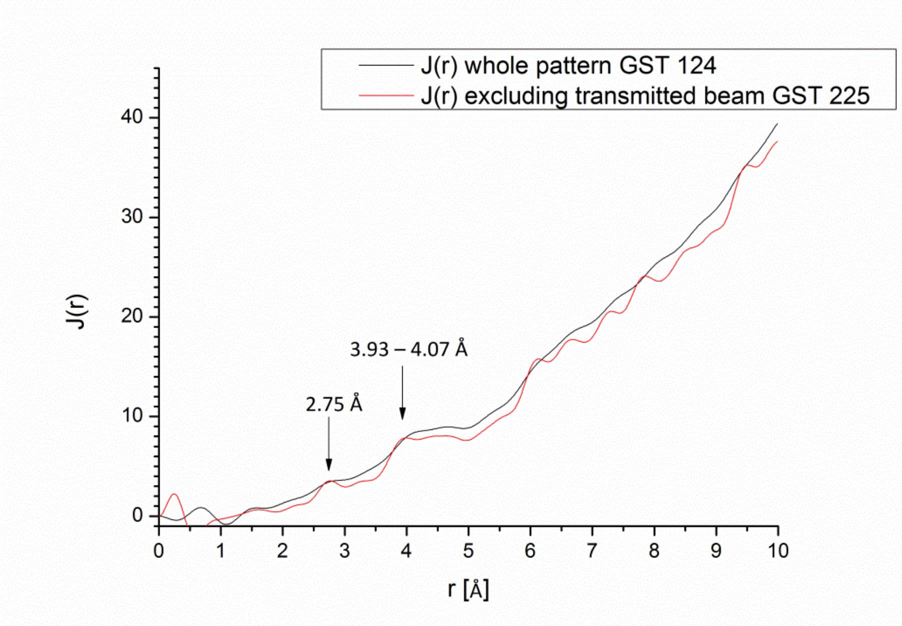

Fig. 3.5: Radial distribution $J(r)$ calculated from Fourier transformation of $I(Q)$ in Figure 3.4 after correction for the independent scattering contribution $N\langle f(Q)^2\rangle$. $J(r)$ is scaled to the radial density of surrounding atoms.

A comparison of SAED diffraction information from amorphous as-deposited thin films produced from a GST124 and a GST225 target is shown in Figures 3.3 – 3.6. The diffuse first diffraction ring in the SAED pattern is typical for disordered amorphous compounds with some persistent short-range ordering. Evaluation of the diffraction information by RDF analysis is rather sensitive to the initial parameters such as composition, average local density and independent scattering factors $f_e(Q)$. The routine used here ("RDF Tools for Digital Micrograph v 1.1" written by D. G. Mitchell)[185] makes use of the parameterization of $f_e(Q)$ given by Ref. [118] in order to fit the average $N\langle f(Q)^2\rangle$ of all components to the experimental data. While these tabulated values are generally well supported, there appears to be a small systematic offset in the low-angle region compared to the experimental background, which often makes a good fit difficult. The resulting calculated reduced density function $G(r) = 4\pi r\, [g(r) - \rho_0]$ may thus appear detailed over a large range, but for the purpose of semi-quantitative discussion it is preferable to only consider the first and second strong peaks, relating to the nearest- and next-nearest neighbour distances. Furthermore some information may be lost due to the finite beam convergence, as well as the various averaging and noise dampening steps in the evaluation.

In both the GST124 and the GST225 amorphous as-deposited sample, the first peak in the $G(r)$ distribution is situated at 2.78 Å (± 0.02 Å due to the pixel resolution), while this peak lies at 3.15 Å in the polycrystalline sample. Previous literature on the amorphous structure of GST compounds investigated by EXAFS[79] and DFT simulation[81] also suggests that average Ge-Te and Sb-Te distances shorten compared to the crystalline cubic phase, however often a distinction is made between distorted tetrahedral arrangements at 2.61 Å and distorted octahedral sites at 2.85 Å.

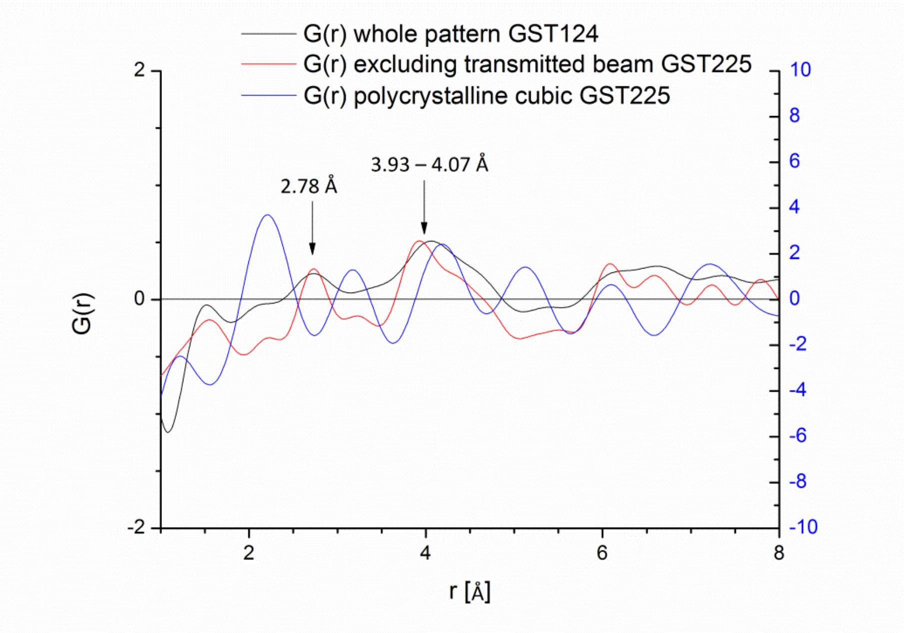

Fig. 3.6: Reduced density function $G(r)$, extracted from the Fourier transformation of the diffraction intensity distribution $I(Q)$ in Figure 3.4, and ρ_0 the average expected density. The $G(r)$ scale thus describes the deviation from the expected parabolic density distribution $J(r)$ (see Figure 3.5) of a uniform amorphous continuum. Deviations below $r = 2.5$ Å have no direct physical interpretation and can be disregarded. Crucially, the first local maximum at 2.78 Å corresponds well to the expected position of defective octahedral Ge-Te[43, 57], while the shift of the second local maximum around 4 Å and the slight indication of a buried second peak around 4.4 Å may signify a higher fraction of homopolar “wrong bonds” in the GST225 sample. For comparison, a $G(r)$ distribution from a polycrystalline SAED pattern of GST225 is also included (blue line, right y-axis), exhibiting strong peaks at 3.15 Å (Ge-Te) and 4.2 Å (Te-Te). The local atomic structure of the crystalline sample (here preliminarily assigned cubic) is discussed in further detail in the following chapter.

While the value measured here lies roughly in-between the two, it needs to be stressed that no clear indication of a bimodal distribution in this range was found, while the first peak in the polycrystalline sample lies close to the expected value for octahedral sites in the metastable lattice (3.05 Å). Similarly, the second-nearest neighbour peak distance at 3.93 – 4.07 Å is slightly smaller than that found corresponding to Te-Te distances in the cubic lattice (4.2 Å). Selected NBD measurements representative for all investigated amorphous structures are shown in Figure 3.7. As can be seen in the left panel, even under NBD microscope conditions an image can be recorded from the HAADF-STEM signal. In fact, since the total beam current is spread over the NBD beam spot, these conditions may be preferable for STEM imaging and spectroscopic mapping of very beam-sensitive materials, if a spatial resolution of better than 3-5 nm is not required. Four NBD patterns from selected positions of a larger line series are shown in the right-side panels of Figure 3.7. Due to the smaller information volume, individual coherently scattered beams can be discerned, rather than the previously shown diffuse rings. Resulting from the disordered nature of the thin film, some strong scattering intensity spots can be found in-between the diffuse rings from preferred short-range ordering.

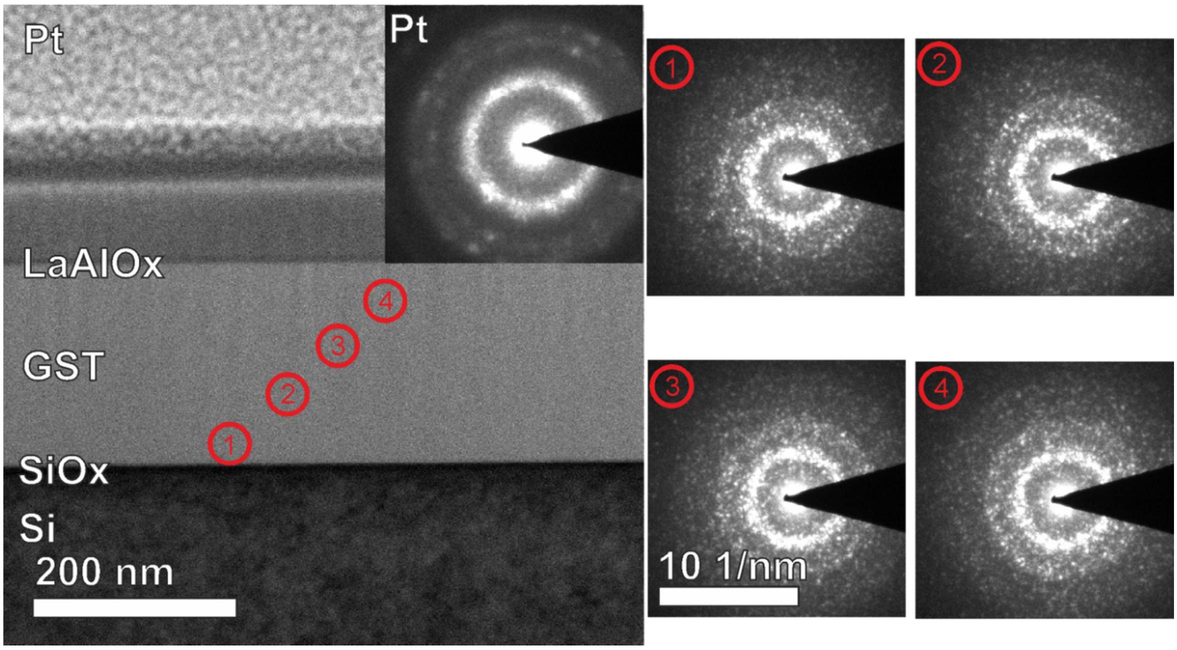

Fig. 3.7: HAADF-STEM scan image acquired with NBD beam settings (left) and NBD diffraction patterns from a linescan across the as-deposited GST sample (right), selected from positions as indicated by red markers. The beam diameter can be estimated from the resolution of the nanocrystalline Pt to be no larger than 5 nm. The overall intensity distribution is similar to the SAED pattern in Figure 3.3, however the granularity of the rings becomes visible, as well as some spot intensities in-between the first and second ring. Also included is an NBD pattern from the e-beam deposited Pt for comparison. The $LaAlO_x$ and SiO_x interface layers are too thin (<5 nm) to be resolved individually by an NBD probe.

They do not appear to be arranged systematically as would be the case in e.g. a small fraction of tetrahedral motifs, although it is difficult to entirely exclude these or differentiate them from the semi-randomness of the amorphous structure. The RDF analysis of the NBD patterns is shown in Figure 3.8. Similar to Figure 3.6, the significant information is contained in the position of the first two peaks. Also included for comparison is the $G(r)$ distribution for an NBD pattern from the Pt nanocrystal layer, with first and third peak matching the peak positions of 2.77 and 4.8 Å for cubic $Fm\bar{3}m$ Pt well, while the second peak at 3.92 Å lies below the abscissa, indicating that the density of the material was overestimated due to its nanocrystalline morphology. All $G(r)$ distributions from GST225 NBD patterns coincide reasonably well, although there are some small variations of peak positions (± 0.04 Å). However, a first peak at slightly smaller radial distance is always compensated by a second peak at slightly larger distance, so that the average spacing (and density) remains roughly the same between measurements.

It is possible to estimate the average bond angles from two peaks in G(r) according to $\frac{\gamma}{2} = \arcsin {}^{r_2}/_{r_1}$, and doing so for the as-deposited sample GST225 consistently results in angles close to 90° (90.5 – 93°), while the small shift in the second peak position in the GST124 sample results in a slightly larger average bond angle of 95°.

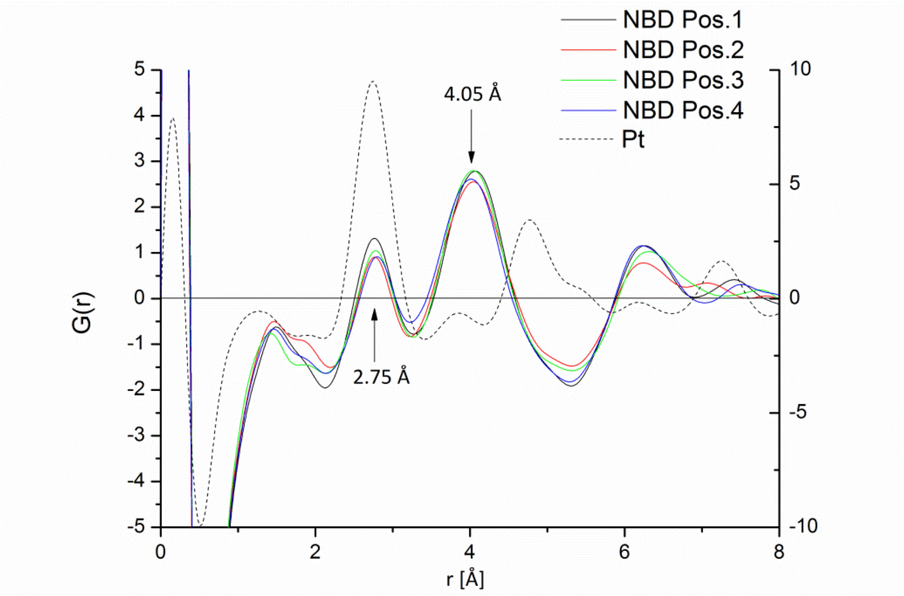

Fig. 3.8: $G(r)$ distributions for NBD patterns shown in Figure 3.7. Results for measurements in the GST thin film (positions 1-4) are plotted on the left y-axis, while the ordered Pt nanocrystallites consequently result in a much sharper pair-correlation and the result of this measurement is scaled to the right y-axis. First and second local maxima lie within a range of 0.04 Å for different measurements.

It thus would appear that the interatomic distances are narrower overall than expected, with the nearest-neighbour peak and bond angle found in the GST225 sample matching approximately the previously reported defective octahedral arrangement. This does however raise the question why the amorphous phase appears to be less dense than expected (as discussed above), and the most ready explanation would be that, if Te vacancies are present, the defective octahedral Ge-Te and Sb-Te motifs in covalently bound square rings enclose clusters of two or more Ge/Sb and Te vacancy pairs in a disordered network.

In summary, while the Ge/Sb-Te and Te-Te distances deduced from these measurements can vary slightly, the amorphous GST225 layer used in subsequent crystallization experiments exhibits a lower density than the literature would suggest, while the RDF measurements generally indicate a distorted octahedral arrangement of the short-range order. The discrepancy between slightly smaller pair-distances and density may possibly be resolved by the incorporation of additional Te vacancies. These may cluster with intrinsic Ge/Sb vacancies, allowing for a greater degree of freedom in the inclination of square-ring motifs against each other. Some of the edges of these motifs may be connected by a small amount of homopolar bonds. Any further quantitative conclusions are problematic due to the inherent randomness of the structure and the limited precision of the measurements and evaluation. Lastly, it is important to recall that these structures are rather sensitive to energetic influences, such as heating through the electron beam. It is thus possible that some distinct disorder features cannot be found by NBD electron beam methods at 300 kV acceleration voltage.

3.3 Ex-situ annealed crystalline thin films

3.3.1 Metastable cubic GST

The most straight-forward way of obtaining crystalline samples is the thermally induced phase transition by annealing after deposition with a controlled thermal profile. Due to the volatility of the components at typical annealing temperatures, it is critical that the surface is protected by a capping layer. Early experiments without the thin $LaAlO_x$ coating resulted in the formation of a Ge-rich surface oxide layer, despite the annealing processes themselves being carried out in a vacuum oven at pressures of less than 10^{-5} mbar. In addition, in the topmost 5-10 nm of these samples, EDX maps reveal a gradient in the relative contents of components. Similar surface layers were observed in laser-irradiation experiments of unprotected GST thin films performed in ambient air[186].

This indicates that, while the ultra-fast phase transformation process itself is regarded as diffusion-less, the higher thermal load during slow annealing enables long-range diffusion, which in annealing experiments is not detrimental in itself since it allows for the formation of large crystalline grains suitable for high-resolution investigation. However, in the case of an open surface, the Ge species form a reactive surface layer while the zone below consequently tends towards Ge-deficient stoichiometry. At good vacuum conditions the driving force for this behaviour should not be primarily the chemical potential of Ge at the surface, but rather the internal energy of the crystalline lattice. Wuttig[20] posited that, following from ab-initio calculations and thermodynamic measurements, compositions of $Ge_{1.5}Sb_2Te_4$ and $Ge_1Sb_{1.5}Te_4$ are more energetically favourable in the metastable phase than $Ge_1Sb_2Te_4$ or $Ge_2Sb_2Te_4$. Which composition had the overall lowest energy depended on local Peierls distortions and distribution of intrinsic vacancies (Ge or Sb), and absolute differences were small. This aspect gains renewed prominence in chapter 3.4.

It is likely that a similar argument holds for the GST225 thin films investigated here, and thus the already slightly Ge-deficient amorphous thin films may eject some Ge content near the surface during transition to the metastable phase when possible. In contrast, thin films with a capping layer did not exhibit any inhomogeneity at the surface after annealing, except for the occasional formation of cracks and delamination at the substrate interface due to the overall volume change.

The central questions for the here observed metastable thin films are thus what the overall lattice configuration is (i.e. symmetry and lattice constants), whether distortions of the mixed sublattice can be identified by atomic-resolution imaging, and if the distribution of of the mixed sublattice components can be resolved.

The amorphous GST thin film on Si(001) substrate / native SiO_x interface with an $LaAlO_x$ capping layer was produced as described in the previous chapter. It was subsequently thermally annealed at 160 °C inside a vacuum oven (Mila ULVAC, quartz tube, pressure $< 10^{-5}$ mbar, 10 min heating ramp = 15 °C/min, 20-30 min hold, natural cooldown). An out-of-plane θ-2θ X-ray diffraction scan from a Cu Kα source (Rigaku Ultima IV type 3 diffractometer) is shown in Figure 3.9, with clearly visible crystalline diffraction maxima. The peak positions indicate that the GST thin film is present in the metastable cubic NaCl-type lattice with a lattice constant of 0.5987 nm, which is in the lower end of the expected range for GST compounds, c.f. 0.60293 nm from ICSD#55294 for $Ge_2Sb_2Te_5$[49] up to 0.60876 nm for $Ge_1Sb_4Te_7$[187]. Critically, the absence of additional peaks from the trigonal phase implies that this phase would, with strong certainty, be identified as the disordered metastable phase by XRD crystallographers[188, 189]. The peak widths indicate an average crystallite size of 30 nm. Since the desired lamella thickness for TEM investigation is in this range, this preliminary investigation thus indicates that the sample should be well-suited in order to investigate the metastable cubic phase of GST. The grain morphology under BF-TEM diffraction contrast and HRTEM conditions is shown in Figures 3.10 and 3.11. Since the thin film geometry restricts the grain growth directions, individual crystalline grains can possess a lateral extension of 60 nm or more, while in perpendicular direction the thin film is often equally divided into a grain close to the surface and one close to the substrate interface.

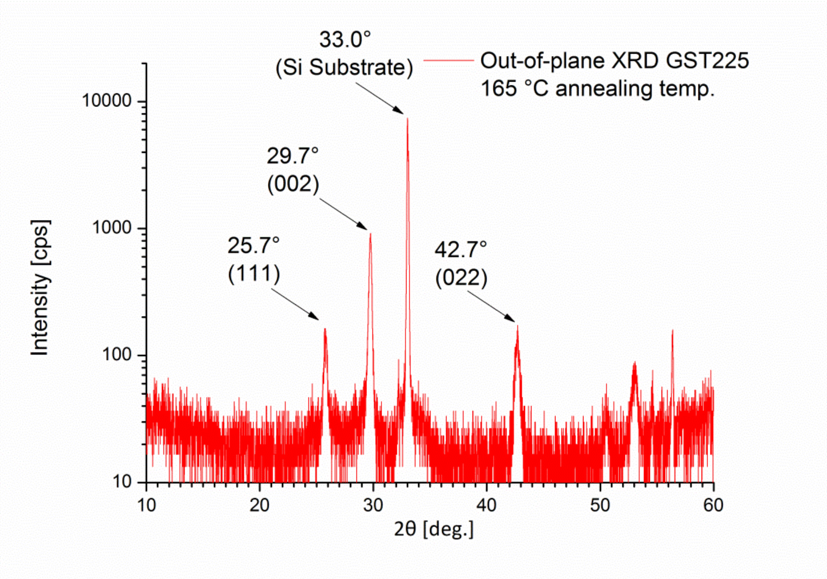

Fig. 3.9: XRD 2θ-scan out-of-plane. Diffraction peaks generally indicate cubic lattice (see indices). While the distinction between cubic and trigonal lattice purely from diffraction information is sometimes difficult, no peak at 39.8° (which would relate to (10-16) planes of the trigonal lattice) is apparent. Peak width indicates 30 nm average crystallite size.

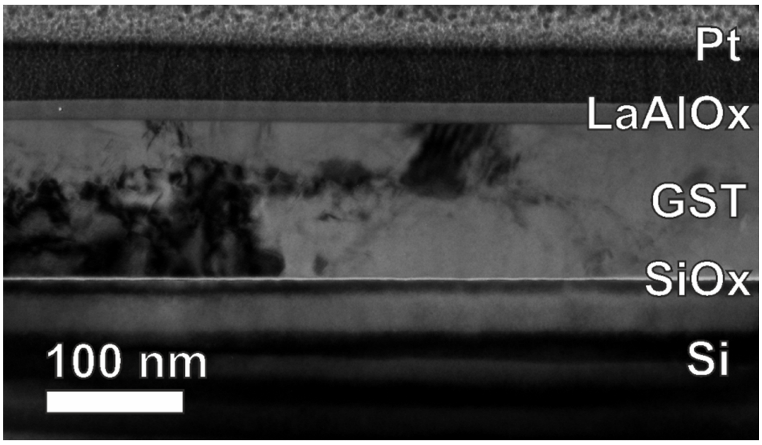

Fig. 3.10: TEM overview image of thin film cross-section, recorded under diffraction contrast conditions. Crystalline grains are generally slightly larger than the average grain size determined by XRD, and grain growth is constrained by the thin film interfaces. While the grain shape does not offer a clear trend, some straight grain interfaces imply anomalous grain growth. Bright lines in the substrate are thickness fringes due to a marked thickness gradient towards the bulk substrate from the specimen preparation process.

This may indicate preferential nucleation and grain growth from the interfaces during slow annealing, although since the sample was investigated after the long annealing had occurred, it is likely that other features that would indicate nucleation characteristics have already disappeared. The crystalline nucleation in a wide range of GST compounds has been extensively studied[186, 190-192], and typically the amorphous interface – crystalline GST interface (formation) energy is considered to be about twice as large as that of the amorphous GST – crystalline GST interface. This has led to the conclusion that crystallization is dominated by bulk nucleation and growth. The grain morphology seen here indicates that either very few crystalline seeds were present in the as-deposited state, or that the annealing time was sufficiently long that some grains were absorbed by those growing from either interface. In either case, this observation is not absolute, since grains that extend across the entire thin film are almost equally as likely to find, and not every individual grain can be discerned from the diffraction contrast overview.

In order to more closely analyse the crystalline structure and orientation across a large area of the thin film, NBD line profile series were acquired, typically recording 20-40 diffraction images across 0.2 - 2 µm of the thin film. Since these revealed that the crystallite orientation appears random, only three selected patterns are shown in Figure 3.12, which showcases some prominent features. For one, after calibration with the Si[110] substrate, (11-1) reflection at 2.8(6) nm^{-1}, (020) reflection at 3.1(2) nm^{-1} and (-202) at 4.6(8) nm^{-1} can be compared with nominal values for the cubic GST225 lattice: 2.872 nm^{-1} for (11-1), 3.317 nm^{-1} for (020) and 4.691 nm^{-1} for (-202). While these values agree reasonably well, the pixellation of the detector and the extension of the diffraction disks due to the finite convergence angle make a closer match or an accurate distinction of small lattice distortions difficult. Rhombohedral GeTe would exhibit diffraction intensity in [001] zone axis symmetry at 2.922 nm^{-1} (100), 3.346 nm^{-1} (110) and 4.791 nm^{-1} (1-10).

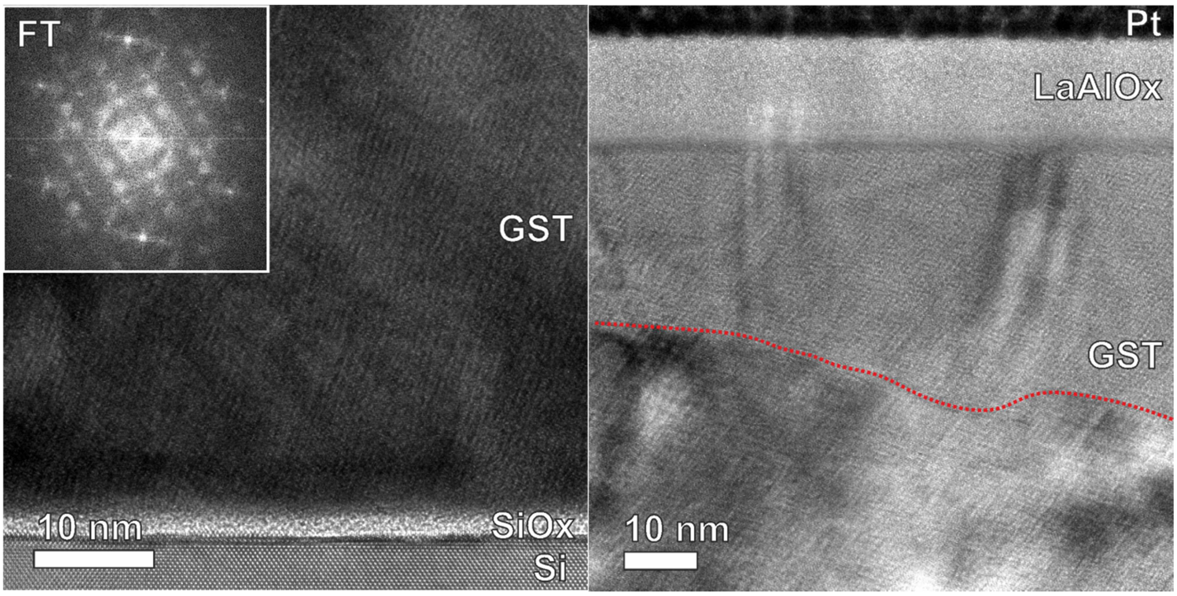

Fig. 3.11: HRTEM image of thin film – substrate interface with amorphous SiOx interlayer (left) and thin film surface with $LaAlO_x$ capping layer (right). Red dashed line in the right panel marks the boundary between two crystallites, FT inset calculated from the GST layer image area in the left panel illustrates lattice plane fringes. The faint grey layer < 1nm at the interface between GST and LaAlOx results from a very thin Ge/Sb enrichment zone as well as projection of surface roughness (see Appendix C.3).

Secondly, occasionally series of weak superstructure reflections are visible. This does however only occur very rarely, and more importantly they can be visible along two major axis in reciprocal space simultaneously.

This would indicate that either two grains with superstructure ordering and similar zone axis alignment would overlap within the NBD spot, in which case individual patterns of only one orientation should have also been found, or that vacancy ordering into {111} planes can occur in all of the three equivalent planes within the same cubic grain. Lastly, some NBD patterns exhibit weak diffuse features similar to the amorphous rings in the previous chapter. Since the beam shape in the sample can be roughly approximated as a cylinder of 5 nm diameter and 35 nm length, the residual amorphous surface layer can contribute 5% of the total probed volume, even if it has been reduced to 1 nm at either open surface. However it is also possible that these diffuse contributions indicate some small amount of amorphous content at microscopic inhomogeneity such as micro-voids or grain boundaries, since as was mentioned above the material may tend to expel some Ge content (see EDX maps Appendix C.3).

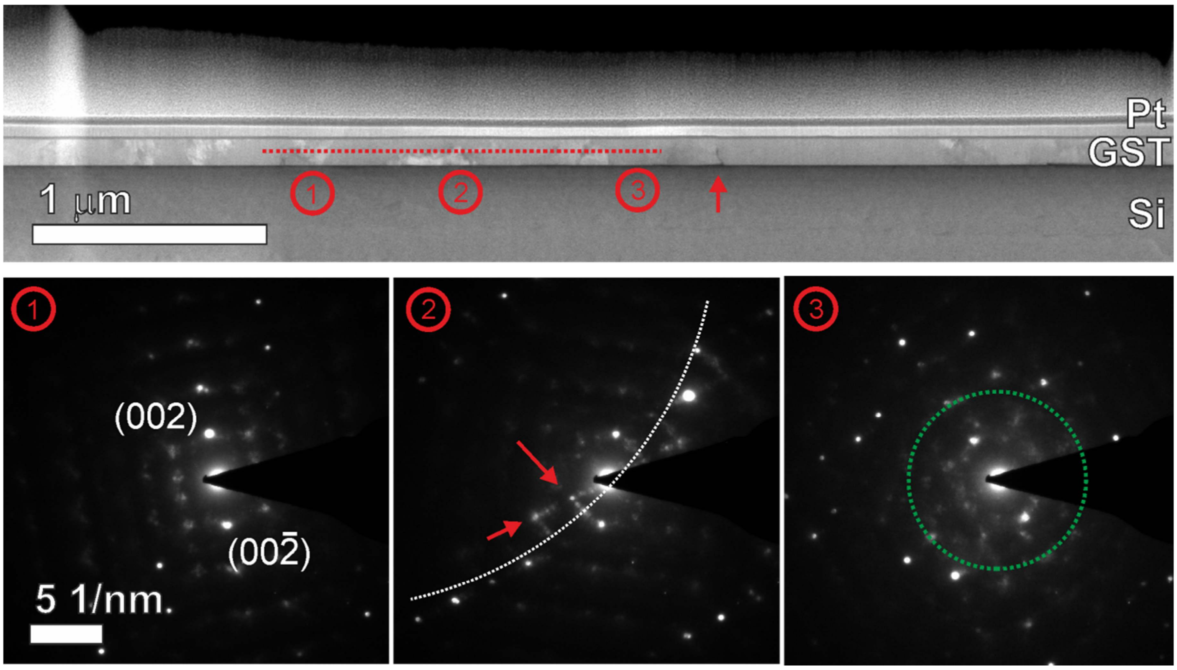

Fig. 3.12: NBD-STEM image of HAADF signal (top), red dashed line indicates position of NBD profile, numbered marks the corresponding NBD patterns shown below. A crack in the GST thin film (red arrow) may result from mechanical stress due to the volume contraction during crystallization. Corresponding NBD pattern (1), (2) and (3), illustrating the random orientation of the crystalline grains. Red arrows in (2) mark faint superstructure reflections from vacancy ordering in two {111}-type planes, dashed white semi-circle indicates about 4° tilt away from [110] zone axis, green circle in (3) indicates a small residual amorphous component visible in the diffuse contribution close to the (002) reflections.

The shape of the grain boundaries is inspected closer in Figures 3.13 and 3.14. BF- and ADF-STEM overview images show that the interface between GST crystallites is faceted. The detailed view of a grain in [110] zone axis reveals that often the densely packed {111} planes form the outermost layer of the lattice. In the image shown in particular, lattice planes appear to continue across the grain boundary. While the exact misorientation angle and thus the Σ coincidence site lattice (CSL, see chapter 1.4.3) cannot be directly determined from the image, such ordered interfaces between grains are typical for coherent low-angle grain boundaries. One plausible candidate would be some form of <111> symmetric tilt boundary, such as the primitive Σ3<111> CSL, or the Σ7<111> CSL which is known to be a high-mobility grain boundary in the FCC lattice. The structure of the GST thin film towards the amorphous interface layers is shown in Figure 3.15, once oriented in the Si[110] substrate zone axis, and once in the GST[100] zone axis of a grain at the LaAlO$_x$ surface. There is no clear indication of an orientation relationship, or the formation of an interface passivation layer. In particular in regards to the single-crystalline substrate, it would have been possible that the flatness of the amorphous interlayer may have been sufficient to induce preferential orientation of the nuclei, which should be more pronounced in thinner layers. While this is still the case in some grains (e.g. the bright crystallite in Figure 3.12 from which the NBD image (2) was acquired, which may also play a role in the formation of a layered superstructure), it does not occur often enough that a systematic behaviour can be postulated from this sample alone.

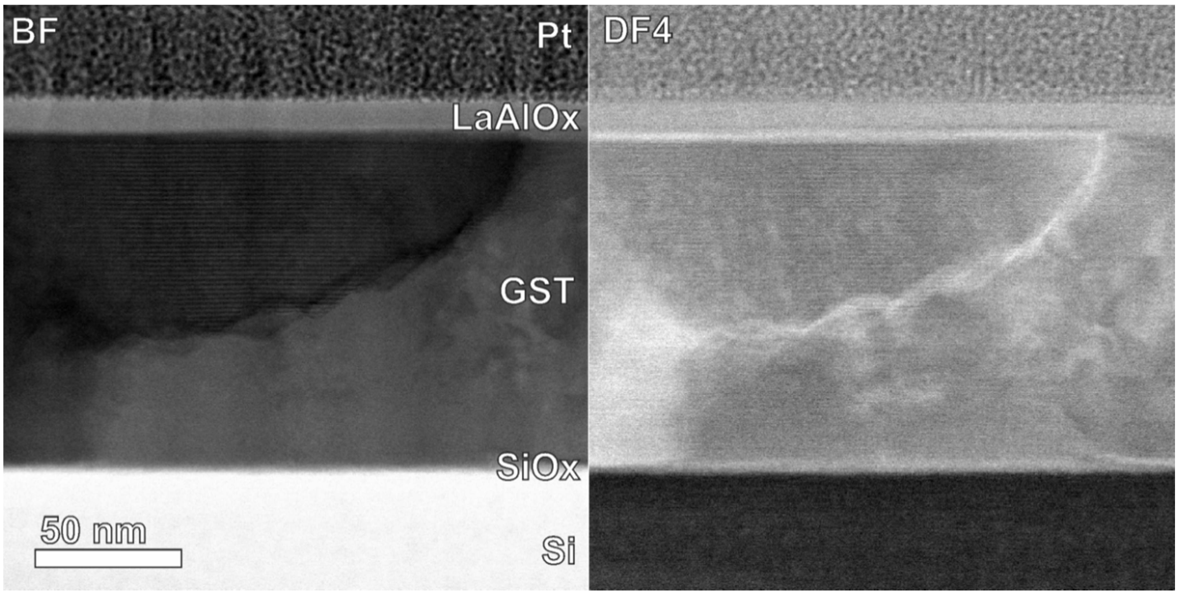

Fig. 3.13: STEM image overview of grain boundary in the GST thin film. Coherent diffraction contrast image (BF-STEM 0 – 7.7 mrad, left) and corresponding intermediate incoherent scattering contrast image (DF4-STEM (ADF) 19.1 – 80 mrad, right). The grain in zone axis orientation appears darker in the BF-STEM image due to strong coherent scattering out of the low-angle region, while the grain boundary itself appears brighter in the DF4-STEM image, possibly due to de-channelling from lattice distortions at the interface.

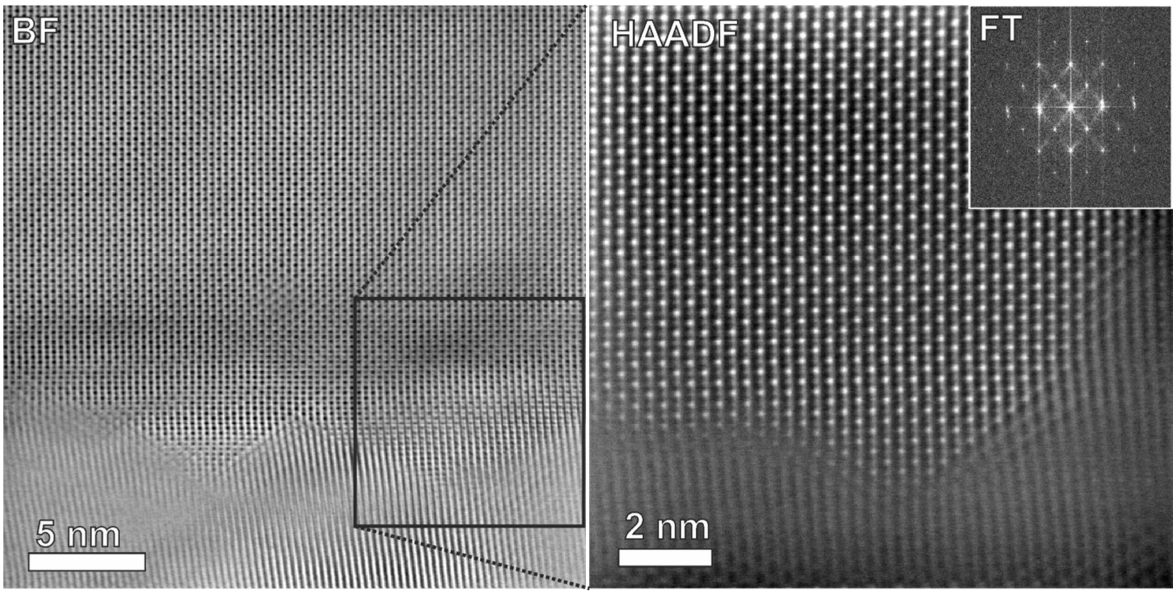

Fig. 3.14: High-resolution BF-STEM (0 – 7.7 mrad) detail of grain in [110] zone axis projection and grain boundary (left), and magnified detail of lattice and grain boundary in HAADF-STEM (80 - 200 mrad) contrast (right). The FT inset illustrates the zone axis symmetry as well as the excellent point resolution (80 pm or better). Black spots in the BF-STEM image correspond to bright spots in the HAADF-STEM image, resulting from the heavy Te columns of the metastable cubic lattice.

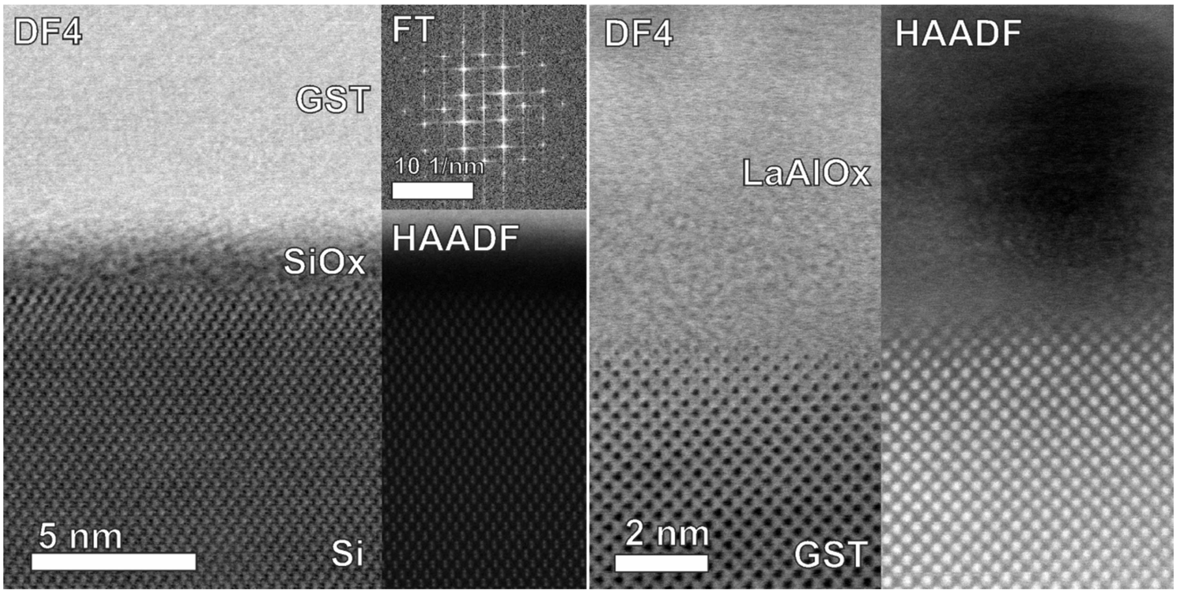

Fig. 3.15: STEM images of amorphous interfaces. DF4-STEM (9.6 – 40 mrad) image of Silicon substrate lattice in [110] zone axis and native oxide interface layer between substrate and GST thin film (left), corresponding HAADF (40 - 200 mrad, C2 = 20 mrad) image and resulting FT of substrate, useful for calibration of magnification and resolution. Similar DF4-STEM and corresponding HAADF image of GST thin film surface and LaAlOx capping layer (right). The amorphous SiOx interface masks any influence of the substrate orientation on the crystalline growth in the GST layer. The apparent size of the dark / bright spots representing the mixed Ge/Sb/Te columns in [100] zone axis projection in the right panel changes due to a local thickness gradient towards the surface.

On the other hand, as will be shown in the subsequent chapter on deposition at elevated temperatures, by increasing the mobility during crystallization this tendency can be exploited in order to produce textured thin films on amorphous interface layers.

One major practical challenge for the STEM imaging of polycrystalline thin films is the alignment of one specific grain into a useful zone axis. Often, the choice is made by selecting individual grains that are coincidentally well-aligned towards the incident beam. Alternatively, by viewing the fluorescent screen while the beam is scanning rapidly over one small area in under-focused conditions, a large angle convergent beam electron diffraction (LACBED) type pattern can be observed, containing Kikuchi features (incoherent scattering and subsequent multiple scattering) and ZOLZ (zero order Laue zone) deficient lines[193] which can be used to tilt the specific area in question into a zone axis (see Appendix C.4). Once a zone axis orientation has been obtained, the next challenge is minimizing image drift during acquisition while still retaining a good signal/noise. Very short dwell times coupled with sample drift correction by cross-correlation and subsequent frame averaging has been used elsewhere in order to obtain atomic resolution EDX maps[180]. However this can result in a loss of spatial resolution due to the imperfect overlap between subsequent images, and for the strong Z-contrast and good instrument stability (<1 nm/min spot drift) in the experiments discussed here, a single image acquisition with a frame time between 5 and 30 secs (depending on image resolution and dwell time) is equally sufficient for imaging purposes. Additionally, the application of image post-processing is a widespread and versatile tool in order to improve images after acquisition, as well as to quantitatively analyse the information contained therein. Two processing routines are regularly applied to the image shown here.

For one, the application of either the radial Wiener filter or radial difference filter[194] provided in the HREM-Filters (HREM Research) plugin for Digital Micrograph serves to reduce high-frequency noise as well as sharpen the lattice image by removing selected Fourier components of the image. Secondly, linear sample drift (continuous drift during acquisition) can be removed from the image by application of the Jitterbug plugin[195], which accepts user input on the ideal lattice in order to correct drift distortion. However, it is important to note that Fourier filtering results in pronounced changes in the local image intensities, while drift distortion correction relies on prior knowledge of the overall expected lattice structure.

The former thus can be applied when evaluating real-space distances in the lattice image, while the latter can be useful for subsequent evaluation of image intensities, although the pixel-interpolation upon adjusting row displacements with sub-pixel resolution needs to be taken into account in the resulting reconstructed image. An example of a GST [100] zone axis lattice image and subsequent image processing steps is shown in Figure 3.16. Also included therein is a map of the local lattice rotation, calculated by means of the geometric phase analysis (GPA)[196].

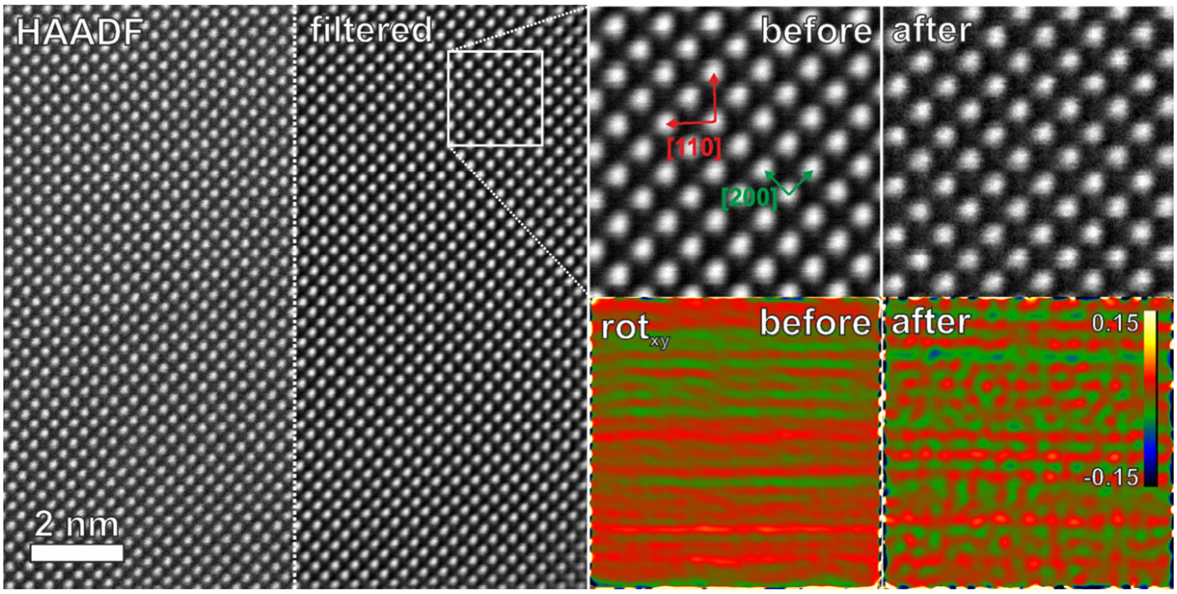

Fig. 3.16: HAADF-STEM (40 - 200 mrad, C2 = 20 mrad) image of GST lattice in [100] zone axis projection, and resulting image after FFT Wiener filtering (panels left). Magnified view of the same lattice image before and after drift correction (top right) and corresponding GPA maps of local lattice rotation, taken from the whole image (bottom right, colour scale is fraction of 2π). While the removal of high-frequency noise significantly improves the image quality, some quantitative information on absolute image intensities is lost. The drift correction works under the assumption of a uniform, distortion-free lattice, which is not necessarily always the case (compare distortion of lattice planes in the lower part of Figure 3.15). Nevertheless, the uniformity of the resulting rot$_{xy}$ map indicates a good reconstruction of the real lattice.

The GPA rotation map shows that, before drift correction, a small change in sample drift rate resulted in a stronger lattice distortion in the lower part of the image (red area), while after correction the rotation of the lattice relative to the reference ideal cubic lattice largely oscillates about 0, with some residual stripes due to scan noise (mechanical or electronic vibrations in the instrument). Image processing is furthermore useful in order to visualize the information on local lattice spacings and intensities from individual atomic columns. The GPA also allows the mapping of local lattice distortions due to uniaxial or biaxial strain fields, or pre-existing deviations due to different than expected lattice geometry. However, this functions best with a primitive symmetric reference lattice, while the sub-angstrom distortions of interest in the complex GST lattices can often only be identified by statistical evaluation of individual real-space distances from profile measurements.

Such profile measurement and fitting steps (elaborated on further below) can also be used to extract the local image intensity from the raw image data. In addition, Zhang et. al. have recently shown how by means of image manipulation the local image intensity ratios, and thus either vacancy distribution or Ge concentration, can be visualized[179]. A similar approach has been taken here (the source code for the Digital Micrograph script can be found in Appendix E, partially adapted from example scripts by D. G. Mitchell).

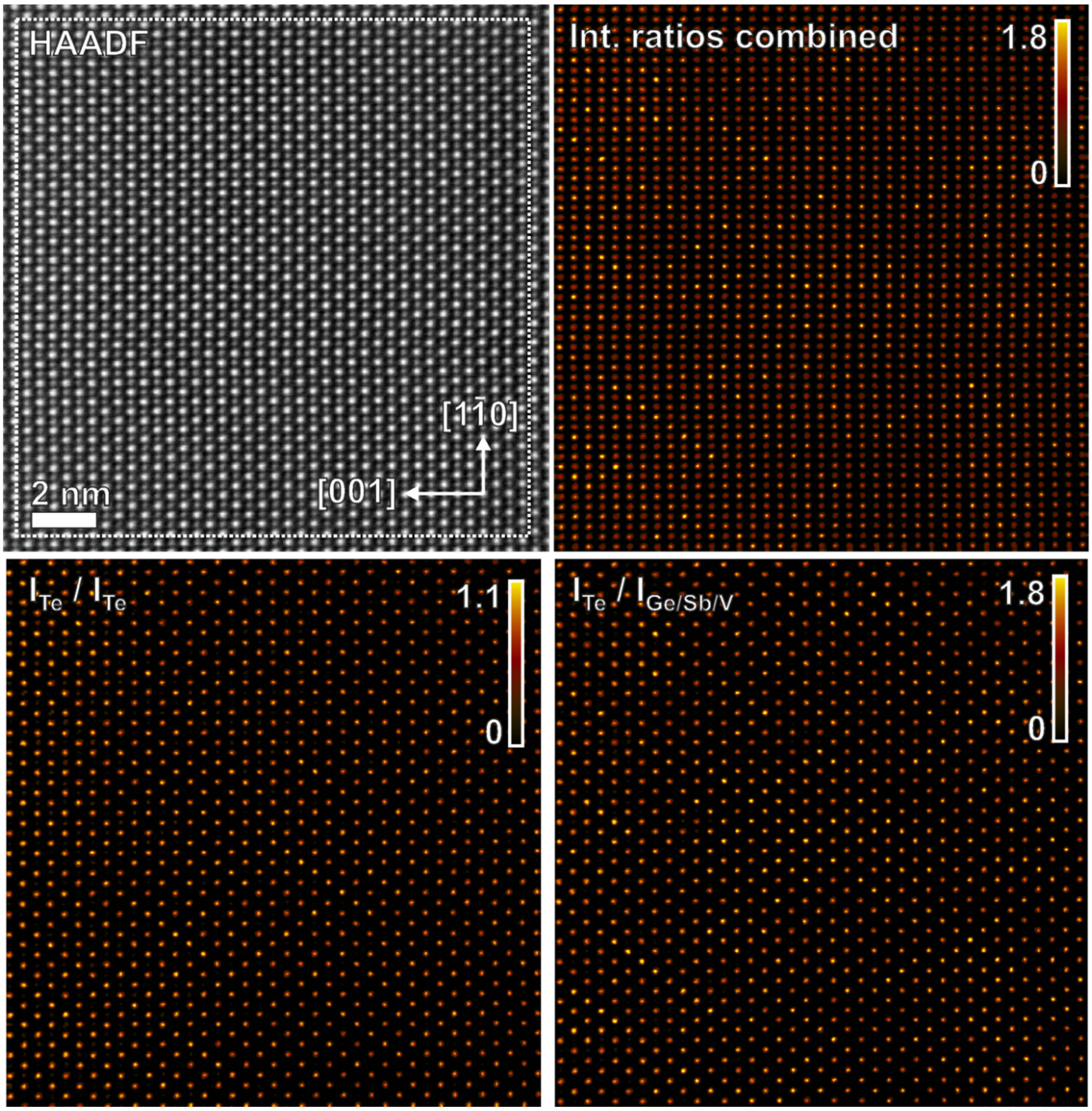

Fig. 3.17: HAADF-STEM (40 - 200 mrad, C2 = 20 mrad) image of GST lattice in [110] zone axis projection (top left), Te:Te intensity ratio map (bottom left) and Te:Ge/Sb/v intensity ratio map (bottom right), calculated by averaging four images which were shifted along [001] and [1$\bar{1}$0] lattice vectors onto the nearest or next-nearest column position, respectively, and overlapped with the original. Due to edge effects, calculated image sizes are cropped to the area indicated by the dashed white line. Sum of both partial lattice intensity ratio images (top right), showing some indication of preferential ordering of either light elements (Ge) or intrinsic vacancies on neighbouring columns in {111} planes, while the Te sublattice is largely uniform.

By defining two non-parallel offset vectors of the ideal lattice along mixed planes, a shifted mask of the original image can be created when selecting only intensity levels above the weak sublattice. The background level is subtracted either by measuring the global minimum or by specifying a user-defined background level (more complex background models are required in the future for images without clearly defined background or with intensity gradients due to thickness/material changes). Subsequently dividing the original image with each mask and averaging the results creates an image of the intensity ratios between Te peaks and neighbouring mixed columns or nearest Te columns depending on the chosen offset vectors. These images can then be combined to create a map of the intensity ratios. The resulting semi-quantitative intensity ratio maps for a [110] zone axis projection image of the metastable GST phase are shown in Figure 3.17.

At an instrument magnification of 7 Mx (1:7 million), where individual atomic columns are visible yet do not occupy more than about 12 -15 pixel width in the image, the intensity ratio map of Te:Te is largely uniform close to 1, as is to be expected from a fully occupied sublattice. In contrast, the intensity ratio map of Te:Ge/Sb/v can vary between 1.4 (very few vacancies, possibly more Sb than Ge) and 2.2 (sometimes even spiking as high as 2.6) indicating local accumulation of vacancies or Ge on the mixed sublattice. Combining the two maps shows that mixed positions with high vacancy concentration can sometimes be organized in {111} type layers over 4-8 neighbouring columns, occasionally even exhibiting systematic ordering towards each other (e.g. the 4-Te layer spacing in the bottom left of the image or the 2-Te layer spacing in the top left) which can be seen as precursors to the 4-Te stacking of $Ge_1Sb_2Te_4$.

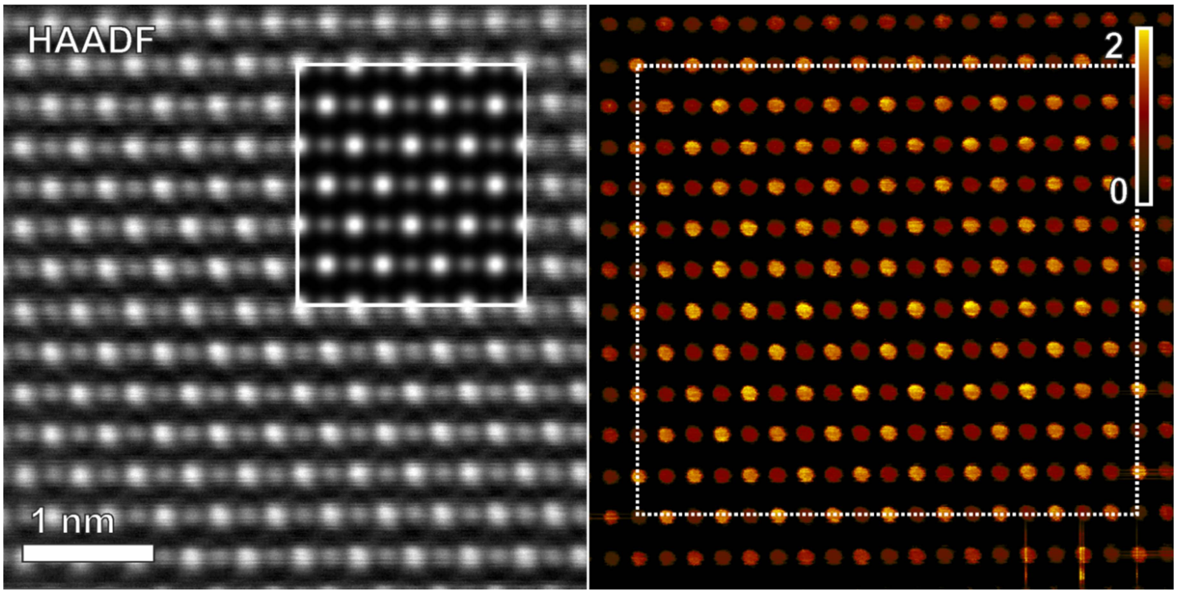

Fig. 3.18: HAADF-STEM (40 - 200 mrad, C2 = 20 mrad) image of GST lattice in [110] zone axis (left) and quantitative image simulation from cubic GST225 model with 20% intrinsic vacancies at 2 nm defocus (inset). While the magnification at 20.5 Mx is very high, pixel resolution was kept at 1024x1024 and dwell time relatively short (6 µs) in order to minimize drift and beam damage, which in turn resulted in slightly reduced signal/noise. Image as shown has been FT-filtered and drift-corrected. Resulting intensity ratio map calculated from raw data (right), dashed line indicates the area free of edge artefacts. The uneven brightness within some Ge/Sb/v column positions indicates local displacements of the atomic columns from the expected centres between neighbouring Te columns. In this particular image, no systematic preferred arrangement of vacancies is immediately evident.

These partial ordering effects are still buried in a mixed sublattice that overall appears fully occupied in the HAADF view, and the systematic arrangement can occur in either of the two {111}-type planes visible in the image. Furthermore, comparing the local intensity ratios given above with simulated images[197] (e.g. the expected intensity ratio for 20% vacancies and equal distribution of Ge and Sb would be close to 1.8, while the expected intensity ratio for 40% vacancies would be 2.2), it becomes apparent that the local vacancy concentration may vary between 10% or less and 40% or more. Since an increase in vacancy concentration and an increase in Ge concentration cannot be distinguished, the concentrations cannot be strictly mapped from the HAADF signal alone, yet the here presented results are a strong indication that vacancies can be partially ordered in the metastable phase. An argument can be made that in order to obtain an equal deviation of the intensity ratio purely by varying the Ge content, the sublattice position would have to be almost exclusively occupied by Ge, in which case an equally higher concentration of Sb elsewhere would be expected. While the difference in atomic number Z between Sb and Te is small, the difference in Debye-Waller factors can be pronounced, and lowest-intensity ratio sites may thus present such Sb-rich positions. Unfortunately, attempts at performing an atomic-resolution EDX mapping for comparison were unsuccessful due to the rapidly accumulating beam damage and sample drift. Similarly, it needs to be kept in mind that the electron beam may have an influence on the observed vacancy ordering especially at very high magnifications[198], although the results shown here were only exposed to a comparatively small electron dose. More likely is that the long annealing time had an influence on the lattice disorder, since the grain morphology is more homogeneous after ultra-fast crystallization[186].

Performing a similar evaluation of intensities at very high magnifications (20 Mx or more) reveals an uneven distribution of intensity ratios within individual mixed columns, while the Te sublattice remains largely uniform (see also Figure 3.18). When measuring atomic column distances, the effect of drift distortion needs to be taken into account. The intercolumn distances measured from the [100] projection in Figure 3.17 are tabulated in Table IV. The results clearly show the biaxial image distortion, as well as the subsequent improvement through drift correction and faster acquisition. However, while the average of two perpendicular lattice vectors matches the nominal structure closely (lattice constant 0.60293 nm), some small difference in individual perpendicular directions always remains. A point of reference for the degree of rhombohedral distortion would be the R3mR phase of pure GeTe, with comparable column distances in R3mR $[11\bar{1}]$ projection of 0.2863/0.3126 nm and 0.4174/0.4281 nm (ICSD#159907). Such a strong rhombohedral distortion results in XRD peak splitting, at $2\theta = 42.2°$ and 43.3°, as well as at 25.17° and 26.039°. Given that the above described potentially observed distortion is significantly smaller than the rhombohedral distortion in GeTe, it is likely that any such additional peaks could be lost in the widths of the diffraction peaks. Similarly, differences in the electron diffraction data between undistorted lattice and observed distortion would be in the range of the pixel resolution even at very large camera lengths.

Tab. IV: Column distances in [100] projection in [nm], as indicated by coloured arrows in Figure 3.16. Values were obtained from multiple profiles over at least 10 columns and subsequent peak fitting.

	Filtered image	Drift corrected	Short acquisition	Average	Nominal
d[200]	0.2954(6)	0.298(0)	0.3010(3)	0.3019(6)	0.3015
d[020]	0.3082(7)	0.3058(8)	0.3034(2)		
d[110]	0.4208(1)	0.4244(2)	0.4204(2)	0.4269(5)	0.4264
d[-110]	0.4331(1)	0.4282(7)	0.4348(7)		

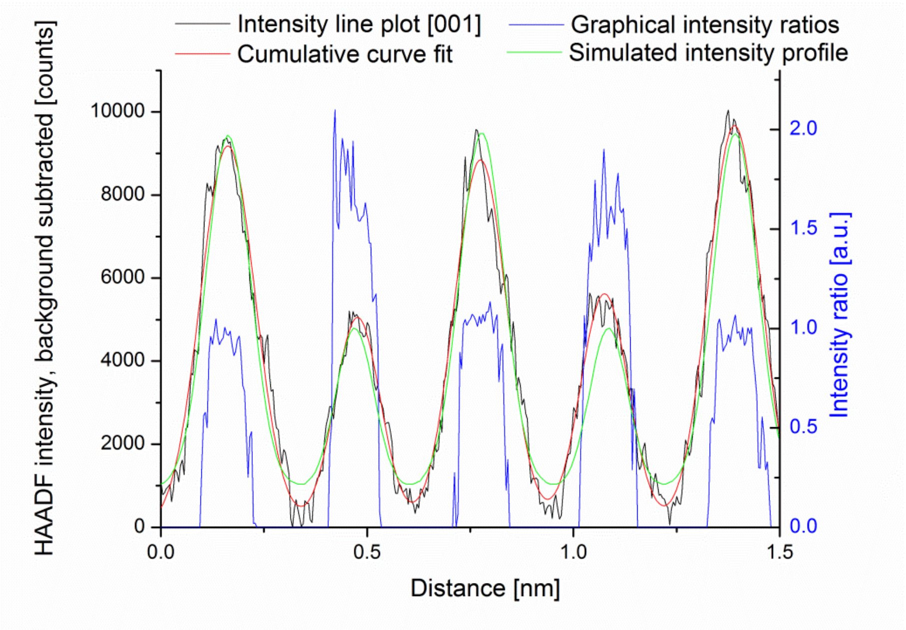

Fig. 3.19: Example comparison between measured HAADF single pixel width intensity line profile along [001] direction within one $[1\bar{1}0]$ projected plane (black), curve fitting routine for identification of individual column positions and intensities (red), quantitative image simulation normalized to the highest Te peak (green) and graphical evaluation of intensity ratios between neighbouring columns (Te:Ge/Sb/v and Te:Te, blue). All data was extracted from Figure 3.18. While overall trends (Te sublattice distances, relative intensities of Te and Ge/Sb/v columns and variation) coincide well, it can also be seen that Ge/Sb/v columns can be distorted by several pm. This results in gradients within individual spots of the intensity ratio maps, while the average intensity ratio of one spot fits well to expected values when a variance in local vacancy concentrations of 5 – 15 % is allowed.

A comparison between intensity line profiles and graphical intensity ratio evaluation from the [110] projection is shown in Figure 3.19. Each individual peak from the intensity distribution in one column is fitted by a Gaussian, with the base level locked to the global minimum background. The deviation between cumulative curve of all Gaussians and experimental data is then minimized via the χ^2 fit. As can be seen, this procedure generally results in a good agreement between curve fit and experimental data, however sharp local spikes (such as in the central Te peak in the profile shown) can result in visible differences between fitted and measured peak intensity. Confidence in intensity ratios can thus be limited to within ±0.15 in the worst case, while a larger integration width of the profiles results in a better peak fitting but reduces the measured maximum peak height due to the averaging effect. Furthermore, the comparison between ideal Ge/Sb/v column positions, fitted positions and graphical intensity ratios underlines that mixed columns can be locally displaced from the centre between neighbouring Te columns, thus as stated above resulting in uneven graphical intensity ratios. By performing such profile measurements and peak fitting evaluations along [001] and $[1\bar{1}0]$ directions in the [110] zone axis projection, the local displacement can be quantified as shown in Table V. As can be seen, for the [001] direction there exists a systematic offset of the mean positions of around 13 - 16 pm, barely above the standard deviation of multiple measurements (N=30). While it is possible to speculate that a minute offset can also be seen in the short $[1\bar{1}0]$ direction, this is still within the scattering width of the data.

Tab. V: Column distances in [nm] from profile evaluation extracted from Figure 3.18. Two values for one direction correspond to left- and right side Ge-Te distance ([001]) or up and down ($[1\bar{1}0]$) in the image.

	Column distances	Standard deviation (1σ)
d[11-1] Te-Te	0.366(4)	0.0086
d[11-1] Ge-Ge	0.365(6)	0.0075
d[1-10] Ge-Te (up)	0.216(7)	0.0109
d[1-10] Ge-Te (down)	0.213(4)	0.0091
d[001] Ge-Te (left)	0.303(3)	0.0072
d[001] Ge-Te (right)	0.290(6)	0.0132

Since the above described displacement of mixed columns is too small to match interstitial sites (tetrahedral sites would occupy column distances of 0.1507 / 0.4252 nm), and no additional columns at those interstitial distances appear even though they should be resolved at 80 pm point resolution provided they are significantly occupied, it is possible to speculate that these displacements are rooted in systematic Peierls-like distortions of the Ge-Te chains. Remarkably, although either direction of the distortion along the [001] axis should be equal, they are predominantly aligned in one direction across the entire evaluated area, and rather than incorporating random structural disorder the unit cell is thus no longer invariant when mirrored at the (001) plane. Whether these distortions thus play a role in the reversible multi-level threshold switching is yet to be fully explored, among other reasons due to the difficulty in identifying them with non-destructive methods. A logical future step would be to compare ab-initio DFT calculations of band structure properties from the symmetric, distorted and vacancy layered arrangement and compare these with experimental property measurements. The individual local displacement measured from profiles in Figure 3.17 is plotted against the local intensity ratio in Figure 3.20. It is unclear whether a correlation can be made between higher intensity ratio and larger displacement, in part since the magnitude of the displacements is at the precision limit of the method.

In summary, after slow annealing of a capped GST thin film at 160 °C, the resulting structure is randomly oriented crystalline with a very small Ge-rich amorphous component at the interfaces. While preliminary XRD indicated a close to ideal cubic structure with a slightly smaller than expected lattice constant, the HR-STEM investigation reveals pm-scale distortions of both the Te framework and the mixed sublattice. Close inspection of the local HAADF intensities and comparison with quantitative image simulations indicates partial ordering of the mixed sublattice within {111} planes. While the idealized model of the symmetric NaCl-type lattice need not be discarded, since it is likely that the ultra-fast crystallization results in increased sublattice disorder, the here observed lattice structure presents a first intermediate step in the phase transformation towards the layered trigonal lattice. The combination of image processing and evaluation tools applied here is thus a promising approach to characterizing with similar precision the various annealed and crystalline-deposited thin films in the following subchapters.

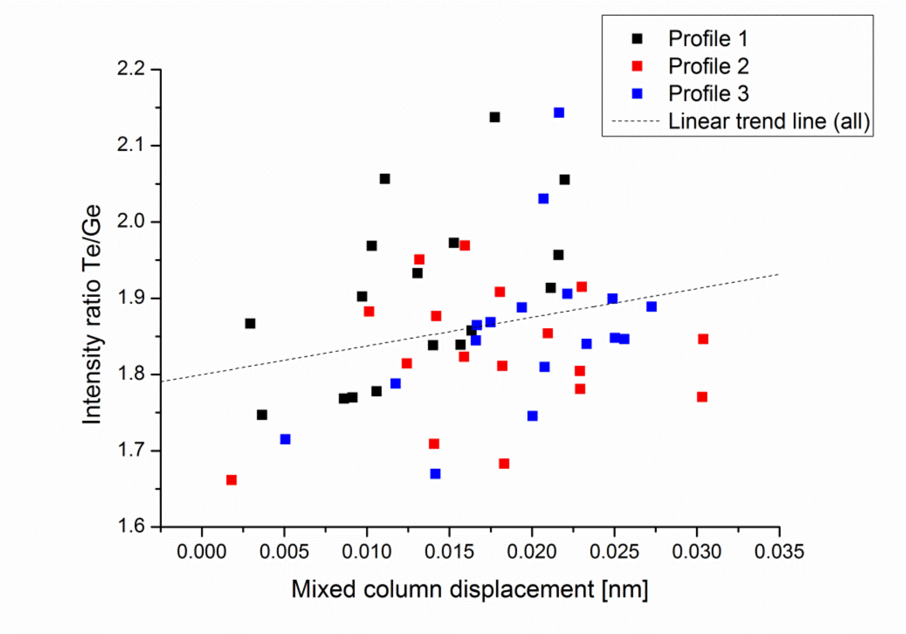

Fig. 3.20: Plot of local intensity ratio Te:Ge/Sb/v vs. column displacement in [001] direction, from three line profile fittings measured in Figure 3.17. While the data points appear randomly distributed around the mean (16 pm displacement and 1.86 intensity ratio), it may be possible to interpret a linear correlation trend between intensity ratio (i.e. vacancy concentration or average atomic number) and local displacement. Average long and short distances are 0.3071 ± 0.0027 nm and 0.2879 ± 0.0037 nm, respectively. Standard deviation of distances is lower than in Table V since the image evaluation at lower magnification is less impacted by noise, however a single peak only occupies on average 13 pixel within its FWHM, and the pixel resolution in combination with residual noise may thus impact the precision.

3.2.2 Vacancy layer ordering in the intermediate cubic lattice

The phase transformation temperature for the metastable cubic to trigonal layered phase transition is typically given as a range e.g. between 230 and 260 °C, however various reported figures can vary even further. The reason for this is clear: While the amorphous – metastable transition occurs very quickly, which makes it technically interesting for fast switching concepts, the metastable – stable transition is kinetically constrained, thus yielding the large range of metastability that is critical for the reliability of PCM cells. However it has become clear that regarding the metastable phase as one monolithic entity is too simplistic, and additional structural changes should be observable to explain multi-level switching behaviour. In addition, the stable layered phase itself has also come under scrutiny for interfacial switching concepts, and the detailed characterization of the stable arrangement as well as possible defect structures has thus gained increased importance.

The main differences between the two crystalline phases are the arrangement of the intrinsic vacancies, the partial chemical ordering, and the structural relaxation resulting in {111} in-plane shifts as well as lattice distortion (all of which are further elaborated on in the following subchapters). As was shown in the previous section, the beginning of the vacancy ordering can already be observed in the metastable phase by careful evaluation of HAADF-STEM intensities. While in the cubic framework the mixed Ge/Sb/v {111} layers are ideally invariant, considering the trigonal lattice in terms of cubic coordinates shows that only one {111} layer orientation can persist between metastable and stable configuration. The phase transformation temperature is heavily reliant on the time profile of the heating process, which is further complicated by the stoichiometric effects. Typically, a preferred stoichiometry of the trigonal phase such as $Ge_1Sb_2Te_4$, $Ge_2Sb_2Te_5$ or $Ge_3Sb_2Te_6$ is meant to be investigated, each yielding different transformation temperatures, while in practice the cubic phases of these compounds do not radically differ and small off-stoichiometric compositions can thus be readily accommodated.

Choosing a temperature profile to investigate for annealing experiments can thus prove challenging. Differential scanning calorimetry (DSC) experiments are typically carried out at constant heating rates. Some examples include [199] who reported fcc ➔ hexagonal transition temperatures between 205 and 230 °C at heating rates from 5 to 70 °C/min. However, they also claimed to have observed an additional endothermic peak relating to a structural transformation between 250 and 330 °C. Meanwhile, [200] reported a phase transformation temperature of 250 – 260 °C for DSC heating rates between 10 and 30 °C/min, while Ref. [5] originally reported a temperature as low as 200 °C at a DSC heating rate of 10°C/min. Even extreme outliers are possible when other methods of characterization are considered, e.g. from electrical resistance measurements[201] a transformation temperature of 310 °C at a slow heating rate of 0.52 °C/min was concluded.
Since the here performed annealing experiments were carried out with a fixed ramp time (10 min) and a plateau between 10 and 30 minutes, it is to be expected that the phase transformation occurs at the lower end of the reported range of transformation

temperatures. In [202] a phase transformation temperature of 230 °C for an annealing experiment of $Ge_2Sb_2Te_5$ with a similar ramp and plateau was reported, yet from XRD information they concluded a large change in composition towards $Ge_1Sb_2Te_4$. In order to investigate the transition state between metastable and stable configuration, the here presented GST thin film on Si(001) substrate with native SiO_x interface layer was annealed at 200 °C (18 °C/min ramp) with a relatively short 10 min plateau. XRD results (Figure 3.21) indicated that the film was still present in the metastable phase with a = 0.5997 nm, while glancing incidence measurements indicated the presence of preferred orientation texturing due to alignment of GST {111} planes with the interface orientation. S/TEM-EDX measurements confirm that the original as-deposited composition was roughly retained, with relative concentrations of $Ge_{21.15}$, $Sb_{22.74}$ and $Te_{56.09}$ at. %. The TEM overview image shows that grains may extend over the entire layer thickness (Figure 3.22), while NBD patterns exhibit pronounced superstructure reflections along the {111} axis.

The BF-TEM view and diffraction information already indicate that some defect structure ordering takes place within the sample, with a preferred orientation in the top 40 nm of the layer. This however is somewhat contradictory to the XRD results, which indicated a cubic symmetry since, as already introduced in the previous chapter, additional diffraction peaks from the trigonal stacking are not present.

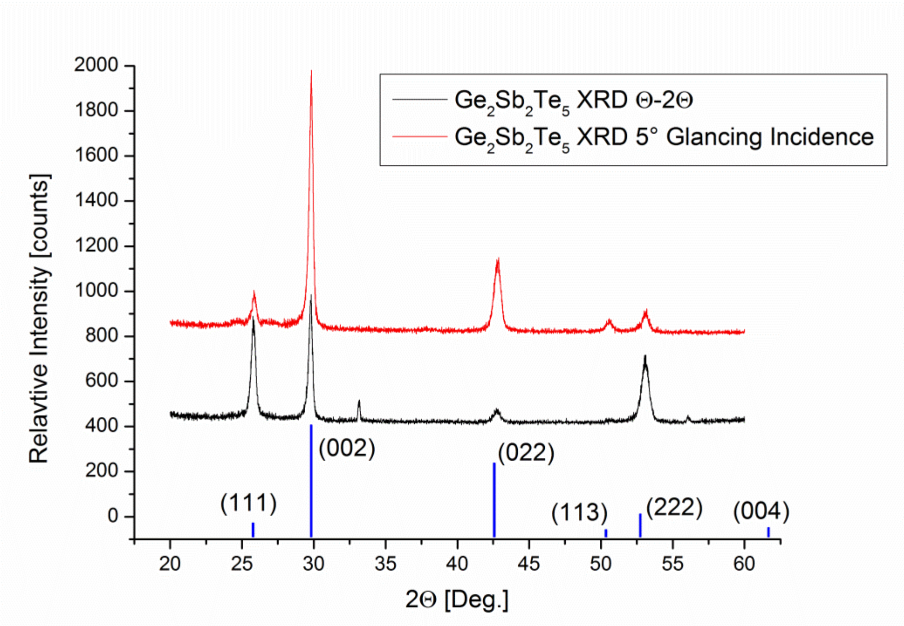

Fig. 3.21: θ-2θ and glancing incidence XRD measurements of GST thin film annealed at 200 °C, as well as calculated relative peak heights from a randomly oriented polycrystalline morphology of cubic GST225 (blue bars). Since in glancing incidence geometry the (111) type diffraction peak is significantly more prominent than the (011) peak, it can be concluded that the thin film possesses a (111)|[001] preferred orientation component.

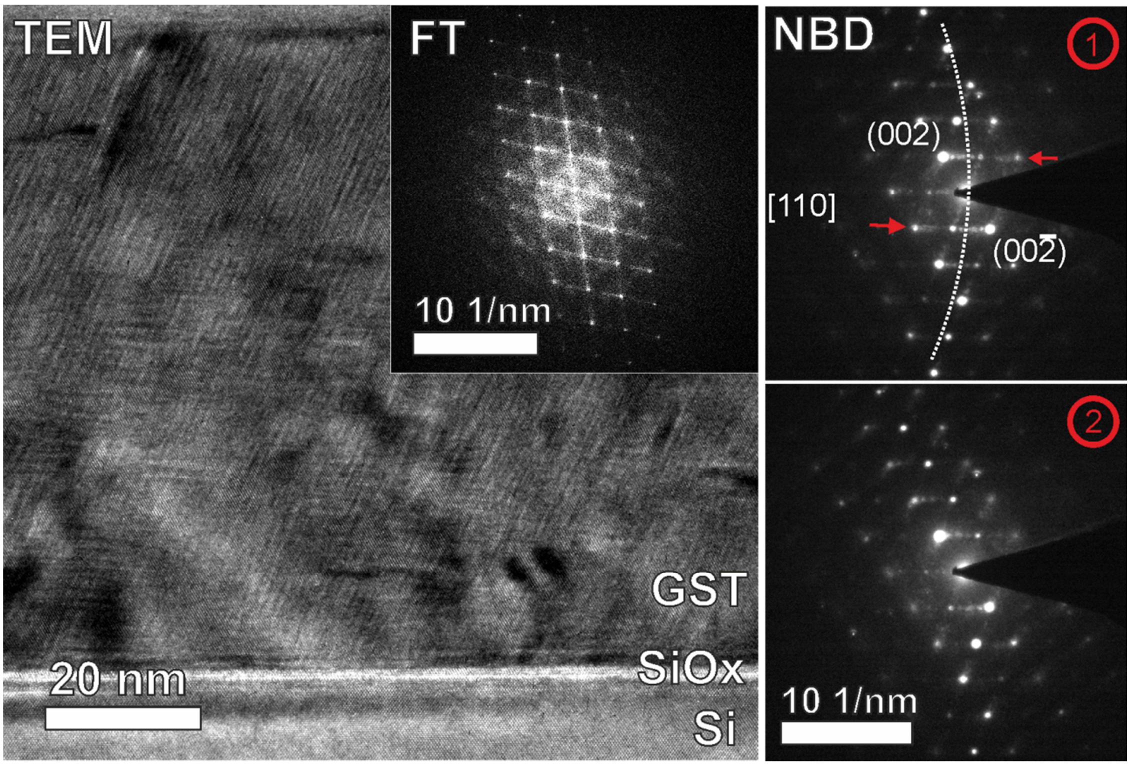

Fig. 3.22: TEM overview image (BF contrast) of GST225 thin film annealed at 200 °C (left) and corresponding FT (inset) exhibiting one crystallite orientation over the entire film thickness. Representative NBD patterns from a larger series, acquired closer to the top (1) and bottom (2) of the thin film. While both patterns exhibit a similar zone axis [110] orientation with a small off-tilt reorientation (the sample was oriented in the Si[011] substrate zone axis), superstructure reflections (marked by red arrows) are slightly more prominent along one {111} variant in pattern (1), while they are weaker in pattern (2) and appear in either of the {111} variants.

This becomes better visible in the HAADF-STEM overview images (Figure 3.23). Vacancy ordering into {111} planes gradually changes from random arrangement in the lower part of the layer towards alignment of vacancy layers with regular spacing of 4, 5 or 6 Te planes. While the transition overall appears continuous, there is some indication that defects may occasionally play a role in separating the two lattice regions (particularly in the central part of Figure 3.24). Visible defects can be categorized largely into three types that were introduced in chapter 1.4.2.

Antisite defects (see Figure 3.24 (c)) are sometimes found when two adjacent regions of the cubic lattice separated by a vacancy layer are shifted against each other by $\frac{a\sqrt{3}}{2}$ within the (111) plane of the vacancy layer[203], thus creating an antiphase boundary. The vacancy gap between {111} Te layers is narrower (0.406 nm) than the simple removal of a mixed sublattice layer would suggest (0.738 nm), yet larger than the average {111} plane spacing in the bulk lattice (0.348 nm). They are thus resulting in a local lattice distortion that can be mapped by the GPA (Figure 3.24 (e)). These planar defects are terminated either at volume defects or by partial edge dislocations.

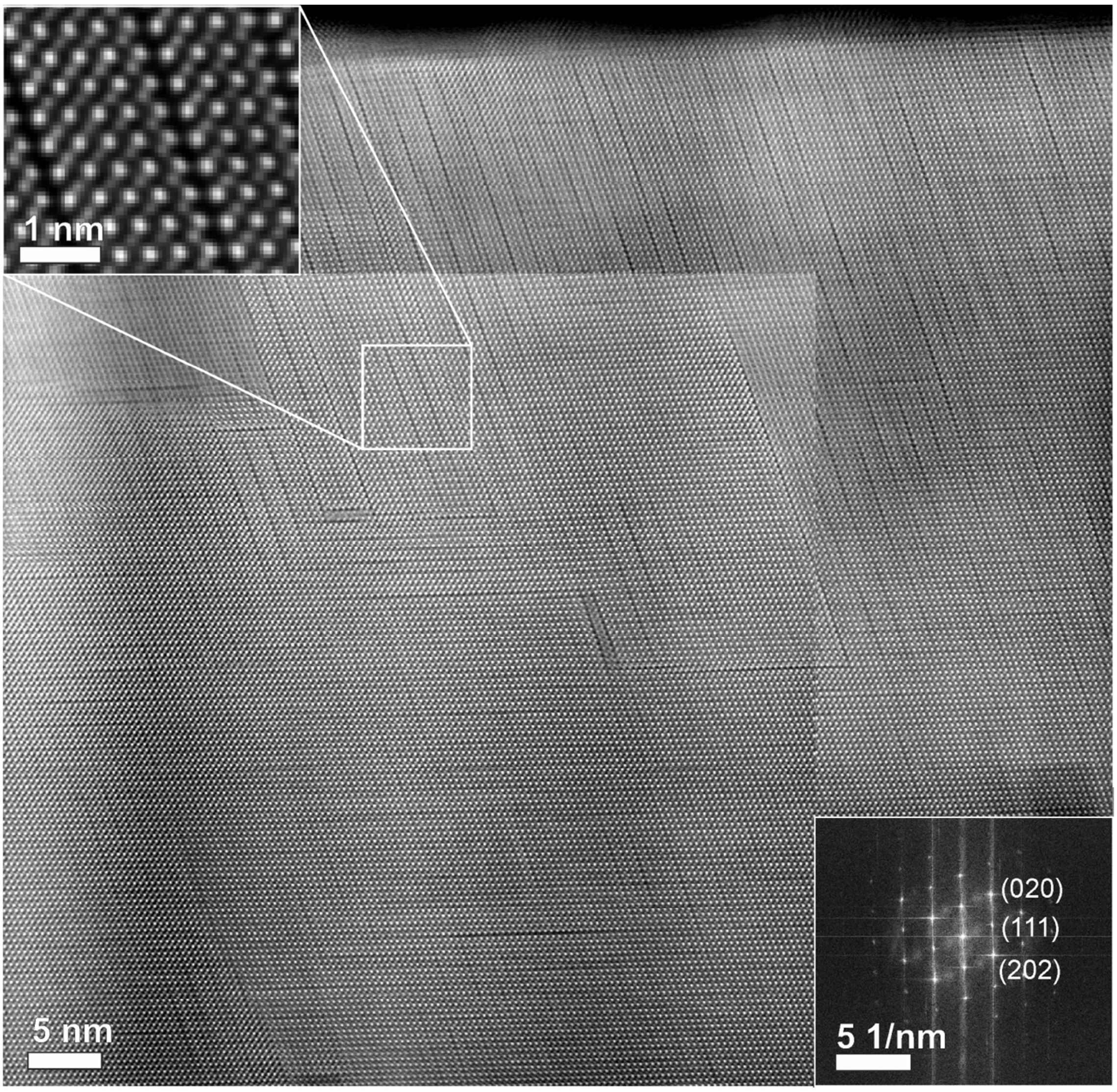

Fig. 3.23: HAADF-STEM composite image of GST lattice in [110] projection. Insets show {111} vacancy layer arrangement in the upper part of the thin film (top left) and Fourier transformed of the image (bottom right) representing the distribution of spatial frequencies comparable to the diffraction information. The systematic arrangement of dark lines (vacancy layers and planar defects) gradually increases towards the surface of the thin film, while the region close to the substrate is disordered with occasional vacancy layers in either of the visible {111} planes.

Volume defects are seen in the form of trapezoidal inclusions, possibly with a different orientation than the surrounding lattice. All observed volume defects consist of three strongly distorted {111} layers bordered by vacancy gaps and planar defects. The HAADF contrast within these volume defects is too diffuse to reveal the exact nature of their orientation, and STEM-EDX measurements did not reveal a marked change in composition. It is thus likely that they consist of distorted intrinsic Te-Ge/Sb/v-Te blocks. Closer inspection of the mixed layers marked by green arrows in Figure 3.25 (a) suggests that the lattice transitions from Ge/Sb/v-Te-VL(antiphase boundary)-Te-Ge/Sb/v stacking towards VL-distorted Te-distorted Ge/Sb/v-distorted Te-VL within the defect, indicating that the structure seen in the volume defect may be the side-view of a screw dislocation with a Burgers vector of $\frac{a}{2} < 111 >$, sandwiched between the VLs.

Classical edge type dislocations may also be present, however due to the diatomic base of the lattice they are associated with very large lattice strain. Only one clear example of such an edge type dislocation involving the removal of a Te-Ge/Sb/v bilayer could be imaged (see Figure 3.25 (b)), and is further associated with a stacking fault and a resulting antiphase boundary. They only play a minor role in the lattice structure overall.

Following from these observations, the defect structures are characterized by the local removal of mixed sublattice {111} planes and distortion of the Te sublattice framework, resulting in partial edge dislocation pairs, stacking faults and antiphase boundaries. Due to the intrinsic tendency towards vacancy layer formation and the lattice strain surrounding defects, the two are closely associated. The information contained in the HAADF intensities can be evaluated as introduced in the previous chapter, by either mapping the Te:Te and Te:Ge/Sb/v intensity ratios or by fitting individual profiles and comparison to expected intensities. In this context it is however important to recall from the theoretical section that in a strained lattice region the thermal displacement parameters and thus the expected incoherent high-angle scattering intensity are not identical to the ideal lattice prediction. Thus, while both vacancy layers and partial vacancy ordering can be mapped well in a larger view of the lattice (see Figure 3.27), the image contrast close to defect sites cannot be directly translated to Ge/v concentration. The most prominent example of this can be seen at the antiphase boundaries (Figure 3.25 (c) and 3.26 (a)). The compressive distortion of the lattice, seen as blue regions in Figure 3.25 (e), results in a HAADF intensity of the first mixed Ge/Sb/v layers around the defect plane that is above what would be expected for an undistorted fully filled Ge/Sb layer without intrinsic vacancies.

When performing profile evaluations of the defect-free lattice similar to chapter 3.2.1 it becomes apparent that Ge/Sb/v-Te distances are similarly distorted as in the previously discussed sample while the Te-Te framework matches the cubic symmetry in the observed projection. In [001] direction Ge/Sb/v-Te distances are split into 0.282/0.319 ±0.010 nm, i.e. an average offset from the NaCl-type lattice position of about 35 pm, while in [1-10] direction the distortion may also be present, measuring 0.197/0.207 ±0.008 nm resulting in an offset of about 10 pm. These values are slightly larger than those in the previously investigated sample, however measuring the offset at different depths inside the GST layer or at different microscope settings can result in values varying by as much as 15 pm (in the [001] direction) due to changing noise levels and sample drift as well as difficulties in the column peak deconvolution at intermediate magnifications.

The evidence is thus not quite conclusive that these displacements in the cubic lattice significantly increase with annealing temperature, as long as the measurement is carried out well removed from defect structures. In contrast, displacements of the mixed columns close to planar defects are more pronounced.

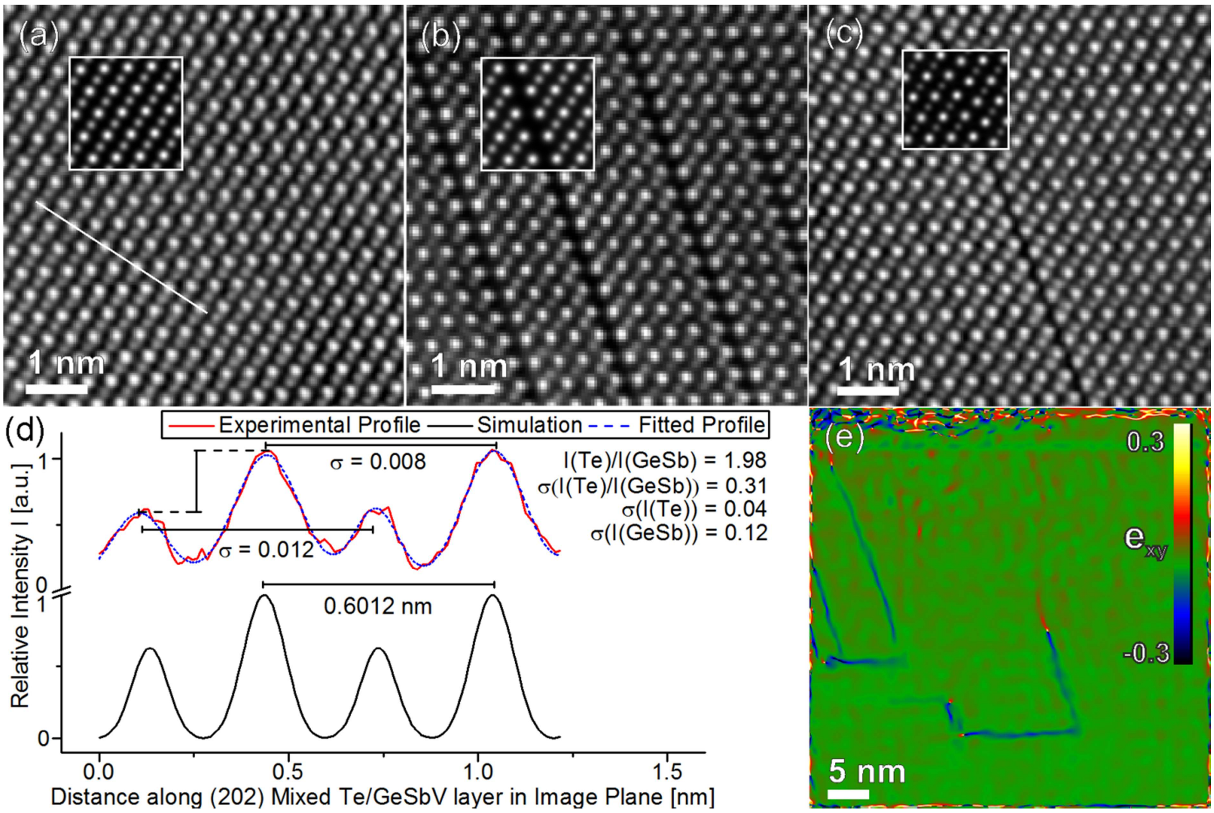

Fig. 3.24: HAADF-STEM lattice images of selected regions of Figure X. (a) Metastable cubic lattice with local distortions as described in the previous chapter, (b) systematic vacancy layer ordering while retaining the cubic symmetry, (c) antiphase boundary defect across as vacancy gap. (d) Intensity line profile measurements along direction indicated by solid white line in (a), and (e) GPA map of local biaxial distortion e_{xy}, calculated from upper image section of Figure 3.23. Strong lattice distortions visible as blue areas in the GPA map are found at the planar defect sites (antiphase boundaries) and small volume defects. Insets in (a)-(c) show simulated images from idealized lattice models of cubic lattice, vacancy layer without lattice relaxation and antiphase boundary.

In particular, mixed {111} layers in the immediate vicinity of an antiphase boundary or vacancy layer are always shifted towards the defect plane. In the presence of an antiphase boundary, the first and second nearest mixed {111} plane are displaced by about 50 pm in the $[1\bar{1}0]$ direction towards the defect plane, while the [001] displacement stays roughly the same. Further away from the strained zone, the lattice again resembles the distorted cubic lattice with a uniform orientation of the mixed column displacement. Similarly, the vacancy layered cubic lattice in the upper part of the GST thin film is characterized by small offsets of the mixed layers in $[1\bar{1}0]$ direction towards the vacancy layer gap (see Figure 3.24 (b)). The expected Te-Te plane distance across a vacancy gap in [110] projection would measure 0.369 nm if the lattice were undistorted based on the cubic model, while measured distances across the vacancy gap are up to 20 pm smaller.

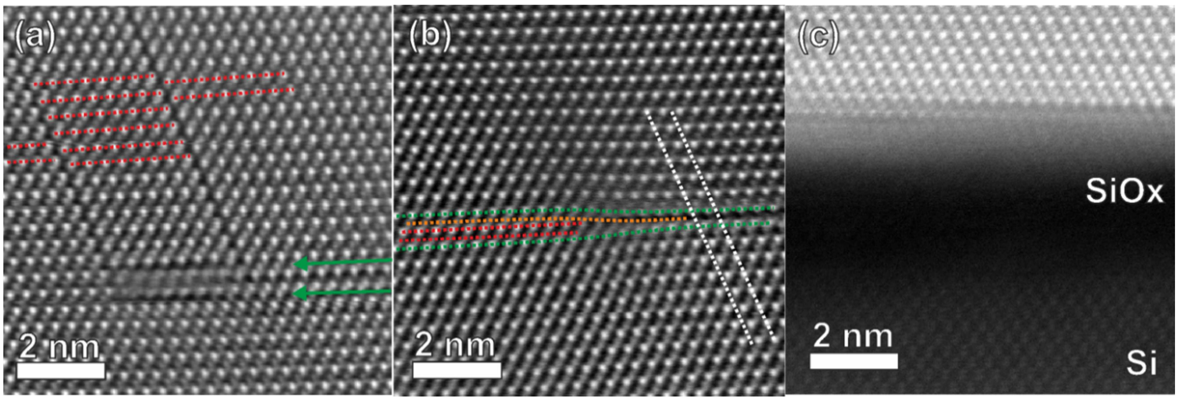

Fig. 3.25: HAADF-STEM image details of defects structures. Volume defect bordered by three antisite defects in a complex arrangement of stacking faults and partial dislocations (a). Edge-type dislocation (b), wherein two lattice half-planes (Te and mixed, marked red) are removed from the lattice, while the mixed plane above (marked orange) at first continues but subsequently is also removed resulting in a antiphase boundary across a vacancy gap (as indicated by white dashed lines). Interface of the GST thin film with the amorphous SiOx substrate surface (c). Despite the limited contrast, there is some indication of vacancy layering close to the interface while the lattice above appears similar to the bulk cubic phase.

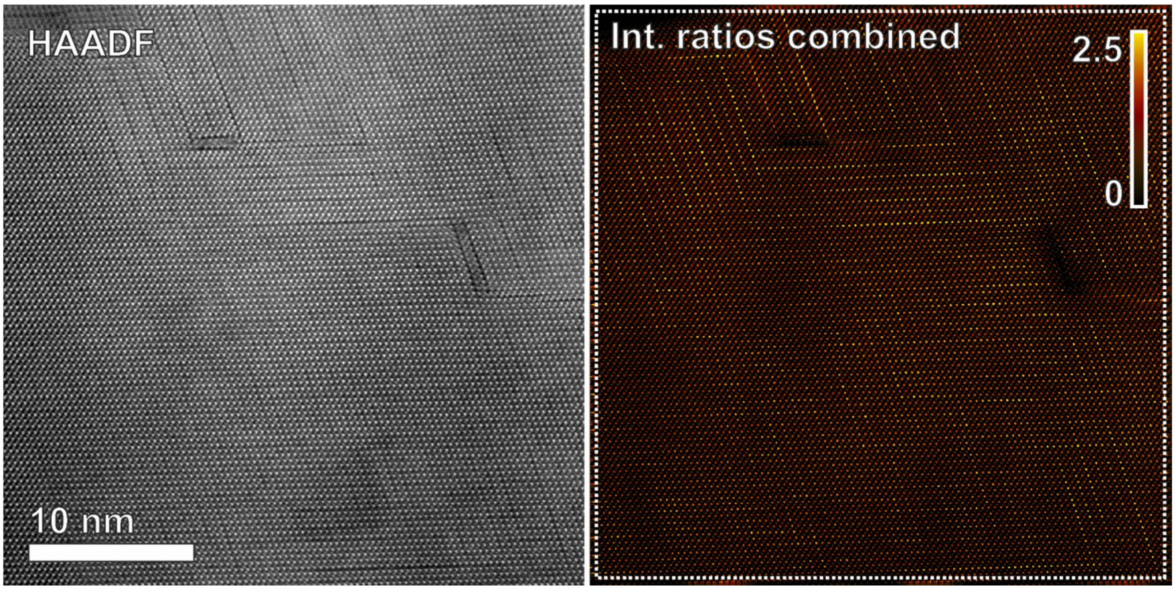

Fig. 3.26: HAADF-STEM lattice image from lower left of Figure 3.23, and corresponding intensity ratio map. The STEM image shows the transition area from disordered cubic lattice to lattice with aligned vacancy layers. The intensity ratio map to the right reveals pre-ordering of vacancies in the disordered phase similar to the previous subchapter, while two volume defects appear dark due to the strong lattice distortion. Diffuse darker areas stem from local changes in the background due to amorphous surface components or contaminants, which are not explicitly adjusted for.

The Te(111) plane spacing within the lattice between VLs is correspondingly slightly larger, thus overall compensating the difference to the ideal plane spacing and, since the lattice in the perpendicular direction in the image projection plane resembles the cubic framework, resulting in a tetragonal distortion of the lattice. It would thus appear that the vacancy layered lattice possesses strong structural similarities to the trigonal stacking of GST225, GST124 or GST326 depending on the VL spacing. However, two major differences are always present:

- The HAADF-scattering intensities do not show a strong chemical reordering into Ge- and Sb-rich layers. Mean intensity ratios Te: Ge/Sb/v are slightly lower (1.4-1.6) due to the depletion of vacancies from the sublattice, yet variation is low and distribution random. A small increase in image intensity in the first-neighbouring {111} mixed layers at the vacancy gap could be equally attributed to the (unknown) change in thermal displacement parameters and STEM beam tail overlap between closely spaced columns, or changes in the 1s channelling conditions due to lattice deformation.
- In the trigonal lattice of stable, vacancy layered GST, the Te(0001) planes (comparable to the Te(111) planes in the cubic lattice) are systematically shifted against each other by $\frac{a\sqrt{3}}{6}$ (in terms of cubic lattice parameter a) across the vacancy gap. In contrast, the here observed structure consistently shows a straight continuation of Te and mixed planes across the vacancy gap.

These two observations lead to the conclusion that the lattice in the upper part of the thin film can be characterized as a vacancy layered cubic disordered structure, and thus presents a second intermediate step towards the complete phase transformation to the stable trigonal structure. Such layered structures of the cubic lattice were previously theoretically predicted[44, 45], albeit without special consideration for Ge/Sb sublattice disorder. In addition, Ref. [204] and more recently [46] have discussed the crucial role of vacancy ordering in the cubic phase for the metal-insulator transition.

Concluding this chapter, the sample annealed at 200 °C exhibits large grains of cubic GST225, with a preferred orientation component (111)|[001] possibly due to vacancy layer formation at the thin film - substrate interface. The lattice structure within grains can be divided into two regions depending on depth inside the film, thus indicating uneven heat distribution during annealing due to the low thermal conductivity of the film, or progressive phase transformation from the surface of the film that was frozen during cooldown. In the lower part of the thin film the lattice is similar to the previously presented sample annealed at 160 °C, possessing small distortions of the mixed sublattice within the cubic Te framework as well as indications of vacancy pre-ordering into mixed {111} planes over multiple atomic columns. The upper part of the thin film exhibits strong systematic vacancy ordering into one preferred {111} plane orientation. Nevertheless, the overall cubic character including the Ge/Sb sublattice disorder is retained in this transitional state. Since the VL spacing in this phase is not strictly fixed, but instead can measure 4, 5 or 6 Te-Te distances, it is likely that this stacking disorder carries over into the resulting trigonal stable structure (as will indeed be shown in the subsequent chapter). Lastly, the central part of the thin film exhibits some prominent defect structures, most importantly the tendency of stacking defects to result in the formation of antiphase boundaries across a narrow {111} vacancy gap.

3.3.3 Trigonal GST lattices after prolonged annealing

The local structure of trigonal GST compounds is of particular interest in two regards. For one, various idealized models of the hexagonal stacking sequence have been previously proposed, as discussed in the introductory section (chapter 1). While the underlying symmetry of rocksalt-type building blocks with alternating cation- and anion layers and intrinsic vacancy gaps is similar across all models, the particular local distortions from octahedral positions as well as the chemical ordering in the mixed cation sublattice vary between models. This is, among other aspects, important for ab-initio studies of the phonon density of states[173] and the electronic band structure[14, 205], which can struggle to incorporate the chemical sublattice disorder. Secondly, the recent prominence of interfacial switching concepts (iPCM)[92, 99, 178, 206] may rely on the exchange of (0001) layers, switching across vacancy gaps or between GeTe and Sb_2Te_3 sub-units. It is likely that such movement of entire lattice planes is facilitated by stacking defects in the lattice, and the closer examination of these in the here presented nominally pure GST lattice as well as in the following section on oriented thin-film growth may facilitate the explanation of the crystalline-crystalline property contrast transition.

In order to investigate the stable trigonal stacking of GST, thin films of as-deposited amorphous GST225 on Si(001) / SiO_x were annealed at 250, 290 and 320 °C. Since the ramp time was kept constant at 10 min, this resulted in a heating rate of 23, 27 and 30 °C/min, respectively. The plateaus of 20 - 30 min facilitated the complete phase transformation. All thin films were covered by an at least 5 nm thick amorphous $LaAlO_x$ layer in order to prevent evaporation during annealing. The sample annealed at 250 °C was deposited to a film thickness of 40 nm, while the samples deposited at 290 and 320 °C were deposited to a film thickness of 120 nm and 160 nm, respectively, in order to obtain large uniform grains for the investigation of the highly ordered phase. The growth rate from PLD parameters (0.5 J/cm^2 at 10 Hz) was thus determined to lie around 5 nm/s, although a certain variance between experiments was observed that could be traced to somewhat imprecise control of the laser fluence through the laser defocus and contamination of the laser entry window to the PLD chamber.

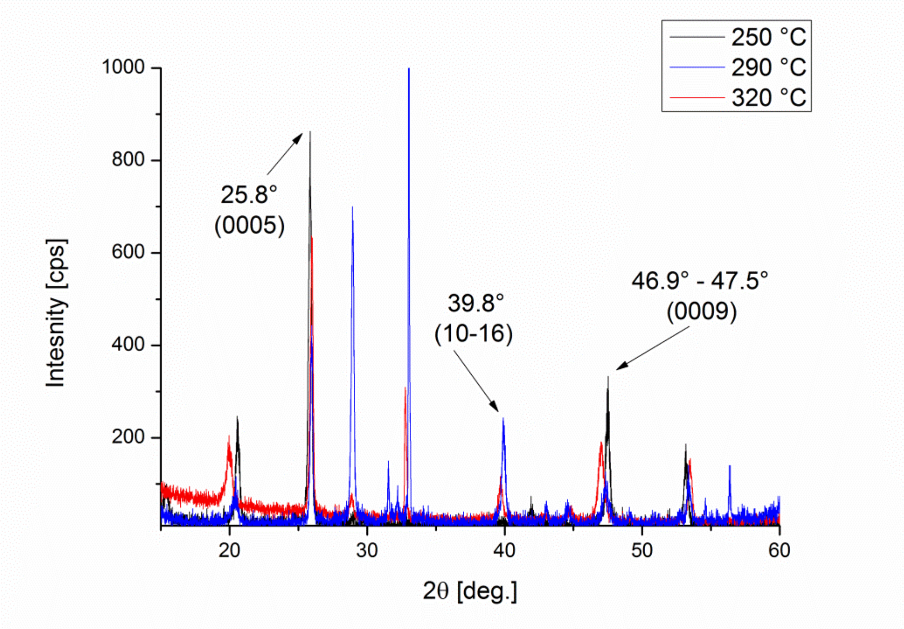

Fig. 3.27: XRD spectra comparison of trigonal thin-film samples. While all samples exhibit strong diffraction maxima relating to the trigonal lattice planes, common peak positions e.g. (0009) can vary by as much as 0.5°. Peak indices are assigned assuming the trigonal GST225 lattice, but the variance in peak positions underscores the need for a locally resolved structure investigation. The prominence of the (0005) peak in particular indicates a [0001] fibre texture in the thin film.

XRD measurements (see Figure 3.27) revealed additional diffraction intensities compared to the previously presented cubic phase, thus indicating a phase transformation to some form of trigonal stacking in all three samples. However, small shifts in peak positions and intensities were observed, revealing that further structural changes may occur in the investigated temperature range.

When matching XRD peaks to the common GST225 stacking symmetry[49, 52, 66], the most pronounced shifts in the (0009) peaks result in a plane spacing of 0.1912 – 0.1931 nm, corresponding to a c-axis lattice constant of 1.7209 – 1.7382 nm. The nominal (0009) spacing and corresponding c-axis lattice constant of 0.19201 nm and 1.72809 nm, respectively, thus lie well within the range of the experimental measurement. Meanwhile the (000 21) plane spacing of GST124 is predicted to measure 0.193 nm and thus would match the largest experimentally determined c-spacing, and the distinction between pure GST124, GST225 or GST326 phases from the c-axis parameter alone is thus difficult. In principle, differences between other peaks particularly in the range of 32 - 33° should be more pronounced, but they possess inherently low signal intensity and the texture component enhances (000*l*)-type peaks in the θ-2θ geometry. The preliminary conclusion was thus that either a phase mixture was observed, or that the GST225 trigonal phase undergoes a further lattice distortion upon annealing.

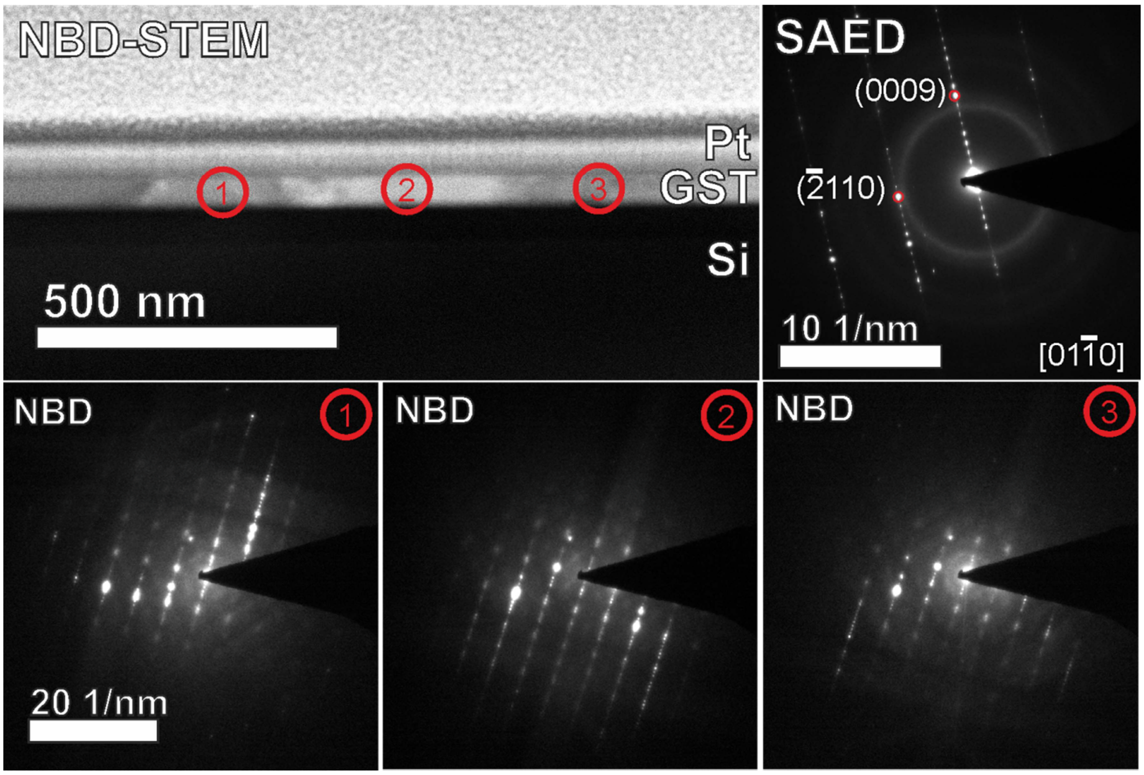

Fig. 3.28: TEM diffraction results from sample annealed at 250 °C. HAADF-STEM image acquired under NBD beam conditions (top left), SAED pattern of GST thin film position close to (2) (top right). The particular grain orientation was determined to lie close to the [01$\bar{1}$0] zone axis, with diffraction indices from the trigonal GST225 phase as indicated. Diffuse rings and some weak spurious reflections in the diffraction pattern originate from the amorphous $LaAlO_x$ and nanocrystalline Pt surface layers. Selected NBD patterns from indicated positions within the GST layer are shown in the bottom row.

Selected results from the electron diffraction experiments on the sample annealed at 250 °C are presented in Figure 3.28. Since the smallest SAED aperture cannot cover the GST thin film exclusively (actual film thickness was measured as 42 ± 1 nm with minimal surface roughness while the demagnified SAED aperture covers a diameter of approximately 100 nm), diffraction contributions from amorphous interface and surface layers are also visible. Nevertheless, very strong superstructure diffraction features are seen in the SAED pattern, thus confirming the highly ordered nature of the grain extending over the entire film thickness. The NBD series, as well as the parallel ADF acquisition, indicate an average lateral grain size of about 200 nm, with some individual grains extending over as much as 400 nm. The thin film is closed, and the rms roughness at the interface of GST and $LaAlO_x$ measures no more than 1 nm.

All NBD patterns exhibit superstructure reflections from the trigonal stacking similar to those observed in the SAED pattern. In fact, the orientation of the superstructure reflection axis largely persists between NBD patterns from different grains. As the direction of the incident electron beam is identical to the viewing direction, the reciprocal lattice is rotated around the surface normal or tilted within the plane spanned by the surface normal and the incident beam direction. However, rotations of grains within the projection plane are small, which as already indicated by the XRD relative peak maxima is the result of a preferred c-axis texturing despite the amorphous nature of the substrate surface. In principle, rotations within the projection plane and tilts within the surface normal – beam direction plane should be equivalent, and the larger effect of rotations observed here may on the one hand be coincidental to the sample position the FIB lamella was prepared from. On the other hand, geometrical considerations of the Ewald sphere construction dictate that, since the radius of the Ewald sphere due to the length of the incident wave vector (wave number from the De-Broglie wavelength of the high-energy electron) is large compared to the reciprocal lattice base vectors, small reorientations of the reciprocal lattice out of the projection plane result in larger changes of diffraction intensity than similar reorientations (rotations) within the projection plane[207], in particular since the most prominent superstructure diffraction features lie close to the transmitted beam due to the large spacing of vacancy layers from which they originate. Nevertheless, the possibility should not be discarded that the texture component within the 2D plane of the sample surface is locally more pronounced in one direction due to a preferential small—angle grain boundary arrangement originating in the initially crystalline cubic phase.

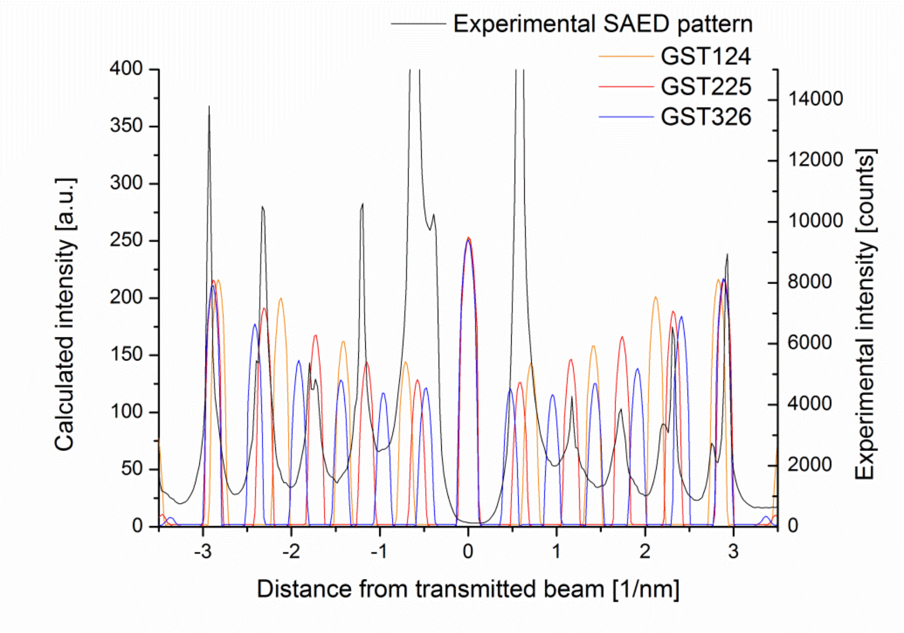

Fig. 3.29: Comparison between experimental SAED diffraction intensity profile along superstructure reflection axis {0001} in [01$\bar{1}$0] zone axis (from SAED pattern in Figure 3.28) and simulated corresponding diffraction features from ideal GST124[208], GST225[52] and GST326[54] structures (coloured lines, 35nm crystal thickness and 0.2 mrad beam half-convergence semiangle, two-beam calculation). While particular diffraction maxima match the GST225 lattice within a small offset, e.g. the second and third peaks relating to (0002) and (0003) planes, unexpected intensities at 2.19 and 2.75 1/nm, next to the (0004) and (0005) maxima, respectively, are also observed.

A comparison of the experimental SAED pattern and theoretical electron diffraction maxima along the (000*l*) axis of the superstructure reflections is shown in Figure 3.29. Major diffraction maxima in the experimental pattern coincide reasonably well with the GST225 phase, thus indicating the preferred 9R stacking. Small offsets remain, and some additional peak intensities cannot be directly traced back to one specific defect structure or additional phase component.

The HAADF-STEM investigation (Figures 3.30 and 3.31) reveals that the lattice is not uniform according to one specific trigonal lattice model. Rather, the spacing of intrinsic vacancy layers can measure 4, 5 or 6 Te-Te distances, as was already observed in the vacancy layered cubic phase. The most characteristic feature defining a single grain is the uniform orientation of the vacancy layers. It is thus possible to discuss the different trigonal phases not solely based on their unit cell, but rather as a stacking sequence of building units (blocks) between vacancy layers. In this context, a 4-Te spacing building block relates to the GST124 lattice model, the 5-Te spacing to the GST225 lattice and the 6-Te spacing to the GST326 lattice. Whether this holds also true for the chemical distribution and the local atomic arrangements within one building block requires a comparison of the experimental and expected simulated HAADF intensities. Before discussing local HAADF-STEM intensities and pm-scale distortions, it is necessary to complete the survey of the overall grain structure.

When considering the total occurrence of 4-Te building blocks across one grain, under the assumption that the chemical composition matches the GST124 phase in these, it is possible to calculate the expected composition of the thin film. Counting the layer sequence is complicated by the diffuse contrast at the interfaces, and as previously mentioned there is a small indication that Ge content in particular at the thin film interface to the surface layer increases. Nevertheless, direct observation of the experimental image shows that about 20% of all building blocks consist of 4-fold Te stacking, while the remaining ones are 5-fold (GST225) with some notable defect structures. Taking into account the relative volume of a building block, i.e. 4-Te occupies 7 layers total plus one vacancy layer while 5-Te occupies 9 layers plus one vacancy layer, the expected Ge concentration over the entire volume is:

$$\frac{1(GeTe)}{8\,layers} \times 0.2 + \frac{2(GeTe)}{10\,layers} \times 0.8 = 0.185\ \left[\frac{at.\%}{100}\right]$$

The presence of 6-Te building blocks shifts the expected composition slightly towards higher Ge content, however since they are very rare in the discussed sample (two across the entire grain in Figure 3.30), the influence is minimal. Thus, the expected composition form stacking sequence lies well within the range of the EDX measurement for this sample ($Ge_{19}Sb_{23}Te_{58}$ ±2 at.%), and the conclusion thus lies close that the local stacking symmetry and the overall composition are causally connected.

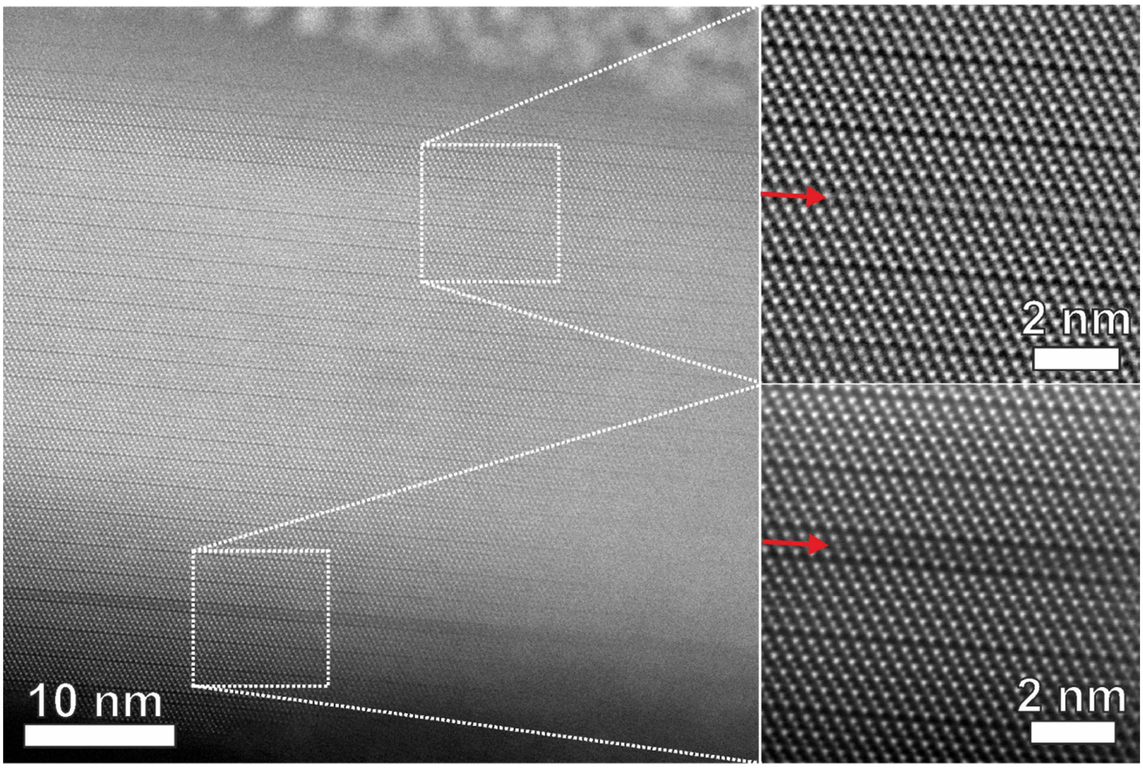

Fig. 3.30: HAADF-STEM overview image of GST thin film annealed at 250 °C in $[11\bar{2}0]$ zone axis projection (left). Due to the large off-tilt of the grain, interfaces to the substrate and cover layer are very diffuse and the HAADF intensity exhibits a thickness gradient towards the interfaces despite the uniform lamella thickness of 35 nm. The Si[110] zone axis was close to 0° sample holder α/β tilt, while the grain zone axis was tilted by $\alpha = 8.5°$ and $\beta = 17.22°$, with the β tilt axis approximately parallel to the substrate interface. Hence, the sample height and thus the defocus also changes across the image from in-focus on the left to under-focused on the right. Right-side panels show selected features (marked by red arrows) recorded at higher magnification: stacking transition between two building units (top) and anomalous stacking unit of two Te and one mixed layer (bottom). The vacancy layer spacing is mixed between 4, 5 and (very occasionally) 6 Te layer stacking within building units.

This is consistent with the hypothetical formation mechanism of the layered trigonal phase from a cubic grain, as partial {111} layer pre-ordering was already found in the cubic parent phase (see previous subchapter, as well as Ref. [198] and [180]). However, an alternative view would be that the coincidental vacancy layer spacing may inform the subsequent chemical composition in the trigonal phase. In either case this raises the question how excess components can be distributed in lattice regions in which the initial vacancy layer spacing and the preferred composition do not match. While this cannot be conclusively answered here, and time-resolved in-situ observations of the crystallization process are somewhat lacking in spatial and chemical resolution[66], it is possible to examine a number of hypotheses.

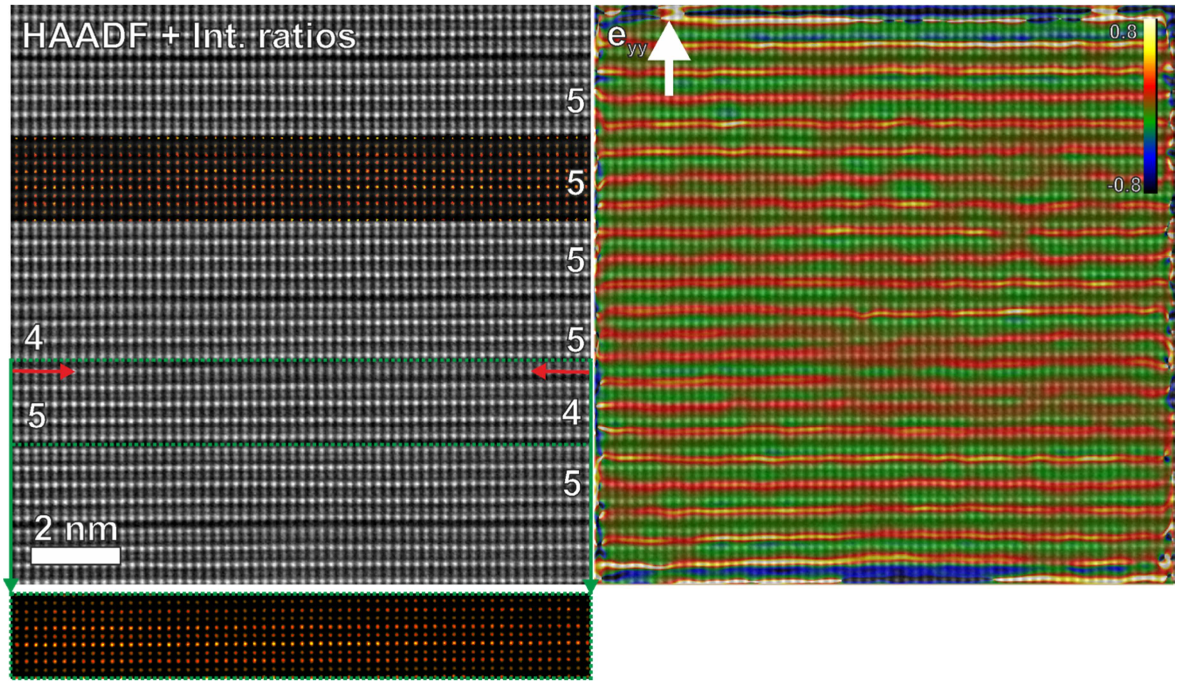

Fig. 3.31: HAADF-STEM image of GST lattice (left) after annealing at 250 °C in [01$\bar{1}$0] projection. Numbers indicate the Te-stacking within the corresponding building unit. A stacking transition (as also shown in the upper right panel of Figure 3.30) is marked by red arrows. The coloured overlay in the left panel shows the intensity ratio map within one individual 5-Te building block (colour scale from 0 to 2.0). Mixed lattice (0001) planes are split into brighter layers (int. ratio around 1.4) close to the vacancy gap, which are thus richer in Sb content, and darker layers (int. ratio around 1.8) in the central part of the building unit, which are thus richer in Ge content. The same HAADF-STEM image is overlaid with the uniaxial lattice distortion from GPA (right). The direction of the lattice vector is indicated by the white arrow, while the length was set to 2.733 1/nm (the average Te-Te reciprocal spacing of (0001) planes). The colour overlay thus represents the local deviation of the Te(0001) spacing from an ideal pseudo-cubic arrangement, averaged over two layers. The intensity ratio variations and (0001) plane offsets correspond well overall with the prediction from the trigonal lattice model. However, offsets in particular are not uniform even outside the distortion zone from the stacking transition.

The initial vacancy layer spacing in the cubic phase can be informed by the observed small distortions in the lattice, rather than local chemical inhomogeneity. The width of the vacancy layer and the position of the first mixed Ge/Sb layer adjacent to the vacancy gap do not match the initial cubic phase. Since the vacancy layered phase is still connected to the cubic parent phase, rather than resembling only one stacking sequence determined by the closest preferred stoichiometry, lattice strain between the two regions is reduced by the formation of defective stacking units. However, differences in lattice parameters between cubic phases of GST124, GST225 and GST326 are small, and if the influence of the lattice distortions on the vacancy layer spacing exists it is expected to be equally small.

The initial vacancy layer spacing can be randomly distributed around the preferred spacing, and subsequently reorders to match the overall composition via the movement of lattice defects. While stacking defects in the lattice are commonly observed, as seen in the top-right panel of Figure 3.30, their occurrence in the ex-situ annealed samples at temperatures of 250 °C and above is not so frequent as to explain an ongoing reordering process of the stacking sequence. These stacking defects are much more common in the textured and epitaxial samples deposited at elevated temperatures, and are thus discussed in more detail in the following subchapter. There, they appear to be coupled to local lattice strain and the chemical reordering may be a secondary effect of the stacking sequence. Nevertheless, it is possible that at the investigated annealing temperature and time, this hypothetical reordering has already largely concluded. Furthermore the lattice very rarely also exhibits a stacking unit consisting only of two Te layers and one weakly scattering mixed layer (see lower-right side panel in Figure 3.30). While none of the existing GST models predict this structure in the equilibrium, the very low HAADF intensity in the central mixed layer hints at a large Ge content or high residual vacancy concentration. Pure GeTe is commonly described as cubic or rhombohedral, depending on the temperature range, while reports on crystal structures of $GeTe_2$ (as would be close to the here hypothesised composition) are sparse. At least one report on metastable $GeTe_2$ exists[209] which refers to the crystal structure as "cubic and isomorphic to β-cristobalite SiO_2" (sic), and makes no mention of intrinsic vacancy ordering. It is possible that the close proximity of two vacancy layers stabilizes a metastable pseudo-cubic arrangement of GeTe or $GeTe_2$ in this individual building block. Since one of the adjacent GST stacking units is that of GST124, the excess Ge in the anomalous stacking unit may originate from there.

Mid-range diffusion (movement over 3-5 intrinsic sites) of Ge and Sb components across a vacancy gap certainly may also play a role in the gradual phase transformation. As was previously reported, an energetic electron beam is able to drive Ge/Sb out of one specific {111} plane in the cubic arrangement, resulting in increased HAADF intensity in the next mixed site due to lower vacancy concentration and/or increased Sb content[198]. If multiple building blocks are able to exchange excess components without structural transformation, then the equilibration of the lattice can occur over longer timeframes without distortion of the vacancy layers. While this appears well-founded, it does implicate that superstructured $(GeTe)_n$-$(Sb_2Te_3)_m$ multilayers for iPCMs should resemble GST building blocks after a sufficient number of switching operations, and similar results have indeed been recently reported of MBE-deposited superlattices[100]. The implications for the functional characteristics of iPCM prototypes have yet to be fully explored.

Lastly, rather than discussing the cubic to trigonal phase transformation within the same crystalline grain, the transition can also be regarded in a wider view as competing anomalous grain growth of hexagonal seed crystals in a cubic matrix. In this context the lattice structure presented in the previous subchapter would be regarded as two adjacent grains of vacancy layered cubic and disordered cubic arrangement. However, the uniform lattice orientation seen therein somewhat contradicts this picture. Nevertheless it is likely that the uniform vacancy layer orientation propagates into the disordered phase along a transition zone of limited atomic movement, thus allowing for the chemical reordering necessary to conform to the later observed trigonal stacking sequences.

The observed trigonal structure shows that the chemical distribution deduced from HAADF intensities does qualitatively match the stacking sequence (see intensity ratio maps in Figure 3.31), with some defect structures of unknown composition as discussed above. It is likely that the phase transformation process is influenced, to a greater or lesser degree, by all of the above described aspects. In addition, there is some indication that equally-spaced building blocks occur in pairs, although this is not a strict rule and isolated blocks or pairs of 4- and 6-Te blocks are equally as likely. Considering that the interaction across the vacancy gap is commonly regarded as weak Van-der-Waals coupling, there is no underlying structural reason that such a double-block arrangement should be preferred, and it thus most probably is coincidental to the chemical distribution in the parent phase.

A closer investigation of the lattice after annealing at 250°C is summarized in Figure 3.31. In the left-hand side panel, an atomically resolved HAADF-STEM image in $[01\bar{1}0]$ projection is shown after image processing (noise filtering and drift correction). In addition to the above discussed stacking disorder, a stacking defect is also captured in this image. Within the width of 16 atomic columns, Ge/Sb and Te layers gradually exchange positions, while the vacancy gap moves accordingly from one side of the Te layer to the other. The lattice to the left of the stacking transition thus resembles a stacking sequence arrangement of GST124 – GST225, while to the right of it the sequence is flipped. This is further illustrated by the semi-quantitative investigation of HAADF-STEM intensity ratios that was introduced in the previous subchapters. Within one 5-Te stacking unit (overlaid on the HAADF image), intensity ratios approximately conform to the GST225 composition. However, the intensity ratios in the mixed Ge/Sb layers in particular are not as uniform as the model structures would suggest. The model by Urban et al. of Ge-deficient GST225 (ICSD#188967) distributes Ge and Sb into Sb-rich layers of $Ge_{0.336}Sb_{0.664}$ and Ge-rich layers of $Ge_{0.604}Sb_{0.362}$, which image simulations predict should result in intensity ratios with the neighbouring fully filled Te layers of about 1.75 and 1.3[176] at 0 defocus and integrating over the FWHM of the individual column peaks.

The graphical I_{Te}/I_{GeSb} intensity ratio evaluation from the experiment indicates that, after constant minimum background subtraction extracted from the vacancy gap, the mean values in the mixed layers match the expected ratios well, however a large amount of variation is observed. Sb-rich columns can yield intensity ratios between 1.1 and 1.4, while Ge-rich columns result in values ranging from 1.6 to 2.0. To a lesser degree this can be traced to the offsets of the layer from the octahedral arrangements, as well as local distortion, which results in varying degrees of overlap between peak intensities in the graphical evaluation. Nevertheless, even a direct observation of the local intensities shows that these are not uniform over more than 5-7 neighbouring atomic columns within one layer, signifying that the relative Ge and Sb content can vary within nominally chemically distinct layers. On the other hand, the intensity ratios do not change so dramatically as to imply an inversion of the stacking sequence, and changes are gradual rather than entirely randomly distributed.

The implication of the observations given above is that the relative Ge/Sb content in the mixed layers of the trigonal phase can vary, in a rough approximation, from $Ge_{75}Sb_{25}$ to $Ge_{55}Sb_{45}$ for Ge-rich layers, and accordingly from $Ge_{25}Sb_{75}$ to $Ge_{40}Sb_{60}$ for Sb-rich layers. Excess components can be clustered within 3-5 or more adjacent columns in the imaged lattice projection. While it is reasonable to assume that an increase in one component in one layer is accompanied by a similar decrease of the same component in the next mixed layer, so as to conserve the overall coordination and binding characteristics of the Te atoms, a conclusive observation of this behaviour is limited by the precision of the method. Some aspects in particular have already been introduced that need to be taken into account since they do not allow for a straight-forward interpretation:

- Thermal displacement factors (B) for different atomic species should differ as well, even if they share a symmetry position. Since only an average B factor is used for one mixed site, changes in site occupancy may result in changes in scattering intensity that are not well modelled when using the original mixed B factor. This also plays into the next point.
- Local lattice distortions can also change the scattering behaviour, for one due to de-channelling effects and partial signal overlap between columns in close proximity, and secondly due to the influence of local strain on the lattice vibrational properties and thus the B factors.
- As indicated by the site occupancies from the model by Urban et al., small deviations in overall composition from the ideal 2:2:5 ratio may result in residual vacancies on the mixed sublattice. In the evaluation of HAADF intensities, the underlying assumption is that all intrinsic vacancies are aggregated in the vacancy layers, and hence excess vacancies result in the formation of 4-fold stacking units as is observable in the experimental data. Nevertheless, the influence of residual vacancies or excess Ge components on the image intensity cannot be distinguished.

Furthermore, the (0001) lattice plane spacings are not as rigid as a periodic model would suggest. Displacements from the predicted [0001] distances have been evaluated in a detailed statistical analysis[55], and the results show that average experimentally determined distances can deviate by as much as 5-10 pm. In particular, mixed positions close to the octahedral sites in the middle of building blocks can be more displaced towards one [0001] direction in the stacking sequence. These differences between model and experiment are extremely small however, and the standard deviation of multiple measurements commonly just about includes the theoretically predicted distances. It is thus also useful to regard the uniformity of the distribution of lattice distortions, for which the geometrical phase analysis (GPA) is a well-suited image processing tool. While the GPA makes use of a simple set of lattice base vectors to construct a reference lattice, the trigonal GST stacking inherently possesses a complex structure with varying Ge/Sb-Te distances that is not as easily reproducible as the cubic arrangement (for which two base vectors are sufficient). As a result, a GPA map of the trigonal lattice such as the right-hand panel in Figure 3.31, which maps the local lattice distortion of a [000 ½] base vector, inherently shows compressive and expansive lattice distortions (red/yellow and green/blue areas in the image) that result from the offsets of the (0001) planes from the octahedral centres. Nevertheless, the distribution of the information in the GPA map is useful to make some observations on the local lattice distortions.

Local lattice distortions over 5-10 neighbouring atomic columns (bright yellow areas in the strain map in Figure 3.31) are present even in building blocks that initially appear undistorted in the HAADF image, and which are removed from defective stacking units. When observing the ADF-STEM scattering behaviour (19.5 – 80 mrad), which collects partially coherent scattering contributions (see Appendix C.5), additional regions in the lattice exhibiting increased partially coherent scattering become visible while the same positions only exhibit diffuse contrast in the corresponding HAADF image. In ADF-STEM images, the contrast is enhanced by local lattice strain, while the contrast in the undistorted building blocks is uniform and not readily interpretable in terms of chemical distribution. However, local layer distortions mapped in the GPA do not always result in these additional contrast features, possibly either because the specific HOLZ Bragg condition is not always met or due to the presence of additional structural defects (i.e. ADF contrast changes may only occur when layer distortions are strongly correlated). However it is important to note that local lattice distortions and strain effects are typically large only in the Sb-rich outer layers of the stacking units. In contrast, the observed variation in intensity ratios is also present in the almost undistorted central Ge-rich layers, and the conclusion that local Ge/Sb content can vary by as much as 10 at.% or more still appears valid.

Strong local distortions in Sb-rich layers occur in conjunction with the neighbouring Te layer adjacent the vacancy gap. The commonly accepted local atomic arrangement of the Sb-rich positions is that of distorted octahedral sites with long and short bonds. An effective coordination number was used by Ref. [75] to describe the local bond environment in various GST compounds, and to conclude that 50% of Sb atoms were situated in an effective coordination of 5.45 for these specific sites in a GST225 lattice model, while an undistorted octahedral site would possess a coordination number of 6. A more involved discussion of the electron localization distribution was carried out[87], which concluded that "lone-pair electrons of the twofold coordinated Te atoms can interact with the Sb atoms in the neighbouring layers creating Te-Sb-Te 3c-4e bonds" (sic), 3c-4e bonds here referring to three-centre four-electron bonds creating a strong bonding environment towards the lone-pair Te layer adjacent the vacancy gap, while bonding towards the other side occurs only through the much weaker back-lobes of the p-orbitals. This may also be a central feature for the topological insulating behaviour of Sb_2Te_3-type layered structures such as Bi_2Se_3[38] and possess a link to the Dirac-semimetal behaviour in superlattices[210], although this area of research still remains to be advanced further. The observation here, that Sb-rich and vacancy-adjacent Te layer are strongly coupled, is very much consistent with this bonding structure. The question does arise how the bonding arrangement would change in Sb-rich layers which are strongly distorted so that the weak bonds are entirely broken, however an Sb-rich layer surface exposed to a vacancy gap is never observed, instead resulting in a stacking transition defect. This highlights that the nature of the weak bonds towards the inner Te layer may be even more important to the layer switching behaviour proposed for interfacial switching concepts than the strong electron localization in the short bonds, as are the less distorted Ge-rich sites.

Finally, the GPA map reveals that in the vicinity of a stacking transition (see red arrows and green box in Figure 3.31, as well as the corresponding intensity ratio map below and the strain map to the right) the [0001] layer distances, aside from the two layers (Sb-rich and Te) partaking in the transition, are overall slightly less distorted from the cubic reference framework than in the equilibrium trigonal phase. In the marked area, the stacking sequence changes from 4-Te towards 5-Te above, and vice versa below. The Intensity ratio map shows that the composition change from Ge-rich layer on the left towards Sb-rich on the right is gradual inside the transition zone. While the GPA map never entirely resembles the uniform cubic lattice, the above mentioned reduced layer distortion and the intermixing of Ge/Sb may imply that the lattice possess a partially cubic character within the transition, which should impact the functional properties. This is somewhat countered by reports on the role of vacancy ordering in the metal-insulator transition[46, 204], since the intrinsic vacancies most probably remain clustered in the two partial vacancy layers in the stacking defect. The lower degree of distortion should impact the local vibrational properties of the lattice and the optical properties[13, 173].

The samples annealed at 290 °C and 320 °C are presented in less detail since many of the above discussed features of the trigonal lattice are also found at higher annealing temperatures. The most notable differences are found in the layer and grain morphology. While the sample annealed at 250 °C presented a closed thin film with very low surface roughness and irregular grain boundaries, the sample annealed at 250 °C shows formation of holes at the GST-SiO_x interface (Figures 3.32 and 3.33). These holes often occur at the tri-junction of two GST grains and the substrate. In addition, the surface roughness is also increased (about 4 nm rms) due to buckling of the surface under the influence of the volume change in the GST layer, although the $LaAlO_x$ surface layer is continuous and shows very good adhesion to the GST thin film. The lateral grain size varies, with the largest grains extending over slightly more than a micrometre, while smaller ones still measure about 100-200 nm.

Notably, the holes and grain boundaries generally appear rounded, without fixed preferred orientations of the grains towards each other. This is further underscored by the NBD measurements (diffraction patterns in Figure 3.34). The Kikuchi line features, some of which are schematically indicated by the red dotted lines, show either very little or no orientation relationship between neighbouring grains.

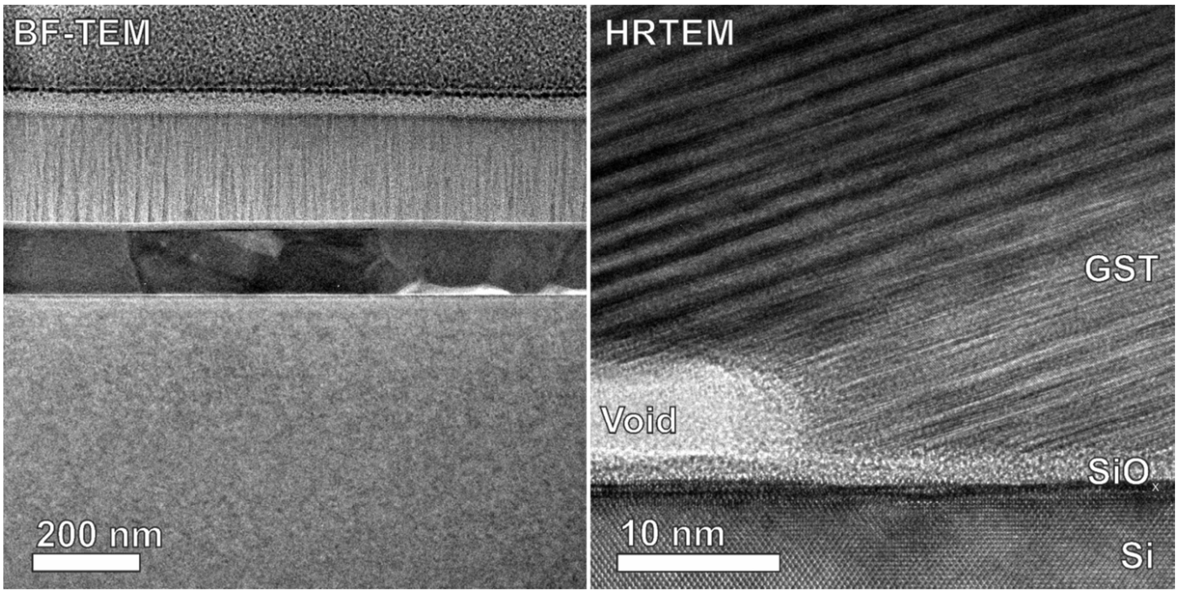

Fig. 3.32: BF-TEM and HRTEM image of GST thin film after annealing at 290 °C. Elongated grains can extend laterally over 500 nm or more. The film thickness of 117 ± 2 nm matches the expected deposition rate reasonably well, while the volume change during crystallization has led to some deformation of the surface / LaAlO$_x$ layer. Most notably, void formation has taken place at the interface to the substrate native oxide layer. The shape of these voids as well the grain boundaries is, contrary to expectation from the grain morphology in the cubic phase, not organized along {111} planes. Overall this indicates that further material transport and lattice reconfiguration take place within the temperature regime.

This is somewhat surprising, since in the previously discussed sample as well as the cubic samples a preferred orientation relationship to the amorphous substrate surface was postulated. One underlying reason for the lower degree of texturing may be found in the change in total film thickness (42 nm at 250 °C and 116 nm at 290 °C, from change in total pulse number during deposition). In the thinner sample, the influence of the sandwiched geometry on the preferred grain orientation is stronger, while in the thicker sample this influence is lost. Although for the application-relevant case very thin films are of interest (20 nm or less of active layer material), larger volumes of material are helpful in the investigation of local atomic structures closer to equilibrium.

The void formation and grain size distribution indicate that significant material transport continues to occur above the phase transformation temperature, and preliminary investigations on GST thin films without cover layer in fact showed that the material is no longer present as a closed thin film at an annealing temperature of 300 °C (see Appendix C.6). The lower interface energy between GST and LaAlO$_x$ compared to the interface of GST and SiO$_x$ enhances the competing grain growth in the thin film, fuelled by material transport along the grain boundaries and open faces of the voids.

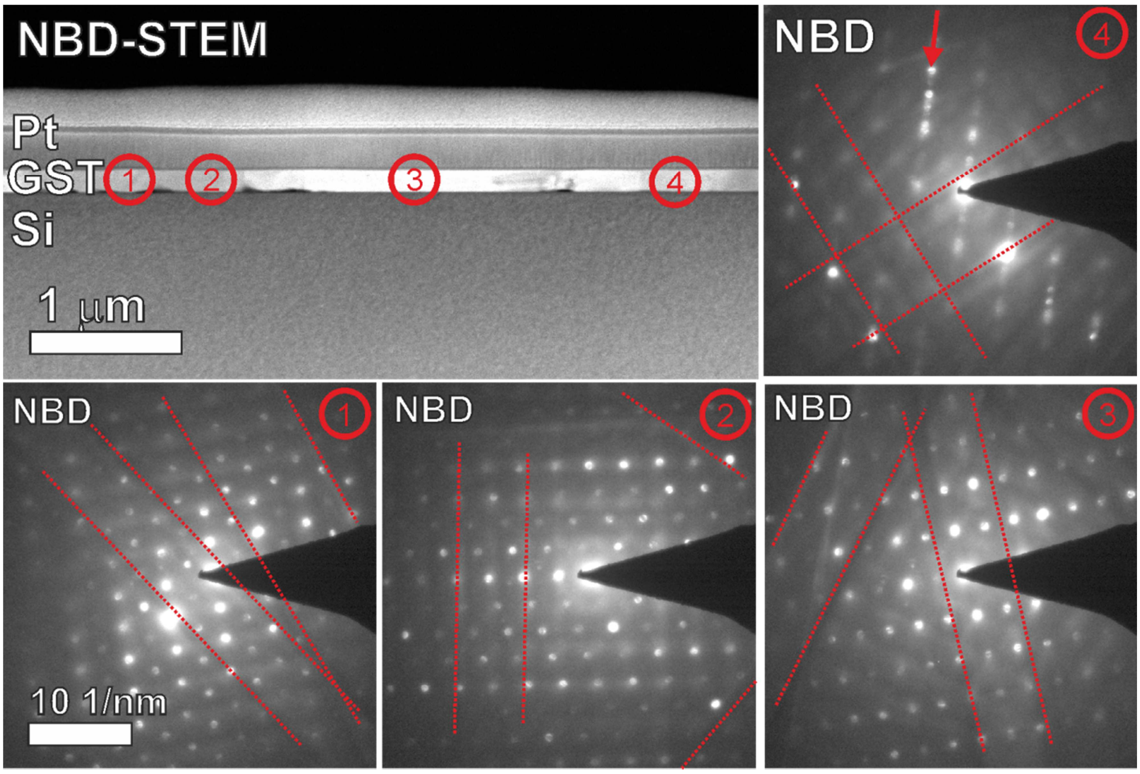

Fig. 3.33: NBD-STEM (HAADF) overview of sample annealed at 290 °C and selected NBD patterns from indicated positions in the GST thin film. Void formation extending from the junctions of grain boundaries and the substrate interface is readily visible across the entire lamella. Dashed lines in the NBD patterns indicate selected Kikuchi line features. Pattern (1) and (3) are close to a low-index zone axis, while (2) and (4) are far away from any readily identifiable orientation. Red arrow in (4) marks the superstructure reflections typical for trigonal phase GST. Individual grains can extend laterally over multiple micrometre, e.g. the grain orientation of (3) extends from the right edge of the (2) marker to the left edge of the (4) marker. Sample was oriented in Si[011] zone axis, and there is thus no apparent orientation relationship with the substrate.

Which grains out-compete the grain growth process appears random, although certain low-angle grain boundary symmetries may be more stable. The stacking arrangement and distribution of local distortions are summarized in Figures 3.34 and 3.35. Overall the lattice structure is similar is to the trigonal lattice seen before, with predominantly 5-Te stacking units yet also about 25% of 4-Te stacking units as well as 10% of 6-Te stacking units. The overall expected composition of Ge-deficient GST225 is thus again matched when assuming GST124, GST225 and GST326 building blocks. Stacking transition defects are also found (not captured in the particular example images shown), while the previously described anomalous Te-Ge-Te stacking units are not evident. Variations in local distortions are similarly also observed, with 6-Te building blocks appearing less distorted from the cubic parent phase than 5-Te building blocks. Very large distortions in the strain map (contrast reversals from yellow to blue) can be attributed to the relatively low resolution used to obtain a large field of view in Figure 3.35, i.e. they occur when the contrast drops off either due to thickness gradient of the crystallite or because individual layers are not well resolved. The higher number of 6-Te stacking units, coupled with the absence of anomalous stacking units, may imply that on occasion 4-Te building blocks and adjacent Ge-Te_2 units have combined to 6-Te stacking units, although these would then be missing Ge components, and additional 4-Te blocks must have also been created by chemical reordering of the lattice. Since the two samples were prepared to different film thicknesses, they are not immediately comparable in every aspect, and these additional 4-Te stacking units may have been already present during the early stages of the phase transformation. Nevertheless the overall impression is that the overall stacking disorder and stacking defect density has slightly increased.

Close inspection of the HAADF-STEM intensities (Figure 3.35) underscores that the individual, defect-free building blocks resemble the preferred stacking sequences well when averaged over multiple columns. The intensity profiles shown were measured from individual building blocks, along the [0001] direction as indicated by the white arrow, and integrated over the entire width of the image. Fitting Gaussian peaks to the column positions shows that the Ge/Sb content in the selected building blocks follows the trend indicated by the reference model structures, with Sb-rich outer layers and Ge-rich inner layers.

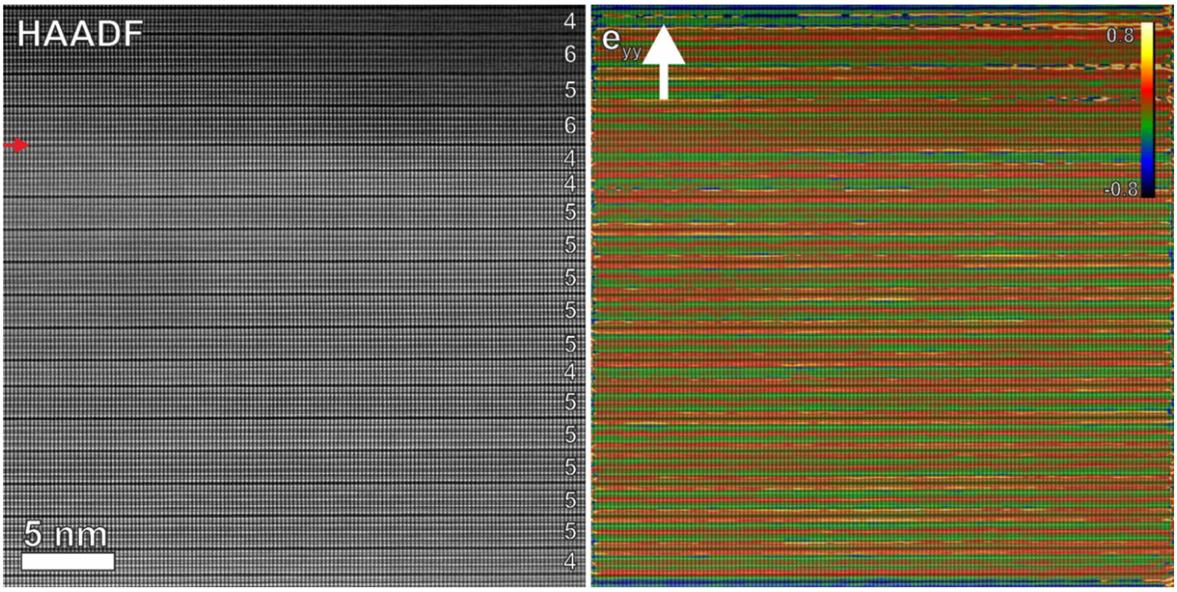

Fig. 3.34: HAADF-STEM overview image of GST lattice in $[01\bar{1}0]$ projection after annealing at 290 °C (left) and corresponding montage of lattice image and local distortion map e_{yy} similar to Figure 3.31. Numbers in the left panel indicate stacking sequence of Te layers between the vacancy gaps. The lattice exhibits very few defects, provided the different stacking units can be regarded as stable lattice configurations. There is some indication that, at 6-Te blocks in particular, individual double layers at the vacancy gap are only weakly bound to the building unit, and one occasion of a half-filled mixed layer at a 6-Te block is marked by the red arrow (see Appendix C.7).

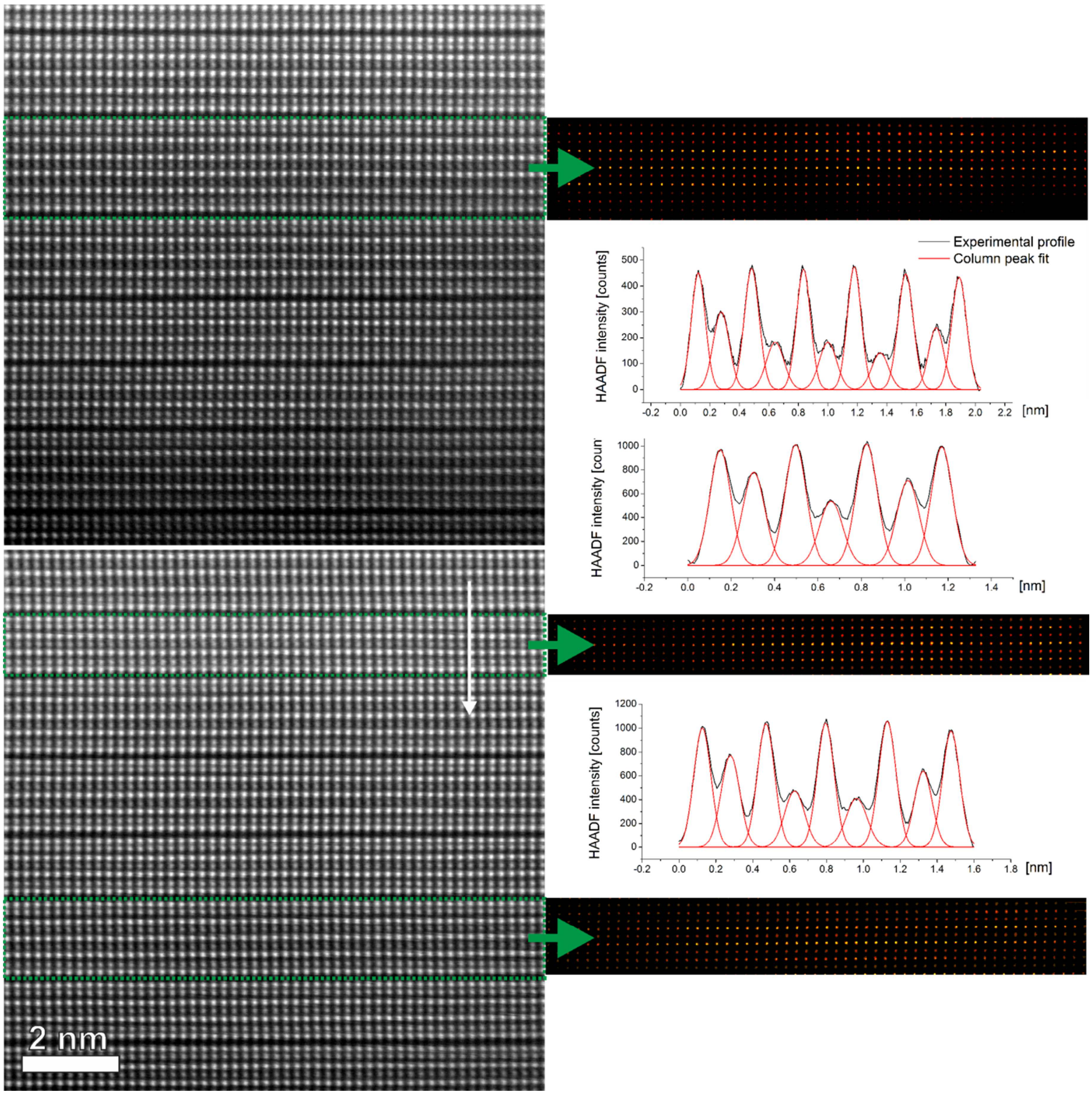

Fig. 3.35: HAADF-STEM images from selected regions in Figure 3.35 at high instrument magnification, and intensity ratio maps from selected regions of the images (marked by dashed green boxes). Due to the deviation of the Te-Te spacing across the vacancy gap and the displacements of the mixed (0001) planes from the octahedral centres, the graphical evaluation struggles to find suitable periodic offset vectors. The intensity ratio maps highlight the preferential chemical ordering into Sb-rich layers strongly displaced towards the vacancy gap and Ge-rich layers only weakly displaced from the centres of GeTe6 octahedrons. Line profiles and corresponding peak fit deconvolutions for 6, 4 and 5 Te layer blocks are also shown. Profiles were measured from raw experimental data along the [0001] direction as indicated by the white arrow and subsequently background subtracted from the residual intensity in the vacancy gap. Crucially, residual lattice disorder remains in the Ge:Sb distribution, and the entire central Ge/Sb planes in the 4- and 6-Te layer building blocks are displaced by up to 15 pm towards either side in [0001] direction[55].

Even the slight increase of Sb content in the central mixed layer of a 6-Te building block can be discerned, although the difference to the next-adjacent Ge-richest layers is minimal (77 vs. 75 at.% Ge according to ICSD#157728[35]), and the visible difference in scattering intensity is, in image simulations, caused by the large difference in B factors (0.8 vs. 1.27 Å²). It is however also notable that, even when averaging over multiple columns, symmetrically identical layers are not necessarily equally occupied. Outer Sb-rich layers do not yield exactly the same peak intensity while adjacent fully occupied Te layers match well against each other (and therefore the Sb-rich signal deviation cannot be attributed to faulty background subtraction or a single layer distortion). This is further reinforced by the intensity ratio maps, although due to the high magnification, local distortions and edge effects, these are not as implicit as in the cubic phase.

Finally, there is also some indication that residual HAADF intensity can be found in the vacancy gaps (Appendix C.7), although this is only observed in some smaller regions of the lattice and it is unclear whether they can be attributed to actual material inside the vacancy layer. As the TEM lamella of the sample annealed at 290 °C was relatively thick (50 ± 10 nm), it is also possible that the spurious signal originated from residual aberrations, de-channelling effects or projection artefacts from overlapping lattice regions of different stacking sequence.

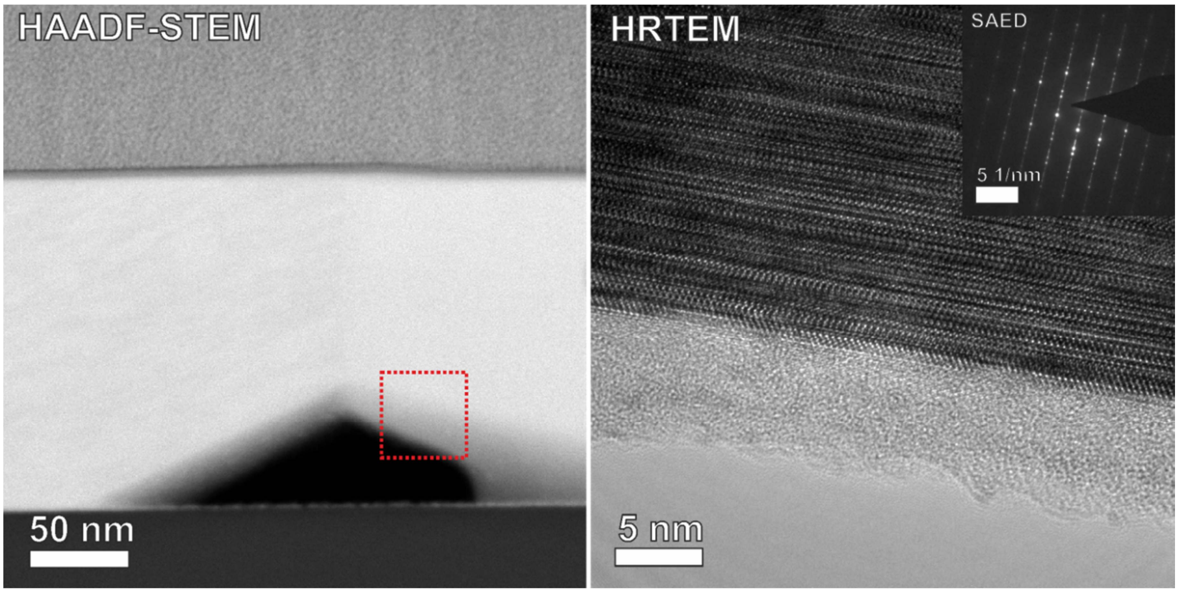

Fig. 3.36: STEM and TEM overview images of GST layer annealed at 320 °C. The HAADF-STEM view (left) shows occasional voids at the junction of large crystalline GST grains and the substrate. In contrast to Figure 3.33, voids are faceted along (0001) planes. In the HRTEM image of the void edge (right) it becomes apparent that due to the shallow angle of the incident ion beam during milling, as well as the thickness gradient of the faceted grain at the void, material from the substrate has been re-deposited into an amorphous surface layer on the GST crystallite. The red dashed box in the left-hand panel approximately indicates the position of the HRTEM image, while the inset shows a SAED pattern from the GST crystallite.

Investigation of the sample annealed at 320 °C, which showed the largest deviation in XRD features from the previous two presented structures, reveals some marked differences while still retaining the trigonal nature of the lattice. The most striking feature at low and intermediate magnification is the morphology of the grains and micro-voids (Figure 3.36 as well as Appendix C.8). Whereas previously the thin film was either closed with diffuse grain boundaries or exhibited rounded voids and grains, now the open faces of the voids are predominantly oriented along (0001) planes, and grain boundaries appear straight. A close inspection of the lattice however reveals that the lattice disorder and defect density has persisted or even further increased. Examples are shown in Figure 3.37. Stacking defects (indicated by red arrows in the left-hand panel of Figure 3.37) are occasionally correlated across one or more stacking units. The effective result of correlated stacking transitions is that they accommodate [0001] shear strain, and accordingly systematic ordering of stacking transitions was observed both as a means to accommodate topographic features in the surface of single-crystalline substrates[176], further discussed in the final chapter, as well as small systematic miss-orientations towards lattice-mismatched substrates[114].

In addition, another distinct type of defect is observed in the form of 60° rotation twins. The zone axis projections $[11\bar{2}0]$ and $[2\bar{1}\bar{1}0]$ can be distinguished by the direction of the shortest Ge/Sb-Te distance i.e. the direction of the $(\bar{1}13) \triangleq (\bar{1}103)$ and $(01\bar{3}) \triangleq (01\bar{1}\bar{3})$ planes (the planes marked by dashed red lines in the bottom-right panel of Figure 3.37). Similar to the formation of correlated stacking defects, the presence of a twin structure accommodates shear strain within the (0001) plane. The underlying reason can be found in the preferred grain boundary symmetry (see top-right panel of Figure 3.37). What initially appeared as a straight grain boundary under close inspection reveals itself to be a saw-tooth structure along a preferential orientation and possibly including defect-rich regions along less dense planes e.g. $(10\bar{2}) \triangleq (10\bar{1}\bar{2})$. Hence, the formation of a twin structure is favourable if it allows both sets of preferred grain boundary planes (above and below the twin plane) to participate in the interface formation.

Ideally it would be preferable to describe the grain boundary entirely by the lattice plane vectors of both surfaces from the neighbouring grains. However, the tilt range of the sample holder is limited, and the second zone axis orientation was not obtained. From the lattice plane spacing, orientation and contrast features at the interface, some observations on the grain interface are possible (see Appendix D). The best match between lattice models and experimental result can be found if the left-hand grain is oriented in $[11\bar{2}0]$ and the right- hand grain in $[\bar{1}2\bar{1}1]$ zone axis projection. The grain boundary then runs at an angle of about 35° to the image plane, along the $(02\bar{2}3)$ plane of the left-hand grain (with aforementioned facets due to twin formation) and the $(1\bar{2}10)$ plane of the right-hand grain. These two lattice planes do not, however, possess a common 2D symmetry (see Appendix D.4), and it is likely that the grain faceting along $(02\bar{2}3)$ planes is a stronger determinant of the grain boundary symmetry than the potential grain boundary CSL.

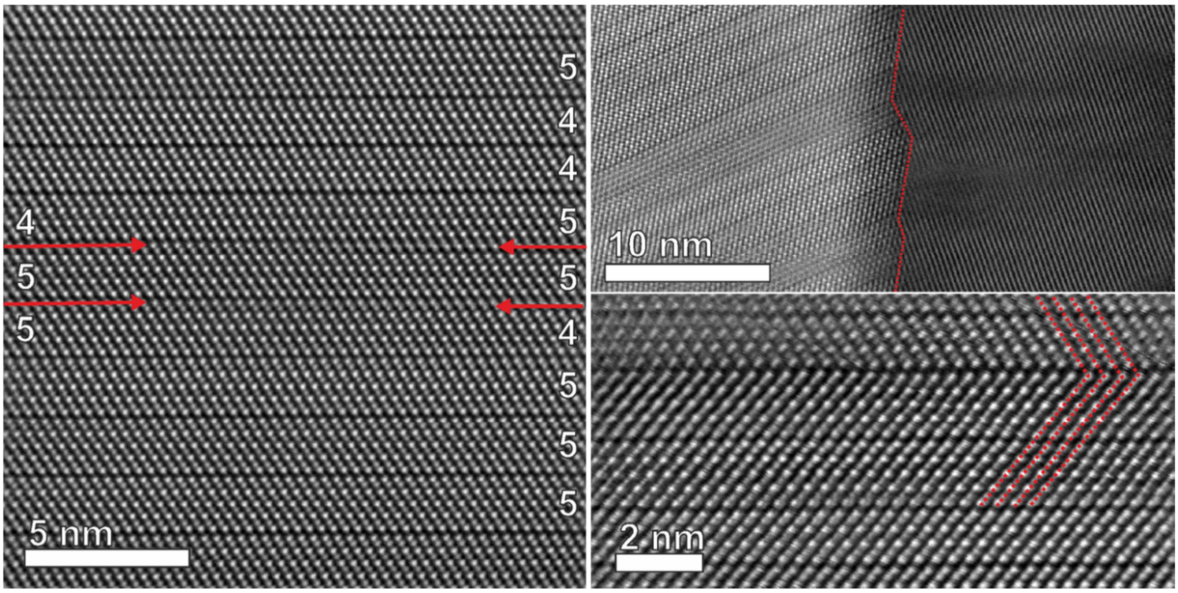

Fig. 3.37: Detailed HAADF-STEM views of GST lattice annealed at 320 °C in $[11\bar{2}0]$ projection. Stacking sequence and stacking transition defect (marked by red arrows, left). The as-deposited GST thin film was slightly more Ge-deficient (Ge:20 Sb:24 Te:56 at.%) than those presented in the previous samples due to a change in the PLD Target, and the stacking is thus dominated by 5- and 4-Te building blocks. Atomic-resolution view of a grain boundary (top right) as seen in Figure X. The sawtooth-like structure originates from the preferred orientation reconstruction of the initially random grain boundary in the parent phase. Twin structure in the trigonal lattice (bottom right). These consist of 60° rotation twins across vacancy layer gaps, thus resulting in a $[11\bar{2}0]$ zone axis orientation in the lower part of the image and a $[2\bar{1}\bar{1}0]$ zone axis orientation in the upper portion of the image. On the left edge of the image, the two lattice orientations overlap within the upper twinned building block, resulting in a complex overlay pattern of multiple columns.

In summary, the local structure in the trigonal lattice is complex and real cases cannot be easily described without special regard for the stacking disorder, chemical sublattice disorder and characteristic defect structures. While typically successively higher annealing temperatures of bulk samples would be expected to result in a gradual increase in ordering, the thin film geometry as well as the volatility of the constituents under experimental conditions results in defect disorder that somewhat subverts this. The increased stacking disorder at higher annealing temperature results in the initially observed offset in the XRD peak characteristics due to the higher portion of 4- and 6-Te stacking units. The observed defect structures can be expected to be characteristic for a range of Van-der-Waals layered crystalline lattices, and need to be taken into account during epitaxial layer growth as well as in the functional properties of layer switching concepts.

3.4 Thin film deposition at elevated substrate temperature

In order to investigate the oriented thin film growth of GST on Si(111), a stage heating element was added to the PLD chamber and calibrated via thermocouple measurements from the empty holder as well as a blank substrates. Substrates for thin film deposition were either used with a native oxide surface layer as-is, or wet-chemically cleaned (RCA wafer cleaning process[211]) and subsequently heated to the desired deposition temperature over an interval of 30 minutes. As such, the cleaned Si(111) surfaces inside the vacuum chamber preceding deposition can be expected to be oxide-free hydrogen-terminated, yet without a specific surface reconstruction. In order to obtain the 7x7 surface of Si(111), the substrate would ideally be heated to above 850 °C and subsequently slowly cooled. Such a substrate treatment was carried out in comparative studies e.g. of the thin film growth by molecular beam epitaxy[212]. Similar experimental studies of the PLD growth on surface reconstructed substrates as well as the influence of prolonged post-deposition annealing within the PLD chamber after epitaxial deposition are being developed. Additionally, the choice of substrates is not limited to semiconductor materials, and the low-temperature deposition process on KCl(100) and BaF_2(111) has been documented in Ref. [175] and [114]. The major drawback of the STEM investigation method for these materials is that the electron beam very easily destroys the interface structure, and atomic resolution images are thus best obtained only from within the thin film itself. While some selected examples can be found in aforementioned publications, the here presented result are focused on the PLD growth process on Si(111) due to its technological relevance and suitability to the investigation method. In order to compare the influence of the substrate surface symmetry with the impact of the intrinsic layer formation of the GST lattice on the thin film morphology, a GST thin film was also deposited onto a Si(111) substrate at elevated temperature with the native amorphous oxide layer left intact. The results on the investigation of textured and epitaxial thin films deposited at elevated substrate temperatures have been published most recently[176]. As such the aforementioned paper gives a good overview of the following chapter, and differences largely involve some additional details regarding the individual samples.

The results of the preliminary XRD investigation generally indicated either a texture component, referring to one or more preferred orientation relationship(s) towards the substrate symmetry within a limited angular range, or epitaxial layer growth i.e. a single crystalline growth orientation on the substrate. An example of XRD pole figure measurements from a highly textured sample deposited at 170 °C and an epitaxial sample deposited at 280 °C is shown in Figure 3.38. The pole figures are recorded in in-plane geometry (for details see e.g. [213]), meaning that the sample is kept at one (horizontal) position while source and detector are positioned so as to fulfil specific diffraction conditions (source position ω, detector at Bragg angle $2\theta_B$ of lattice planes *hkl*) for a set of planes at a given tilt angle α, and the actual arrangement in the sample is then determined by rotating the sample around the full 360° (φ) range.

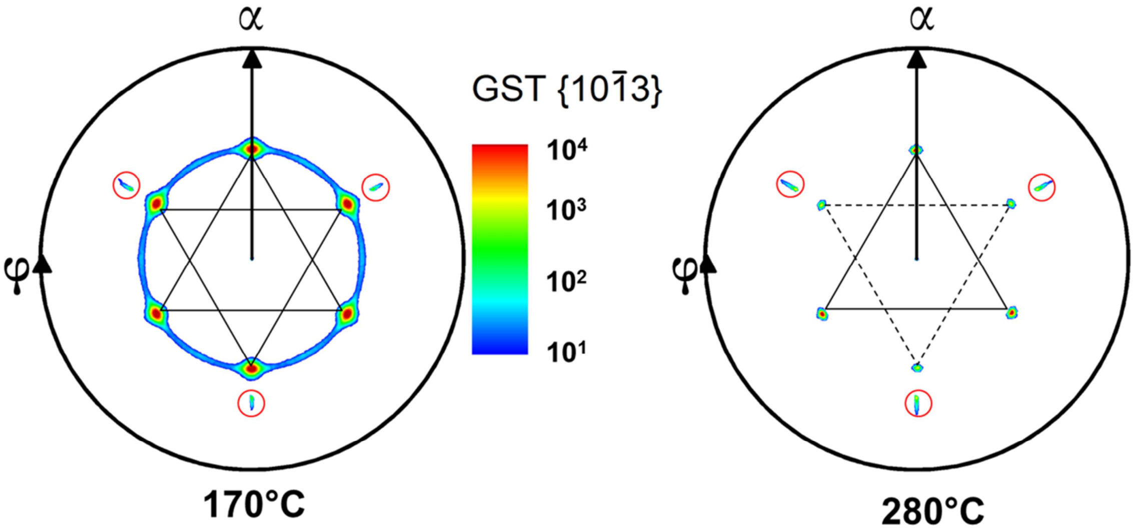

Fig. 3.38: XRD pole figures of GST {10-13} planes, from thin films deposited onto Si(111) at elevated substrate temperatures. Textured thin films (example shown on the left, deposited at 170 °C) produce maxima relating to two preferred orientations within a limited angular range. Epitaxial thin films (right, deposited at 280 °C) exhibit discreet maxima due to the fixed orientation relationship towards the substrate. The two triangles (solid and dashed line) again relate to two possible configurations which, as will be shown further on, originate from the 60° rotation twinning. Additional intensities marked by red circles are the result of substrate contributions. Figure adapted from Ref. [115].

Source and detector are then repositioned so as to fulfil the diffraction conditions at a small tilt angle α offset, and the φ-rotation repeated. The recorded intensity after repeating this process through the full 90° α-range is then plotted on a logarithmic scale in a stereographic projection of the diffraction space. Hence, a large randomly oriented sample volume of the same crystalline structure would resemble a continuous random distribution of intensity, while a preferred orientation of the tilt angle between lattice planes and substrate results in a ring distribution (left panel of Figure 3.38). If the rotation angle between thin film and substrate is also fixed, as is the case in an epitaxial relationship, then the φ-scan results in discreet maxima at specific angular positions of α (synonymous with the commonly used χ due to the fixed horizontal position of the sample in the specific instrument used) and φ (right panel of Figure 3.38). Thus, the preliminary conclusion from diffraction measurements was that all samples deposited at temperatures of 110 °C or above possess some degree of texturing, and thin films deposited above 170 °C on cleaned substrate exhibit an epitaxial relationship GST(0001)||Si(111), GST[1$\bar{1}$03]||Si[001]. The transition between varying degrees of ordering appears fluid, and at low deposition temperatures the distinction between partial layer ordering and cubic components can be imprecise. As one of the aims of the investigation was to characterize the PLD process for highly-oriented thin film deposition of layered GST, with subsequent interest in the deposition of superlayer structures for iPCM concepts, the here presented samples are chosen so as to characterize the onset of layered growth as well as possible difficulties due to morphological and composition changes at high deposition temperatures.

Tab. VI: PLD parameters for samples deposited onto amorphous interface Si(111)/SiOx and chemically cleaned Si(111) substrates. EDX composition measurements were evaluated from STEM-EDX hypermaps.

Substrate	Deposition temperature [°C]	Pulse No.	Hz [1/s]	Thickness [nm]	Ge [at.%]	Sb [at.%]	Te [at.%]
Si/SiOx	180	4000	10	53	21	24	55
Si(111)	110	7200	2	154	23	24	53
Si(111)	170	7200	2	142	22	23	55
Si(111)	185	7200	2	124	22	24	54
Si(111)	280	7200	2	19	10	33	57

A summary of the deposition parameters of the subsequently discussed samples is given in Table VI. The standard deviations of composition measurements from hypermaps across the entire layer thickness are ±1.4 at.% Ge, ±2.5 at.% Sb and ±6 at.% Te, respectively, due to the close overlap between Sb and subsequent Te L-lines, as well as the relatively short acquisition times (typically 5 minutes at around 400x300 pixel resolution depending on layer thickness, in order to reveal potential inhomogeneity) used to reduce electron beam influences. Nevertheless, average compositions at low deposition temperatures match the expected Ge-deficient GST225 target stoichiometry, while at high deposition temperatures there is a marked drop in the relative amount of Ge as well as the overall layer thickness. Interface roughnesses (rms) at the surface of the GST layers towards the $LaAlO_x$ capping layers range from 1 - 2 nm, measured by BF-TEM image evaluation from the textured samples, to 3 - 4 nm, measured from the HAADF-STEM images of epitaxial samples. A close inspection of the thin film surface in the textured samples indicates that the lower roughness measured in these may be a result of the lower interface contrast due to the larger range of grain orientations compared to the epitaxial samples, and thus reveals a weakness in the precision of the evaluation method. As the larger point of interest in the surface roughness is whether the thin films are closed or exhibit surface faceting, the conclusion can still be drawn that all samples exhibit largely flat, closed surfaces, with the residual nm-scale roughness resulting from the disordered growth zone.

The marked drop in Ge content appears to be a systematic effect even when the substrate composition is varied. Figure 3.39 shows a compilation of the composition measurements from a larger number of samples, including those deposited onto $BaF_2(111)$. While at similar temperatures (e.g. at RT) the compositions on the two substrates deviate somewhat, possibly due to the difference in thermal conductivity of the substrate, all measurements follow the same trend. Below 150 – 200 °C, the observed thin film composition matches the expected target composition reasonably well within the error of the measurements. Above 200 °C substrate temperature, relative concentrations of Ge and Sb deviate significantly. The solid lines in the graph are exponential growth fit curves of the type $y = y_0 + A * exp(x/t)$, where y_0, A and t are fitting parameters for each series of data points. While this appears related to the Arrhenius equation $k = A * exp(E_a/k_B T)$, and might thus be assumed to be a thermally activated process as a function of the difference in surface binding energies, the influence of chemical effects on the GST stoichiometry is unclear. A similar change in thin film composition was described in Ref. [214], who concluded that an increase in effective surface temperature during MBE deposition leads to preferential desorption of GeTe. As the incident kinetic energies in the PLD process tend to be higher (typically in the range of 1- 100 eV [215]), and the deposition rate, and hence the increase in surface temperature, equally larger, this effect may play an even larger role in the here presented deposition process.

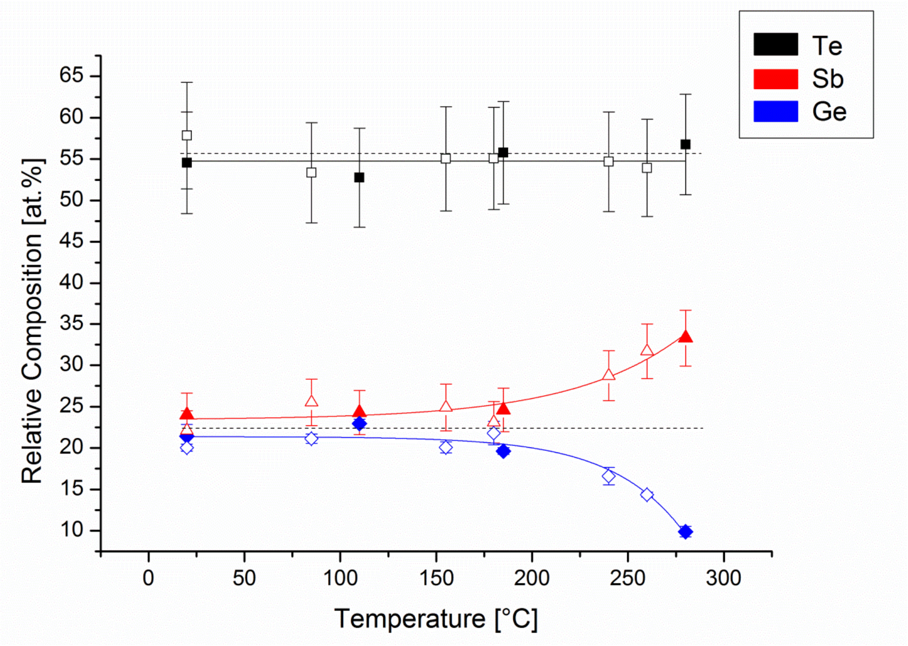

Fig. 3.39: Relative composition of GST thin films deposited onto SiO_x, Si(111) (closed symbols) or BaF_2(111) (open symbols). Dashed lines indicate nominal GST225 composition.

Since the overall deposition rate deduced from final layer thickness also drastically decreases at high temperatures, increased desorption of all components certainly is an important effect to take into account. Since the target stoichiometry is the primary factor determining the concentrations in the plasma plume (excluding differences in absorption coefficients)[215], the relative particle flux cannot be as easily adjusted as in an MBE process using separate effusion cells. Adjusting the substrate thermocouple temperature to a constant, stoichiometric desorption rate of GeTe in an experiment aimed at investigating the high-temperature epitaxial growth from a GST225 target is not feasible since the substrate temperature would then never exceed 200 °C. An alternative view can be proposed in that it was found[20] that the removal of antibonding states from the bulk lattice via a reduction of the Ge content in metastable GST compositions was energetically favourable. Hence, if the crystalline growth proceeds via the metastable phase, a preferential removal of Ge from the lattice would be plausible. Spatially resolved composition measurements (see Appendix C.9) indicate that a Ge depletion zone and Ge-rich surface layer can be found as the deposition temperature is increased, and the surface region generally exhibits increased disorder. The composition gradient at the substrate interface (Appendix C.10) is small bar a delay in the Te content signal that is further discussed in the context of the interface structure.

Regardless of the specific mechanism that leads to this loss of Ge content, the EDX measurements make it clear that direct stoichiometric transfer can only be achieved in a limited temperature window, which potentially may be extend by fine-tuning the deposition parameters. At the same time, the crystalline microstructure of the thin films deposited at low temperatures is not of ideal epitaxial quality, as already indicated by the XRD data shown above. This can be further quantified by a comparative analysis of NBD series data. As shown in the inset of Figure 3.40, the texture component results in an orientation relationship between substrate zone axis and trigonal superstructure diffraction (intense row of closely-spaced diffraction spots). The tilt distribution of the GST{000*l*} reflections against the substrate, within the diffraction plane i.e. the Si[110] zone axis plane of the substrate, can be statistically analysed in order to give a quantitative measure for the particular degree of texture relationship equivalent to the out-of-plane direction in XRD measurements.

Comparison of such data from three samples deposited at different temperatures and on either Si(111) or SiO_x, as in Figure 3.40, reveals that the deposition at 110 °C on Si(111) results in a similar tilt distribution width (± 10°) as the deposition onto SiOx at 180 °C (± 13°). At a deposition temperature of 185 °C, the tilt distribution on cleaned Si(111) is very sharp (< ± 2°) indicating epitaxial growth behaviour. Since the amorphous interface layer offers no preferred surface symmetry and possesses a small residual roughness (< 1nm rms), it can be concluded that any low-roughness, chemically passive substrate may be suitable for texture growth of GST(0001) planes parallel to the substrate surface.

Close inspection of the Si-SiO_x-GST interface (Figure 3.41) also reveals an evolution of the GST lattice from the amorphous interface. While vacancy layer ordering in the $[01\bar{1}0]$ projection (in addition to the diffraction data) indicates the trigonal lattice symmetry, the GST arrangement at the interface itself often consists of cubic regions over 8-10 Te layers without clear vacancy ordering, visible chemical ordering of the Ge/Sb distribution or marked distortions from the octahedral centres. However, the image quality may be insufficient to measure the latter with the required pm-scale precision. The overall grain morphology as seen in the TEM image consists of distinct columnar grains with a tilt and twist (rotation) reorientation component towards the substrate, as well as twin domains as was previously indicated by XRD pole figures similar to Figure 3.38. Interpreting the interface structure on amorphous SiO_x is particularly difficult due to the diffuse contrast of amorphous structures. Judging from the limited information available in the ADF-STEM image, there is no indication that the vacancy layer formation plays a role in the initial grain growth orientation on the amorphous interface.

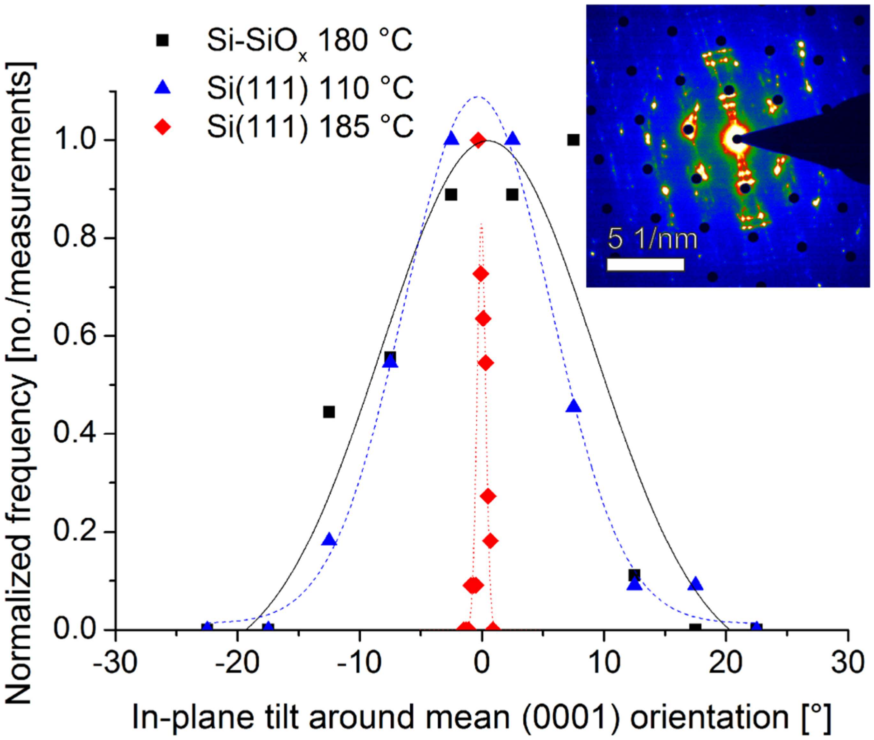

Fig. 3.40: Analysis of NBD series data of 20-40 diffraction patterns each across 2 µm of the GST thin films from three samples deposited onto Si(111) and SiO$_x$ at elevated temperatures. The tilt misorientation of the GST(0001) planes against the substrate Si[110] zone axis is evaluated via normalized frequency statistics with a binning of 5° for the textured samples (black and blue data points) and 0.2° for the epitaxial sample (red data points). Solid lines represent Gaussian normal distribution fit curves. Inset in the top-right shows a SAED pattern from the GST thin film deposited onto Si(111) at 185 °C, with the substrate contributions removed (black spots) and in false colours for improved visibility.

The GST lattice close to the interface can be described to possess a cubic character within the first few nanometres, although the size of this region is variable due to the grain alignment influenced by the local roughness features and occasional vacancy layers intersecting from above. The same region of the lattice in the textured sample deposited onto cleaned Si(111) at 110 °C reveals the formation of a distinct surface passivation monolayer (see Figure 3.42). The exact composition of the surface passivation layer is unclear, while the strong intensity in HAADF contrast indicates heavy, strong scattering species (Sb or Te). This aspect is discussed further below in the context of the epitaxial samples, since there it is possible to image both substrate (interface) and GST thin film simultaneously with atomic resolution.

In contrast, the GST grains in the textured sample can be misaligned towards the substrate by 13° or more, as was shown in the NBD evaluation, which also holds true for the rotation out of the image plane. Crucially, the passivation layer always resembles the Si(111) surface geometry, and the column spacing is thus 10% distorted from the expected spacing in a GST(0001) layer.

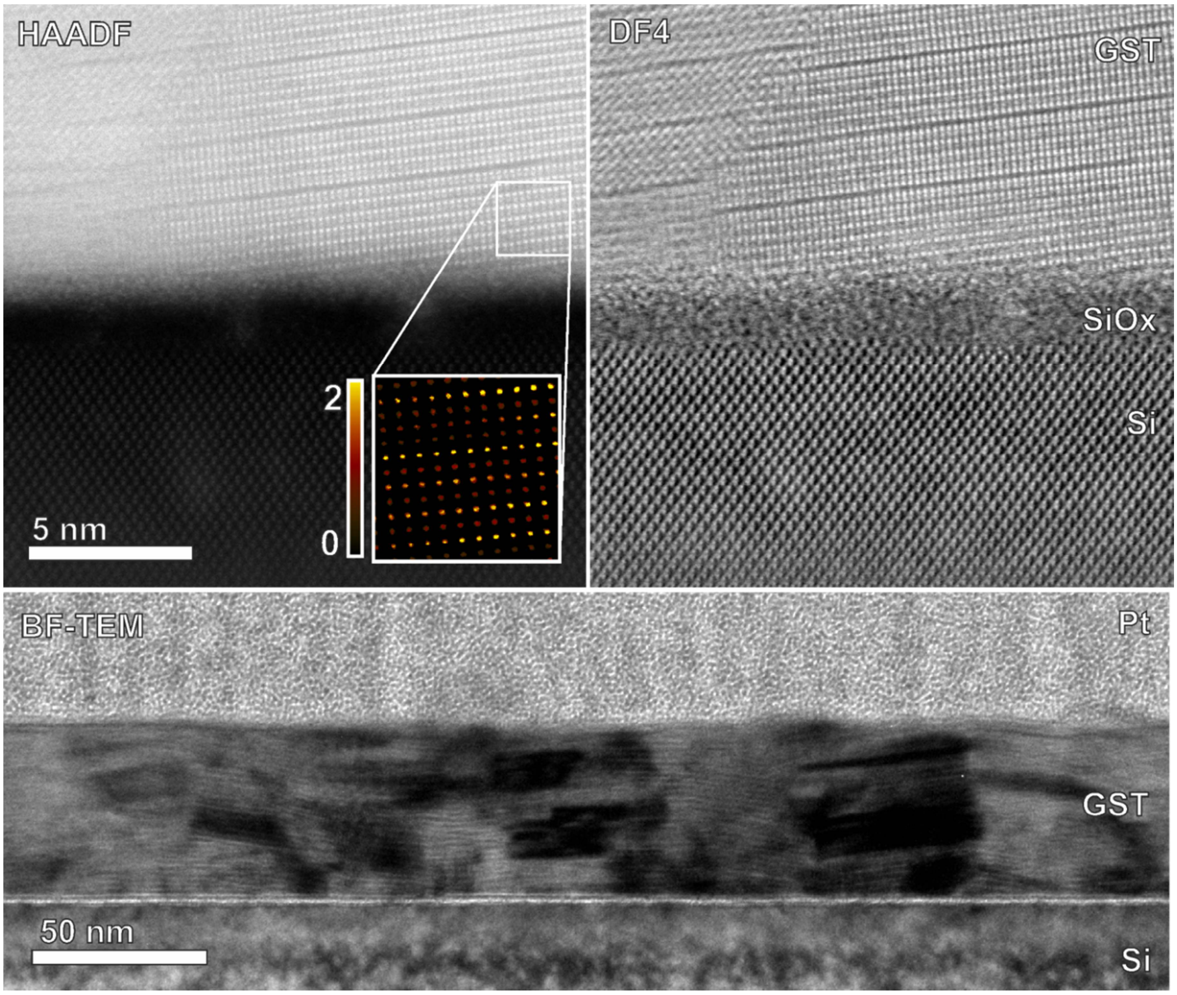

Fig. 3.41: HAADF- and ADF-STEM images of interface between Si(001) with native oxide layer and GST thin film, deposited at 180 °C. The GST lattice structure is oriented at a small tilt angle towards the substrate lattice, and the interface between oxide layer and GST exhibits some residual roughness (ca. 0.5 nm, although the amorphous structure of the interface cannot be well resolved). Notably, while the lattice within the bulk of the GST layer is trigonal as evidenced by the vacancy layering, these are not always present in the immediate vicinity (first 2 nm) of the interface. Inset shows a combined intensity ratio map from a selected area, with bright (yellow) dots indicating Ge-rich positions in the mixed sublattice and less intense (red) dots indicating the Te sublattice. Below is shown a BF-TEM overview image of the GST thin film, exhibiting textured columnar grains of 30 - 40 nm widths. The dark stripes relate to diffraction contrast from coherent scattering out of the zero-beam due to twin domains within individual grains.

Due to the residual minimal surface roughness from monolayer steps in the Si substrate, contrast features at the interface at realistic projection depth (depth of field and influence of sample thickness) often appear diffuse. Nevertheless it is clear that the orientation of the passivation layer and the grain texture above are somewhat decoupled, and the first three layers above the passivation layer can be disordered.

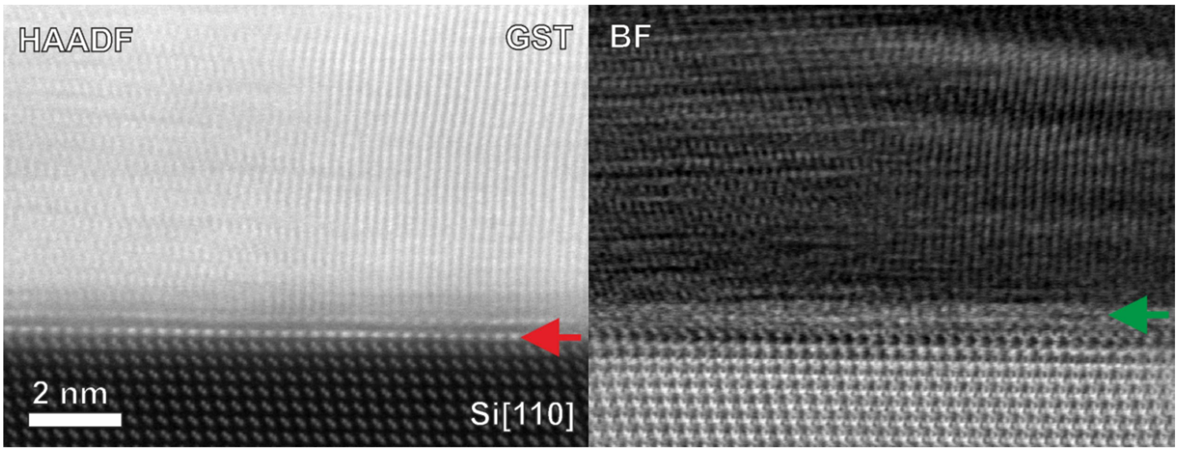

Fig. 3.42: HAADF-STEM image of interface between cleaned Si(111) in [110] zone axis and a textured GST layer, deposited at 110 °C. The red arrow marks the surface passivation layer which matches the Si(111) plane symmetry, while the GST grain(s) above are misaligned. In addition, there is some indication of a vacancy gap and second in-zone axis layer above the passivation layer. The BF-STEM (0 – 19.5 mrad) image on the right reveals a disordered zone (green arrow) above the passivation layer (dark spots in coherent phase contrast), although the exact defocus relevant for BF-contrast is not well-defined (within a range of ± 10 nm) and the grey intermediate area may also partially construe a defocus artefact.

In this context, it can be speculated that the textured growth of GST on Si(111) occurs in a similar process as the textured growth on the amorphous SiO_x interface, despite the formation of the passivation layer. The lattice structure within the GST thin films of both textured trigonal samples is dominated by aforementioned twin domains as well as highly characteristic stacking transition disorder. A BF-TEM overview image of the GST thin film deposited at 110 °C on Si(111) is shown in Figure 3.43, and a combined HAADF-STEM / GPA image of a single columnar grain in zone axis orientation is shown in Figure 3.44. The 60° rotation twin domains were already briefly introduced in the first chapter (Figure 1.10) and occasionally seen in the post-deposition annealed trigonal samples. These can be mapped in the local phase-amplitude image of the GPA (right side of Figure 3.44), by evaluating the Fourier component equivalent to the $(\bar{1}13) \triangleq (\bar{1}103)$ plane normal. As can be seen, twin domains are much more common in the columnar grains, occupying up to 30% of the lattice volume. In addition, the stacking disorder of the vacancy layers is similarly more pronounced, with an average of 50% of stacking units in the 5-fold Te sequence, while the remaining 50% are split between 4-fold Te and 6-fold Te, effectively preserving the Ge-deficient stoichiometry when again assuming a structure-stoichiometry relationship. When observing the grain shape, lattice orientation and arrangement of twin domains, in combination with the interface structure, it can be concluded that the twin domains serve to approximately accommodate the offset between growth direction and grain boundary orientation. They are thus a consequence of the texture tilt distribution.

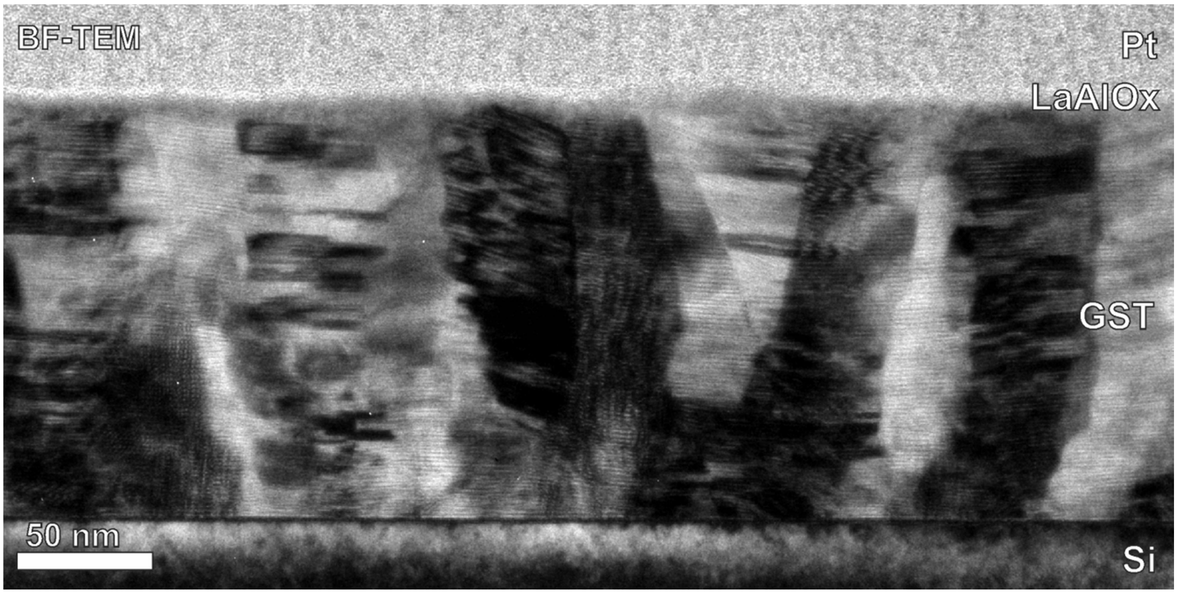

Fig. 3.43: BF-TEM image of textured columnar grain growth, deposited onto cleaned Si(111) at 110 °C. Columnar grains are slightly narrower (25 – 30 nm at the base) than in the sample deposited onto amorphous SiO_x, yet extend over the entire layer.

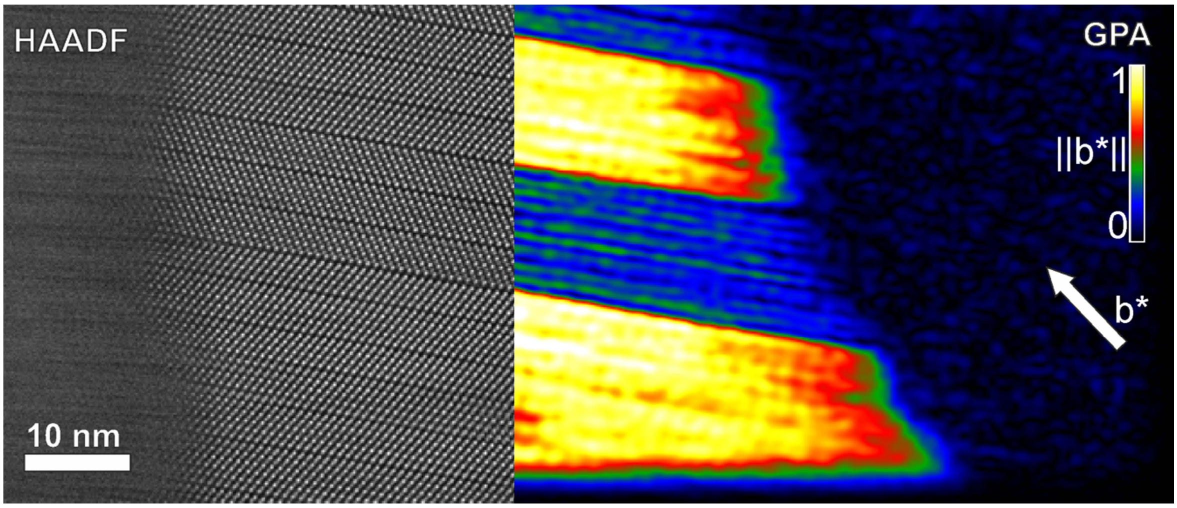

Fig. 3.44: HAADF-STEM image of columnar grain in Figure 3.43, in zone axis (left) and resulting local phase-amplitude map of the GPA, overlaid on the right half of the image. The HAADF-STEM image can be found at full resolution in Appendix C.12.

This indicates that the growth process possesses a Stranski-Krastanov type character[216] in the lower range of the investigated temperature regime. The formation of the initial passivation layer is followed by 1-3 disordered monolayers leading into the crystalline growth of cubic islands with orientation coincidental to the underlying sub-nanometre roughness topography (see Figure 3.45). While there is an occasional indication of a vacancy gap above the passivation layer, the contrast at the interface is often difficult to resolve, and it is likely that this feature forms only after the growth onset of the crystalline layer.

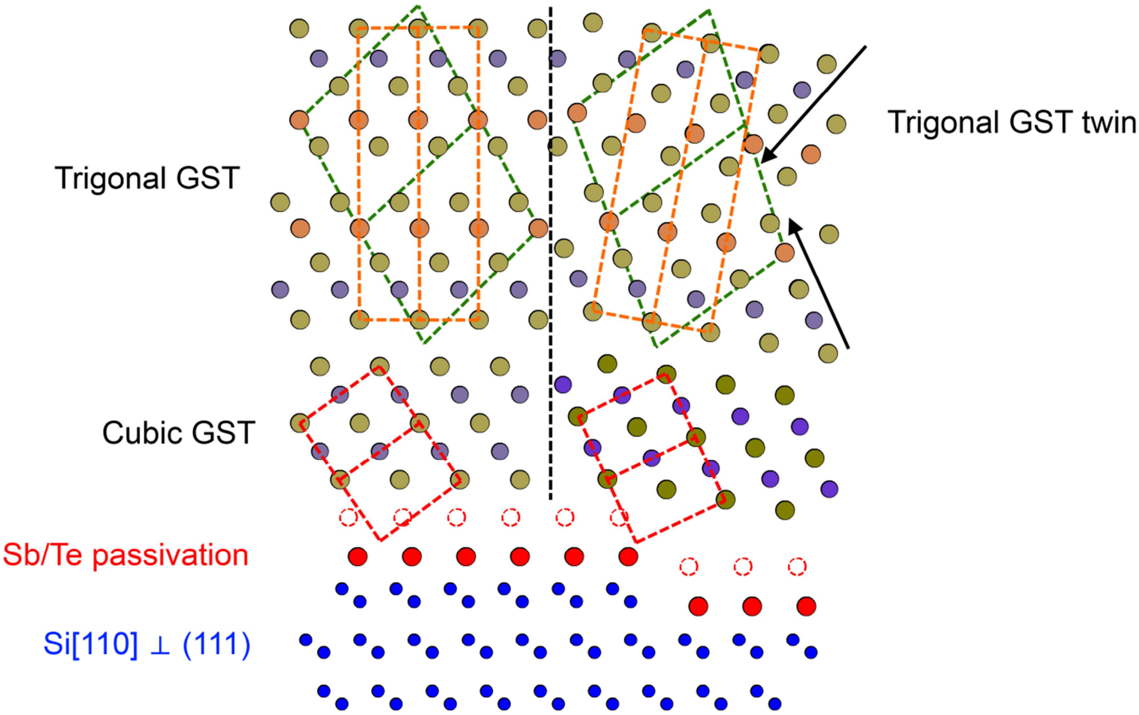

Fig. 3.45: Model of structural evolution during deposition of GST on cleaned Si(111) at 110 °C. The Si substrate (blue circles) is covered by a passivation layer (solid red circles) and a disordered zone or vacancy gap (dashed red circles). The orientation of the cubic lattice (unit cell indicated by dashed red lines) conforms to the local surface topography. Rotational reorientations within the interface plane have been excluded in this schematic drawing. Dashed black line indicates a 10° tilt grain boundary in the vicinity of a substrate surface step. Lattice subsequently reorders into the trigonal phase (unit cell indicated by dashed orange lines), the original cubic unit cell thus undergoing a rhombohedral distortion (indicated by dashed green lines, unit cell size expanded to encompass one trigonal unit cell). The difference in initial grain orientation and thus the direction of the rhombohedral distortion results in biaxial lattice strain and thus the local formation of rotation twins (solid black arrows).

The islands form the bases of the columnar grains, which continue to grow upwards without significant coalescence (i.e. the diameter of the grains changes very little from the base to the top) since the small-angle grain boundaries act as diffusion barriers. Meanwhile, the bulk mobility and total deposition time is sufficient to allow the phase transformation towards the stable trigonal phase within individual grains, and twins are formed to accommodate the lattice strain that occurs when two adjacent misaligned cubic regions of the lattice undergo the rhombohedral distortion during transformation to the trigonal phase. While much of the above is based on speculation from the available post-deposition data, the resulting grain morphology largely supports the two-step process of initial cubic growth and subsequent trigonal lattice formation. Since recently an in-situ RHEED system inside the PLD chamber has become available, future work will presumably include a closer examination of the initial growth process at comparable temperatures. Similar to the increased occurrence of twins as well as the distribution of 4-, 5- and 6-Te stacking units, the lattice within the textured grains also exhibits an increased amount of stacking defects that were already briefly introduced in the previous chapter. These have recently become of prominent interest in the switching mechanism of superlattices[100, 217], and as such warrant a detailed description.

High-resolution HAADF-STEM views of the trigonal lattice and stacking defects are shown in Figure 3.46, in the $[11\bar{2}0]$ and $[01\bar{1}0]$ projection from comparable, albeit not identical, regions of the lattice within the bulk of the thin film. The observed width of the stacking transitions (constrained by the depth of focus) is variable, indicating that the defect line may run at a variety of angles towards the image plane. In select cases however, the stacking defect in $[11\bar{2}0]$ projection can be seen to extend over only 2-3 adjacent Te positions along the vacancy gap, and it is likely that many of the observed defects share a structural similarity.

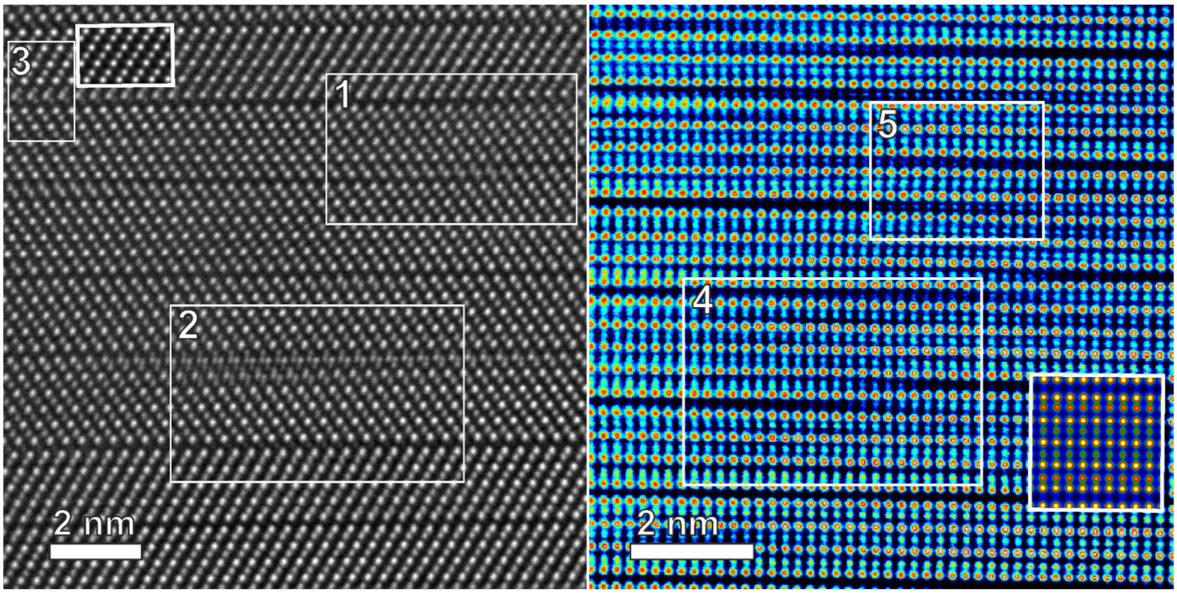

Fig. 3.46: HAADF-STEM images of defect structures in trigonal GST, in $[11\bar{2}0]$ projection (left) and 60° rotation variants thereof; and in $[01\bar{1}0]$ projection (right), colourized on a temperature scale. Insets in the image show simulated HAADF-STEM images of undistorted GST124 (left) and GST225 (right) trigonal structures in the corresponding lattice projections. Numbered boxes mark specific instances of stacking disorder: (1) stacking transition with the defect line close to parallel to the $[11\bar{2}0]$ projection vector; (2) stacking transition with defect line along the $[\bar{1}2\bar{1}0]$ direction, i.e. at a 60° angle to the image plane, including a second partial correlated stacking transition below; (3) stacking transition with defect line along $[\bar{1}2\bar{1}0]$ direction of the lower building block with a 60° twinned building block above; (4) stacking transition along $[11\bar{2}0]$ as seen in (1), but rotated by 30° into the $[01\bar{1}0]$ projection; (5) bilayer stacking transition with defect line along $[11\bar{2}0]$, viewed in $[01\bar{1}0]$ projection, wherein the vacancy gap skips over one mixed layer of the lattice.

In addition, due to the 3-fold symmetry of the lattice and the presence of 60° rotation twins, defects of the same type yet at a different angle towards the projection plane, or between two stacking units of different twin orientation, can result in the various observed contrast features. An idealized model of the stacking defect running exactly along the $[11\bar{2}0]$ view direction was thus proposed, as shown in Figure 3.47. It must be noted that, while the majority of the stacking disorder can be explained by the specific stacking transitions modelled here, exceptions are also possible. In particular, bilayer stacking transitions as marked by (5) in Figure 3.46 are also found. In the single-layer transitions the majority of the lattice distortion occurs in the central Te layer, the Sb-rich adjacent layer switches sides thus creating the motion of the vacancy gap, and the next-nearest mixed layers require chemical re-ordering from Sb-rich to Ge-rich and vice versa in order to reconstruct the preferred stoichiometric stacking sequence. In the bilayer stacking transition, the central layer is a Sb-rich layer which switches orientation of the short Sb-Te bonds, while the Te layers remain relatively static. The next- adjacent mixed (Ge-rich) layers are depleted or filled to create the motion of the vacancy gap, while subsequently the second-nearest mixed layers are required to undergo chemical reordering in order to reconstruct the appropriate stacking sequence. An example of a simulated HAADF-STEM image of the proposed defect structure using undistorted B_{iso} parameters is shown in Appendix C.11.

The interplay between stacking sequence and defect structures is thus complex, but the underlying driving forces can be surmised to be an entropic component, the strain component in [0001] direction, and the preferred chemical ordering of the GST124, GST225 and GST326 phases. It is also noteworthy that in some portions of the images, taken from the textured sample deposited at 110 °C, building blocks adjacent stacking defects may possess more than 6 Te layers. Due to the smaller displacement of the mixed sublattice positions in the central parts of these blocks, as well as the less pronounced chemical ordering of the sublattice sites, these can be viewed as partially cubic regions of the lattice. As the GST phases with larger numbers of Te layers between vacancy gaps are those with a higher Ge content, and the sample itself is slightly Ge deficient, it seems unlikely that the larger stacking units can be correlated to a stoichiometric phase. Since the lattice in the sample in question exhibited the largest amount of structural disorder of all observed trigonal samples, these occasional anomalous regions may also be seen as aberrations, since they reconfigure to the preferred 4-, 5- and 6-Te stacking units via additional stacking transitions.

In contrast, the stoichiometric correct stacking units correlate well with specific models of the appropriate GST phases when comparing the HAADF-STEM intensities within one block with the simulated scattering intensities. This is shown in Figures 3.48-3.50 and Table VII. The larger deviation, and corresponding lower cross-correlation coefficient, between 4-Te building block and GST124 models can be traced to the deviation of the right-most Te peak due to its vicinity to a stacking transition defect (marked by (3) in Figure 3.46).

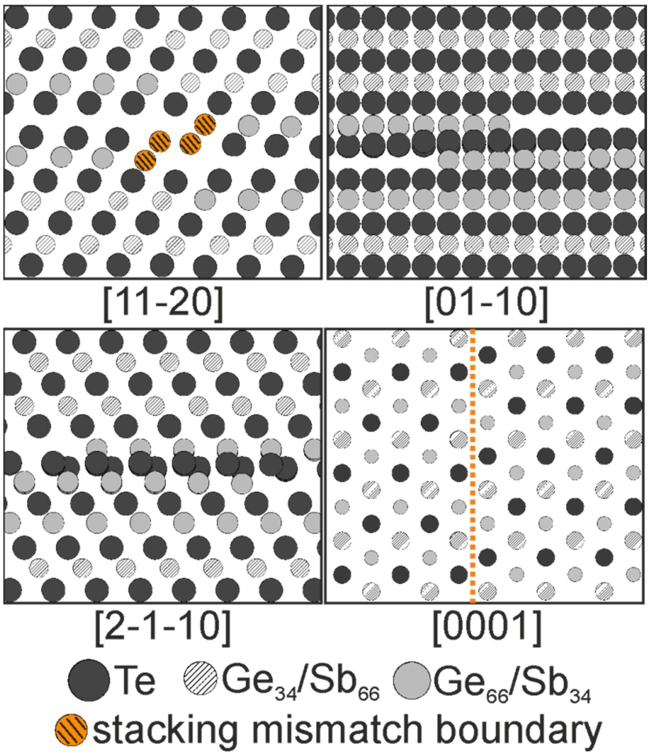

Fig. 3.47: Idealized model of stacking defect (stacking mismatch boundary) as seen in Figure 3.46. The top-down view of the [0001] projection is a cut-out of three layers (one Te and two mixed Sb/Ge) involved in the defect structure. The offset in the $[11\bar{2}0]$ direction seen in the [0001] projection (i.e. along the dashed orange line) is speculative since the structure is experimentally unavailable. It is based on the assumption that all Sb species in the defect retain a six-fold $SbTe_6$ coordination environment, with one bond across the defect boundary stretched to 0.42 nm.

Nevertheless, the overall trend of the undistorted peak intensities favours the match with the structure model by Karpinsky, due to the larger experimentally observed jump in intensity between B1 and B2 mixed sites as well as a better match with the B2 (outer, Sb-rich) site position. Referencing Table VII, it can be seen that the difference in site occupancies between the two models is small, while the B_{iso} factors are much larger in the Matsunaga model (since they were measured at 873 K) and appear inverted, i.e. Matsunaga notes a larger temperature factor for the Sb-rich sites than for the Ge-rich sites. While e.g. Gao et. al.[218] have shown that for a range of materials the temperature dependence of the Debye-Waller factor well above the Debye temperature can be modelled by a fourth-degree polynomial parameterization for each site, an inversion of relative factors for two distinct positions in the same sublattice would still be surprising. Since such regression parameters are not known for the specific materials, and in fact the temperature dependence may deviate from the cited elemental or zinc-blende materials, the GST124 model by Yamada is of questionable usefulness for quantitative image simulation at standard TEM experiment conditions.

Tab. VII: Parameters for HAADF-STEM simulation of profiles shown in Fig. 3.48-3.50, and comparison with experimental data. Sources for site positions, occupancies at the mixed Ge/Sb sites and corresponding temperature factors are, as previously introduced: [53, 208] for 4-Te stacking, [49, 52] for 5-Te stacking and [35, 54] for 6-Te stacking. The cross-correlation (Cc-) coefficients are calculated between experimental and simulated profiles.

Stacking	Source	Ge:Sb ratio [at. fraction]	B_{iso} [Å²]	Cc-coefficient (Pearson)
4-Te	Matsunaga	B1: 0.49(3):0.50(7)	4.08(9)	0.924
		B2: 0.25(3):0.74(7)	5.23(8)	
4-Te	Karpinsky	B1: 0.43(0):0.57(0)	1.389(6)	0.912
		B2: 0.26(0):0.72(0)	1.105(4)	
5-Te	Matsunaga	B1: 0.55(9):0.44(1)	1.800(2)	0.929
		B2: 0.44(1):0.55(9)	1.871(3)	
5-Te	Urban	B1: 0.60(4):0.36(2)	2.163(4)	0.976
		B2: 0.33(7):0.66(4)	1.713(4)	
6-Te	Matsunaga	B1: 0.76(9):0.23(1)	1.271(0)	0.972
		B2: 0.75(4):0.24(6)	1.207(0)	
		B3: 0.32(0):0.63(8)	0.821(3)	
6-Te	Schneider	B1: 0.73(0):0.27(0)	2.684(5)	0.995
		B2: 0.76(9):0.23(1)	2.566(1)	
		B3: 0.55(2):0.44(9)	2.368(7)	

The match between model and experiment is significantly improved for the 5-Te and 6-Te building blocks, as is reflected in the Cc-coefficients closer to unity. The 5-Te profile comparison favours the GST225 model by Urban et. al., since it correctly predicts the uniform peak intensity of the Te peaks as well as the more pronounced contrast between B1 and B2 sites. For the 6-Te building block, the match to the two GST326 models selected from literature is roughly equal, with a slight favour towards the model by Schneider et. al. It must be noted that, as indicated by the error bars, peak intensities in particular in the central mixed site (B1) of the experimental 6-Te measurement can vary significantly, indicating that a small change in Sb concentration on the less distorted sites has a large influence on the scattering intensity. In addition, the model by Matsunaga of GST326 was based on X-ray diffraction data recorded at 90 K, while other measurements are taken at approximately room temperature (300 K). As previously noted, the Debye temperature of GST compounds is typically larger than 90 K [29, 219-221], and thus the vibrational properties may change significantly compared to RT measurements or under the influence of the electron beam.

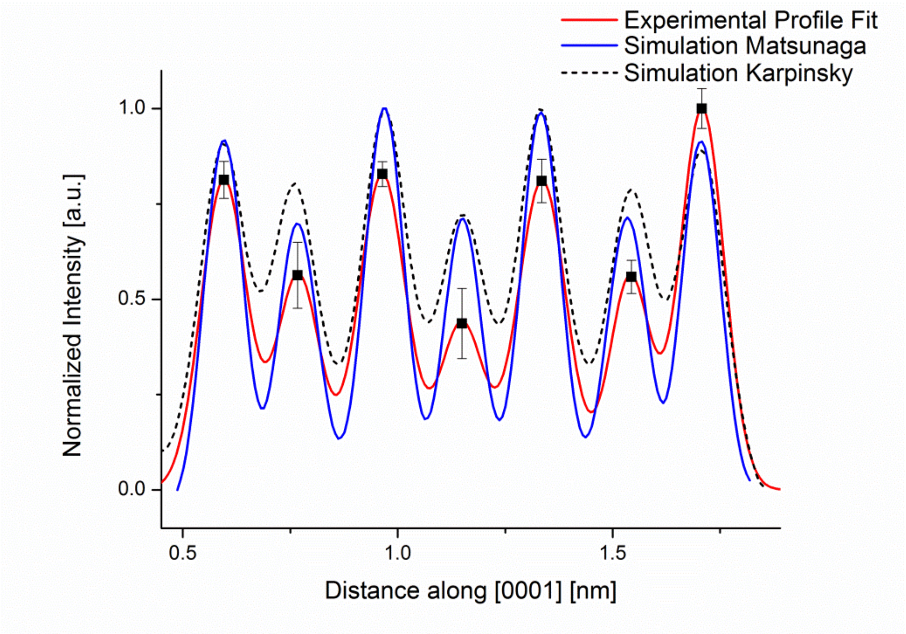

Fig. 3.48: Comparison between experimental intensity line profiles extracted from 4-Te building block in Figure 3.46 and from simulated HAADF-STEM images according to Table VII. Parameter set for all (absorptive potential multislice) simulations was: C2 = 25 mrad, detector = 80 – 200 mrad, Cs = 200 nm, C5 = 0.4 mm, sample thickness of 30 nm, defocus = -4 nm. While the profiles show the average (laterally integrated) intensity over at least 15 adjacent atomic columns, after constant minimum background subtraction, the error bars in the experimental curve represent the standard deviation of peak intensity measurements from all individual atomic columns.

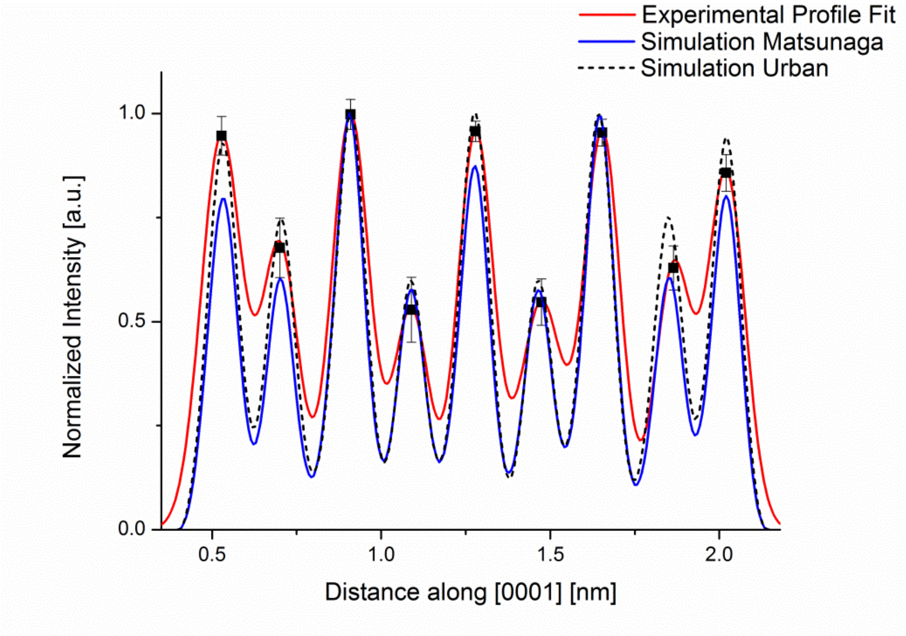

Fig. 3.49: Comparison between experimental and simulated intensities similar to Figure 3.48, for a selected undistorted 5-Te building block in Figure 3.46.

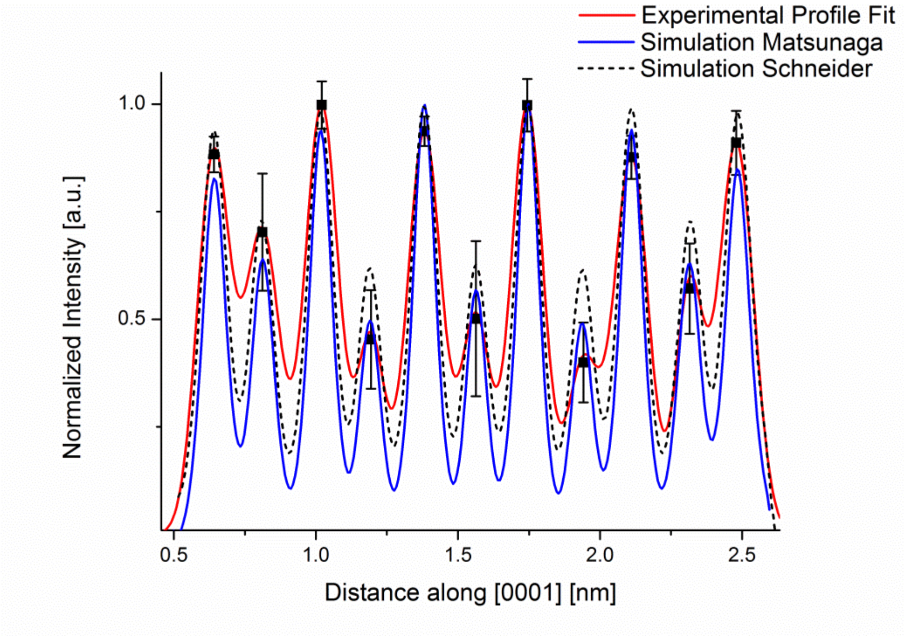

Fig. 3.50: Comparison between experimental and simulated intensities as in Figure 3.48, for a selected 6-Te building block in Figure 3.46.

While due to previously stated arguments the comparison between simulation and experiment can only be considered semi-quantitative, the experimental data clearly reveals that building blocks of 4-, 5- or 6-Te stacking correlate with the chemical ordering of the mixed sublattice. This is in particular notable since the observed textured sample deposited at a substrate temperature of 110 °C exhibits this ordering effect in an otherwise very heterogeneous lattice with a large number of structural defects. In general, a distance of few atomic columns from a structural defect is sufficient for the lattice to reconfigure into the stacking-appropriate chemical order.

An increase in the deposition temperature results in a significant improvement in crystalline tilt distribution towards the cleaned substrate, as was already indicated by the NBD evaluation. While the uniformity of the in-plane rotation also improves, the oriented layer structure at intermediate deposition temperatures is not as rigidly connected to the substrate orientation as would be expected for a conventional epitaxial growth mode. Figure 3.51 shows HAADF-STEM and HRTEM images of the GST thin film deposited at 170 °C, in Si[110] zone axis orientation. As seen in the HAADF-STEM image, the substrate – thin film interface exhibits a single surface passivation layer and a continuous vacancy gap, immediately followed by building blocks of trigonal GST above that are somewhat decoupled from the substrate surface symmetry. While some regions appear close to $[01\bar{1}0]$ zone axis, others are visibly rotated out of the image plane, and the transition between either domains appears smooth. The rotation misalignment out of the interface plane can also be seen in the Fourier transformed of the HRTEM image, in the prominence of the $[2\ \bar{4}\ 2\ l]$ and $[\bar{2}4\ \bar{2}\ l]$ periodic maxima. In the larger field of view of the HRTEM image it can be speculated that domains of different rotation alignment are

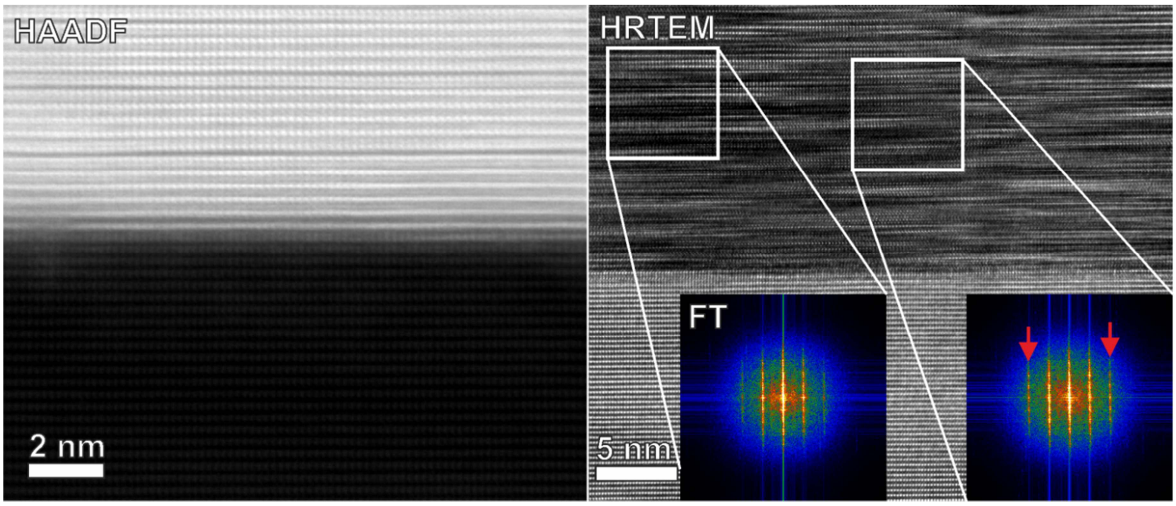

Fig. 3.51: HAADF-STEM and HRTEM (20 nm nominal defocus) images of interface between Si(111) substrate in $[2\bar{1}\bar{1}]$ zone axis and GST thin film deposited at 185 °C. The HAADF-STEM image clearly shows the surface passivation layer, while individual atomic columns are not well resolved due to the thickness of the sample (50 nm) and the close vicinity of columns in the lattice projection. Fourier transformed diffractograms from selected areas of the HRTEM image illustrate the local variance of rotation out of the interface plane, however differences (marked by red arrows) are generally small and domain boundaries appear smooth. The HRTEM image can be found at full resolution in Appendix C.13.

oriented approximately parallel to the growth direction, similar to the grain boundaries in the textured sample. While the HRTEM image was adjusted close to minimum contrast defocus at the amorphous edge (0.4 * Scherzer focus, with Scherzer focus ≈ 48 nm for the instrument in use), the true defocus at the actual interface position is unknown. Due to the significant (uncorrected) spherical aberration, contrast features cannot be easily interpreted as atomic layer positions as a result of the phase-contrast delocalization. Nevertheless the observed features indicate that a continuous distribution of in-plane rotations is present.

A slight increase in the deposition temperature to 185 °C does not significantly change the morphology of the sample, although as indicated by the EDX results the relative Ge content in the thin film can be interpolated to deviate from the nominal composition as the deposition temperature approaches 200 °C. A gradual further increase of the lattice orientation uniformity allows for a closer inspection of interface structure and GST lattice. Figure 3.52 shows a HAADF-STEM image of the interface region, as well as two background subtracted profiles across the interface. The profiles are affected by noise due to the jump in contrast/background ratio between substrate and layer, and the GST layer orientation was still not ideally uniform. The background fitting in the GST region, from local minima between peaks, thus may overestimate the background contribution and the comparison of intensities should not be viewed as quantitative. Nevertheless it can be seen both in the image as well as the profiles from raw data that the scattering intensity from the passivation layer systematically exceeds the mixed Ge/Sb layers in the GST thin film.

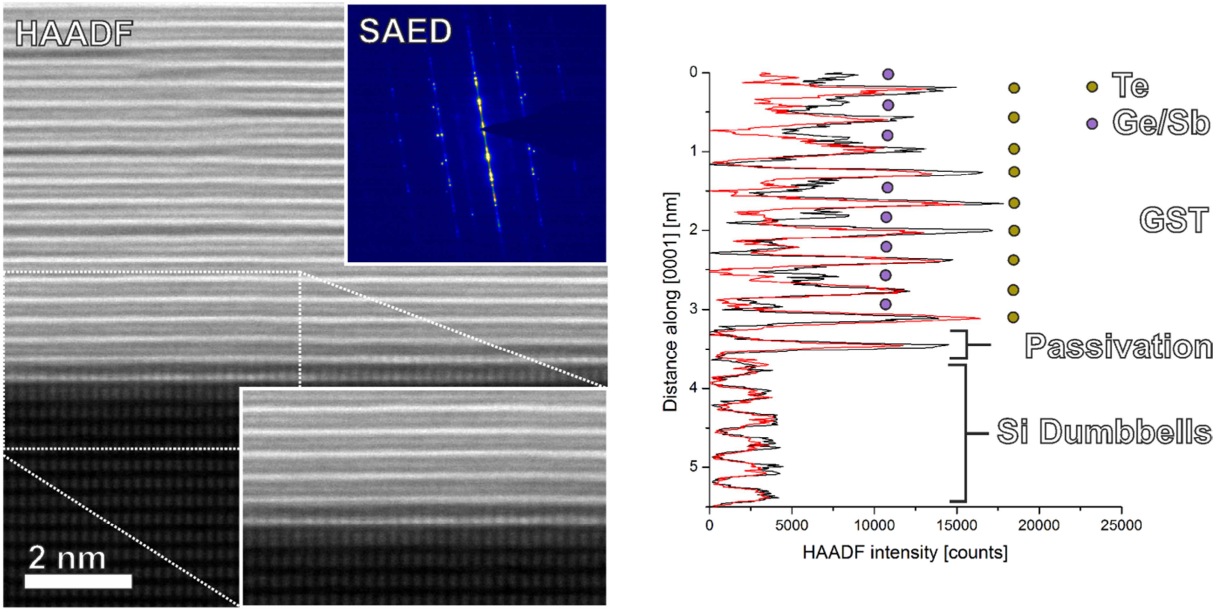

Fig. 3.52: HAADF-STEM view (left) of interface between GST, deposited at 185 °C substrate temperature, and Si(111) in $[2\bar{1}\bar{1}]$ projection. While GST layers are only visible as lines due to the rotation misalignment, individual columns in the passivation layer can be discerned. The electron diffraction information (SAED in false colours, inset) indicates that the tilt alignment of the layers is very uniform across the entire (ca. 100 nm diameter) aperture, and the 10% misfit between substrate and GST is visible in the doubling of diffraction spots in the direction perpendicular to the interface. Profiles on the right show two HAADF intensity line plots (10 pixel integration width) along planes perpendicular to the interface, extracted from a separate image of slightly improved GST layer alignment and background subtracted.

This gives another strong indication that the passivation layer predominantly consists of Te species. The significant variance in peak intensities within the layer implies either local distortion, an inhomogeneous mix of Sb and Te, or both, and since accurate temperature factors are lacking HAADF-STEM images of the structure cannot yet be reliably simulated in order to verify.

Meanwhile, a closer view of the lattice structure within the GST thin film (Figure 3.53) reveals that the previously described stacking defects and twin domains remain present. Stacking transitions in particular are sometimes correlated across multiple building blocks, meaning that multiple transitions across adjacent building blocks often proceed in the same direction. While excess periodic intensity within undistorted vacancy gaps can sometimes be found, the continuous overlap between regions of slightly altered rotation within the interface plane results in diffuse contrast transitions as well as overlapping periodic structures in the projection. The domain boundaries are not clearly defined by discontinuous grain interfaces, and twin boundaries can occur within individual building blocks, while a qualitative comparison between NBD patterns and simulated diffraction images indicates rotation realignment between domains of approximately 2°.

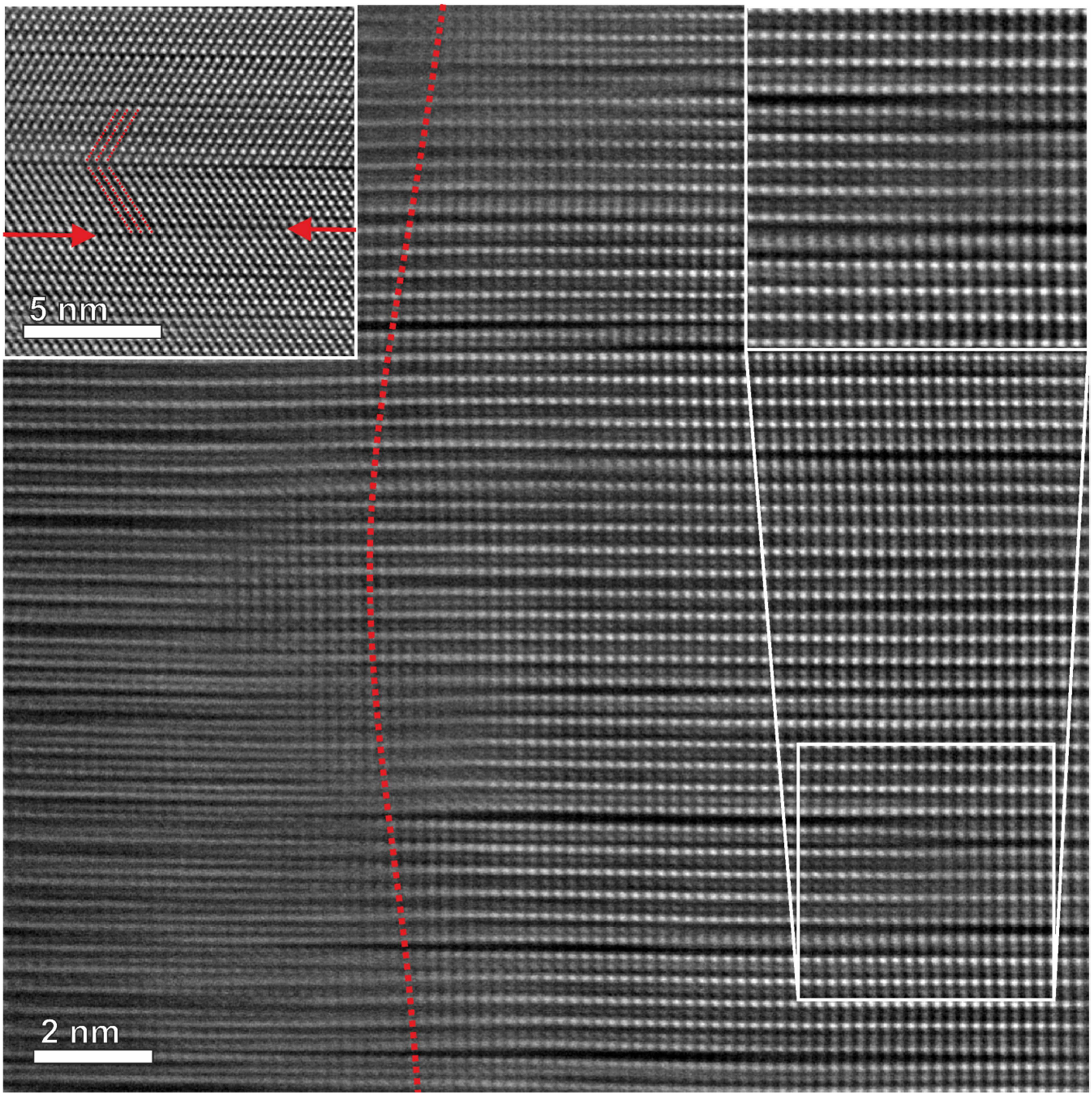

Fig. 3.53: HAADF-STEM view of lattice within the GST layer deposited at 185 °C, close to $[01\bar{1}0]$ projection. The density of stacking defects (inset top right) has not been significantly reduced compared to the textured sample deposited at 110 °C, and twin domains remain present throughout the thin film (inset top left). The domain boundary is associated with a strong local distortion of the layers, yet does not appear discontinuous.

It would thus be intuitive that, as the crystalline growth approaches the layered growth mode with increasing substrate temperature, the in-plane (interface) misfit strain due to symmetry mismatch and difference in thermal expansion coefficients gains prominence in the driving force for defect formation. It must however be emphasized that the relation between passivation layer symmetry and GST thin film orientation across the vacancy gap still appears flexible, and rotation domains may as well run along vacancy layers (i.e. parallel to the interface). Reports on a strictly preferred interface symmetry[113, 214] can only be partially supported by these results.

When the deposition temperature is further increased to 280 °C, the Ge content in the thin films is radically reduced, and the deposition rate evaluated from the final film thickness falls off. At the same time, the experiment still presents useful data since the Ge content can potentially be adjusted via the target composition, the GST124 composition is also known for phase-change behaviour, and the resulting thin films are highly oriented along GST(0001)||Si(111), GST[$1\bar{1}03$]||Si[001]. A HAADF-STEM view of the GST thin film is shown in Figure 3.54. Twin domains have virtually disappeared, which indicates that the lattice experienced less in-plane shear stress compared to the previous samples. The stacking sequence is dominated by 4-Te building blocks. Since the measured Ge content lies even slightly below the GST124 stoichiometry, the occasional appearance of 3-Te units (Sb_2Te_3 blocks) is logically consistent. Furthermore, stacking defects extend laterally over broader distances, and since these typically involve the movement of a Sb-rich layer, some regions of the lattice may consist of Sb_2Te_3 units between two Sb-rich defective bilayers. At the same time, differences in column spacing between passivation layer (0.33(0) nm) and first Te layer within the building block above (0.36(6) nm) persist. The structure thus indicates that the Van-der-Waals epitaxy growth regime was reached[222] (see also Figure 3.55), i.e. the thin film is highly oriented without in-plane misfit strain.

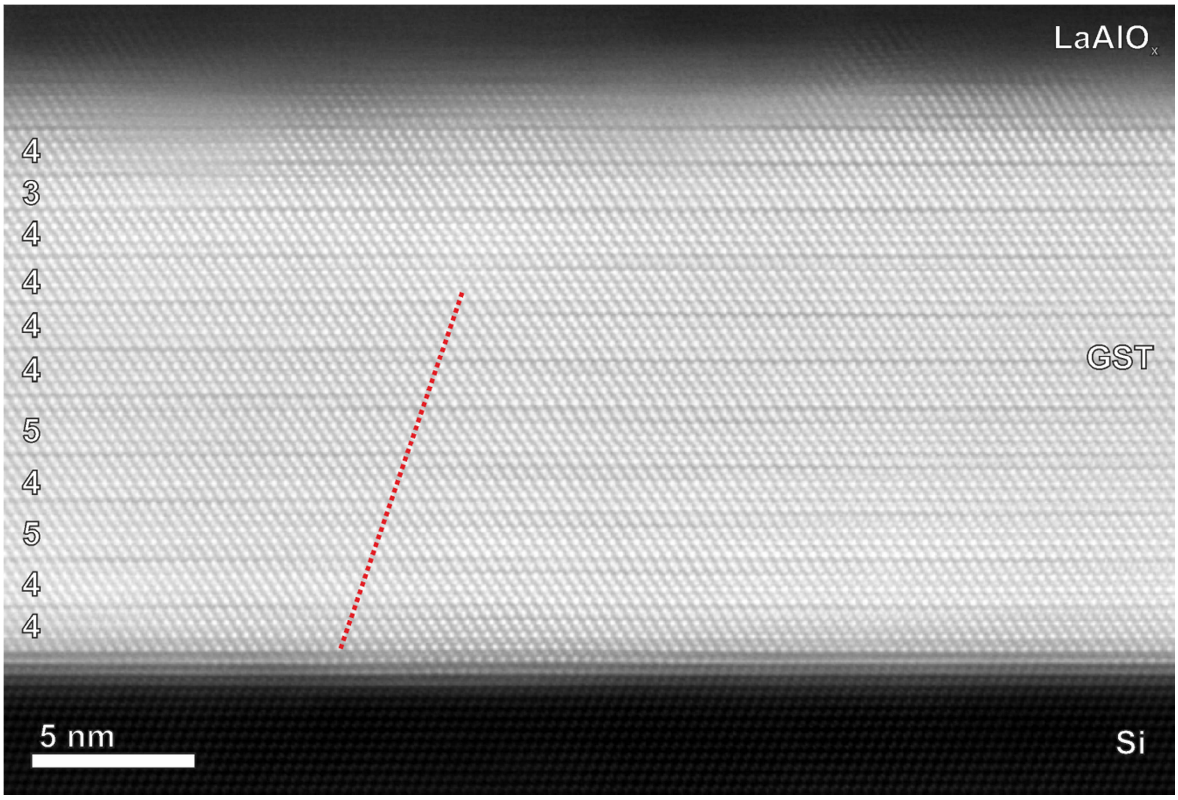

Fig.3.54: HAADF-STEM view of the GST thin film deposited at 280 °C onto Si(111), in Si[110] zone axis orientation. The thin film composition (from STEM-EDX) is approximately $Ge_{10}Sb_{33}Te_{57}$. The dashed red line indicates correlated stacking defects originating from a surface step in the silicon substrate topography. The stacking sequence is dominated by 4-Te building blocks, with occasional 5-Te (GST225) and 3-Te (Sb_2Te_3) building blocks also present.

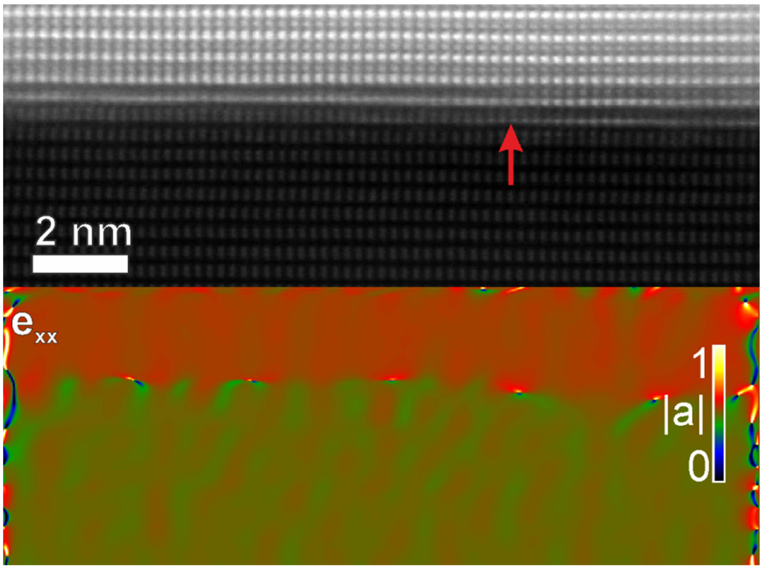

Fig. 3.55: Van-der-Waals epitaxy interface between passivation layer and GST thin film in GST[$01\bar{1}0$] projection, deposited at 185 °C. HAADF-STEM image (top), with red arrow marking a step in the surface topography, and in-plain strain map from GPA analysis (bottom), illustrating the strain-free discontinuous transition between substrate and layer.

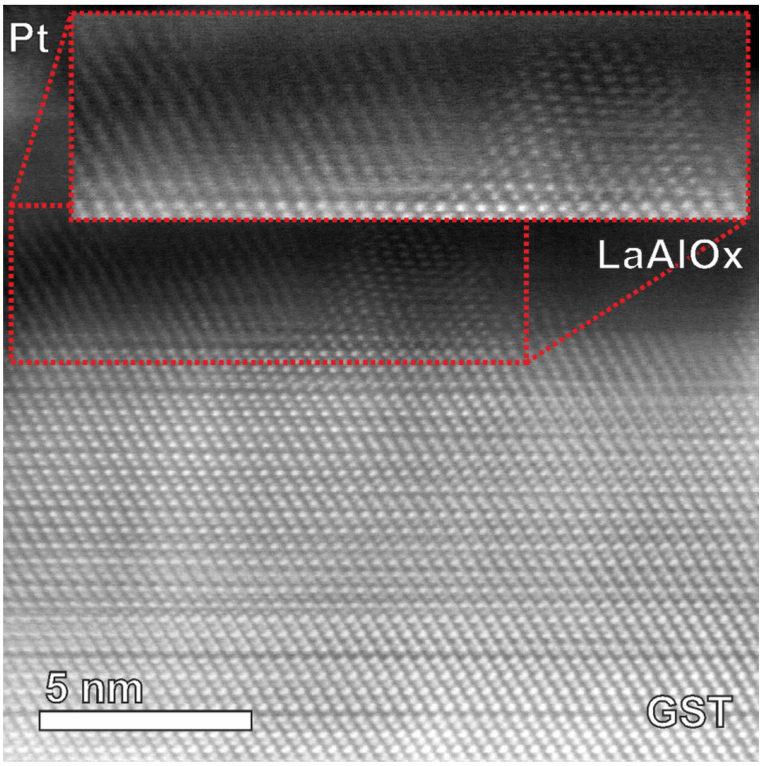

Fig. 3.56: HAADF-STEM image of surface region of the sample deposited at 280 °C. The dashed box highlights crystalline contrast in the disordered growth zone, although the structure may have undergone changes during the cooldown process and sample preparation steps.

While the expected Te GST124$[11\bar{2}0]$ column spacing in the (0001) planes at room temperature would measure 0.3699 nm, and column spacings throughout the thin film measure 0.36(7) nm, the general inhomogeneity of the lattice and the limitations to the precision of the calibration would allow for such a pm-scale deviation. It is thus suggested that the layer is either completely relaxed or is stressed due to the difference in thermal expansion (2.6^{-6} °C^{-1} for Si vs. 5.02^{-5} °C^{-1} for GST124[208], which is likely anisotropic[18]). Since the layer morphology is not perfectly orientated at all times, but rather domains of very small in-plane rotation (< 2°) persist, thermal stresses can be accommodated within domain boundaries with little strain within the domains. At the very surface of the sample much of the HAADF-STEM contrast is lost due to the topography, yet occasional cubic regions free of vacancy layers, no thicker than 3 nm, lend credence to above given arguments for the two-step crystalline growth from the metastable phase, even at very high temperatures (see Figure 3.56).

Since the substrate surface is not perfectly flat, steps in the surface Si(111) planes lead to c-axis strain in the GST layer, due the difference in spacing between Si(111) (0.314) planes and the offset of the GST(0001) Te planes (0.369 nm), as well as the required rearrangement of the preferred stacking order above. This results in the formation of correlated stacking defects, as indicated by the red dashed line in Figure 3.54. At the same time, only Sb-rich layers (i.e. those adjacent vacancy gaps) are involved in the stacking transitions. Defective stacking bilayers may thus contain some of the excess Sb in the sample, or stated inverse, excess Sb content may facilitate the formation of broader stacking transitions.

An EDX linescan across the substrate-thin film interface region in an epitaxial sample (see Appendix C.10) is not conclusive due to the limited (spatial and composition) resolution and accumulating beam damage. The epitaxial growth of Sb_2Te_3 and GeTe thin films was investigated by e.g. [223] and [224], in their particular case characterizing the MBE growth by in-situ RHEED measurements, XRD and HRTEM imaging. They concluded that a surface passivation of Si(111) $\left(\sqrt{3}\ \times\ \sqrt{3}\right)$ R30 Sb was favourable to the epitaxial growth of GST materials, although in the case of GeTe this surface-passivated growth reportedly competed with the simple GeTe(0001) 1×1 unreconstructed surface. Accompanying DFT calculations indicated that a Te-termination of the cubic structures was favourable at both interfaces[225] (at the surface and above the passivation layer), which is logically consistent with the vacancy layer formation mechanism and tentatively supported by the here presented experimental data from Ge-deficient GST. The tendency towards vacancy layer alignment on top of a surface passivation layer has been expanded upon[113] in what was termed “self-organized Van der Waals epitaxy” (sic) in order to propose depositing epitaxial thin films on a range of substrates, independent of structure. The selection criterion therein was based on the reactivity of the substrate with Sb and Te, and it was concluded that in the case of Sb_2Te_3 on Si, a Te surface passivation layer is expected to form. This runs somewhat counter to the previously mentioned literature on Sb surface passivation during MBE growth of Sb_2Te_3 on surface reconstructed Si(111). While the surface reconstruction may play a role in the selectivity, the here presented results on non-reconstructed Si(111) surfaces indicate either a pure Te or mixed Sb/Te passivation layer.

It was thus shown that GST thin films deposited at elevated temperatures exhibit distinct growth regimes. While oriented growth free of vacancy ordering can occur at low temperatures[114], samples in the here discussed temperature range always exhibit at least some degree of vacancy ordering. This can be traced to the relatively long deposition times as well as high bulk and surface mobilities, enhanced by sample surface heating during deposition. In the intermediate, textured growth regime, a two-step growth model via the metastable cubic phase was proposed that leads to columnar grain growth of the trigonal phase. While the texture tilt distribution depends on the sub-nm roughness of the substrate surface, the lattice symmetry of the substrate only plays a larger role in the layer orientation when the deposition temperature is further increased. Since at very high temperatures preferential desorption results in a significant change in deposition rate and resulting thin film composition, a narrow window between approximately 180 °C and 200 °C was thus identified which is optimal for the growth of oriented GST thin films.

A characteristic surface passivation layer, consisting of heavy Te species, was shown to form even in the textured growth regime. The passivation layer essentially presents an extension of the Si lattice that facilitates the formation of a vacancy gap above. The Van-der-Waals growth regime is reached when the vacancy layer is immediately followed by an oriented building block of the GST lattice. Lattice in-plane reorientations of approximately 2° organized in columnar domains confirm that, due to the significant misfit between substrate and thin film, a domain mismatch epitaxy model is preferred to a 1:1 surface reconstruction (see also reports of 2° and 7° rotation CSL domains of GeTe on Si(111)[223]) at intermediate deposition temperatures. At very high temperatures these rotations are diminished due to the increased cohesion of the 3- and 4-Te stacking units, and the thin film forms a single continuous epilayer. Under the assumption that the Te passivation layer exactly resembles the Si(111) symmetry, one can attempt to construct a CSL from the Si($\bar{1}10$) and GST225($\bar{1}100$) spacing within the interface plane (0.384 nm and 0.4226 nm, respectively). Following Ref. [226], and using ψ = 30° and 60° as high-symmetry rotation angles similar to [223] one can use these values to calculate a CSL rotation angle:

$$\cos\theta = \frac{a_{Si(-110)}}{a_{GST(-110)}} sin^2\Psi + \cos\Psi \sqrt{1 - \frac{{a_{Si(-110)}}^2}{{a_{GST(-110)}}^2} sin^2\Psi} \tag{3.2}$$

This results in CSL rotation angles of 2.9° and 8.1°, respectively, i.e. a 2.9° rotation CSL between Si($\bar{1}10$) and GST($\bar{1}100$) spacing within the interface plane matches the small rotation reorientations qualitatively determined by NBD well. Projections of 0°, 3° and 8° rotation CSL in the interface planes are shown in Appendix C.14 – C.16.

The trigonal lattice in all samples exhibits a large degree of stacking inhomogeneity, as well as characteristic stacking transition defect structures. By performing a semi-quantitative comparison between model structures and selected experimental results, it was concluded that specific stacking sequences correlate well with a preferred stoichiometry of the pseudo-binary GST system, while on the other hand the shortcomings in some models regarding the temperature factors were highlighted. Lastly, the majority of the observed stacking defects were matched to one specific symmetric stacking mismatch boundary arrangement that can be assumed to be characteristic for a range of vacancy-layered chalcogenide compounds. Both the intermixing of chemically distinct building blocks as well as the characteristic stacking defects are of preeminent interest for current and future work on crystalline superlattices for interfacial switching applications. The same stacking disorder and transitions may also find prominence in other topics of research beyond the field of phase-change applications, such as work on thermoelectric, ferroelectric or even topological properties of novel materials.

4. Summary and conclusions

The advanced Cs-corrected STEM investigation of amorphous, metastable and stable phase change material thin films posed a number of particular challenges. The preparation of electron-transparent specimens by focused ion beam methods was optimized for the characteristic structural instability of the material. Monte-Carlo calculations and experimental observations confirmed that the low-energy ion milling step under cooling conditions reduces the surface modification layer down to 1 - 1.5 nm thickness. Detailed theoretical considerations on the STEM image contrast formation by coherent and incoherent scattering were presented that put the quantitative STEM image simulation by absorptive potential and frozen phonon methods in the necessary context. In particular, the eminent importance of realistic thermal displacement factors in the calculation of high-angle scattering intensity was highlighted.

The structural investigation of Ge-Sb-Te thin films produced by PLD from a $Ge_2Sb_2Te_5$ target covered the entire regime of functional relevant phases, although it must be highlighted that the as-deposited and melt-quenched amorphous phases may possess structural differences that were not explored in this work. The RDF analysis from electron diffraction information confirmed the predominance of defective octahedral short-range order in the amorphous phase. Discrepancies between material density and pair-distribution function can potentially be resolved by the incorporation of intrinsic Te vacancies on defective octahedral sites in the as-deposited state.

Crystalline metastable cubic, intermediate vacancy layered cubic and stable trigonal thin films were produced by ex-situ annealing of the as-deposited state. The atomic-resolution HAADF-STEM results were refined by image processing methods and evaluated regarding local structure and scattering intensity by applying detailed strain mapping, intensity ratio mapping and peak profile fitting routines. The two most prominent results in the course of investigating the metastable phase were the presence of partial {111} ordering on the mixed Ge/Sb/v sublattice as well as the systematic behaviour of pm-scale distortions on the mixed sites. The vacancy-layered cubic phase presents an intermediate transformation step in the phase transition to the trigonal structure. The structure of the ex-situ annealed trigonal phase revealed intrinsic disorder of the stacking sequence, which was correlated with the local stoichiometric composition by layer-by-layer evaluation and intensity ratio mapping of the HAADF signal.

Both the ex-situ annealed trigonal phases as well as textured and epitaxial thin films deposited at elevated substrate temperature were found to exhibit characteristic stacking defects in the vacancy gaps, as well as twin structure formation enhanced by lattice stress. These features are of particular interest in the design and operation of interfacial switching superlattice concepts. The semi-quantitative comparison between individual building blocks of the trigonal lattice and various model structures revealed the complex sublattice order behaviour of the mixed sites, yet also highlighted the need for improved models of the anisotropic phonon dispersion for the prediction of Debye-Waller factors.

Lastly, the gradual increase of the deposition temperature resulted in an incremental transformation of the growth behaviour from textured grains on amorphous surface layers towards epitaxial layer growth in a pseudo-Van-der-Waals epitaxy arrangement. The change in chemical composition due to preferential desorption of Ge, identified by STEM-EDX, narrows the optimal temperature window for deposition of highly-oriented thin films. The presence of a surface passivation layer was found both in the textured and epitaxial growth regime on cleaned Si(111), however it did not prove a requirement for textured growth as evidenced by its absence on the amorphous native oxide layer. As it is followed by a small amorphous component in the low-temperature, textured regime on cleaned Si(111), the mere presence of a passivation layer is also not solely sufficient to induce VdW-epitaxy growth behaviour, somewhat in contrast to Ref. [113].

Current and future work, based on the achieved observations, includes the RHEED observation of the initial layer growth steps, the deposition of oriented GeTe thin films, the deposition of layered superstructures by alternating the PLD target material, as well as the design of property measurement experiments and subsequent comparison with the above-described structures. On the methodological side, refinements of model parameters from first principles are required in order to improve the quantitativeness of the STEM simulation approach, and which in conjunction with monochromated energy-loss experiments may also open up an avenue to the investigation of chemical states in the various structures.

Bibliography

1. Ovshinsky, S.R., *Reversible Electrical Switching Phenomena in Disordered Structures.* Physical Review Letters, 1968. **21**(20): p. 1450-1453.
2. Feinleib, J., S. Moss, and S. Ovshinsky, *Rapid reversible light-induced crystallization of amorphous semiconductors.* Applied Physics Letters, 1971. **18**(6): p. 254-257.
3. Von Gutfeld, R. and P. Chaudhari, *Laser writing and erasing on chalcogenide films.* Journal of Applied Physics, 1972. **43**(11): p. 4688-4693.
4. Yamada, N., M. Takao, and M. Takenaga. *Te-Ge-Sn-Au Phase change recording film for optical disk*. in *30th Annual Technical Symposium*. 1987.: p. 79-85 International Society for Optics and Photonics.
5. Yamada, N., E. Ohno, K. Nishiuchi, N. Akahira, and M. Takao, *Rapid-phase transitions of* $GeTe\text{-}Sb_2Te_3$ *pseudobinary amorphous thin films for an optical disk memory.* Journal of Applied Physics, 1991. **69**(5): p. 2849-2856.
6. Zhou, G.-F. and B.A. Jacobs, *High performance media for phase change optical recording.* Japanese journal of applied physics, 1999. **38**(3S): p. 1625.
7. Lee, B.C., P. Zhou, J. Yang, Y. Zhang, B. Zhao, E. Ipek, O. Mutlu, and D. Burger, *Phase-change technology and the future of main memory.* IEEE micro, 2010. **30**(1): p. 143.
8. Lencer, D., M. Salinga, B. Grabowski, T. Hickel, J. Neugebauer, and M. Wuttig, *A map for phase-change materials.* Nat Mater, 2008. **7**(12): p. 972-977.
9. Wuttig, M. and N. Yamada, *Phase-change materials for rewriteable data storage.* Nat Mater, 2007. **6**(11): p. 824-832.
10. Raoux, S., G.W. Burr, M.J. Breitwisch, C.T. Rettner, Y.C. Chen, R.M. Shelby, M. Salinga, D. Krebs, S.H. Chen, H.L. Lung, and C.H. Lam, *Phase-change random access memory: A scalable technology.* IBM Journal of Research and Development, 2008. **52**(4.5): p. 465-479.
11. Tanaka, K., *Structural phase transitions in chalcogenide glasses.* Physical Review B, 1989. **39**(2): p. 1270-1279.
12. Frumar, M., B. Frumarova, P. Nemec, T. Wagner, J. Jedelsky, and M. Hrdlicka, *Thin chalcogenide films prepared by pulsed laser deposition – new amorphous materials applicable in optoelectronics and chemical sensors.* Journal of Non-Crystalline Solids, 2006. **352**(6–7): p. 544-561.
13. Park, J.-W., S.H. Eom, H. Lee, J.L.F. Da Silva, Y.-S. Kang, T.-Y. Lee, and Y.H. Khang, *Optical properties of pseudobinary GeTe,* $Ge_2Sb_2Te_5$, $GeSb_2Te_4$, $GeSb_4Te_7$, *and* Sb_2Te_3 *from ellipsometry and density functional theory.* Physical Review B, 2009. **80**(11): p. 115209.
14. Caravati, S., M. Bernasconi, T.D. Kühne, M. Krack, and M. Parrinello, *First-principles study of crystalline and amorphous* $Ge_2Sb_2Te_5$ *and the effects of stoichiometric defects.* Journal of Physics: Condensed Matter, 2009. **21**(25): p. 255501.
15. Kolobov, A.V., D.J. Kim, A. Giussani, P. Fons, J. Tominaga, R. Calarco, and A. Gruverman, *Ferroelectric switching in epitaxial GeTe films.* APL Materials, 2014. **2**(6): p. 066101.
16. Kooi, B.J. and B. Noheda, *Ferroelectric chalcogenides—materials at the edge.* Science, 2016. **353**(6296): p. 221-222.
17. Tominaga, J., A.V. Kolobov, P.J. Fons, X. Wang, Y. Saito, T. Nakano, M. Hase, S. Murakami, J. Herfort, and Y. Takagaki, *Giant multiferroic effects in topological GeTe-*Sb_2Te_3 *superlattices.* Science and Technology of Advanced Materials, 2016. **16**: 014402
18. Lee, J., Z. Li, J.P. Reifenberg, S. Lee, R. Sinclair, M. Asheghi, and K.E. Goodson, *Thermal conductivity anisotropy and grain structure in* $Ge_2Sb_2Te_5$ *films.* Journal of Applied Physics, 2011. **109**(8): p. 084902.
19. Welzmiller, S., T. Rosenthal, P. Ganter, L. Neudert, F. Fahrnbauer, P. Urban, C. Stiewe, J. de Boor, and O. Oeckler, *Layered germanium tin antimony tellurides: element distribution, nanostructures and thermoelectric properties.* Dalton Transactions, 2014. **43**(27): p. 10529-10540.

20. Wuttig, M., D. Lusebrink, D. Wamwangi, W. Welnic, M. Gilleszen, and R. Dronskowski, *The role of vacancies and local distortions in the design of new phase-change materials.* Nat Mater, 2007. **6**(2): p. 122-128.
21. Wuttig, M., *Phase change materials: The importance of resonance bonding.* physica status solidi (b), 2009. **246**(8): p. 1820-1825.
22. Lencer, D., M. Salinga, and M. Wuttig, *Design Rules for Phase-Change Materials in Data Storage Applications.* Advanced Materials, 2011. **23**(18): p. 2030-2058.
23. Raoux, S., W. Wełnic, and D. Ielmini, *Phase Change Materials and Their Application to Nonvolatile Memories.* Chemical Reviews, 2009. **110**(1): p. 240-267.
24. Dutil, Y., D.R. Rousse, N.B. Salah, S. Lassue, and L. Zalewski, *A review on phase-change materials: Mathematical modeling and simulations.* Renewable and Sustainable Energy Reviews, 2011. **15**(1): p. 112-130.
25. Li, X.-B., X. Liu, X. Liu, D. Han, Z. Zhang, X. Han, H.-B. Sun, and S. Zhang, *Role of electronic excitation in the amorphization of Ge-Sb-Te alloys.* Physical review letters, 2011. **107**(1): p. 015501.
26. Pirovano, A., A.L. Lacaita, A. Benvenuti, F. Pellizzer, and R. Bez, *Electronic switching in phase-change memories.* Electron Devices, IEEE Transactions on, 2004. **51**(3): p. 452-459.
27. Almasov, N., N. Bogoslovskiy, N. Korobova, S. Kozyukhin, S. Fefelov, L. Kazakova, S. Jakovlev, K. Tsendin, and N. Guseinov, *Switching and memory effects in partly crystallized amorphous* $Ge_2Sb_2Te_5$ *films in a current controlled mode.* Journal of Non-Crystalline Solids, 2012. **358**(23): p. 3299-3303.
28. Pirovano, A., A. Lacaita, A. Benvenuti, F. Pellizzer, S. Hudgens, and R. Bez. *Scaling analysis of phase-change memory technology*. in *Electron Devices Meeting, 2003. IEDM'03 Technical Digest. IEEE International*. 2003: p. 29-6 IEEE.
29. Zalden, P., K.S. Siegert, S.p. Rols, H.E. Fischer, F. Schlich, T. Hu, and M. Wuttig, *Specific Heat of* $(GeTe)_x$ $(Sb_2Te_3)_{1-x}$ *Phase-Change Materials: The Impact of Disorder and Anharmonicity.* Chemistry of Materials, 2014. **26**(7): p. 2307-2312.
30. Salinga, M., *Phase change materials for non-volatile electronic memories*. Thesis, 2008, Fachgruppe Physik RWTH Aachen.
31. Papandreou, N., A. Pantazi, A. Sebastian, M. Breitwisch, C. Lam, H. Pozidis, and E. Eleftheriou. *Multilevel phase-change memory*. in *Electronics, Circuits, and Systems (ICECS), 2010 17th IEEE International Conference on*. 2010: p. 1017-1020 IEEE.
32. Shelby, R.M. and S. Raoux, *Crystallization dynamics of nitrogen-doped* $Ge_2Sb_2Te_5$*.* Journal of Applied Physics, 2009. **105**(10): p. 104902.
33. Ghezzi, G., J.-Y. Raty, S. Maitrejean, A. Roule, E. Elkaim, and F. Hippert, *Effect of carbon doping on the structure of amorphous GeTe phase change material.* Applied Physics Letters, 2011. **99**(15): p. 151906.
34. Kosyakov, V., V. Shestakov, L. Shelimova, F. Kuznetsov, and V. Zemskov, *Topological characterization of the Ge-Sb-Te phase diagram.* Inorganic materials, 2000. **36**(10): p. 1004-1017.
35. Matsunaga, T., R. Kojima, N. Yamada, K. Kifune, Y. Kubota, and M. Takata, *Structural investigation of* $Ge_3Sb_2Te_6$*, an intermetallic compound in the GeTe-Sb2Te3 homologous series.* Applied physics letters, 2007. **90**(16): p. 1919.
36. Bordas, S., M. Clavaguer-Mora, B. Legendre, and C. Hancheng, *Phase diagram of the ternary system Ge-Sb-Te: II. The subternary Ge-GeTe-*Sb_2Te_3*-Sb.* Thermochimica acta, 1986. **107**: p. 239-265.
37. Anderson, T.L. and H.B. Krause, *Refinement of the* Sb_2Te_3 *and* Sb_2Te_2Se *structures and their relationship to nonstoichiometric* Sb_2Te_{3-y} Se_y *compounds.* Acta Crystallographica Section B: Structural Crystallography and Crystal Chemistry, 1974. **30**(5): p. 1307-1310.
38. Zhang, H., C.-X. Liu, X.-L. Qi, X. Dai, Z. Fang, and S.-C. Zhang, *Topological insulators in* Bi_2Se_3, Bi_2Te_3 *and* Sb_2Te_3 *with a single Dirac cone on the surface.* Nature physics, 2009. **5**(6): p. 438-442.
39. Venkatasubramanian, R., E. Siivola, T. Colpitts, and B. O'Quinn, *Thin-film thermoelectric devices with high room-temperature figures of merit.* Nature, 2001. **413**(6856): p. 597-602.

40. Zhao, J., H. Liu, L. Ehm, Z. Chen, S. Sinogeikin, Y. Zhao, and G. Gu, *Pressure-induced disordered substitution alloy in* Sb_2Te_3. Inorganic chemistry, 2011. **50**(22): p. 11291-11293.
41. Chattopadhyay, T. and J. Boucherle, *Neutron diffraction study on the structural phase transition in GeTe.* Journal of Physics C: Solid State Physics, 1987. **20**(10): p. 1431.
42. Krbal, M., A.V. Kolobov, P. Fons, J. Tominaga, S.R. Elliott, J. Hegedus, A. Giussani, K. Perumal, R. Calarco, T. Matsunaga, N. Yamada, K. Nitta, and T. Uruga, *Crystalline GeTe-based phase-change alloys: Disorder in order.* Physical Review B, 2012. **86**(4): p. 045212.
43. Akola, J. and R. Jones, *Structural phase transitions on the nanoscale: The crucial pattern in the phase-change materials* $Ge_2Sb_2Te_5$ *and GeTe.* Physical Review B, 2007. **76**(23): p. 235201.
44. Sun, Z., J. Zhou, and R. Ahuja, *Structure of Phase Change Materials for Data Storage.* Physical Review Letters, 2006. **96**(5): p. 055507.
45. Da Silva, J.L., A. Walsh, and H. Lee, *Insights into the structure of the stable and metastable* $(GeTe)_m$ $(Sb_2Te_3)_n$ *compounds.* Physical Review B, 2008. **78**(22): p. 224111.
46. Bragaglia, V., F. Arciprete, W. Zhang, A.M. Mio, E. Zallo, K. Perumal, A. Giussani, S. Cecchi, J.E. Boschker, and H. Riechert, *Metal-Insulator Transition Driven by Vacancy Ordering in GeSbTe Phase Change Materials.* Scientific Reports, 2016. **6**: 23843
47. Bragaglia, V., K. Holldack, J. Boschker, F. Arciprete, E. Zallo, T. Flissikowski, and R. Calarco, *Far-Infrared and Raman Spectroscopy Investigation of Phonon Modes in Amorphous and Crystalline Epitaxial GeTe-*Sb_2Te_3 *Alloys.* Scientific Reports, 2016. **6**.: 28560
48. Matsunaga, T., H. Morita, R. Kojima, N. Yamada, K. Kifune, Y. Kubota, Y. Tabata, J.-J. Kim, M. Kobata, and E. Ikenaga, *Structural characteristics of GeTe-rich GeTe-*Sb_2Te_3 *pseudobinary metastable crystals.* Journal of Applied Physics, 2008. **103**(9): p. 093511-093511.
49. Matsunaga, T., N. Yamada, and Y. Kubota, *Structures of stable and metastable* $Ge_2Sb_2Te_5$*, an intermetallic compound in GeTe-*Sb_2Te_3 *pseudobinary systems.* Acta Crystallographica Section B, 2004. **60**(6): p. 685-691.
50. Kooi, B. and J.T.M. De Hosson, *Electron diffraction and high-resolution transmission electron microscopy of the high temperature crystal structures of* $GexSb_2Te_{3+x}$ *(x= 1, 2, 3) phase change material.* Journal of applied physics, 2002. **92**(7): p. 3584.
51. I.I. Petrov, R.M.I., Z.G Pinsker, *Electron-diffraction determination of the structures of* $Ge_2Sb_2Te_5$ *and* $GeSb_4Te_7$. Kristallografiya, 1968. **13**(417): p. 339-342
52. Urban, P., M.N. Schneider, L. Erra, S. Welzmiller, F. Fahrnbauer, and O. Oeckler, *Temperature dependent resonant X-ray diffraction of single-crystalline* $Ge_2Sb_2Te_5$. CrystEngComm, 2013. **15**(24): p. 4823-4829.
53. Karpinsky, O.G., L.E. Shelimova, M.A. Kretova, and J.P. Fleurial, *An X-ray study of the mixed-layered compounds of* $(GeTe)_n$ $(Sb_2Te_3)_m$ *homologous series.* Journal of Alloys and Compounds, 1998. **268**(1–2): p. 112-117.
54. Schneider, M.N. and O. Oeckler, *Unusual Solid Solutions in the System Ge-Sb-Te: The Crystal Structure of* $33R\text{-}Ge_{4-x}Sb_{2-y}Te_7$ *(x, y ≈ 0.1) is Isostructural to that of* $Ge_3Sb_2Te_6$. Zeitschrift für anorganische und allgemeine Chemie, 2008. **634**(14): p. 2557-2561.
55. Lotnyk, A., U. Ross, S. Bernütz, E. Thelander, and B. Rauschenbach, *Local atomic arrangements and lattice distortions in layered Ge-Sb-Te crystal structures.* Scientific reports, 2016. **6**: 26724
56. Burdett, J.K. and S. Lee, *Peierls distortions in two and three dimensions and the structures of AB solids.* Journal of the American Chemical Society, 1983. **105**(5): p. 1079-1083.
57. Larrucea, J., J. Akola, and R. Jones, *Polymorphism in amorphous* $Ge_2Sb_2Te_5$*: comparison of melt-quenched and as-deposited structures.* Fast Methods for Long-Range Interactions in Complex Systems, 2011: p. 9.
58. Houška, J., E.M. Peña-Méndez, J. Kolář, J. Přikryl, M. Pavlišta, M. Frumar, T. Wágner, and J. Havel, *Laser desorption time-of-flight mass spectrometry of atomic switch memory* $Ge_2Sb_2Te_5$ *bulk materials and its thin films.* Rapid Communications in Mass Spectrometry, 2014. **28**(7): p. 699-704.

59. Kalb, J.A., *Crystallization kinetics in antimony and tellurium alloys used for phase change recording.* Thesis, 2006, RWTH Aachen
60. Novikov, V., Y. Ding, and A. Sokolov, *Correlation of fragility of supercooled liquids with elastic properties of glasses.* Physical Review E, 2005. **71**(6): p. 061501.
61. Novikov, V. and A. Sokolov, *Poisson's ratio and the fragility of glass-forming liquids.* Nature, 2004. **431**(7011): p. 961-963.
62. Angell, C.A., K.L. Ngai, G.B. McKenna, P.F. McMillan, and S.W. Martin, *Relaxation in glassforming liquids and amorphous solids.* Journal of Applied Physics, 2000. **88**(6): p. 3113-3157.
63. Orava, J., A. Greer, B. Gholipour, D. Hewak, and C. Smith, *Characterization of supercooled liquid $Ge_2Sb_2Te_5$ and its crystallization by ultrafast-heating calorimetry.* Nature materials, 2012. **11**(4): p. 279-283.
64. Chebli, K., J. Saiter, J. Grenet, A. Hamou, and G. Saffarini, *Strong-fragile glass forming liquid concept applied to GeTe chalcogenide glasses.* Physica B: Condensed Matter, 2001. **304**(1): p. 228-236.
65. Egerton, R.F., P. Li, and M. Malac, *Radiation damage in the TEM and SEM.* Micron, 2004. **35**(6): p. 399-409.
66. Kooi, B.J., W.M.G. Groot, and J.T.M. De Hosson, *In situ transmission electron microscopy study of the crystallization of $Ge_2Sb_2Te_5$.* Journal of Applied Physics, 2004. **95**(3): p. 924-932.
67. Ruitenberg, G., A.K. Petford-Long, and R.C. Doole, *Determination of the isothermal nucleation and growth parameters for the crystallization of thin $Ge_2Sb_2Te_5$ films.* Journal of Applied Physics, 2002. **92**(6): p. 3116-3123.
68. Jóvári, P., I. Kaban, J. Steiner, B. Beuneu, A. Schöps, and A. Webb, *'Wrong bonds' in sputtered amorphous $Ge_2Sb_2Te_5$.* Journal of Physics: Condensed Matter, 2007. **19**(33): p. 335212.
69. Tominaga, J. and N. Atoda, *Study of the crystallization of GeSbTe films by Raman spectroscopy.* Japanese journal of applied physics, 1999. **38**(3B): p. L322.
70. Carria, E., A. Mio, S. Gibilisco, M. Miritello, F. d'Acapito, M. Grimaldi, and E. Rimini, *Polymorphism of amorphous $Ge_2Sb_2Te_5$ probed by EXAFS and raman spectroscopy.* Electrochemical and Solid-State Letters, 2011. **14**(12): p. H480-H482.
71. Akola, J., R.O. Jones, S. Kohara, S. Kimura, K. Kobayashi, M. Takata, T. Matsunaga, R. Kojima, and N. Yamada, *Experimentally constrained density-functional calculations of the amorphous structure of the prototypical phase-change material $Ge_2Sb_2Te_5$.* Physical Review B, 2009. **80**(2): p. 020201.
72. Cockayne, D.J., *The study of nanovolumes of amorphous materials using electron scattering.* Annu. Rev. Mater. Res., 2007. **37**: p. 159-187.
73. Akola, J. and R. Jones, *Density functional study of amorphous, liquid and crystalline $Ge_2Sb_2Te_5$: homopolar bonds and/or AB alternation?* Journal of Physics: Condensed Matter, 2008. **20**(46): p. 465103.
74. Matsunaga, T., P. Fons, A. Kolobov, J. Tominaga, and N. Yamada, *The order-disorder transition in GeTe: Views from different length-scales.* Applied Physics Letters, 2011. **99**(23): p. 231907.
75. Da Silva, J.L.F., *Effective coordination concept applied for phase change $(GeTe)_m(Sb_2Te_3)_n$ compounds.* Journal of Applied Physics, 2011. **109**(2): p. 023502.
76. Luo, M. and M. Wuttig, *The Dependence of Crystal Structure of Te-Based Phase-Change Materials on the Number of Valence Electrons.* Advanced Materials, 2004. **16**(5): p. 439-443.
77. Caravati, S., M. Bernasconi, T. Kühne, M. Krack, and M. Parrinello, *Coexistence of tetrahedral-and octahedral-like sites in amorphous phase change materials.* Applied Physics Letters, 2007. **91**(17): p. 171906.
78. Liu, X., X. Li, L. Zhang, Y. Cheng, Z. Yan, M. Xu, X. Han, S. Zhang, Z. Zhang, and E. Ma, *New structural picture of the $Ge_2Sb_2Te_5$ phase-change alloy.* Physical review letters, 2011. **106**(2): p. 025501.

79. Kolobov, A.V., P. Fons, A.I. Frenkel, A.L. Ankudinov, J. Tominaga, and T. Uruga, *Understanding the phase-change mechanism of rewritable optical media.* Nat Mater, 2004. **3**(10): p. 703-708.
80. Deringer, V.L., R. Dronskowski, and M. Wuttig, *Microscopic Complexity in Phase-Change Materials and its Role for Applications.* Advanced Functional Materials, 2015. **25**(40): p. 6343-6359.
81. Akola, J. and R. Jones, *Amorphous structures of Ge/Sb/Te alloys: Density functional simulations.* physica status solidi (b), 2012. **249**(10): p. 1851-1860.
82. Shportko, K., S. Kremers, M. Woda, D. Lencer, J. Robertson, and M. Wuttig, *Resonant bonding in crystalline phase-change materials.* Nat Mater, 2008. **7**(8): p. 653-658.
83. Lucovsky, G. and R. White, *Effects of resonance bonding on the properties of crystalline and amorphous semiconductors.* Physical Review B, 1973. **8**(2): p. 660.
84. Gaspard, J., F. Marinelli, and A. Pellegatti, *Peierls instabilities in covalent structures.* EPL (Europhysics Letters), 1987. **3**(10): p. 1095.
85. Kolobov, A., P. Fons, and J. Tominaga, *Understanding Phase-Change Memory Alloys from a Chemical Perspective.* Scientific reports, 2015. **5**: 13698
86. Kastner, M., D. Adler, and H. Fritzsche, *Valence-alternation model for localized gap states in lone-pair semiconductors.* Physical Review Letters, 1976. **37**(22): p. 1504.
87. Kolobov, A.V., P. Fons, J. Tominaga, and S.R. Ovshinsky, *Vacancy-mediated three-center four-electron bonds in* $GeTe$-Sb_2Te_3 *phase-change memory alloys.* Physical Review B, 2013. **87**(16): p. 165206.
88. Rütten, M., M. Kaes, A. Albert, M. Wuttig, and M. Salinga, *Relation between bandgap and resistance drift in amorphous phase change materials.* Scientific reports, 2015. **5**: 17362
89. Lee, B.-S., J.R. Abelson, S.G. Bishop, D.-H. Kang, B.-k. Cheong, and K.-B. Kim, *Investigation of the optical and electronic properties of* $Ge_2Sb_2Te_5$ *phase change material in its amorphous, cubic, and hexagonal phases.* Journal of Applied Physics, 2005. **97**(9): p. 093509.
90. Siegrist, T., P. Jost, H. Volker, M. Woda, P. Merkelbach, C. Schlockermann, and M. Wuttig, *Disorder-induced localization in crystalline phase-change materials.* Nature materials, 2011. **10**(3): p. 202-208.
91. Kim, J., J. Kim, and S.-H. Jhi, *Prediction of topological insulating behavior in crystalline Ge-Sb-Te.* Physical Review B, 2010. **82**(20): p. 201312.
92. Simpson, R.E., FonsP, A.V. Kolobov, FukayaT, KrbalM, YagiT, and TominagaJ, *Interfacial phase-change memory.* Nat Nano, 2011. **6**(8): p. 501-505.
93. Yu, X. and J. Robertson, *Modeling of switching mechanism in GeSbTe chalcogenide superlattices.* Scientific Reports, 2015. **5**: 12612.
94. Junji, T., V.K. Alexander, J.F. Paul, W. Xiaomin, S. Yuta, N. Takashi, H. Muneaki, M. Shuichi, H. Jens, and T. Yukihiko, *Giant multiferroic effects in topological* $GeTe$-Sb_2Te_3 *superlattices.* Science and Technology of Advanced Materials, 2015. **16**(1): p. 014402.
95. Tominaga, J., R.E. Simpson, P. Fons, and A.V. Kolobov, *Electrical-field induced giant magnetoresistivity in (non-magnetic) phase change films.* Applied Physics Letters, 2011. **99**(15): p. 152105.
96. Bang, D., H. Awano, J. Tominaga, A.V. Kolobov, P. Fons, Y. Saito, K. Makino, T. Nakano, M. Hase, and Y. Takagaki, *Mirror-symmetric Magneto-optical Kerr Rotation using Visible Light in* $[(GeTe)_2(Sb_2Te_3)_1]_n$ *Topological Superlattices.* Scientific reports, 2014. **4**: 5727
97. Tominaga, J., J. Richter, Y. Saito, A. Kolobov, P. Fons, and S. Murakami, *Spintronics using interfacial phase change memory, iPCM.*
98. Yu, X. and J. Robertson, *Modeling of switching mechanism in GeSbTe chalcogenide superlattices.* Scientific reports, 2015. **5**: 12612
99. Momand, J., R. Wang, J.E. Boschker, M.A. Verheijen, R. Calarco, and B.J. Kooi, *Interface formation of two- and three-dimensionally bonded materials in the case of* $GeTe$-Sb_2Te_3 *superlattices.* Nanoscale, 2015. **7**(45): p. 19136-19143.

100. Wang, R., V. Bragaglia, J.E. Boschker, and R. Calarco, *Intermixing during epitaxial growth of van der Waals bonded nominal GeTe/*Sb_2Te_3 *superlattices.* Crystal Growth & Design, 2016. **16**(7): p. 3596-3601
101. Tominaga, J., P. Fons, A. Kolobov, T. Shima, T.C. Chong, R. Zhao, H.K. Lee, and L. Shi, *Role of Ge switch in phase transition: Approach using atomically controlled GeTe/*Sb_2Te_3 *superlattice.* Japanese Journal of Applied Physics, 2008. **47**(7S1): p. 5763.
102. Casarin, B., A. Caretta, J. Momand, B.J. Kooi, M.A. Verheijen, V. Bragaglia, R. Calarco, M. Chukalina, X. Yu, and J. Robertson, *Revisiting the Local Structure in Ge-Sb-Te based Chalcogenide Superlattices.* Scientific reports, 2016. **6**: 22353
103. Zhou, J., Z. Sun, Y. Pan, Z. Song, and R. Ahuja, *Vacancy or not: An insight on the intrinsic vacancies in rocksalt-structured GeSbTe alloys from ab initio calculations.* EPL (Europhysics Letters), 2011. **95**(2): p. 27002.
104. Persson, C., Y.-J. Zhao, S. Lany, and A. Zunger, *n-type doping of* $CuInSe_2$ *and* $CuGaSe_2$. Physical Review B, 2005. **72**(3): p. 035211.
105. Giannuzzi, L. and F. Stevie, *A review of focused ion beam milling techniques for TEM specimen preparation.* Micron, 1999. **30**(3): p. 197-204.
106. Hannay, N., *Defects in solids*. 2012: Springer Science & Business Media.
107. Kelly, A.A. and K.M. Knowles, *Crystallography and crystal defects*. 2012: John Wiley & Sons.
108. Drabold, D.A. and S.K. Estreicher, *Theory of defects in semiconductors*. 2007: Springer.
109. Adler, D., *Defects in amorphous chalcogenides and silicon.* Le Journal de Physique Colloques, 1981. **42**(C4): p. C4-3-C4-14.
110. Cowley, J.M., *Electron diffraction techniques*. Vol. 2. 1992: Oxford University Press.
111. Braun, W., R. Shayduk, T. Flissikowski, M. Ramsteiner, H.T. Grahn, H. Riechert, P. Fons, and A. Kolobov, *Epitaxy of Ge-Sb-Te phase-change memory alloys.* Applied Physics Letters, 2009. **94**(4): p. 41902.
112. Hwang, J., M. Kim, D. Campbell, H.A. Alsalman, J.Y. Kwak, S. Shivaraman, A.R. Woll, A.K. Singh, R.G. Hennig, and S. Gorantla, *van der Waals epitaxial growth of graphene on sapphire by chemical vapor deposition without a metal catalyst.* Acs Nano, 2012. **7**(1): p. 385-395.
113. Saito, Y., P. Fons, A.V. Kolobov, and J. Tominaga, *Self-organized van der Waals epitaxy of layered chalcogenide structures.* Physica Status Solidi B-Basic Solid State Physics, 2015. **252**(10): p. 2151-2158.
114. Thelander, E., J. Gerlach, U. Ross, A. Lotnyk, and B. Rauschenbach, *Low temperature epitaxy of Ge-Sb-Te films on* BaF_2 *(111) by pulsed laser deposition.* Applied Physics Letters, 2014. **105**(22): p. 221908.
115. Thelander, E., *Epitaxial Ge-Sb-Te Thin Films by Pulsed Laser Deposition.* Thesis, 2014, University Leipzig,
116. Erni, R., *Aberration-Corrected Imaging in Transmission Electron Microscopy.* 2010.
117. Pennycook, S.J. and P.D. Nellist, *Scanning transmission electron microscopy: imaging and analysis*. 2011: Springer Science & Business Media.
118. Kirkland, E.J., *Advanced computing in electron microscopy*. 2010: Springer Science & Business Media.
119. Williams, D.B. and C.B. Carter, *Transmission electron microscopy*. 1996, Springer.
120. Fuchs, E., H. Oppolzer, and H. Rehme, *Particle beam microanalysis: fundamentals, methods and applications*. 1990: VCH.
121. Egerton, R.F., *Physical principles of electron microscopy: an introduction to TEM, SEM, and AEM*. 2006: Springer Science & Business Media.
122. Lotnyk, A., D. Poppitz, U. Ross, J.W. Gerlach, F. Frost, S. Bernütz, E. Thelander, and B. Rauschenbach, *Focused high- and low-energy ion milling for TEM specimen preparation.* Microelectronics Reliability, 2015. **55**(9-10): p. 2119-2125.
123. Malis, T., S. Cheng, and R. Egerton, *EELS log‐ratio technique for specimen‐thickness measurement in the TEM.* Journal of electron microscopy technique, 1988. **8**(2): p. 193-200.

124. Ziegler, J.F., M.D. Ziegler, and J.P. Biersack, *SRIM–The stopping and range of ions in matter (2010).* Nuclear Instruments and Methods in Physics Research Section B: Beam Interactions with Materials and Atoms, 2010. **268**(11): p. 1818-1823.
125. Cowley, J.M., *Image contrast in a transmission scanning electron microscope.* Applied Physics Letters, 1969. **15**(2): p. 58-59.
126. Kunath, W., F. Zemlin, and K. Weiss, *Apodization in phase-contrast electron microscopy realized with hollow-cone illumination.* Ultramicroscopy, 1985. **16**(2): p. 123-138.
127. Howie, A. and M.J. Whelan, *Diffraction Contrast of Electron Microscope Images of Crystal Lattice Defects. II. The Development of a Dynamical Theory.* Proceedings of the Royal Society of London A: Mathematical, Physical and Engineering Sciences, 1961. **263**(1313): p. 217-237.
128. Cowley, J.M. and A.F. Moodie, *The scattering of electrons by atoms and crystals. I. A new theoretical approach.* Acta Crystallographica, 1957. **10**(10): p. 609-619.
129. Pennycook, T.J., A.R. Lupini, H. Yang, M.F. Murfitt, L. Jones, and P.D. Nellist, *Efficient phase contrast imaging in STEM using a pixelated detector. Part 1: Experimental demonstration at atomic resolution.* Ultramicroscopy, 2015. **151**: p. 160-167.
130. Shibata, N., S.D. Findlay, Y. Kohno, H. Sawada, Y. Kondo, and Y. Ikuhara, *Differential phase-contrast microscopy at atomic resolution.* Nat Phys, 2012. **8**(8): p. 611-615.
131. Shibata, N., S.D. Findlay, H. Sasaki, T. Matsumoto, H. Sawada, Y. Kohno, S. Otomo, R. Minato, and Y. Ikuhara, *Imaging of built-in electric field at a p-n junction by scanning transmission electron microscopy.* Scientific Reports, 2015. **5**: 10040.
132. Müller, K., F.F. Krause, A. Béché, M. Schowalter, V. Galioit, S. Löffler, J. Verbeeck, J. Zweck, P. Schattschneider, and A. Rosenauer, *Atomic electric fields revealed by a quantum mechanical approach to electron picodiffraction.* Nature Communications, 2014. **5**: p. 5653.
133. A. Muller, D., B. Edwards, E. J. Kirkland, and J. Silcox, *Simulation of thermal diffuse scattering including a detailed phonon dispersion curve.* Ultramicroscopy, 2001. **86**(3–4): p. 371-380.
134. Peng, Y., P.D. Nellist, and S.J. Pennycook, *HAADF-STEM imaging with sub-angstrom probes: a full Bloch wave analysis.* Journal of Electron Microscopy, 2004. **53**(3): p. 257-266.
135. Hillyard, S., R.F. Loane, and J. Silcox, *Annular dark-field imaging: Resolution and thickness effects.* Ultramicroscopy, 1993. **49**(1): p. 14-25.
136. LeBeau, J.M., S.D. Findlay, X. Wang, A.J. Jacobson, L.J. Allen, and S. Stemmer, *High-angle scattering of fast electrons from crystals containing heavy elements: Simulation and experiment.* Physical Review B, 2009. **79**(21): p. 214110.
137. Klenov, D.O. and S. Stemmer, *Contributions to the contrast in experimental high-angle annular dark-field images.* Ultramicroscopy, 2006. **106**(10): p. 889-901.
138. Ishizuka, K., *A practical approach for STEM image simulation based on the FFT multislice method.* Ultramicroscopy, 2002. **90**(2): p. 71-83.
139. Scherzer, O., *Über einige Fehler von Elektronenlinsen.* Zeitschrift für Physik, 1936. **101**(9-10): p. 593-603.
140. Scherzer, O., *Sphärische und chromatische Korrektur von Elektronen-Linsen.* Optik, 1947. **2**: p. 114-132.
141. Rose, H., *Elektronenoptische Aplanate.* Optik, 1971. **34**(285): p. 12.
142. Haider, M., H. Rose, S. Uhlemann, B. Kabius, and K. Urban, *Towards 0.1 nm resolution with the first spherically corrected transmission electron microscope.* Journal of electron microscopy, 1998. **47**(5): p. 395-405.
143. Scherzer, O., *The theoretical resolution limit of the electron microscope.* Journal of Applied Physics, 1949. **20**(1): p. 20-29.
144. Kaiser, U., J. Biskupek, J.C. Meyer, J. Leschner, L. Lechner, H. Rose, M. Stöger-Pollach, A.N. Khlobystov, P. Hartel, H. Müller, M. Haider, S. Eyhusen, and G. Benner, *Transmission electron microscopy at 20 kV for imaging and spectroscopy.* Ultramicroscopy, 2011. **111**(8): p. 1239-1246.

145. Freitag, B., S. Kujawa, P.M. Mul, J. Ringnalda, and P.C. Tiemeijer, *Breaking the spherical and chromatic aberration barrier in transmission electron microscopy.* Ultramicroscopy, 2005. **102**(3): p. 209-214.
146. Haider, M., P. Hartel, H. Müller, S. Uhlemann, and J. Zach, *Information Transfer in a TEM Corrected for Spherical and Chromatic Aberration.* Microscopy and Microanalysis, 2010. **16**(04): p. 393-408.
147. Rose, H., *Optics of high-performance electron microscopes.* Science and Technology of Advanced Materials, 2008, **9**: 014107
148. Hartel, P., H. Müller, S. Uhlemann, and M. Haider. *Residual aberrations of hexapole-type C s-correctors*. in *Proc. 13th European Microscopy Congress*. 2004.
149. Dwyer, C., R. Erni, and J. Etheridge, *Method to measure spatial coherence of subangstrom electron beams.* Applied Physics Letters, 2008. **93**(2): p. 021115.
150. Krivanek, O., P. Nellist, N. Dellby, M. Murfitt, and Z. Szilagyi, *Towards sub-0.5 Å electron beams.* Ultramicroscopy, 2003. **96**(3): p. 229-237.
151. Krivanek, O., G. Corbin, N. Dellby, B. Elston, R. Keyse, M. Murfitt, Z. Szilagyi, and J. Woodruff, *An electron microscope for the aberration-corrected era.* Ultramicroscopy, 2008. **108**(3): p. 179-195.
152. Born, M. and E. Wolf, *Principles of optics: electromagnetic theory of propagation, interference and diffraction of light*. 2000: CUP Archive.
153. Lotnyk, A., D. Poppitz, J.W. Gerlach, and B. Rauschenbach, *Direct imaging of light elements by annular dark-field aberration-corrected scanning transmission electron microscopy.* Applied Physics Letters, 2014. **104**(7): 071908
154. Nellist, P.D. and S.J. Pennycook, *Incoherent imaging using dynamically scattered coherent electrons.* Ultramicroscopy, 1999. **78**(1–4): p. 111-124.
155. Peng, L.-M., *Electron atomic scattering factors and scattering potentials of crystals.* Micron, 1999. **30**(6): p. 625-648.
156. Peng, L.-M., *Electron atomic scattering factors, Debye–Waller factors and the optical potential for high-energy electron diffraction.* Journal of Electron Microscopy, 2005. **54**(3): p. 199-207.
157. Sears, V. and S. Shelley, *Debye–Waller factor for elemental crystals.* Acta Crystallographica Section A: Foundations of Crystallography, 1991. **47**(4): p. 441-446.
158. Hillyard, S. and J. Silcox, *Detector geometry, thermal diffuse scattering and strain effects in ADF STEM imaging.* Ultramicroscopy, 1995. **58**(1): p. 6-17.
159. Perovic, D., C. Rossouw, and A. Howie, *Imaging elastic strains in high-angle annular dark field scanning transmission electron microscopy.* Ultramicroscopy, 1993. **52**(3): p. 353-359.
160. Doyle, P.t. and P. Turner, *Relativistic Hartree–Fock X-ray and electron scattering factors.* Acta Crystallographica Section A: Crystal Physics, Diffraction, Theoretical and General Crystallography, 1968. **24**(3): p. 390-397.
161. Weickenmeier, A. and H. Kohl, *Computation of absorptive form factors for high-energy electron diffraction.* Acta Crystallographica Section A: Foundations of Crystallography, 1991. **47**(5): p. 590-597.
162. Hall, C. and P. Hirsch. *Effect of thermal diffuse scattering on propagation of high energy electrons through crystals*. in *Proceedings of the Royal Society of London A: Mathematical, Physical and Engineering Sciences*. 1965. The Royal Society.
163. Findlay, S.D., L.J. Allen, M.P. Oxley, and C.J. Rossouw, *Lattice-resolution contrast from a focused coherent electron probe. Part II.* Ultramicroscopy, 2003. **96**(1): p. 65-81.
164. Muller, D.A. and J. Silcox, *Delocalization in inelastic scattering.* Ultramicroscopy, 1995. **59**(1–4): p. 195-213.
165. Ohtsuka, M., T. Yamazaki, Y. Kotaka, H. Fujisawa, M. Shimizu, K. Honda, I. Hashimoto, and K. Watanabe, *Nonlocality in spherical-aberration-corrected HAADF STEM images.* Acta Crystallographica Section A, 2013. **69**(3): p. 289-296.
166. Cosgriff, E.C. and P.D. Nellist, *A Bloch wave analysis of optical sectioning in aberration-corrected STEM.* Ultramicroscopy, 2007. **107**(8): p. 626-634.

167. Kim, S., Y. Oshima, H. Sawada, T. Kaneyama, Y. Kondo, M. Takeguchi, Y. Nakayama, Y. Tanishiro, and K. Takayanagi, *Quantitative annular dark-field STEM images of a silicon crystal using a large-angle convergent electron probe with a 300-kV cold field-emission gun.* Journal of electron microscopy, 2011. **60**(2): p. 109-116.
168. Van Aert, S., J. Verbeeck, R. Erni, S. Bals, M. Luysberg, D.V. Dyck, and G.V. Tendeloo, *Quantitative atomic resolution mapping using high-angle annular dark field scanning transmission electron microscopy.* Ultramicroscopy, 2009. **109**(10): p. 1236-1244.
169. Watanabe, K., T. Yamazaki, I. Hashimoto, and M. Shiojiri, *Atomic-resolution annular dark-field STEM image calculations.* Physical Review B, 2001. **64**(11): p. 115432.
170. Loane, R.F., P. Xu, and J. Silcox, *Thermal vibrations in convergent-beam electron diffraction.* Acta Crystallographica Section A: Foundations of Crystallography, 1991. **47**(3): p. 267-278.
171. Rosenauer, A. and M. Schowalter, *STEMSIM—a new software tool for simulation of STEM HAADF Z-contrast imaging*, in *Microscopy of Semiconducting Materials 2007*. 2008, Springer. p. 170-172.
172. Shalini, A., Y. Liu, F. Katmis, W. Braun, G. Srivastava, and R. Hicken, *Coherent phonon modes of crystalline and amorphous* $Ge_2Sb_2Te_5$ *thin films: A fingerprint of structure and bonding.* Journal of Applied Physics, 2015. **117**(2): p. 025306.
173. Sosso, G., S. Caravati, C. Gatti, S. Assoni, and M. Bernasconi, *Vibrational properties of hexagonal* $Ge_2Sb_2Te_5$ *from first principles.* Journal of Physics: Condensed Matter, 2009. **21**(24): p. 245401.
174. Ross, U., A. Lotnyk, E. Thelander, and B. Rauschenbach, *Direct imaging of crystal structure and defects in metastable* $Ge_2Sb_2Te_5$ *by quantitative aberration-corrected scanning transmission electron microscopy.* Applied Physics Letters, 2014. **104**(12): 121904
175. Thelander, E., J.W. Gerlach, U. Ross, F. Frost, and B. Rauschenbach, *Epitaxial growth of Ge-Sb-Te films on KCl by high deposition rate pulsed laser deposition.* Journal of Applied Physics, 2014. **115**(21): 213504
176. Ross, U., A. Lotnyk, E. Thelander, and B. Rauschenbach, *Microstructure evolution in pulsed laser deposited epitaxial Ge-Sb-Te chalcogenide thin films.* Journal of Alloys and Compounds, 2016. **15**: p. 582-590
177. Mukhopadhyay, S., J. Sun, A. Subedi, T. Siegrist, and D.J. Singh, *Competing covalent and ionic bonding in Ge-Sb-Te phase change materials.* Scientific Reports, 2016. **6**: 25981.
178. Kalikka, J., X. Zhou, E. Dilcher, S. Wall, J. Li, and R.E. Simpson, *Strain-engineered diffusive atomic switching in two-dimensional crystals.* Nat Commun, 2016. **7**: 11983
179. Zhang, B., X.-P. Wang, Z.-J. Shen, X.-B. Li, C.-S. Wang, Y.-J. Chen, J.-X. Li, J.-X. Zhang, Z. Zhang, and S.-B. Zhang, *Vacancy Structures and Melting Behavior in Rock-Salt GeSbTe.* Scientific reports, 2016. **6**: 25453
180. Zhang, B., W. Zhang, Z. Shen, Y. Chen, J. Li, S. Zhang, Z. Zhang, M. Wuttig, R. Mazzarello, E. Ma, and X. Han, *Element-resolved atomic structure imaging of rocksalt* $Ge_2Sb_2Te_5$ *phase-change material.* Applied Physics Letters, 2016. **108**(19): 191902.
181. Singh, R.K. and J. Narayan, *Pulsed-laser evaporation technique for deposition of thin films: Physics and theoretical model.* Physical Review B, 1990. **41**(13): p. 8843.
182. Holzapfel, B., B. Roas, L. Schultz, P. Bauer, and G. Saemann-Ischenko, *Off-axis laser deposition of* $YBa_2Cu_3O_{7-\delta}$ *thin films.* Applied Physics Letters, 1992. **61**(26): p. 3178-3180.
183. Thon, F., *Notizen: Zur Defokussierungsabhängigkeit des Phasenkontrastes bei der elektronenmikroskopischen Abbildung.* Zeitschrift für Naturforschung A, 1966. **21**(4): p. 476-478.
184. Mu, X., D. Wang, T. Feng, and C. Kübel, *Radial distribution function imaging by STEM diffraction: Phase mapping and analysis of heterogeneous nanostructured glasses.* Ultramicroscopy, 2016. **168**: p. 1-6.
185. Mitchell, D.R. and T. Petersen, *RDFTools: A software tool for quantifying short-range ordering in amorphous materials.* Microscopy research and technique, 2012. **75**(2): p. 153-163.

186. Sun, X., M. Ehrhardt, A. Lotnyk, P. Lorenz, E. Thelander, J.W. Gerlach, T. Smausz, U. Decker, and B. Rauschenbach, *Crystallization of* $Ge_2Sb_2Te_5$ *thin films by nano-and femtosecond single laser pulse irradiation.* Scientific reports, 2016. **6**: 28246
187. Morales-Sanchez, E., E. Prokhorov, J. Gonzalez-Hernandez, and A. Mendoza-Galvan, *Structural, electric and kinetic parameters of ternary alloys of GeSbTe.* Thin Solid Films, 2005. **471**(1): p. 243-247.
188. Nonaka, T., G. Ohbayashi, Y. Toriumi, Y. Mori, and H. Hashimoto, *Crystal structure of GeTe and* $Ge_2Sb_2Te_5$ *meta-stable phase.* Thin Solid Films, 2000. **370**(1–2): p. 258-261.
189. Kato, N., I. Konomi, Y. Seno, and T. Motohiro, *In situ X-ray diffraction study of crystallization process of GeSbTe thin films during heat treatment.* Applied Surface Science, 2005. **244**(1–4): p. 281-284.
190. Raoux, S. and D. Ielmini, *Phase change materials and their application to nonvolatile memories.* Chemical reviews, 2009. **110**(1): p. 240-267.
191. Bai, G., R. Li, H.N. Xu, Y.D. Xia, Z.G. Liu, H.M. Lu, and J. Yin, *The thickness dependence of the crystallization behavior in sandwiched amorphous* $Ge_2Sb_2Te_5$ *thin films.* Physica B: Condensed Matter, 2011. **406**(23): p. 4436-4439.
192. Arciniega, J.G., E. Prokhorov, F.E. Beltran, and G. Trapaga, *Crystallization of Ge:Sb:Te Thin Films for Phase Change Memory Application*. 2012: INTECH Open Access Publisher.
193. Tanaka, M., Saito, R., Ueno, K. and Harada, Y. , *Large-angle convergent beam electron diffraction.* Journal of Electron Microscopy, 1980. **29**: p. 408-412. .
194. Kilaas, R., *Optimal and near‐optimal filters in high‐resolution electron microscopy.* Journal of Microscopy, 1998. **190**(1-2): p. 45-51.
195. Lincoln, B. and A. Cervin. *Jitterbug: A tool for analysis of real-time control performance*. in *Decision and Control, 2002, Proceedings of the 41st IEEE Conference on Decision and Control*. 2002: p. 1319-1324 IEEE.
196. Hÿtch, M., E. Snoeck, and R. Kilaas, *Quantitative measurement of displacement and strain fields from HREM micrographs.* Ultramicroscopy, 1998. **74**(3): p. 131-146.
197. Ross, U., A. Lotnyk, E. Thelander, and B. Rauschenbach, *Direct imaging of crystal structure and defects in metastable* $Ge_2Sb_2Te_5$ *by quantitative aberration-corrected scanning transmission electron microscopy.* Applied Physics Letters, 2014. **104**(12): 121904
198. Lotnyk, A., S. Bernütz, X. Sun, U. Ross, M. Ehrhardt, and B. Rauschenbach, *Real-space imaging of atomic arrangement and vacancy layers ordering in laser crystallised* $Ge_2Sb_2Te_5$ *phase change thin films.* Acta Materialia, 2016. **105**: p. 1-8.
199. Kozyukhin, S., A. Sherchenkov, E. Gorshkova, V.K. Kudoyarova, and A. Vargunin, *Structural transformations in thin* $Ge_2Sb_2Te_5$ *films.* Inorganic Materials, 2009. **45**(4): p. 361-365.
200. Baowei, Q., L. Yunfeng, F. Jie, L. Yun, L. Yinyin, T. Ting'ao, C. Bingchu, and C. Bomy, *Study of* $Ge_2Sb_2Te_5$ *film for nonvolatile memory medium.* J. Mater. Sci. Technol, 2005. **21**(1): p. 95-99
201. Friedrich, I., V. Weidenhof, W. Njoroge, P. Franz, and M. Wutting, *Structural transformations of* $Ge_2Sb_2Te_5$ *films studied by electrical resistance measurements.* Journal of Applied Physics, 2000. **87**(9; PART 1): p. 4130-4134.
202. Bragaglia, V., B. Jenichen, A. Giussani, K. Perumal, H. Riechert, and R. Calarco, *Structural change upon annealing of amorphous GeSbTe grown on Si (111).* Journal of Applied Physics, 2014. **116**(5): p. 054913.
203. Zhou, J., Z. Sun, Y. Pan, Z. Song, and R. Ahuja, *Ab initio study of antisite defective layered* $Ge_2Sb_2Te_5$. Materials Chemistry and Physics, 2012. **133**(1): p. 159-162.
204. Zhang, W., A. Thiess, P. Zalden, R. Zeller, P.H. Dederichs, J.Y. Raty, M. Wuttig, S. Blügel, and R. Mazzarello, *Role of vacancies in metal–insulator transitions of crystalline phase-change materials.* Nat Mater, 2012. **11**(11): p. 952-956.
205. Tsafack, T., E. Piccinini, B.-S. Lee, E. Pop, and M. Rudan, *Electronic, optical and thermal properties of the hexagonal and rocksalt-like* $Ge_2Sb_2Te_5$ *chalcogenide from first-principle calculations.* Journal of Applied Physics, 2011. **110**(6): p. 063716.

206. Makino, K., Y. Saito, P. Fons, A.V. Kolobov, T. Nakano, J. Tominaga, and M. Hase, *Coherent phonon study of* $(GeTe)_l(Sb_2Te_3)_m$ *interfacial phase change memory materials.* Applied Physics Letters, 2014. **105**(15): p. 151902.
207. Ewald, P., *Zur Theorie der Interferenzen der Röntgenstrahlen.* Phys. Z, 1913. **14**: p. 465-472.
208. Matsunaga, T. and N. Yamada, *Structural investigation of* $GeSb_2Te_4$*: A high-speed phase-change material.* Physical Review B, 2004. **69**(10): p. 104111.
209. Fukumoto, H., K. Tsunetomo, T. Imura, and Y. Osaka, *Structural Changes of Amorphous* $GeTe_2$ *Films by Annealing (Formation of Metastable Crystalline* $GeTe_2$ *Films).* Journal of the Physical Society of Japan, 1987. **56**(1): p. 158-162.
210. Tominaga, J., A. Kolobov, P. Fons, T. Nakano, and S. Murakami, *Ferroelectric Order Control of the Dirac-Semimetal Phase in GeTe-*Sb_2Te_3 *Superlattices.* Advanced Materials Interfaces, 2014. **1**(1): 1300027
211. Reinhardt, K. and W. Kern, *Handbook of silicon wafer cleaning technology*. 2008: William Andrew.
212. Perumal, K., W. Braun, H. Riechert, and R. Calarco, *Growth control of epitaxial GeTe–*Sb_2Te_3 *films using a line-of-sight quadrupole mass spectrometer.* Journal of crystal growth, 2014. **396**: p. 50-53.
213. Spieß, L., G. Teichert, R. Schwarzer, H. Behnken, and C. Genzel, *Moderne Röntgenbeugung: Röntgendiffraktometrie für Materialwissenschaftler, Physiker und Chemiker*. 2009: Springer-Verlag.
214. Perumal, K., *Epitaxial growth of Ge-Sb-Te based phase change materials*. Thesis, 2013, Humboldt-Universität zu Berlin, Mathematisch-Naturwissenschaftliche Fakultät I.
215. Willmott, P. and J. Huber, *Pulsed laser vaporization and deposition.* Reviews of Modern Physics, 2000. **72**(1): p. 315.
216. Stranski, I.N. and L.v. Krastanow, *Zur Theorie der orientierten Ausscheidung von Ionenkristallen aufeinander.* Monatshefte für Chemie/Chemical Monthly, 1937. **71**(1): p. 351-364.
217. Lee, J.-Y., J.-H. Kim, D.-J. Jeon, J. Han, and J.-S. Yeo, *Atomic Migration Induced Crystal Structure Transformation and Core-Centered Phase Transition in Single Crystal* $Ge_2Sb_2Te_5$ *Nanowires.* Nano Letters, 2016. **16**(10): p. 6078-6085
218. Gao, H. and L.-M. Peng, *Parameterization of the temperature dependence of the Debye–Waller factors.* Acta Crystallographica Section A: Foundations of Crystallography, 1999. **55**(5): p. 926-932.
219. Lyeo, H.-K., D.G. Cahill, B.-S. Lee, J.R. Abelson, M.-H. Kwon, K.-B. Kim, S.G. Bishop, and B.-k. Cheong, *Thermal conductivity of phase-change material* $Ge_2Sb_2Te_5$*.* Applied Physics Letters, 2006. **89**(15): p. 151904.
220. Lee, J., E. Bozorg-Grayeli, S. Kim, M. Asheghi, H.-S.P. Wong, and K.E. Goodson, *Phonon and electron transport through* $Ge_2Sb_2Te_5$ *films and interfaces bounded by metals.* Applied Physics Letters, 2013. **102**(19): p. 191911.
221. Giraud, V., J. Cluzel, V. Sousa, A. Jacquot, A. Dauscher, B. Lenoir, H. Scherrer, and S. Romer, *Thermal characterization and analysis of phase change random access memory.* Journal of Applied Physics, 2005. **98**(1): p. 013520.
222. Koma, A., *Van der Waals epitaxy—a new epitaxial growth method for a highly lattice-mismatched system.* Thin Solid Films, 1992. **216**(1): p. 72-76.
223. Wang, R., J.E. Boschker, E. Bruyer, D.D. Sante, S. Picozzi, K. Perumal, A. Giussani, H. Riechert, and R. Calarco, *Toward Truly Single Crystalline GeTe Films: The Relevance of the Substrate Surface.* The Journal of Physical Chemistry C, 2014. **118**(51): p. 29724-29730.
224. Boschker, J.E., J. Momand, V. Bragaglia, R. Wang, K. Perumal, A. Giussani, B.J. Kooi, H. Riechert, and R. Calarco, *Surface Reconstruction-Induced Coincidence Lattice Formation Between Two-Dimensionally Bonded Materials and a Three-Dimensionally Bonded Substrate.* Nano Letters, 2014. **14**(6): p. 3534-3538.
225. Deringer, V.L., M. Lumeij, and R. Dronskowski, *Ab Initio Modeling of α-GeTe (111) Surfaces.* The Journal of Physical Chemistry C, 2012. **116**(29): p. 15801-15811.

226. Grey, F. and J. Bohr, *A symmetry principle for epitaxial rotation.* EPL (Europhysics Letters), 1992. **18**(8): p. 717.
227. Wiedemeier, H. and P. Siemers, *The thermal expansion of GeS and GeTe.* Zeitschrift für anorganische und allgemeine Chemie, 1977. **431**(1): p. 299-304.
228. D'Alfonso, A.J., S.D. Findlay, M.P. Oxley, S.J. Pennycook, K. van Benthem, and L. Allen, *Depth sectioning in scanning transmission electron microscopy based on core-loss spectroscopy.* Ultramicroscopy, 2007. **108**(1): p. 17-28.
229. Kothleitner, G., M. Neish, N. Lugg, S. Findlay, W. Grogger, F. Hofer, and L. Allen, *Quantitative elemental mapping at atomic resolution using X-ray spectroscopy.* Physical Review Letters, 2014. **112**(8): p. 085501.
230. Meisenkothen, F., R. Wheeler, M.D. Uchic, R.D. Kerns, and F.J. Scheltens, *Electron channeling: A problem for x-ray microanalysis in materials science.* Microscopy and Microanalysis, 2009. **15**(02): p. 83-92.
231. Mitchell, D.R., *Determination of mean free path for energy loss and surface oxide film thickness using convergent beam electron diffraction and thickness mapping: a case study using Si and P91 steel.* Journal of microscopy, 2006. **224**(2): p. 187-196.
232. Kalb, J., C. Wen, F. Spaepen, H. Dieker, and M. Wuttig, *Crystal morphology and nucleation in thin films of amorphous Te alloys used for phase change recording.* Journal of applied physics, 2005. **98**(5): p. 54902-54902.
233. Kim, M. and H. Kim, *Preparation and observation of an artifact-free* $Ge_2Sb_2Te_5$ *TEM specimen by the small angle cleavage technique.* Materials characterization, 2006. **56**(3): p. 245-249.
234. Raoux, S., G.M. Cohen, M. Hopstaken, S. Maurer, and J.L.J. Sweet. *Properties of Phase Change Materials Modified by Ion Implantation*. in *MRS Proceedings*. 2011. Cambridge Univ Press.
235. Swanson, L., G. Schwind, A. Bell, and J. Brady, *Emission characteristics of gallium and bismuth liquid metal field ion sources.* Journal of Vacuum Science & Technology, 1979. **16**(6): p. 1864-1867.
236. Ishitani, T. and T. Yaguchi, *Cross-sectional sample preparation by focused ion beam: A review of ion-sample interaction.* Microscopy research and technique, 1996. **35**(4): p. 320-333.
237. McCaffrey, J., M. Phaneuf, and L. Madsen, *Surface damage formation during ion-beam thinning of samples for transmission electron microscopy.* Ultramicroscopy, 2001. **87**(3): p. 97-104.
238. Goldstein, J., J. Costley, G. Lorimer, and S. Reed, *Quantitative X-ray analysis in the electron microscope.* Scanning Electron Microscopy, 1977. **1**(315): p. 24.
239. Borisevich, A.Y., A.R. Lupini, and S.J. Pennycook, *Depth sectioning with the aberration-corrected scanning transmission electron microscope.* Proceedings of the National Academy of Sciences of the United States of America, 2006. **103**(9): p. 3044-3048.

Appendix A: Summary of GeTe – Sb_2Te_3 compositions and crystallographic parameters

Tab. A.I: Structural data from literature for common GeTe-Sb_2Te_3 compounds. Vacancies or VdW gaps are denoted by “v”.

Composition	Space group	Lattice parameters	Angles	Stacking sequence of (111) layers (cubic, rhombohedral distortion) or (0001) layers (trigonal)	
GeTe	225	a = b = c = 6.009 Å	$\alpha = \beta = \gamma = 90°$	-Ge-Te-…	[227]
GeTe	160	a = b = c = 4.281 Å	$\alpha = \beta = \gamma = 58.358°$	-Ge*-Te-… *Ge positions at (0.521, 0.521, 0.521)	[41]
Sb_2Te_3	166	a = b = 4.264 Å c = 30.458 Å	$\alpha = \beta = 90°$ $\gamma = 120°$	-Te-Sb-Te-v-Te-Sb-…	[37]
$(GeTe)_{1-x}$- $(Sb2Te_3)_x$ (metastable)	255	a = b = c = 6.0293 Å * *cell parameters for different Sb_2Te_3 concentrations vary between 6.0 and 6.05 Å	$\alpha = \beta = \gamma = 90°$	-Ge/Sb/v*-Te-… *random mixing of Ge, Sb and vacancies models assume (0.5, 0.5, 0.5) positions	[49]
$Ge_1Sb_2Te_4$	166	a = b = 4.2721 Å c = 41.686 Å	$\alpha = \beta = 90°$ $\gamma = 120°$	-$Ge_{0.49}Sb_{0.51}$-Te-$Ge_{0.25}Sb_{0.75}$-Te-v-Te-$Ge_{0.25}Sb_{0.75}$-Te-…	[53]
$Ge_2Sb_2Te_5$	164	a = b = 4.2257 Å c = 17.2809 Å	$\alpha = \beta = 90°$ $\gamma = 120°$	-Te-$Ge_{0.68}Sb_{0.32}$-Te-$Ge_{0.32}Sb_{0.68}$-Te-v-Te-$Ge_{0.32}Sb_{0.68}$-Te-$Ge_{0.68}Sb_{0.32}$-…* *Ge/Sb distribution varies from sources between 56:44 and 68:32 models with complete demixing[50, 51] can be considered outdated	[49] [52] [51]
$Ge_3Sb_2Te_6$	166	a = b = 4.189 Å c = 62.1700 Å	$\alpha = \beta = 90°$ $\gamma = 120°$	-$Ge_{0.73}Sb_{0.27}$-Te-$Ge_{0.77}Sb_{0.23}$-Te-$Ge_{0.55}Sb_{0.45}$-Te-v-Te-$Ge_{0.55}Sb_{0.45}$-Te-$Ge_{0.77}Sb_{0.23}$-Te-…	[35]
$Ge_1Sb_4Te_7$	164	a = b = 4.2360 Å c = 23.7609 Å	$\alpha = \beta = 90°$ $\gamma = 120°$	-Te-$Ge_{0.15}Sb_{0.85}$*-Te-v-Te-$Ge_{0.16}Sb_{0.84}$-Te-$Ge_{0.38}Sb_{0.62}$-Te-$Ge_{0.16}Sb_{0.84}$-Te-v-Te-$Ge_{0.15}Sb_{0.85}$-… *very low Ge concentrations may indicate a Sb_2Te_3 - $Ge_1Sb_2Te_4$ superstructure	[54]

Appendix B: TEM specimen preparation by focused ion beam methods

The sample preparation process is of critical importance in order to obtain the best possible results from an electron microscopy study. The transmission geometry necessitates the manufacture of very thin cross-sections. Specifically, absorption and the complexity of dynamical scattering effects demands that foil thicknesses remain well below the mean free path of electrons at the chosen acceleration voltage. While in principle, for best point resolution in purely imaging oriented studies, the thinnest obtainable samples are ideal, some other practical aspects impose a lower limit on the desired thickness. The region of preparation artefacts near the free surfaces remains largely constant for a given preparation step, and the defective volume fraction thus increases with reduced sample thickness. Additionally, the finite detector sensitivity both in a charge-couple array (CCD) and a semiconductor-scintillator plate detector necessitate an appropriate minimum signal to noise (S/N) ratio in order to avoid long averaging times which are associated with increased beam damage and drift phenomena. Lastly, analytical methods such as electron energy loss spectroscopy (EELS) and EDX require a significant sample volume to generate statistically meaningful signal counts within a reasonable timeframe. Conversely, while EDX signals are continuously improved by increased sample volumes since most X-ray photons can escape thin samples without further interaction, the large beam convergence angles used in STEM lead to a broadening of the beam for interactions occurring far away from the focal disc. The depth of focus can be estimated by the FWHM of the probe extension along beam direction[228]:

$$z_{FWHM} \approx 1.772 \frac{\lambda}{\alpha^2} \tag{B.1}$$

Here, λ denotes the relativistic wavelength of the electrons and α the convergence semiangle of the probe. For a primary beam energy of 300 keV and a half-convergence angle of 25 mrad typical for Cs-corrected high-resolution STEM, the depth of focus thus can reach close to 3 nm beyond which the probe intensity distribution significantly broadens. In incoherent thermally diffuse scattering (TDS) STEM imaging from high angles, the depth of focus can result in an increased diffuse background contribution as well as nonlinear variations in scattering intensities at small sample thicknesses, while the inelastic interaction with neighbouring atoms results in a loss of resolution in EDX. Strong electron channelling in highly oriented crystalline samples can furthermore significantly enhance the localization of the probe within specific atomic columns[229, 230], however the dynamical effects then complicate the quantification of EDX results since uniform standard Cliff-Lorimer factors can no longer be strictly applied. Thus, small convergence angles and off-axis orientations are sought for easy EDX analysis, which runs directly counter to the requirements for atomic resolution STEM. Similarly, the finite inelastic cross-sections for energy loss processes measured in EELS mean that high beam currents, significant sample volumes or long measurement times are required, while the results are often readily interpretable only if single interaction events need to be accounted for, i.e. the sample thickness lies well below the electron mean free path. The most relevant example is the local thickness determination by EELS spectroscopy using the log-ratio method[123] which estimates the mean free path as:

$$\lambda_{mfp} \approx \frac{106\, F\, E_0}{E_m \ln\left(2\beta\, {}^{E_0}\!/_{E_m}\right)} \tag{B.2}$$

F denotes a relativistic correction factor, E_0 the primary beam energy, E_m the mean energy loss without plural scattering and β the collection angle of the spectrometer entrance aperture. Mitchell in particular[231] discussed how dynamical diffraction effects can further impact the accuracy of the measurements in the log-ratio method, and experimental measurements using the software plugin described therein can deviate from real values by up to 20%.

Thus, strong requirements need to be met in sample stability, uniformity, thickness control and fidelity to the initial sample structure. Ancillary demands include a well-defined sample orientation, the ability to target particular features in the original specimen and, in modern Cs-corrector equipped analytical TEMs, ideally contain uniform amorphous or nanocrystalline structures for image and probe aberration correction, respectively.

In this study in particular, the matter is further complicated by the metastability of amorphous and crystalline structures to be investigated. As was shown in the introductory section, the crystallization temperatures for the amorphous – cubic and the cubic – hexagonal transition of $Ge_2Sb_2Te_5$ lie around 100 °C and 200 °C, respectively. Thermal treatment of the sample during preparation steps therefore needs to be virtually excluded if amorphous or metastable structures are of interest. The classical mechanical sample preparation consists of a series of steps designed to incrementally lower the cross-section thickness at one microscopic position of a macroscopic sample region by means of mechanical grinding, polishing and a final broad beam argon ion milling finishing. As such, it can influence the structure of the sample by a multitude of mechanisms. For one, cutting and grinding steps are accompanied by friction heating, as is evident in e.g. the necessity of water cooling in a diamond wire saw used during early preparation steps. Bonding of coated sample wafer pieces using two-component epoxy glue can require additional heating of the sample. Furthermore, the mechanical shear stresses acting on a thin film coating during classical preparation can, on a microscopic scale, lead to extrinsic defect formation and on a macroscopic scale to delamination as shown in Figure B.1.

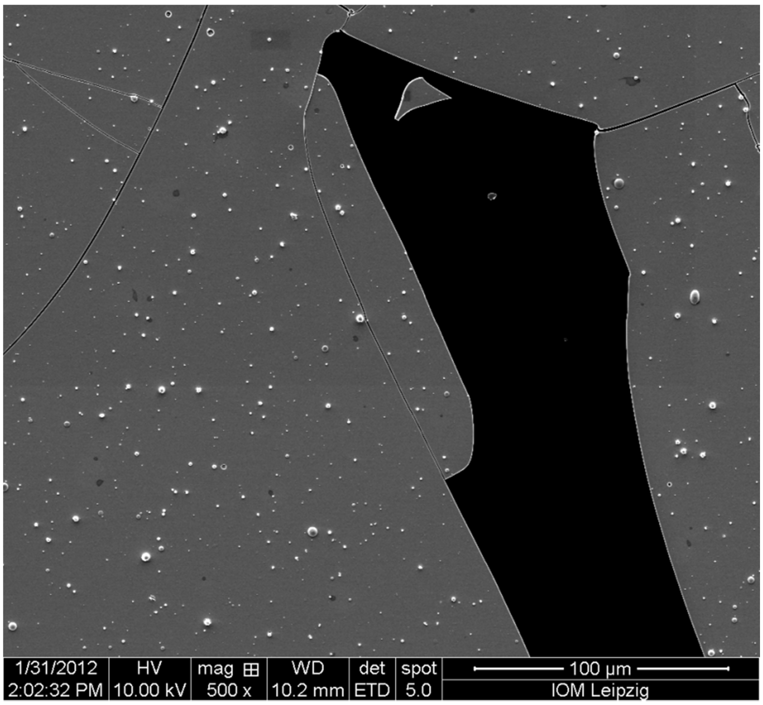

Fig. B.1: SEM secondary electron image of delamination of an amorphous GST coating from a silicon wafer substrate. Cracks in the surface, presumably partially due to thermal stresses in a relatively thick GST layer (200 nm), lead to easy detachment of thin film flakes from the substrate undergoing shear stress. The spherical particles embedded in the surface coating are micrometre scale droplets of target material that were in later optimized deposition processes vastly reduced.

Lastly, the chemical agents required e.g. to dissolve wax used in some intermediate steps to temporarily fix the sample to a mounting can lead to unforeseen chemical surface damage to the sample, as shown in fig. B.2. The classical mechanical sample preparation has been successfully applied to stable trigonal phase and superstructured thin films elsewhere[232], and therefore need not be discarded entirely. Nevertheless, it is evident that the optimization of an alternative sample preparation process for metastable and amorphous PCMs is beneficial.

While alternative classical preparation techniques exist that aim to minimize the mechanical work required, such as the small-angle cleavage technique[233], the samples in this study were prepared using subsequent steps of focused ion beam milling (FIB) with gallium ions at 30 keV and 5 keV (low-kV FIB) as well as focused argon ion thinning (Nanomill) at very low energies between 300 eV and 900 eV and low temperatures by liquid N_2 cooling. A final reactive H_2/O_2 plasma cleaning step immediately precedes the transfer of the sample into the TEM instrument.

FIB preparation of TEM specimens possesses many advantages that match the requirements introduced above. Using the focused gallium ion beam, specific regions of the specimen can be targeted for sample preparation with a resolution of less than a micrometre. A thin cross-section lamella from FIB can, under ideal conditions, be uniform in thickness over a width of up to 10 micrometre.

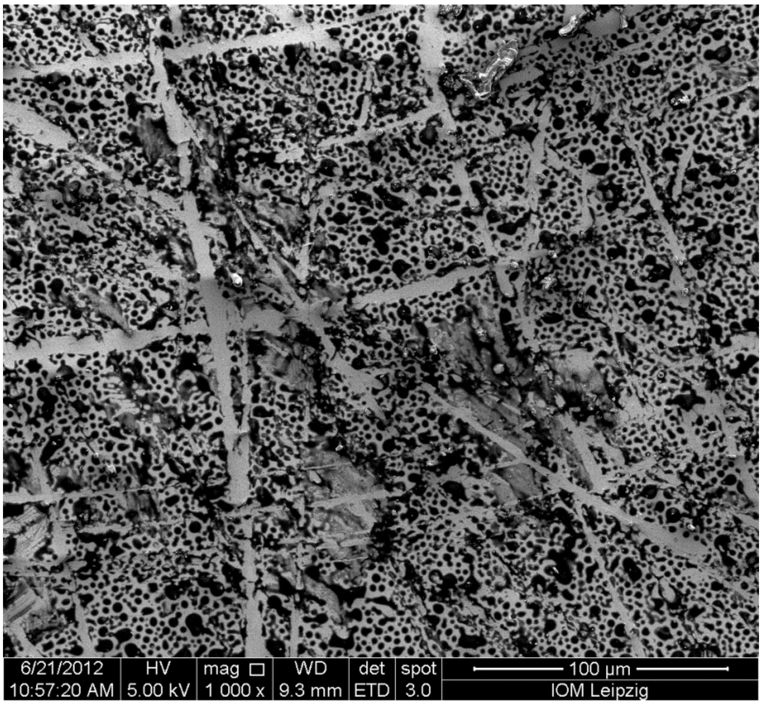

Fig. B.2: SEM secondary electron image of GST surface similar to Figure B.1, partially dissolved after being submerged in an acetone bath for about 1 min and subsequently dried in air. The original sample structure for TEM investigation is irredeemably destroyed.

Protective surface layers consisting of nanocrystalline Pt or amorphous carbon can be deposited by the introduction of carrier gasses into the FIB beam path using a gas injection system (GIS). These structures are also ideal for Cs-correction in STEM and HRTEM, respectively. The sample preparation process using a Zeiss Auriga FIB-SEM to manufacture a cross-section lamella down to 100 nm foil thickness, and subsequently thinning the sample down to 30 nm or less using a Fishione Nanomill has been extensively documented and published[122]. It involves, as already indicated, the preparation of a FIB cross-section lamella with a FIB-deposited Pt surface protective layer. The lamella is then affixed to an Omniprobe copper grid in the lift-out process and the thickness subsequently reduced down to the onset of electron transparency using 30 keV gallium ions at 1.5° grazing incidence angle to the lamella. In the event that the substrate is electrically isolating, such as BaF_2 and KCl, a conductive gold layer is electron-beam sputter-deposited onto the sample surface preceding the FIB process, thus minimizing charging effects during SEM imaging and FIB milling. The thickness of the lamella is further reduced in the low-keV thinning step down to about 100 nm (initial experimentally estimated thicknesses typically ranged between 100 nm and 150 nm) using a 5 keV gallium ion beam at 0.8 – 1.6° glancing angle tilt to beam, and then transferred to the Nanomill system. The Nanomill sample holder is cooled down to -185 °C from a liquid nitrogen reservoir. In the Nanomill, the lamella is further thinned from both sides (front and back) with a scanned focused argon ion beam at 900 eV and 10° glancing angle tilt to the beam, typically for 15 minutes per side depending on the initial estimated thickness, at about 60 pA beam current. The surface is further polished by 500 eV or 300 eV argon ions for 20 minutes per side at the same tilt angle and similar beam currents. The resulting remaining sample thickness (see Figure B.3) is estimated by recording thickness maps from EFTEM, and the Nanomill process iteratively repeated if necessary. The choice of final ion energy depends largely on the expected structures to be investigated. While crystalline thin film samples can withstand 500 eV ions and display minimal surface amorphization of 1-2 nm at the sample edges, amorphous structures are treated with 300 eV ions in order to minimize implantation effects and crystal seed nucleation as far as possible. The thinning rates for GST strongly depend on the specific parameters used as well as the thin film composition, ranging from 0.8 nm/min for crystalline GST at 900 eV down to below 0.2 nm/min for amorphous GST at 500 eV or less. This introduces the central question that arises during energetic ion bombardment for TEM sample preparation: How the impact of ions modifies the sample structure and how the remaining influence of the preparation process can be estimated.

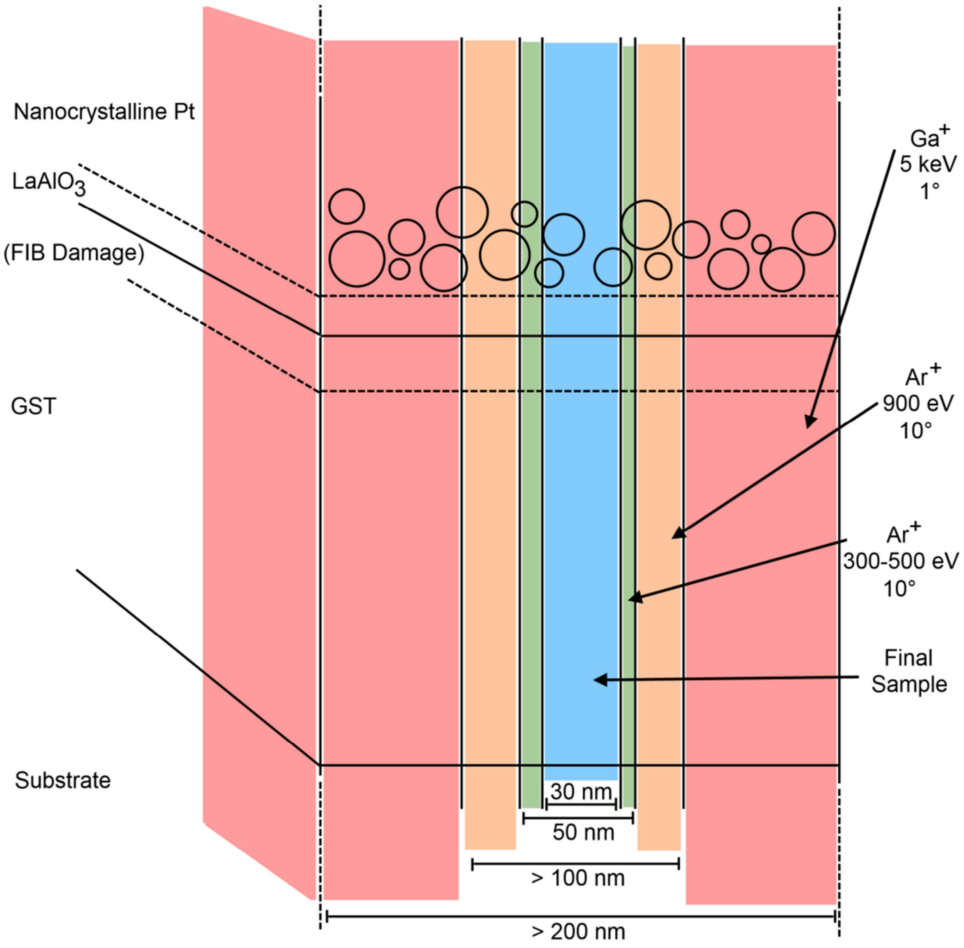

Fig. B.3: Successive reduction of sample thickness by low-keV FIB thinning and argon ion milling.

The effect of gallium ion irradiation on amorphous and crystalline GST thin films has been the investigative subject of previous literature. One such study observed the crystallinity of GST by X-ray diffraction before and after ion implantation experiments[234]. Therefore, perpendicular incidence and comparatively high primary energies up to 120 keV were used. The authors concluded that a metastable cubic thin film of 16 nm thickness was entirely amorphized after a beam dose of 4 x 10^{13} gallium ions/cm² at 30 keV. They furthermore found that amorphous thin films increased in mass density from 5.5 g/cm³ in the as-deposited state by magnetron sputtering up to 5.83 g/cm³ after ion implantation and subsequent annealing without crystallization. And lastly, they described a significant increase in the crystallization temperature by 20 – 60 °C depending on implantation dose and species. This gives a first impression on the implantation and amorphization effect of energetic ions on GST. Some factors confound the comparison with the here presented preparation steps. For one, due to the scanning motion of the ion beam in FIB and Nanomill, the exact implantation dose is not known. In the Nanomill process in particular the beam spot is somewhat broad, and does not always hit the lamella exclusively. Secondly, the purpose of the ion thinning is to remove material from the sample surface by sputtering processes without strong implantation effects. Therefore the incident ion beam angles are shallow and the energies low. In order to assess the effects of the ion bombardment on the thin sample, three processes are thus of particular importance, the ejection of sputtered and reflected atoms and clusters, the implantation of ion species and disordering of the structure, and lastly the energy transfer to the sample and heat dissipation.

In order to investigate these processes at least semi-quantitatively, SRIM (Stopping and Range of Ions in Matter)[124] calculations were performed for various ion species, primary energies and angles of incidence. The SRIM program uses a Monte Carlo approach to simulate a large number of collision cascades based on the binary collision approximation, and thus yields a statistical description of implantation and sputtering effects. As such, the required input parameters include displacement, lattice binding and surface binding energies. These are quantities that are not explicitly known for GST, in particular since each structural state should possess its distinct set of parameters. Furthermore, the SRIM calculations base their collision model on a continuous distribution in the target based on its mass density, disregarding crystalline lattice orientation effects such as forward channelling which can potentially result in deep implantation. Lastly, the calculations are always done under the initial conditions, while in practice a sputtering process from a compound target leads to a dynamical equilibrium state at the surface. While the incident ions lead to a disordering of the sample near the surface, the same region will be removed by the sputtering process. In ion implantation experiments, an analogous effect results in the steady state implantation profile. The experimentally observed amorphous surface layers therefore tend to be no thicker than the mean range of implanted ions. In the presence of preferential sputtering of one component over the other and a crystalline target, the sputtering processes predominantly occurs from an amorphized surface layer that is deficient in the preferentially sputtered species. Lastly, during the initial ion bombardment, existing surface oxidation can also lead to different sputtering behaviour than expected from the bulk material. The input parameters for simulations were thus estimated from a uniform mixture of the pure components, and the results can only give an approximate impression of the relative sputtering yields, ion implantation range and energy transfer.

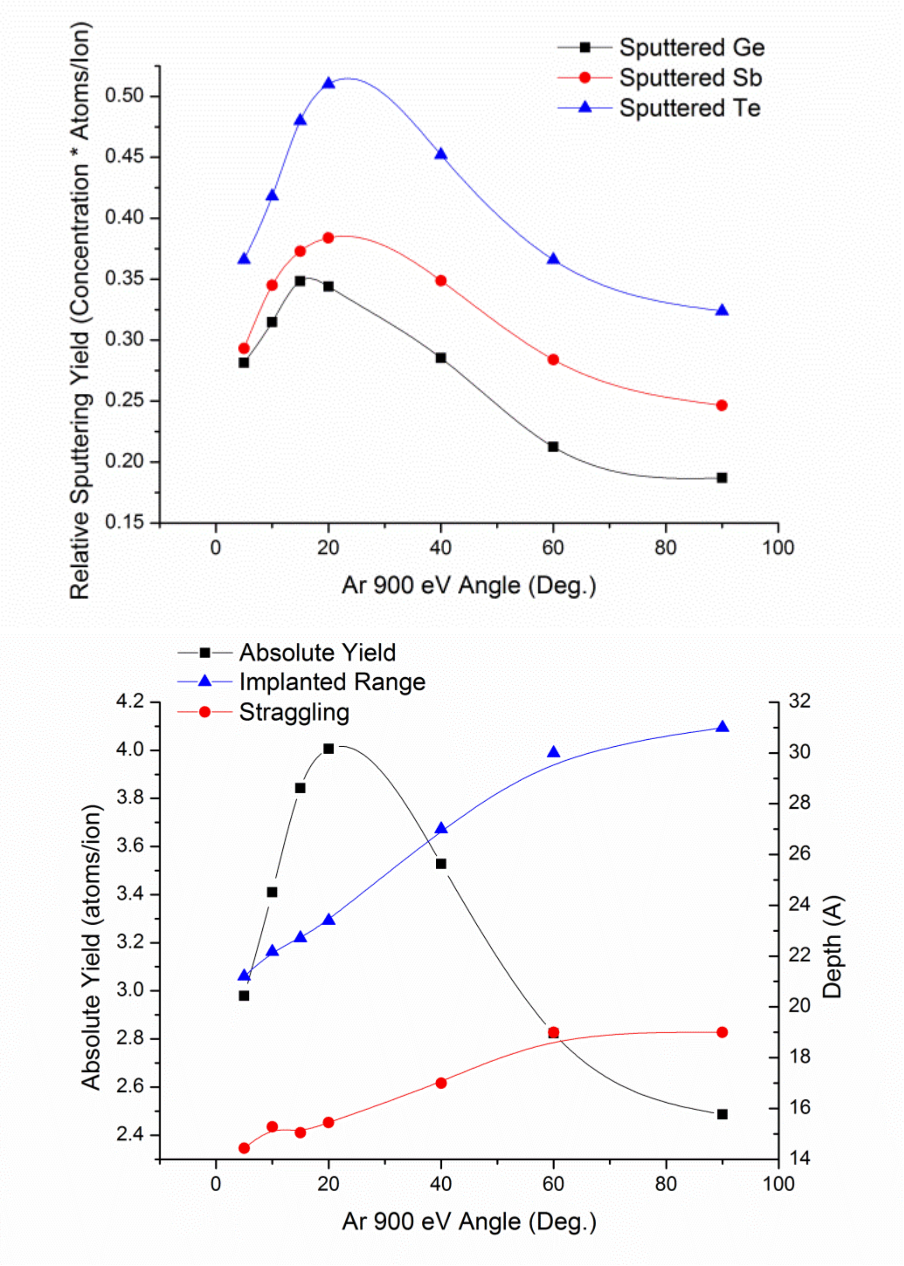

Fig. B.4: Relative sputter yield from amorphous Ge2Sb2Te5 (top), total yield and implantation profile (bottom) for argon ions at 900 eV vs. glancing angle, fitted with a bicubic spline.

In Figure B.4, the results for 900 eV argon ions at various glancing angles are illustrated. The top panel shows the dependence of sputter yield on incident angle. It can be seen that, for the chosen parameters, heavier species are more like to be sputtered from the surface, with Te being almost twice as likely as Ge even after correction for relative concentration in the sample. This leads to enrichment of Ge in the surface amorphization layer. The bottom panel of Figure B.4 shows a comparison of the total sputtering yield from 900 eV argon ions with the mean implantation depth and extension (straggling) of the implantation profile. The implantation profile is shifted into the layer as the glancing angle increases, but generally only the top 2-3 nm are heavily impacted at the chosen energy. Nevertheless the subsequent 300-500 eV thinning step is beneficial to further reduce the resulting disordered surface volume. While this effect is small for low-energy ion milling since the majority of knock-on displacements and subsequent sputter ejections occur close to the surface, under heavy gallium bombardment at higher energies and bold angles to the surface, such as during the initial steps of the FIB process, both implantation and knock-on cascades reach significant depths in the sample. This leads to large disordered layers at the top of the thin film if left unprotected, which are rich in Ge and tend to oxidize under ambient conditions (see EDX Appendix C.3). A solution for this challenge was only found by depositing an additional amorphous $LaAlO_3$ layer onto the GST thin film in vacuo during the PLD process. This capping layer both protects against further oxygen indiffusion and ion implantation, while having the additional advantage of being virtually transparent at wavelengths used for optical switching experiments and inhibiting evaporation.

The dissipation of incident energy in the sample is certainly the most complex issue to consider. Not only is the dissipation dependent on sample geometry and transfer mechanism, but the total ion dose per unit time in a scanning focused ion probe with a realistic probe shape is difficult to extract. Since individual sample positions are only exposed in intervals, a dynamic equilibration of incident energy and heat dissipation over time will set in. In order to make any prediction about ion beam induced sample heating at all, in the following the edge case of static exposure to a high-energy ion current at bold incident angle is considered.

Only a fraction of the incident ion kinetic energy is absorbed by the sputter ejection of material. The simulations predict that only about 5 % of the incident energy for light low-energy ions and 15 % for heavy high-energy ions are transferred to sputtered species. The remaining energy loss is split between ionizations (ca. 20 – 25 %), generation of vacancies (ca. 7 %) and phonon excitations (ca. 70 – 75 %). Similarly, the thermal conductivity of amorphous and metastable GST is dominated by the phonon component k_{ph}, around 0.25 W/m*K to 0.45 W/m*K for amorphous and metastable GST, respectively, while the electronic contribution k_{el} is an order of magnitude smaller. These are average literature values for the room temperature regime. The depth distribution of the phonon excitations by gallium ions at 90° is shown in Figure B.5.

In the following, the exact distribution of excitations is disregarded, as is the decay of electronic excitations into thermal states. Rather, the simplifying argument is made that, in a thermally insulating UHV chamber, the vast majority of the phonon excitations originating from the collision cascades need to traverse a volume close to the thin film surface in order to dissipate towards the heat sink. The ion current density in the FIB beam as well as the dose rate is required in order to be able to estimate the flux of energy input.

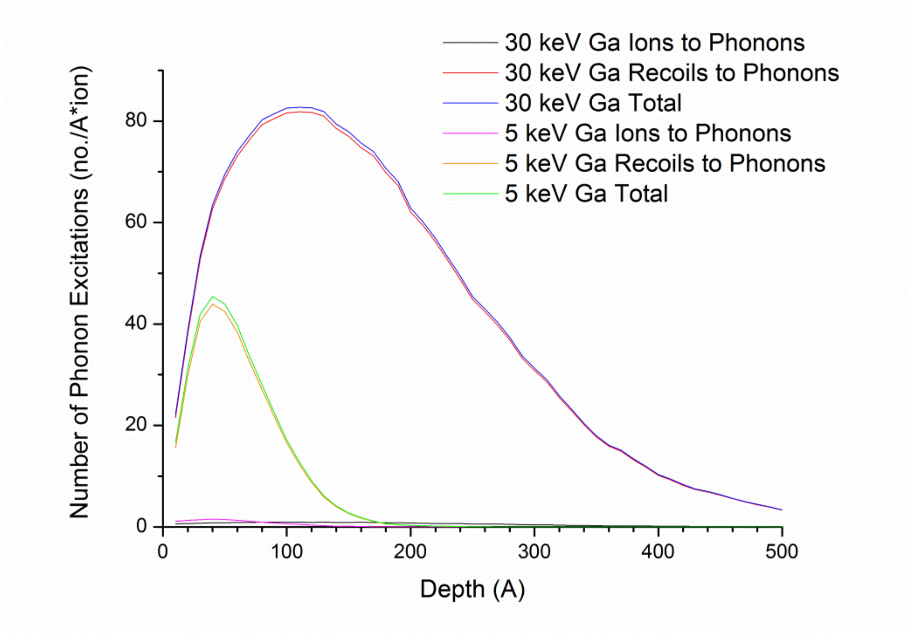

Fig. B.5: Phonon excitations by gallium ion irradiation at 90° glancing angle. The vast majority of phonons are generated by recoil collisions, and thus the curve approximately follows the DPA profile.

The probe size in the FIB is dependent on the desired current, with typical values around 25 nm probe diameter at 50 pA current for imaging and 1.8 μm diameter at 12 nA for milling at 30 keV. In Figure B.6, the lateral beam size can be estimated to 344 nm at 600 pA. If the probe shape at low currents is approximated to a cylindrical top-hat function with radius of the probe FWHM, the current equals to 6.46 x 10^{-15} A/nm².

In a liquid gallium ionization source of the type used in the Zeiss Auriga FIB, the charge particle distribution at operating voltages is heavily skewed towards single charge ions, with [Ga2+]/[Ga+] ca. 10^{-4} [235]. The current densities given above can thus be converted to ion dose rates with single elemental charges, yielding 4.035 x 10^{4} ions/nm²s.

If one could simplify the problem to a plane geometry by averaging the individual phonon excitation cascades to a macroscopic uniform heat source (i.e. a 2D heat source on top of a thin film of known thickness and composition, on a bulk heat sink at room temperature and surrounded by a thermally insulating vacuum), a 1D steady state heat conduction equation would be used to predict the temperature increase ΔT:

$$\Delta T = \dot{Q} t_{film} / k_{ph} A \tag{B.3}$$

Here, $\dot{Q}$ denotes the energy influx to the surface layer per unit area, t_{film} the film thickness and A in this case the unit area i.e. 1 nm². Inserting values from above for a 100 nm thick amorphous GST film and taking the entire energy transfer to phonons per incident ions into account, about 19.125 keV/ion or 3.06 * 10^{-15} J/ion at 30 keV primary ion energy, one obtains ΔT = 49 K, which is larger than the range of similar reported values[236] due to the low thermal conductivity of the layer material and the above discussed approximations. In this case the ion beam would not be scanned over the surface but rather be static at one point, and the heat source describes an intifisimal layer depth below the excitation volume. Since in reality the heat flow from a spot source also occurs in radial direction, and the true dose rate during the scanning motion is lower, real values for the local temperature increase can be expected to be much lower. At 600 pA and 30 kV milling, typical values for the scanning motion are 100 μs pixel dwell time and 200 % pixel fill factor meaning ratio of spot area to pixel size i.e. every pixel gets effectively exposed roughly twice. The dose rate for the above values even in the extreme example of a repeated line scan such as in Figure B.6 would thus be considerably lower (by two orders of magnitude), and each position would have about 1.5 milliseconds between exposure intervals to freely radiate heat.

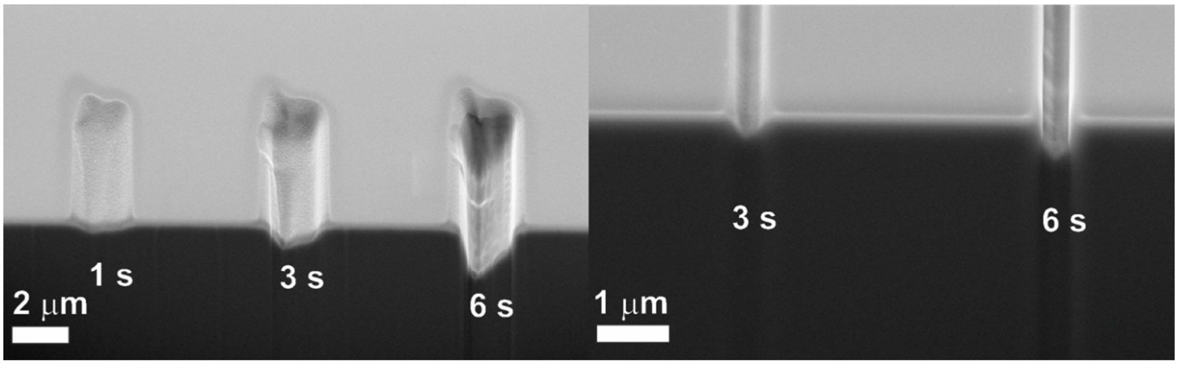

Fig. B.6: Cross-sections of FIB trenches with 30 keV Ga^+ beam. Asymmetric beam profiles at 12 nA beam current (left) and symmetric profiles at 600 pA beam current (right). The times indicated correspond to the total milling time of a single pixel wide and 10 μm long line object. The dark streaks in the bulk of the cross-section may result from channeling in the (111) oriented silicon wafer.

It is also important to note that this approach is only reasonable if $k_{substrate} >> k_{film}$, and on a thermal insulator such as BaF_2 the thin film may experience additional heat buildup. Furthermore, in the case of a thin cross section such as during low-keV thinning, or for very thin films, the geometric thickness approaches the mean free scattering length of the phonons which results in an overall lower thermal conductivity than in the bulk material. A complete description of focused ion beam induced sample heating by ab-initio or finite elements approaches is unfortunately still lacking in part due to the large uncertainties regarding transfer mechanisms, and most published work is limited to experimental studies of its effects. Since the plane geometry models the 30 keV direct incidence case, it may still give an impression of the upper boundary for the expected temperature increase in the sample. Nevertheless, even small increases in temperature, if prolonged, can lead to the modification of metastable amorphous and crystalline GST. The final thinning steps were thus performed under liquid N_2 cooling of the sample stage, and the expected sample preparation artefacts are therefore limited to ballistic knock-on effects near the surface.

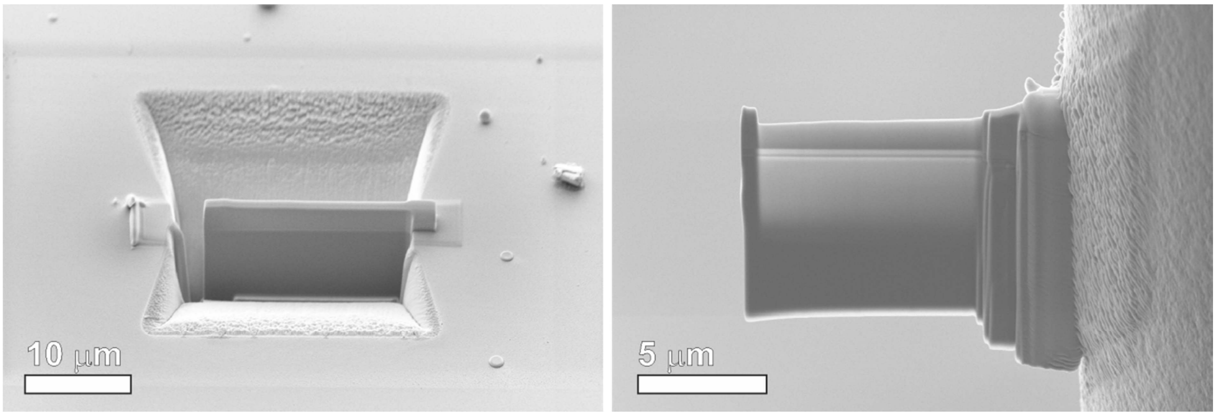

Fig. B.7: Secondary electron images from cross-section lamella of GST on BaF_2 with thin conductive Au coating and sacrificial Pt buffer, in the FIB-cut trench before liftout (left) and affixed to an Omniprobe Cu grid (right). The thick frame left after low-keV Ga^+ thinning promotes mechanical stability of the sample.

While under ideal conditions the FIB + low-keV process yields excellent results (see Figure B.7), it is necessary to mention two focused ion milling artefacts that can negatively impact the final sample. For one, re-deposition of sputtered material can lead to surface contamination by adsorption of sputtered species. The source of re-deposition can be twofold. In cases where the ion beam does not hit the lamella exclusively, but rather also skirts the copper grid or the back-wall of a trench during different preparation steps, some amount of foreign material may be sputtered towards the sample. This type of extrinsic contaminant is significantly reduced by subsequent low-keV thinning steps, but residual surface contaminants can appear as background signal in chemical mappings. The other source of redeposition is intrinsic to the sample geometry. A cross-section lamella of a thin film coating consist of a stack of different layers, e.g. Pt buffer layer, $LaAlO_3$ capping layer, GST thin film coating and Si substrate. Each individual layer possesses a distinct sputtering coefficient for the chosen set of parameters. This can result in surface steps at interfaces between harder and softer materials. If the ion beam hits such a feature in the surface topography at a shallow incident angle, some material from the softer layer that is sputtered in forward trajectory may then become absorbed on the sloped face of the surface step, or some material that is removed from the slope in the harder layer may be ejected back in the direction of the softer layer. This process can be enhanced at low sample temperature due to the enhanced sticking coefficient of sputtered species with low energies onto the surface.

The effect is most prominent at the interface between the single-crystalline substrate and a soft amorphous layer. Intrinsic redeposition in GST-Si coatings of GST onto the substrate can be pronounced, however since the substrate is usually not of particular interest for the investigation except for its general crystallographic orientation, does not necessarily have a major impact on the results.

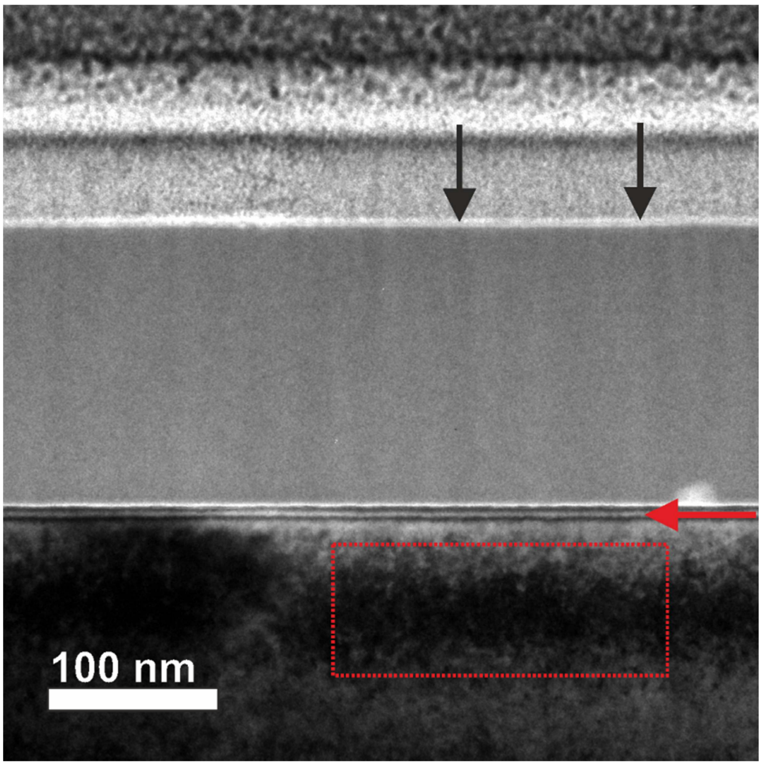

Figure B.8: BF-TEM image of amorphous GST coating on Si substrate with native SiO_x interface layer, after initial low-keV argon ion thinning. Black arrows indicate slight curtaining, while the fringes at the substrate interface indicated by the red arrow result from the local thickness gradient at the interface edge. Grainy features on the substrate surface of the lamella can be partially related to re-deposition effects.

The curtaining effect refers to periodic variations in local thickness of a uniform layer which align with the microstructure in the layer above (see Figure B.8). Various mechanisms can be responsible for curtaining effects in FIB preparation. The beam tails overlap when the pixel fill factor is chosen such that the beam positions are closely spaced, potentially leading to enhanced sputtering in the overlap regions, while a too large spacing can lead to deficient sputtering in-between beam positions. In the presence of multiple crystalline grains of random orientation, selective ion channelling along crystallographic axes can lead to oriented removal of material in some grains. The most relevant process for the case of GST with a Pt buffer layer on top is the uneven removal of material in the presence of density variations in the nanocrystalline top layer. Denser regions are sputtered more slowly, and at shallow angles the ion beam will be shadowed by the resulting topography, thus projecting the uneven thinning of the buffer layer onto the nominally uniform thin film coating. Curtaining can be reduced by back-side ion milling[237], however the effect is only pronounced in amorphous GST (where the absolute sample thickness is not as important) while crystalline samples are typically largely uniform.

Appendix C: Supplementary figures

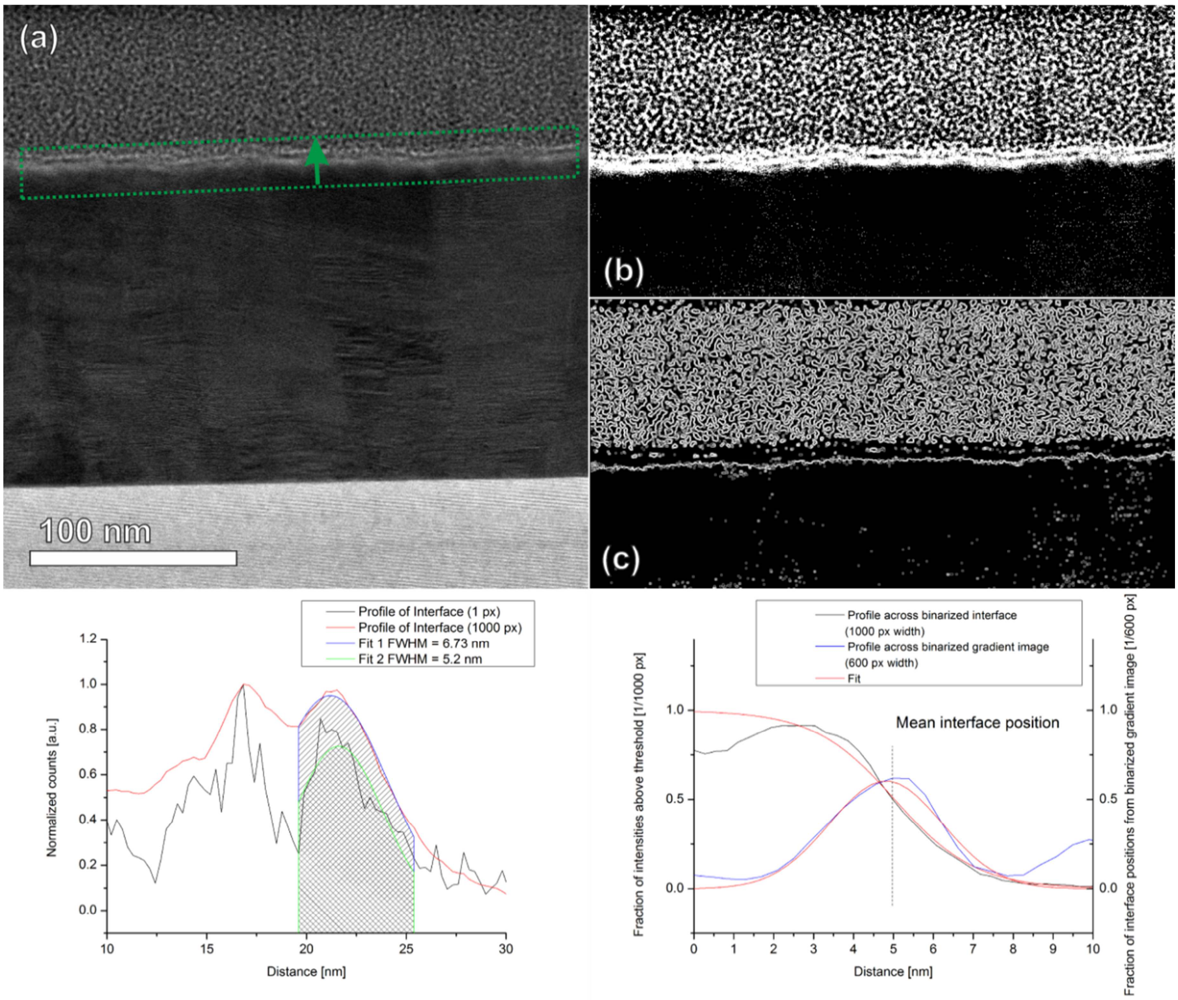

Appendix C.1: Interface roughness evaluation, carried out on a DF-TEM image of a columnar textured GST thin film (a). A minimum level of image contrast is required. The image is then binarized around the brightness level at the interface (b), and subsequently gradient (Sobel) filtered (c). A profile perpendicular to the mean interface orientation then yields a distribution of interface positions across the profile integration width (graph bottom right). The intensity distribution of a similar profile across the unprocessed image is shown for comparison (bottom right), as well as FWHM fittings of a simple Gaussian roughness model.

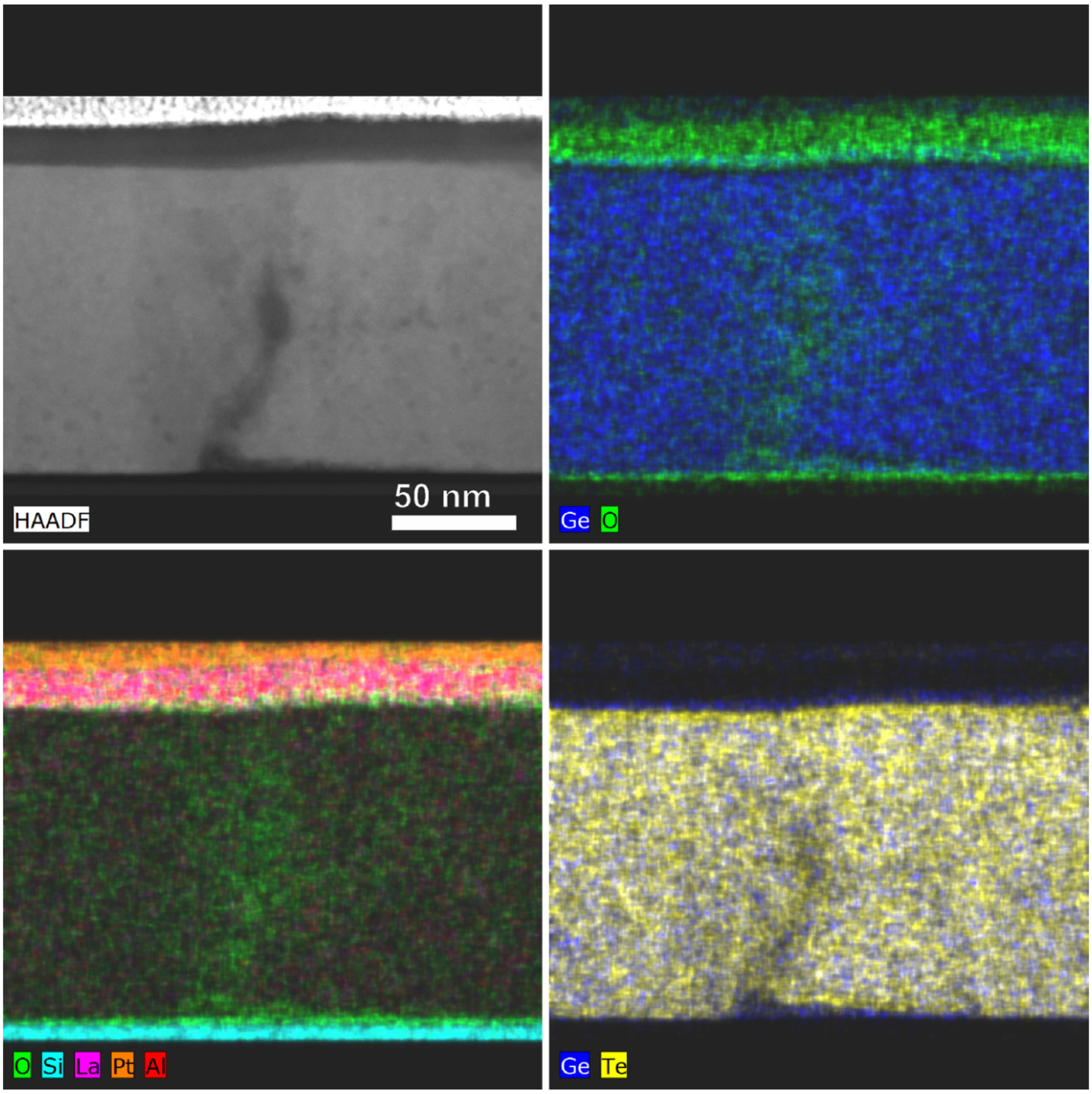

Appendix C.3: EDX mappings of microvoid in annealed GST225 thin film (chapter 3.2). The Ge/O and Ge/Te maps indicate slightly more Ge (blue) at the LaAlOx interface and inside the void, which correlates with a rise in the Oxygen signal. Presumably, Ge segregates at the interface and open surface and oxidizes after the lamella is exposed to ambient air. The overall composition within the bulk of the thin film (Ge:20.3 Sb:23.6 Te:55.9 [at.%]) still matches the as-deposited composition (chapter 3.1) reasonably well, with about 1-2 at.% of Ge and Sb (within the margin of error) less in the post-annealing GST compound.

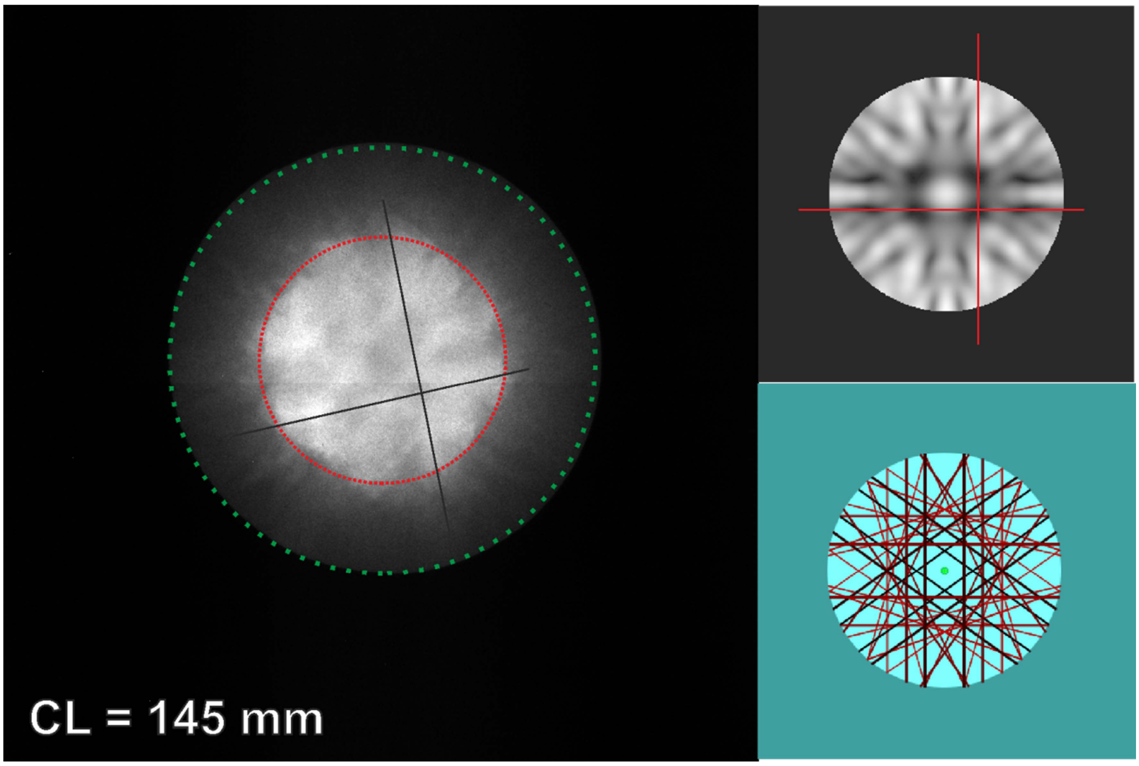

Appendix C.4: Blurred convergent electron beam diffraction pattern recorded from the CCD while scanning the beam over a small focus area in a crystalline thin film at large defocus (left). Dashed green line marks the edge of the HAADF detector plate, corresponding to 40 mrad at the chosen camera length. Simulated LACBED pattern of [110] zone axis cubic GST (top right) and corresponding ZOLZ deficiency lines (bottom right), calculated with the JEMS software by P. Stadelmann. Solid black (left) and red (top right) lines mark similarities in Kikuchi features, useful for adjusting the zone axis orientation.

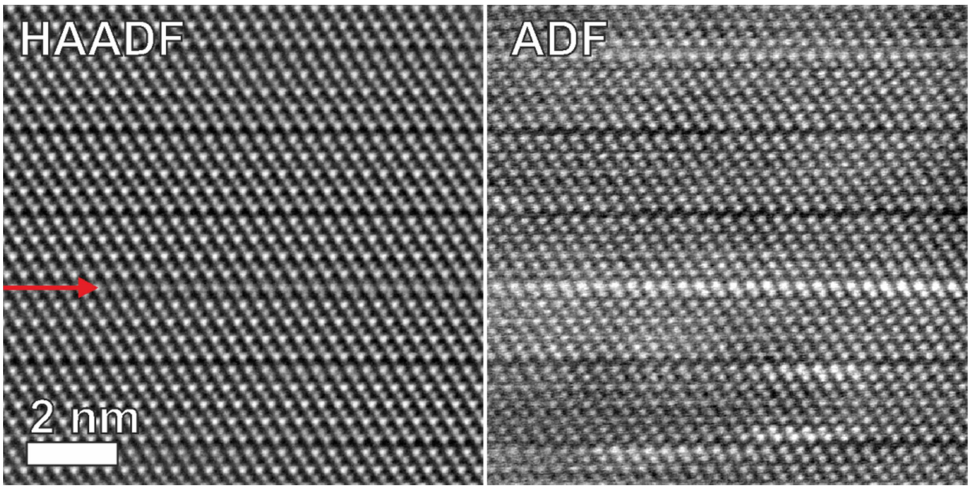

Appendix C.5: Comparison of HAADF (left, 80 - >200 mrad) and ADF (right, 19.1 – 80 mrad) STEM images acquired in parallel from sample annealed at 250 °C. In the Z-contrast image from high-angle scattering, only one lattice defect (stacking transition, marked by red arrow) is readily visible. The ADF image also includes coherent scattering contributions. As a consequence, lattice distortions can result in strong ADF contrast changes, while the same only result in a more diffuse HAADF contrast. ADF contrast is however also more sensitive to defocus changes and amorphous contributions, and the atomic structure in the stacking defect is not as clearly resolved as in the HAADF image.

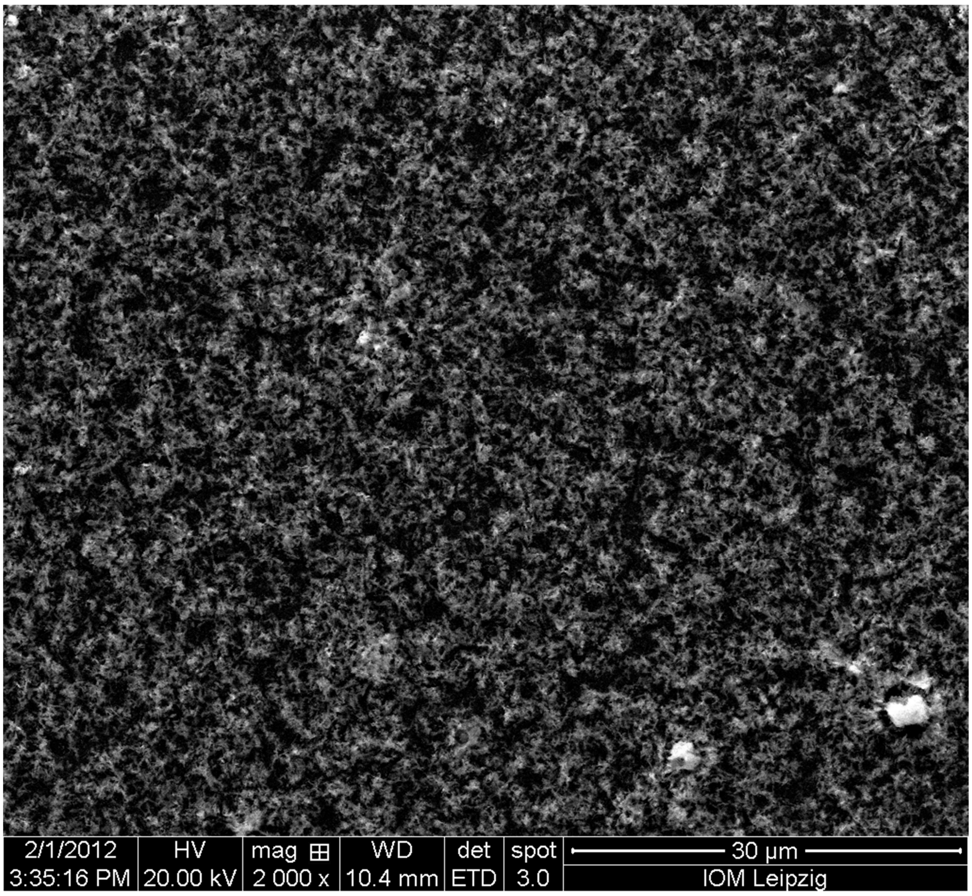

Appendix C.6: SEM image (SE detector) of uncovered GST thin film on Si/SiO$_x$ after annealing at 300 °C. The material has delaminated and is crystallized into a dense needle-like morphology. In addition, material is lost to evaporation in the vacuum oven, predominantly from the Germanium component.

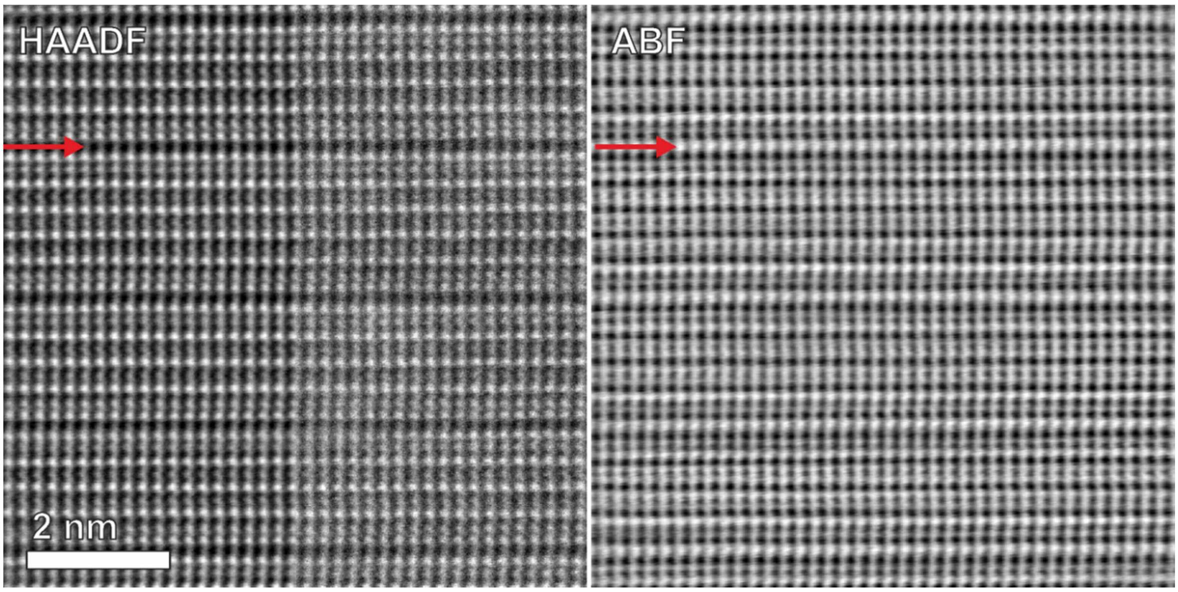

Appendix C.7: HAADF (80 – 200 mrad) and ABF (0 – 10 mrad) images of GST sample annealed at 290 °C, acquired in parallel. The right half of the HAADF image shows the unprocessed HAADF signal, while the left half as well as the ADF image were FT-filtered (Radial Difference Filter). Red arrows indicate the same layer position in both images, exhibiting unexpected weak intensity in the nominally empty vacancy gaps. In the ABF signal, the contrast is inverted and predominantly composed of coherent scattering contributions as well as the transmitted beam (i.e. maps the loss of primary beam intensity due to coherent scattering). The image is slightly distorted due to non-linear drift. The additional intensity in the vacancy gaps may originate from diffusive material transport between building blocks, although this is not conclusive due to the large lamella thickness (55 nm) in conjunction with a minimal tilt out of the [01-10] zone axis and residual condenser astigmatism. A further alternative explanation would be that de-channelling and defocus effects are more readily visible at this large lamella thickness, however contrast delocalization due to de-channelling in image simulations is typically predominantly observed between neighbouring fully occupied layers within one building block, while additional HAADF intensity from the sample past the depth of focus (about 4 nm) should only result in an increased diffuse background (as can be seen in the noisiness of the unprocessed image).

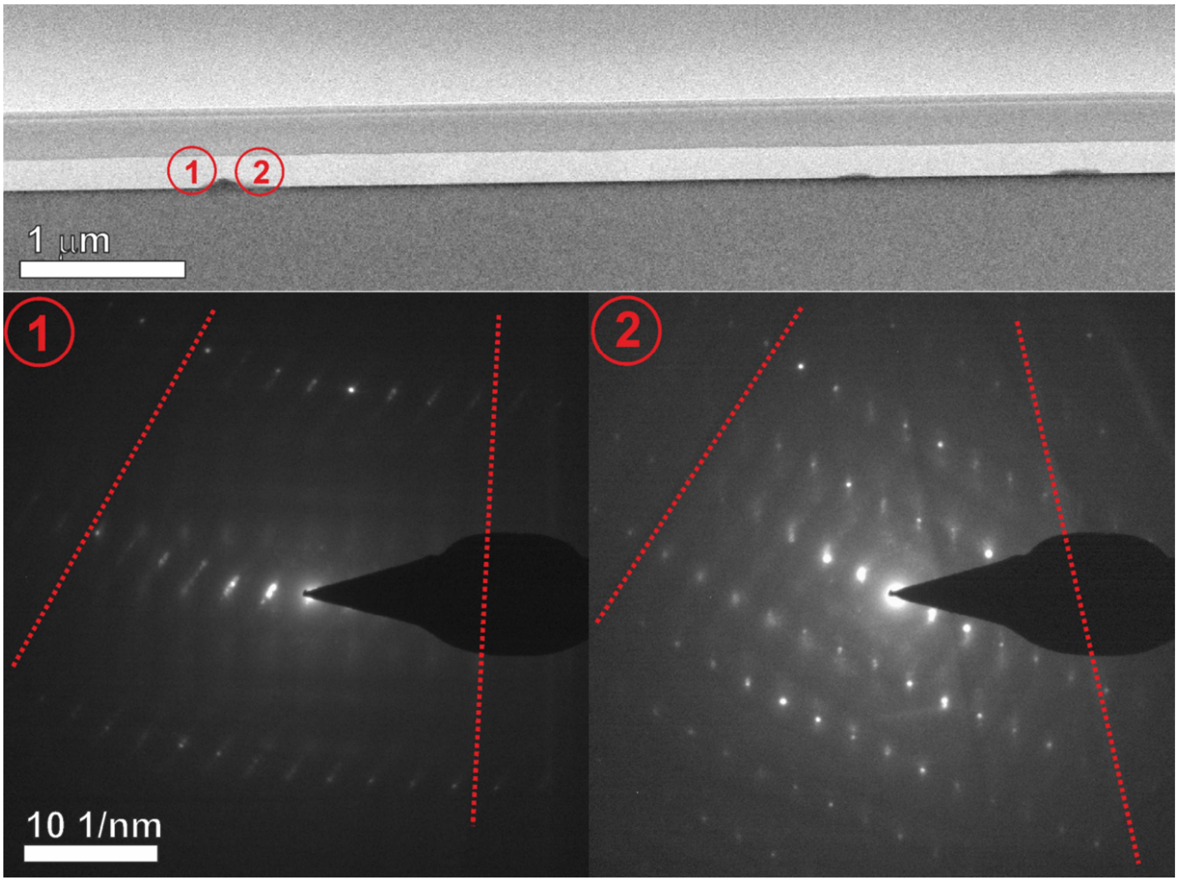

Appendix C.8: NBD-STEM overview image (HAADF) of GST thin film with $LaAlO_x$ cover layer, annealed at 320 °C (top), and two selected NBD patterns from positions marked in the image, corresponding to the two grains adjoined by the grain boundary shown in Figure 3.38. The sample is oriented in Si(111) substrate zone axis parallel to the surface and both grains are thus tilted out of GST zone axis, by approximately similar angles (as can be seen by the Kikuchi bands schematically indicated by the dashed red lines). The closest low-index zone axis however appears to be dissimilar, as confirmed by the subsequent high-resolution investigation.

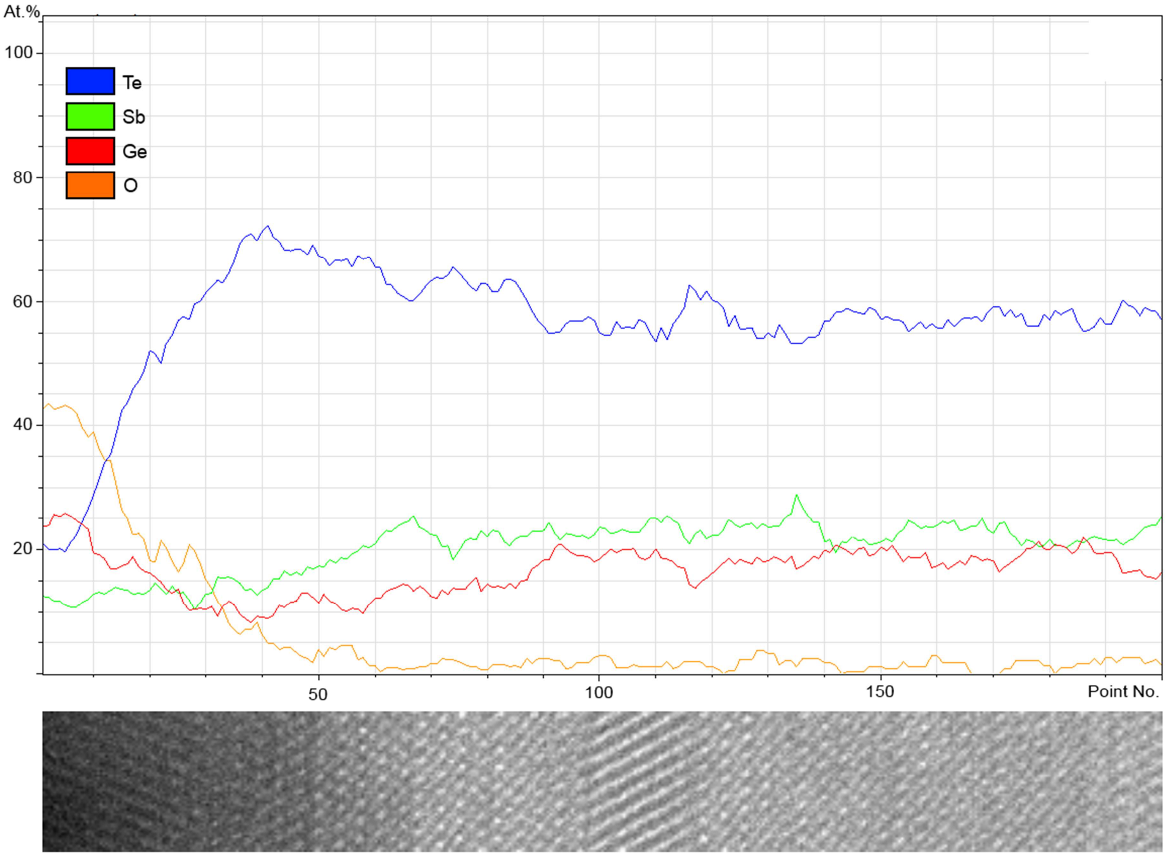

Appendix C.9: EDX-linescan of rel. at.% composition measurement from oriented thin film on cleaned Si(111), deposited at 185 °C, and corresponding HAADF image below. Composition profiles are averaged over 7 adjacent measurement points in order to reduce noise spikes. While the composition within the thin film (right half of the plot) roughly matches the target composition, significant deviations in Te, Ge and Sb content are visible in the top 3-5 nm near the surface (left side of plot). In particular, a slight drop in the Ge content followed by a marked increase at the very surface indicates at Ge depletion zone and Ge-rich surface layer. The sharp increase in Oxygen content at the surface can be attributed to post-deposition oxidation of the Ge-rich surface layer in ambient air, since the sample was not subsequently covered by a $LaAlO_x$ protection layer. The EDX evaluation of light elements in compounds, and thus the O-K peak, by the Cliff-Lorimer method[238] is however less precise due to the lower fluorescent yield compared to heavy elements. The particular behaviour of Ge depletion and surface layer formation is enhanced at deposition temperatures above 220 °C.

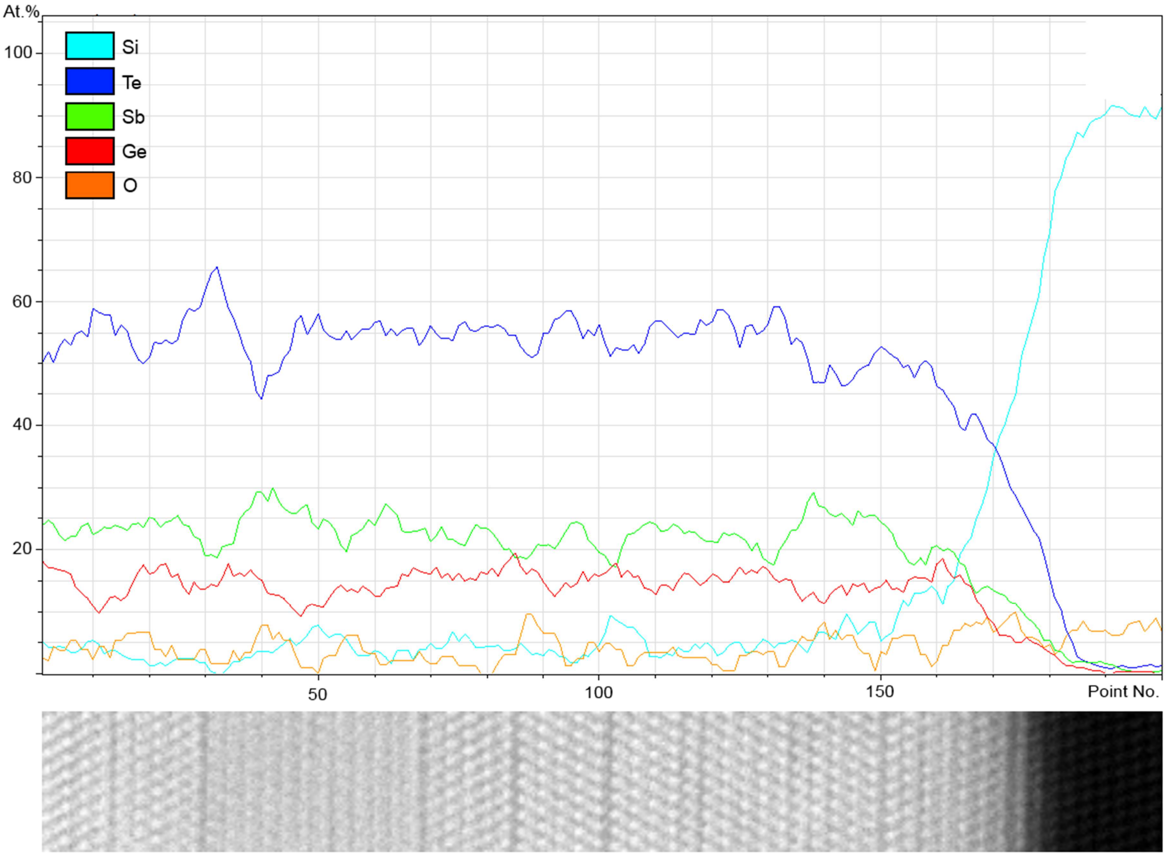

Appendix C.10: EDX linescan across interface between GST thin film and substrate, deposited at 185 °C. In order to minimize beam damage, a relatively short acquisition time was chosen (2 min, scanning across 200 points in a line with an 18 µs dwelltime), which however lead to statistical noise in addition to the residual spatial drift. Profiles as shown were thus averaged over 5 adjacent measurement points, and indicate a small excess of Te in the surface passivation layer.

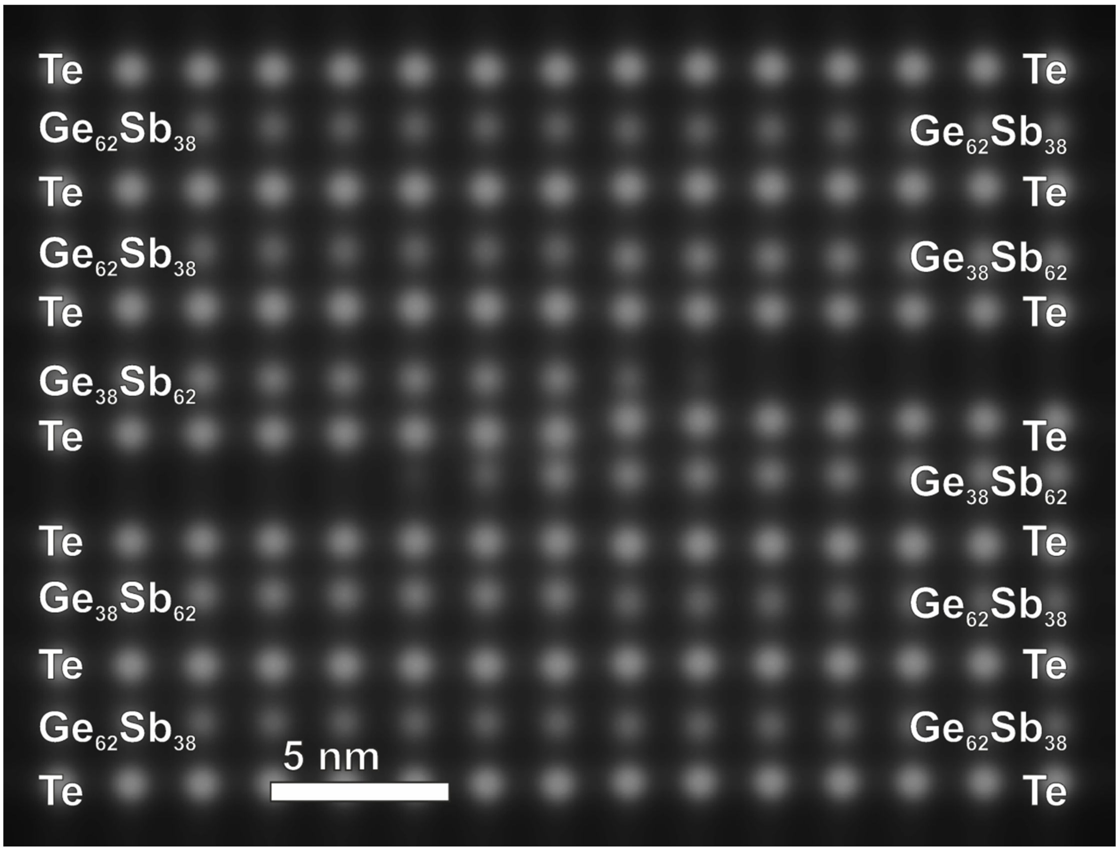

Appendix C.11: Simulated HAADF-STEM image (C2 = 25 mrad, Detector = 80 - 200 mrad, defocus = -2 nm) of idealized defect structure model in $[01\bar{1}0]$ projection, based on the GST225 model by Urban et.al. The observed gradual change in scattering intensity approximately matches the experimental data, although real defects may extend the lattice distortion in the defect core over multiple adjacent positions.

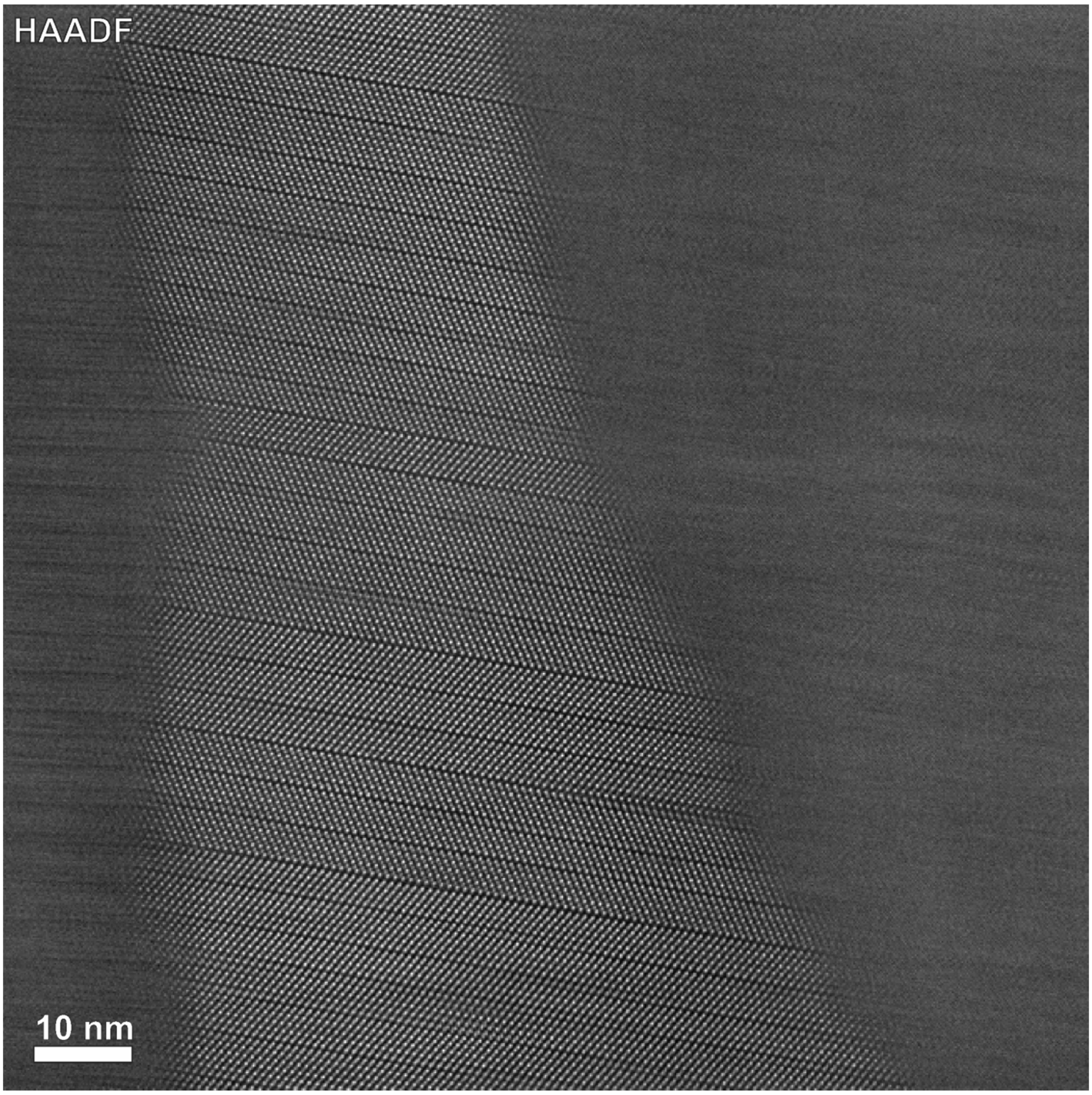

Appendix C.12: Columnar grain deposited at 110 °C onto cleaned Si(111), as seen in Figure 3.44.

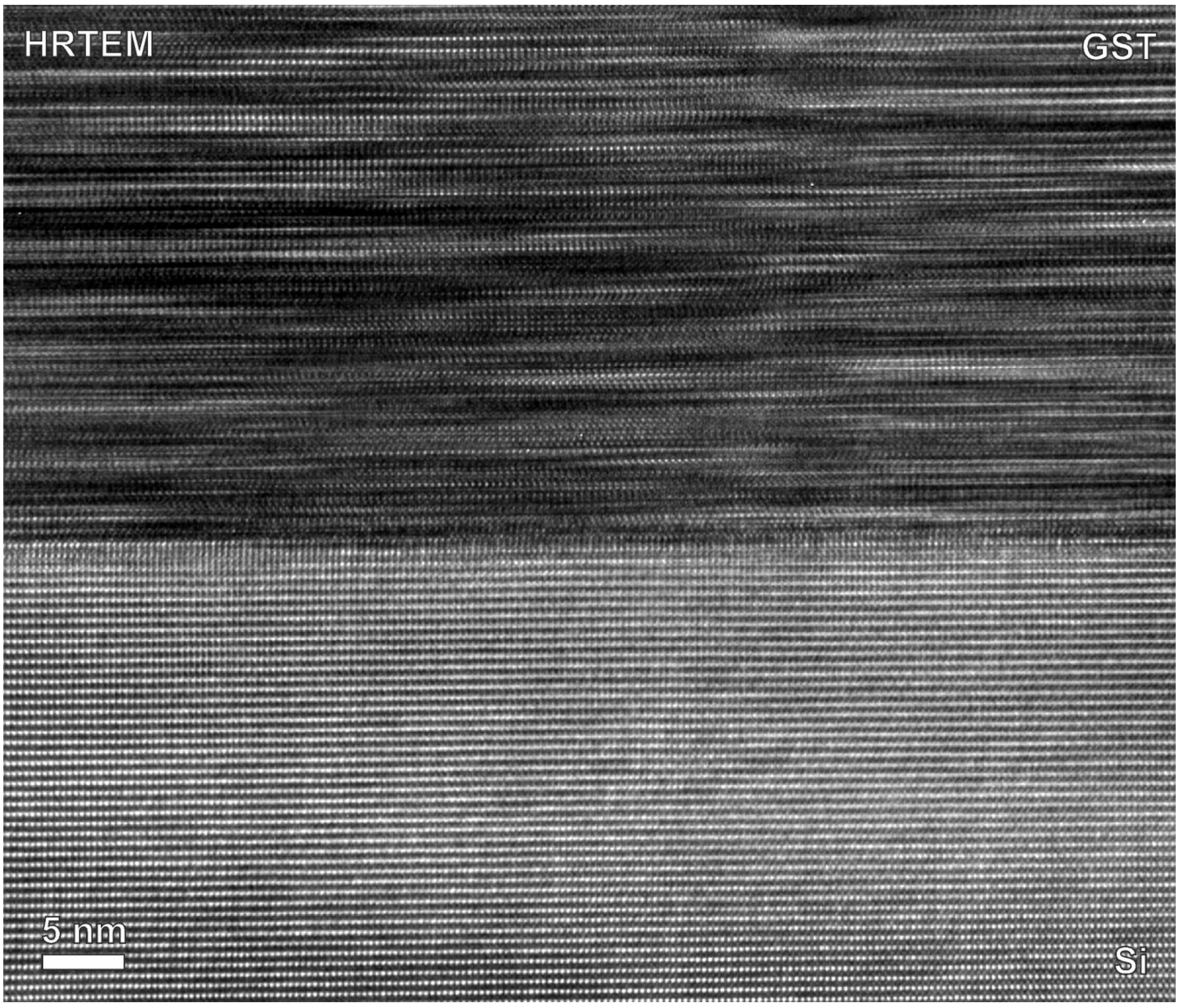

Appendix C.13: HRTEM view of interface between cleaned Si(111) and GST thin film deposited at 185 °C, as seen in Figure 3.51.

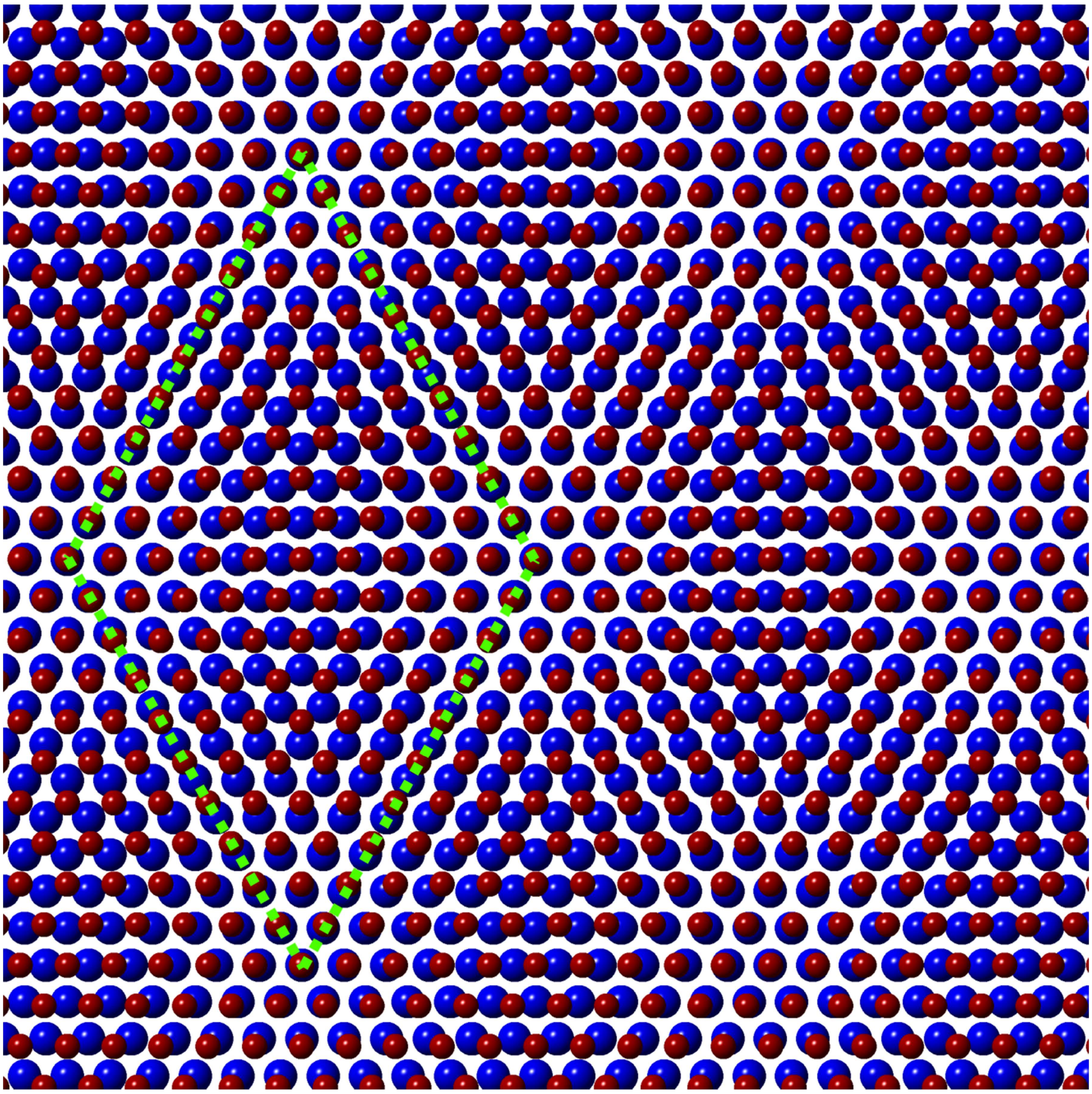

Appendix C.14: 0° rotation CSL between Si(111) (blue spheres) and GST(0001) (red spheres) Te-Te planes.

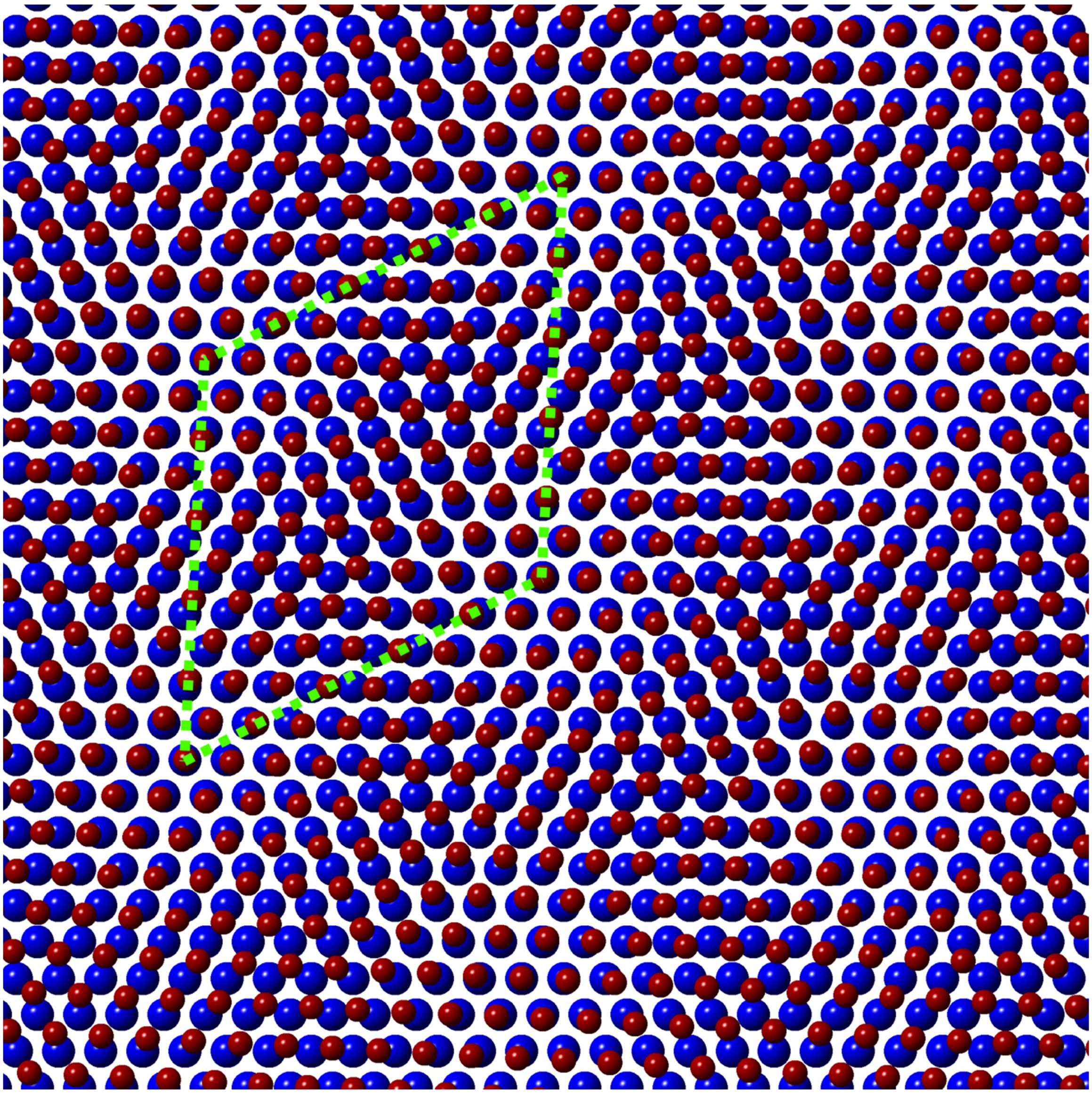

Appendix C.15: 3° rotation CSL between Si(111) (blue spheres) and GST(0001) (red spheres) Te-Te planes.

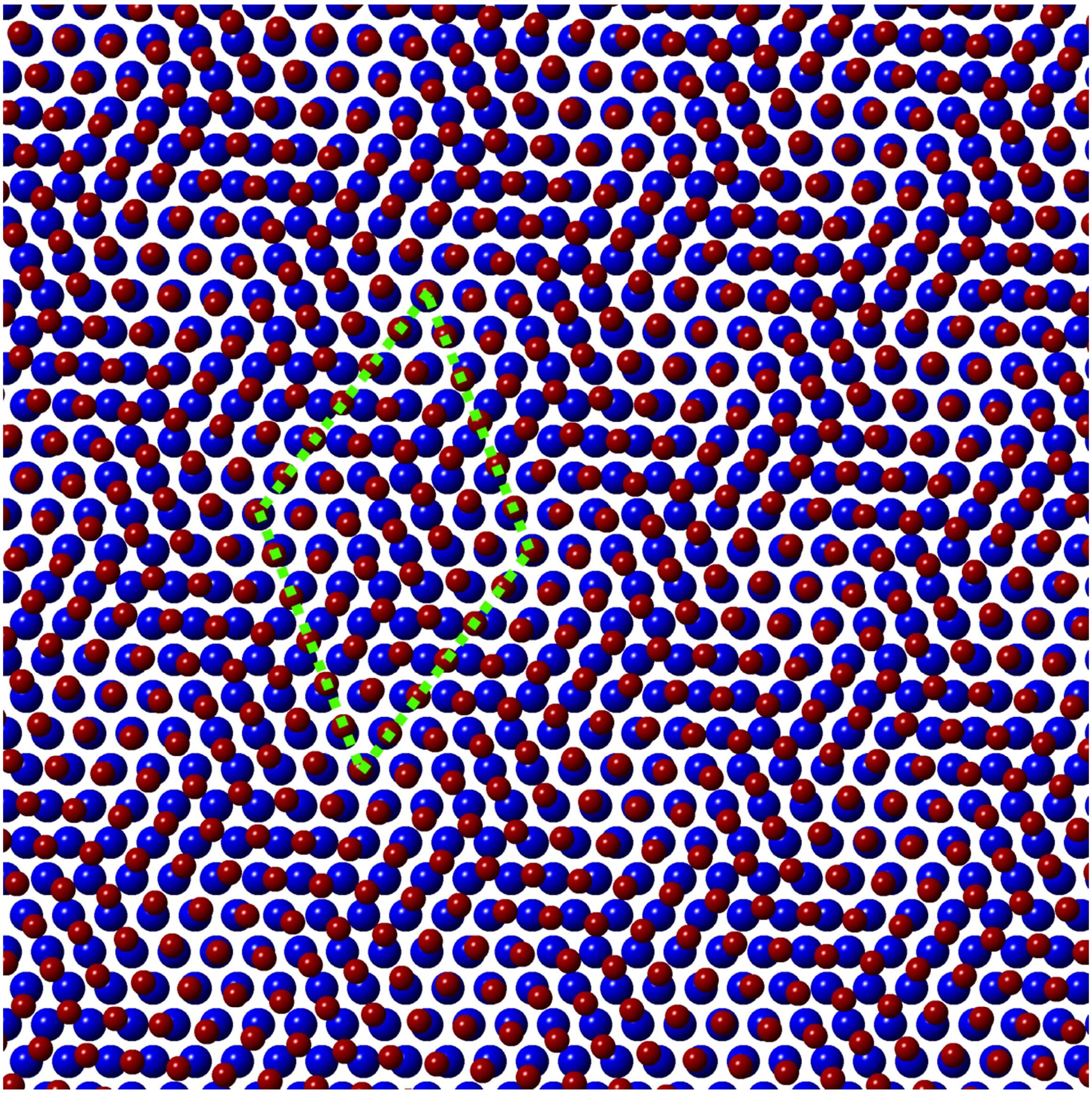

Appendix C.16: 8° rotation CSL between Si(111) (blue spheres) and GST(0001) (red spheres) Te-Te planes.

Appendix D: Grain boundary symmetry between trigonal lattices

In the presented case (Figure 3.37), one grain is tilted in zone axis $[11\bar{2}0]$ projection, while it can be seen that the densely occupied planes in the second grain are inclined towards the first, within the image plane, by 54°. The second grain however is also rotated out of the zone axis of the image plane, and the grain boundary does not run exactly along the $(103) \triangleq (2\bar{1}\bar{1}9)$ planes of the first but rather at an out-of-plane tilt angle resulting in the gradual change in background intensity at the edge of the grain, where the two overlap. Comparing the width of the edge region (variable, ca. 2.5 nm on average) with the depth of field at the chosen microscope settings ($\approx$ 3 nm under ideal conditions at 25mrad C2 aperture and 300 kV acceleration voltage[152, 239]) lets one approximate the angle between the projection plane and the grain boundary to measure $tan^{-1}\left({}^{2.5}\!/_{3}\right) \approx 40°$, however the contrast region at the grain interface is not well defined and the depth resolution of the microscope is based on a rough approximation, and such an estimate may prove unreliable. Nevertheless, from the contrast behaviour and the visible faceting the conclusion lies close that the grain boundary cuts across the image at an oblique angle along one specific set of planes of the left-hand grain (see Figure D.1), in a faceted arrangement so as to retain the overall grain boundary direction. For a more exact description of the grain boundary symmetry it would be necessary to tilt the sample until the incident beam direction runs along the grain boundary, and additionally to tilt both grains into low-index zone axis. This is unfortunately hindered by the distance of the objective pole pieces in the microscope and the specific sample holder in use, which limit the maximum tilt angle of the sample holder. It may be reasonable to assume that the diffuse lines seen in the right-hand side grain result from the $(01\bar{1}\bar{3})$ planes since their spacing (0.31 nm) approximately matches the predicted value (0.309 nm). Furthermore the rotation angle between the zone axis vector $[110] \triangleq [11\bar{2}0]$ and a low-index viewing direction down a $(01\bar{3}) \triangleq (01\bar{1}\bar{3})$ plane, e.g. $[031] \triangleq [\bar{1}2\bar{1}1]$ is roughly 54°, and it is possible that the right-side grain in the image is close to the latter projection (in which a strong overlap between neighbouring atoms results in a diffuse line along the $(01\bar{1}\bar{3})$ plane. The residual miss-orientation between neighbouring grains results in local strain at the grain interfaces, which in turn facilitates the formation of the observer correlated stacking defects and twin structures possible due to the weak bonding interaction across the intrinsic vacancy gaps.

The preferred grain boundary orientation is further illustrated in Figures D.2 – D.3, expanding on the above discussed sets of planes and zone axis projections. From the schematic view down a $[1\bar{1}\,2/3]$ projection (Figure D.2), it can be seen that the most probable candidate for a low-index, high-symmetry plane of the left-hand grain in the grain boundary is the $(023) \triangleq (02\bar{2}3)$ plane which runs at a 34° angle to the [110] projection plane. The orientation of the right-hand grain cannot be refined further from the STEM image in Figure 3.38, however if it does match the [031] zone axis orientation, then the $(1\bar{2}10)$ planes would be the closest low-index planes to the 34° angle of the left-hand grain (Figure D.3). These planes however do not fit well into a low-Σ CSL due to their differing in-plane symmetries and the complex stacking of the trigonal lattice (see Figure D.4). Provided that the grain orientations and interface planes were identified successfully, which for the right-hand grain is not certain, this would indicate that the grain boundary itself is not stabilized significantly by octahedral bonding arrangements across the interface.

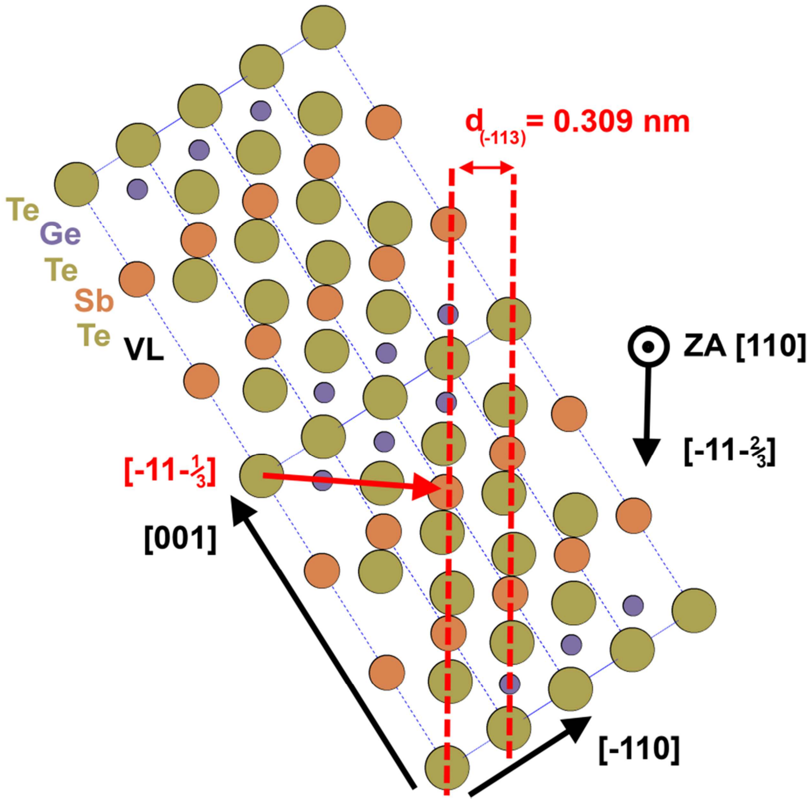

Fig. D.1: Lattice model of 2x2x2 trigonal unit cells of GST225, in $[110] \triangleq [11\bar{2}0]$ projection. The dashed red lines indicating $(\bar{1}13) \triangleq (\bar{1}103)$ planes correspond to the dashed lines in the top-right panel and partially to those in the bottom-right panel of Figure 3.37.

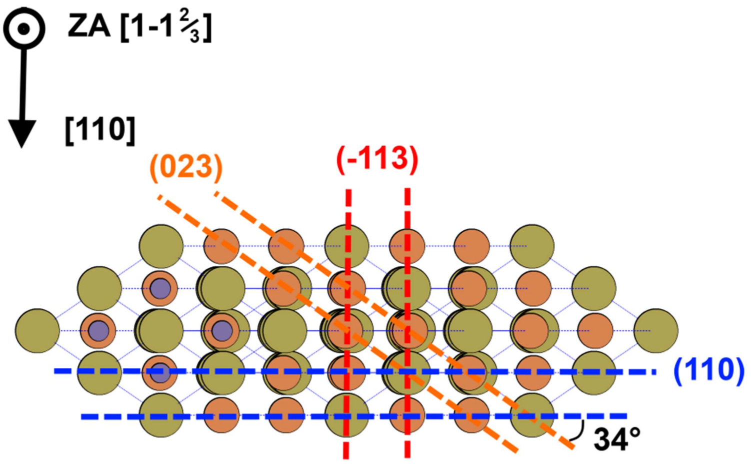

Fig. D.2: Lattice model from Figure D.1, viewing direction rotated by 90° around the $(\bar{1}1\,\overline{1/3})$ vector into $(1\bar{1}\,2/3)$ projection. The (023) planes indicated by dashed orange lines are a strong candidate for the grain boundary interface due to their low-index symmetry and appropriate angle towards the [110] projection plane.

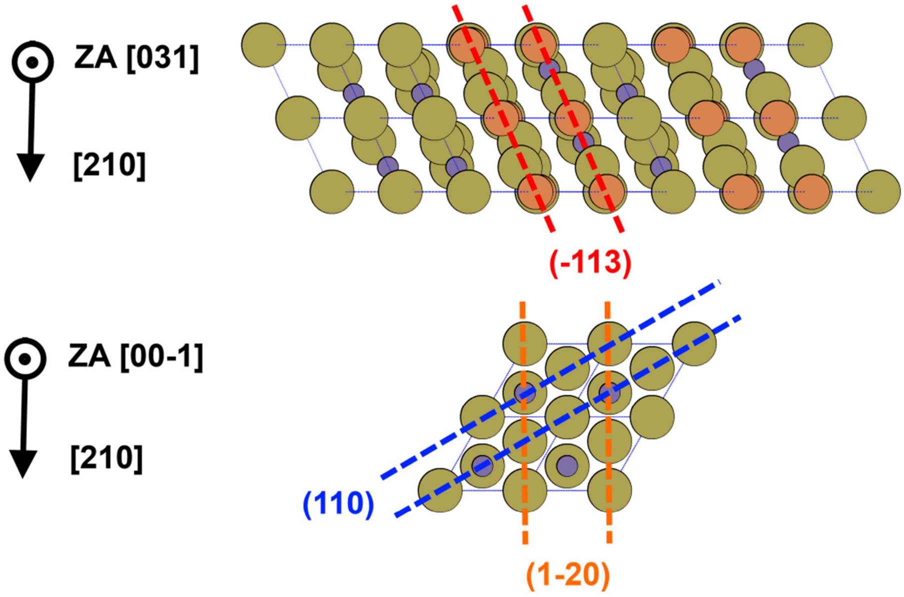

Figure D.3: Lattice model of 2x2x2 trigonal unit cells, analogous to Figure D.1. Zone axis projection [031] ≙ $[\bar{1}2\bar{1}1]$ (top) approximately matches the contrast features of the right-hand grain in Figure 3.37, although $(\bar{1}13)$ planes appear diffuse in the HAADF image due to overlapping columns. Rotating the model around the [210] vector by 36° results in the $[00\bar{1}]$ zone axis projection (bottom), possibly corresponding to the view down the grain boundary in the right-hand grain and matching the above described 34° angle between image projection plane and grain boundary orientation well.

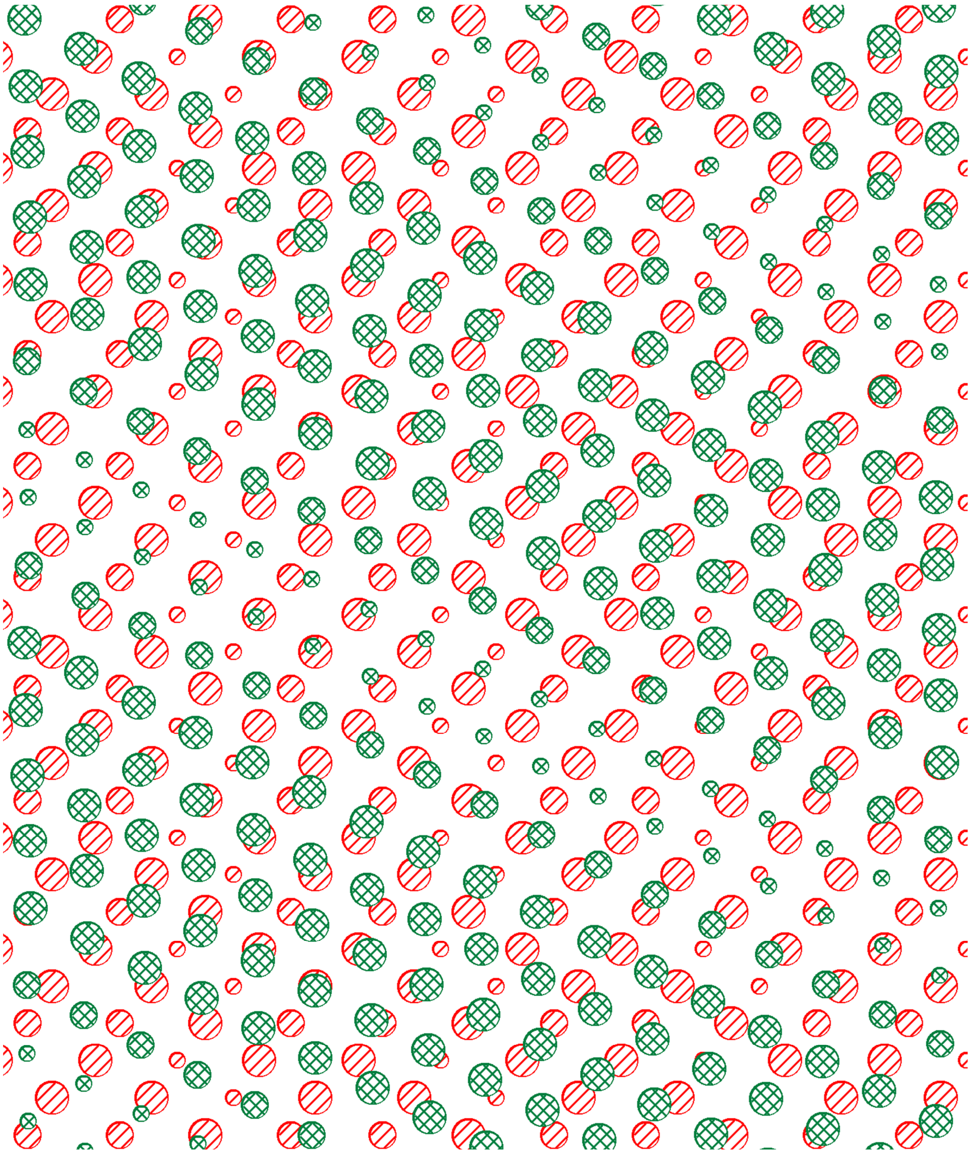

Appendix D.5: Overlay of one $(02\bar{2}3)$ (green circles) and one $(1\bar{2}10)$ (red circles) plane within the hypothetical grain boundary. Large circles correspond to Te atoms, intermediate ones to Sb-rich positions and small circles to Ge-rich positions. No low-Σ CSL arrangement is readily visible in which all positions conform to octahedral arrangements. While small rotation or shift rearrangements may improve the symmetry match, the underlying in-plane geometries (hexagonal for $(02\bar{2}3)$ and tetragonal for the$(1\bar{2}10)$ plane) as well as the intrinsic vacancy gaps crossing the $(1\bar{2}10)$ plane make a high-symmetry arrangement very unlikely. Furthermore such small reorientations should not exceed 3° since otherwise the experimentally observed contrast features (Figure 3.37) would no longer match.

Appendix E: Script code for intensity ratio evaluation

```
// This script is a quick fix to create intensity ratio maps from Digital Micrograph images
// and was written and tested in the DGM 2.11.1404.0 script environment.
// It is by no means optimized. The routine to read three image coordinates from the
// mouse pointer position is adapted from D.G.Mitchells “measure angles” script (see
// DGM script database online).

// Call image, create display object and image document, create dialog, declare variables

image frontimage := GetFrontImage()
imageDisplay img_disp = frontimage.ImageGetImageDisplay(0)
imageDocument  img_doc=getfrontimagedocument()
documentwindow img_win=ImageDocumentGetWindow(img_doc)
showimage(frontimage)
updateimage(frontimage)
number zoom=0
zoom=getzoom(frontimage)
string imagename=getname(frontimage)

number xsize, ysize, mousex, mousey
getwindowsize(frontimage, xsize, ysize)
okdialog("Define three points of the lattice (origin first) by hovering the cursor and hitting space, move on to next step by hitting space again. Note the total spacing!")
updateimage(frontimage)
number annotationID
number n, mouse_win_x, mouse_win_y
number img_view_t, img_view_l, img_view_b, img_view_r
number v2w_off_x, v2w_off_y, v2w_scale_x, v2w_scale_y
number img_win_t, img_win_l, img_win_b, img_win_r
number i2v_off_x, i2v_off_y, i2v_scale_x, i2v_scale_y
number i2w_off_x, i2w_off_y, i2w_scale_x, i2w_scale_y
number mouse_img_x, mouse_img_y

// Loop to mark the three points of interest

for(n=1; n<4; n++)
        {
                While(getkey()!=32)
                        {
                        windowgetmouseposition(img_win, mouse_win_x, mouse_win_y)
                        }
```

```
// The transformation is to map screen to image coordinates

img_disp.ImageDisplayGetImageRectInView( img_view_t, img_view_l, img_view_b,
img_view_r )
img_doc.ImageDocumentGetViewToWindowTransform( v2w_off_x, v2w_off_y, v2w_scale_x,
v2w_scale_y )
ObjectTransformTransformRect( v2w_off_x, v2w_off_y, v2w_scale_x, v2w_scale_y\ ,
img_view_t, img_view_l, img_view_b, img_view_r\ , img_win_t, img_win_l, img_win_b,
img_win_r );
img_disp.ComponentGetChildToViewTransform( i2v_off_x, i2v_off_y, i2v_scale_x, i2v_scale_y
)
ObjectTransformCompose( v2w_off_x, v2w_off_y, v2w_scale_x, v2w_scale_y\ , i2v_off_x,
i2v_off_y, i2v_scale_x, i2v_scale_y\, i2w_off_x, i2w_off_y, i2w_scale_x, i2w_scale_y )
ObjectTransformUntransformPoint( i2w_off_x, i2w_off_y, i2w_scale_x, i2w_scale_y\ ,
mouse_win_x, mouse_win_y, mouse_img_x, mouse_img_y );
mousex=mouse_img_x
mousey=mouse_img_y

string annotationstring=""+n
annotationID=createtextannotation(frontimage, mousey, mousex, annotationstring)
setnumbernote(frontimage, "Angles:Annotation no "+n, annotationid)
SetAnnotationBackground( frontimage, annotationID, 1 )
SetAnnotationFont( frontimage, annotationID, "helvetica")
SetAnnotationJustification(frontimage, annotationID, -1)
SetAnnotationSize( frontimage, annotationID, 12 )

// Information on the position of the pointer is stored as an image tag

setnumbernote(frontimage, "Angles:"+annotationstring+" X position = ",mousex)
setnumbernote(frontimage, "Angles:"+annotationstring+" Y position = ",mousey)
updateimage(frontimage)
			}

// Loop ends
// Data on the position of the marked points is retrieved from the image tags

number x1, y1, x2, y2, x3, y3
getnumbernote(frontimage, "Angles:1 X position = ",x1)
getnumbernote(frontimage, "Angles:1 Y position = ",y1)
getnumbernote(frontimage, "Angles:2 X position = ",x2)
getnumbernote(frontimage, "Angles:2 Y position = ",y2)
getnumbernote(frontimage, "Angles:3 X position = ",x3)
getnumbernote(frontimage, "Angles:3 Y position = ",y3)

// Data is output to the results window and onto the image
```

```
documentwindow reswin
result("Image Name = "+imagename+"\n \n")
updateimage(frontimage)

// Pressing the space bar removes all the annotations on the image and deletes the tags

While(getkey()!=32)
        {
        }
for(n=1; n<4; n++)
        {
                getnumbernote(frontimage, "Angles:Annotation no "+n, annotationid)
                deleteannotation(frontimage,annotationid)
        }
deletenote(frontimage,"Angles")
openandsetprogresswindow("","","")

// x1,x2,x3,y1,y2,y3 are read by the main script (i.e. most code above could be
// encapsulated in an object )
// Create lattice vectors from positions 1,2,3
// Create offset vectors by asking for the lattice periodicity along both vectors

number multiple1, multiple2
getnumber("Multiples of vector 1:", 1, multiple1)
getnumber("Multiples of vector 2:", 1, multiple2)
number vector1x, vector1y, vector2x, vector2y
vector1x=x2-x1
vector1y=y2-y1
vector2x=x3-x1
vector2y=y3-y1
number shift1x, shift1y, shift2x, shift2y
shift1x=(vector1x/multiple1)
shift1y=(vector1y/multiple1)
shift2x=(vector2x/multiple2)
shift2y=(vector2y/multiple2)

// Write vector parameters (in image scale units) to the results window for confirmation

number scalex, scaley
number length1v, length2v
string unitstring
getscale(frontimage, scalex, scaley)
getunitstring(frontimage, unitstring)
length1v=sqrt((shift1x*shift1x)+(shift1y*shift1y))
```

```
length2v=sqrt((shift2x*shift2x)+(shift2y*shift2y))

result("Origin set at ("+x1*scalex+" , "+y1*scaley+") ["+unitstring+"] \n")
result("Vector1 is ("+shift1x*scalex+" , "+shift1y*scaley+") ["+unitstring+"], length is
"+length1v*scalex+" ["+unitstring+"] \n")
result("Vector2 is ("+shift2x*scalex+" , "+shift2y*scaley+") ["+unitstring+"], length is
"+length2v*scaley+" ["+unitstring+"] \n \n")

// Confirm vectors or accept manual input (if e.g. a previous map should be recreated with
// a different offset multiplier)

number manual
getnumber("Image shift parameters have been written to results window. Substitute manual
values instead? (1=true / 0=false) ", 0, manual)
if(manual==1)
	{
	result("Manually adjusting vectors. \n In case of sublattice off-centering, measure offset
from line profiles along vector1/2 and adjust so that new length fits desired image displacement.
\n Keep in mind that only some image shifts may be useful in case of asymmetry. \n \n")
	getnumber("Vector1 x-component ["+unitstring+"]: ", shift1x*scalex, shift1x)
	shift1x=shift1x/scalex
	getnumber("Vector1 y-component ["+unitstring+"]: ", shift1y*scaley, shift1y)
	shift1y=shift1y/scaley
	getnumber("Vector2 x-component ["+unitstring+"]: ", shift2x*scalex, shift2x)
	shift2x=shift2x/scalex
	getnumber("Vector2 y-component ["+unitstring+"]: ", shift2y*scaley, shift2y)
	shift2y=shift2y/scaley
	}

// Ask for highest intensity limit of the weak sublattice (+ noise level)
// Doing this manually is not ideal, since it needs to be measured beforehand
// Should be the easiest next fix, from local maxima in a bimodal histogram
// Ask for manual background level or substitute the background level with the constant
// global minimum. A more complex background model (e.g. a 2D spline fit between
// minima of sectors) would be much preferable in the case of inhomogeneous images

number limit, background
getnumber("Upper intensity limit for weak sublattice (below will be truncated). \n HAS to lie
above background.", 0, limit)
getnumber("Constant (global) minimum background subtraction? (1=true / 0=manual background
level) ", 0, background)
image workingimage=frontimage
if(background==0)
	{
	getnumber("Specify constant background level manually:", 0, limit)
```

```
	workingimage=workingimage-min(workingimage)
	}
if(background==1)
	{
	limit=limit-min(workingimage)
	result("Global minimum background is "+min(workingimage)+" \n \n")
	workingimage=workingimage-min(workingimage)
	}

// Create four intermediate output images, each from a shift along plus or minus one vector

image out1=workingimage
image out2=workingimage
image out3=workingimage
image out4=workingimage
out1=offset(workingimage, shift1x, shift1y)
out2=offset(workingimage, shift2x, shift2y)
out3=offset(workingimage, (-1)*shift1x, (-1)*shift1y)
out4=offset(workingimage, (-1)*shift2x, (-1)*shift2y)

// Create binary mask of the strong sublattice, apply mask to intermediate images

out1=out1*tert(out1<limit, 0, 1)
out2=out2*tert(out2<limit, 0, 1)
out3=out3*tert(out3<limit, 0, 1)
out4=out4*tert(out4<limit, 0, 1)

// Create four intermediate ratio maps by division with original

out1=out1/workingimage
out2=out2/workingimage
out3=out3/workingimage
out4=out4/workingimage

setunitstring(out1, unitstring)
setscale(out1, scalex, scaley)
setname(out1, "Shift by +vector1")
setunitstring(out2, unitstring)
setscale(out2, scalex, scaley)
setname(out2, "Shift by +vector2")
setunitstring(out3, unitstring)
setscale(out3, scalex, scaley)
setname(out3, "Shift by -vector1")
setunitstring(out4, unitstring)
```

```
setscale(out4, scalex, scaley)
setname(out4, "Shift by -vector2")

// Show intermediate images

showimage(out1)
showimage(out2)
showimage(out3)
showimage(out4)

// Create final intensity ratio map, show image, exit

workingimage=(out1+out2+out3+out4)/4
setunitstring(workingimage, unitstring)
setscale(workingimage, scalex, scaley)
setname(workingimage, "4-image average result")
showimage(workingimage)

exit(0)
```

List of Publications

Peer-reviewed publications and contributions:

1. **Ross, U.**, A. Lotnyk, E. Thelander, and B. Rauschenbach, *Microstructure evolution in pulsed laser deposited epitaxial Ge-Sb-Te chalcogenide thin films.* Journal of Alloys and Compounds, **2016**. **676**: p. 582-590.
2. Lotnyk, A., **U. Ross**, S. Bernütz, E. Thelander, and B. Rauschenbach, *Local atomic arrangements and lattice distortions in layered Ge-Sb-Te crystal structures.* Scientific reports, **2016**. **6**: 26724
3. **Ross, U.**, A. Lotnyk, E. Thelander, and B. Rauschenbach, *Direct imaging of crystal structure and defects in metastable $Ge_2Sb_2Te_5$ by quantitative aberration-corrected scanning transmission electron microscopy.* Applied Physics Letters, **2014**. **104**(12): 121904

4. Lotnyk, A., S. Bernütz, X. Sun, **U. Ross**, M. Ehrhardt, and B. Rauschenbach, *Real-space imaging of atomic arrangement and vacancy layers ordering in laser crystallised $Ge_2Sb_2Te_5$ phase change thin films.* Acta Materialia, **2016**. **105**: p. 1-8.
5. Lotnyk, A., D. Poppitz, **U. Ross**, J.W. Gerlach, F. Frost, S. Bernütz, E. Thelander, and B. Rauschenbach, *Focused high- and low-energy ion milling for TEM specimen preparation.* Microelectronics Reliability, **2015**. **55**(9-10): p. 2119-2125.
6. Thelander, E., J. Gerlach, **U. Ross**, A. Lotnyk, and B. Rauschenbach, *Low temperature epitaxy of Ge-Sb-Te films on BaF_2 (111) by pulsed laser deposition.* Applied Physics Letters, **2014**. **105**(22): 221908.
7. Thelander, E., J.W. Gerlach, **U. Ross**, F. Frost, and B. Rauschenbach, *Epitaxial growth of Ge-Sb-Te films on KCl by high deposition rate pulsed laser deposition.* Journal of Applied Physics, **2014**. **115**(21): 213504

8. Zhao, J., R. Ma, X. Chen, B. Kang, X. Qiao, J. Du, X. Fan, **U. Ross**, C. Roiland, and A. Lotnyk, *From Phase Separation to Nanocrystallization in Fluorosilicate Glasses: Structural Design of Highly Luminescent Glass-Ceramics.* The Journal of Physical Chemistry C, **2016**. **120**(31): p. 17726-17732.
9. Hennes, M., A. Jakob, F. Lehnert, **U. Ross**, A. Lotnyk, and S. Mayr, *Nanometer-resolved quantification of mechanical response in nanoparticle-based composites.* Nanoscale, **2016**. **8**(17): p. 9398-9404.
10. Hennes, M., J. Buchwald, **U. Ross**, A. Lotnyk, and S. Mayr, *Equilibrium segregation patterns and alloying in Cu/Ni nanoparticles: Experiments versus modeling.* Physical Review B, **2015**. **91**(24): p. 245401.

Conference proceedings (oral presentations, posters):

11. **Ross, U.**, A. Lotnyk, E. Thelander, B. Rauschenbach. *Real structure of highly oriented Ge-Sb-Te thin films investigated by Cs-corrected STEM*. in *European Microscopy Conference 2016*. **2016**. Lyons/France. (Poster)
12. **Ross, U.**, A. Lotnyk, E. Thelander, B. Rauschenbach. *Epitaxial and textured Ge-Sb-Te phase-change thin films investigated by Cs-corrected STEM*. in *DPG Frühjahrstagung 2015*. **2015**. Berlin/Germany. (Oral)
13. **Ross, U.**, A. Lotnyk, E. Thelander, B. Rauschenbach. *High-resolution STEM investigation of textured and epitaxial Ge-Sb-Te thin films*. in *E\PCOS*. **2015**. Amsterdam/Netherlands. (Poster,awarded 2nd poster prize)
14. **Ross, U.**, A. Lotnyk, E. Thelander, B. Rauschenbach. *Cs-corrected STEM characterisation of textured and epitaxial Ge-Sb-Te thin films*. in *Microscopy Conference 2015*. **2015**. Göttingen/Germany. (Poster)

15. **Ross, U.**, A. Lotnyk, E. Thelander, B. Rauschenbach. *Quantitative structural and chemical investigation of amorphous and metastable crystalline phase-change alloy thin films by Cs-corrected STEM*. in *International Microscopy Conference 18*. **2014**. Prague/Czech Republic. (Oral)
16. **Ross, U.**, A. Lotnyk, E. Thelander, B. Rauschenbach. *Atomic resolution investigation of defect structures in textured metastable $Ge_2Sb_2Te_5$ by aberration corrected high resolution STEM*. in *DPG Frühjahrstagung 2014*. **2014**. Dresden/Germany. (Oral)
17. **Ross, U.**, A. Lotnyk, E. Thelander, B. Rauschenbach. *Characterization of laser-deposited Ge-Sb-Te thin films by Cs corrected STEM*. in *Microscopy Conference 2013*. **2013**. Regensburg/Germany. (Poster)
18. **Ross, U.**, A. Lotnyk, E. thelander, B. Rauschenbach. *Quantiative investigation of laser-deposited $Ge_2Sb_2Te_5$ by aberration corrected STEM/EELS*. in *DPG Frühjahrstagung 2013*. **2013**. Regensburg/Germany. (Poster)

19. Lotnyk, A., S. Bernütz, X. Sun, **U. Ross**, M. Erhardt, B. Rauschenbach. *Electron beam induced in situ writing and recovering of vacancy layers in $Ge_2Sb_2Te_5$*. in *European Microscopy Conference 2016*. **2016**. Lyons/France.
20. Lotnyk, A., **U. Ross**, S. Bernütz, E. Thelander, B. Rauschenbach. *Evaluation of local atomic arrangements and lattice distortions in layered Ge-Sb-Te crystal structures*. in *European Microscopy Conference 2016*. **2016**. Lyons/France.
21. Lotnyk, A., **U. Ross**, S. Bernütz, E. Thelander, B. Rauschenbach. *Analysis of local atomic arrangement in layered Ge-Sb-Te crystal structures by advanced scanning transmission electron microscopy*. in *DPG Frühjahrstagung 2016*. **2016**.
22. Kienle, L., T. Dankwort, J. Strobel, W. Ge, R.L. de Miranda, E. Quandt, M. Wuttig, A.L. Hansen, J.D. König, M. Winkler, A. Lotnyk, **U. Ross**, W. Bensch, D.C. Johnson. *TEM on energy materials*. in *International Workshop on Advanced and In-situ Microscopies of Functional Nanomaterials and Devices*. **2015**. Hamburg/Germany.
23. Lotnyk, A., S. Bernütz, **U. Ross**, X. Sun, E.Thelander, M. Erhardt, B. Rauschenbach. *Atomic structure of Ge-Sb-Te thin films studied by high-resolution Cs-corrected STEM*. in *International Workshop on Advanced and In-situ Microscopies of Functional Nanomaterials and Devices*. **2015**. Hamburg/Germany.
24. Thelander, E., J.W. Gerlach, **U. Ross**, B. Rauschenbach. *Epitaxial growth of pulsed laser deposited $Ge_2Sb_2Te_5$ thin films*. in *DPG Frühjahrstagung 2014*. **2014**. Dresden/Germany.
25. Thelander, E., H. Lu, **U. Ross**, B. Rauschenbach. *Phase transitions in GST-films using single nanosecond UV pulses*. in *DPG Frühjahrstagung 2013*. **2013**. Regensburg/Germany.
26. Thelander, E., **U. Ross**, X. Sun, A. Lotnyk, H. Lu, B. Rauschenbach. *Pulsed laser deposition of $Ge_2Sb_2Te_5$ thin films for phase change data storage applications*. in *Conference on Laser Ablation*. **2013**. Ischia/Italy.

Other public presentations:

27. **Ross, U.** *Oriented growth of GeSbTe compounds investigated by high-resolution STEM*. in *Doktorandenseminar IOM Leipzig*. **2015**. Leipzig/Germany. (Oral)
28. **Ross, U.**, A. Lotnyk, E. Thelander, B. Rauschenbach. *Quantitative Cs-corrected STEM investigation of $Ge_2Sb_2Te_5$ phase-change alloy thin films*. in *2nd Workhop Leibniz-Network Nano and 3rd PhD Retreat of Section D*. **2014**. Berlin/Germany. (Poster)
29. **Ross, U.** *Cs-corrected STEM investigation of $Ge_2Sb_2Te_5$ phase-change alloy thin films*. in *Doktorandenseminar IOM Leipzig*. **2014**. Leipzig/Germany. (Oral)
30. **Ross, U.** *Cs-corrected STEM investigation of $Ge_2Sb_2Te_5$ phase-change alloy thin films*. in *Seminar Talk, Group L. Kienle*. **2014**. Kiel/Germany. (Oral)
31. **Ross, U.** *TEM investigation of GeSbTe based phase-change materials*. in *Doktorandenseminar IOM Leipzig*. **2013**. Leipzig/Germany. (Oral)
32. **Ross, U.**, D. Poppitz, A. Lotnyk, B. Rauschenbach. *Aberration-corrected Transmission Electron Microscopy of Thin Films*. in *Doktorandenforum Leibniz Gemeinschaft Sektion D*. **2013**. Berlin/Germany. (Poster and Oral)

Acknowledgements

I would like to thank Prof. Dr. Lorenz Kienle, who provided both an open door at the CAU Kiel at any time as well as the opportunity to submit the thesis under his guidance.

Next, I would like to thank Prof. Dr. Dr. h.c. Bernd Rauschenbach, who provided both the excellent scientific opportunities at the IOM Leipzig and a stimulating research environment in the administration of the institute, and, not least, supported numerous opportunities for academic exchange both within the Leibniz association as well as in highly-rated national and international conferences. I am especially thankful for the readily provided access to interpersonal exchange, and above all the freedom to pursue well-founded topics of interest as well as the patience shown in the financial support.

My closest supervisor, Dr. Andriy Lotnyk, deserves special thanks for the lively exchange of knowledge in his research group, the professional assistance both in the operation of the scientific equipment as well as his work on development of simulation and evaluation techniques of these highly complex methods and materials. In addition, his support in the formulation of this thesis was of crucial importance, as can also be seen in the peer-reviewed published work.

As the work carried out here was a product of close collaboration with Dr. Erik Thelander, who tirelessly operated the PLD and XRD equipment, my thanks to him can also not be overstated. In a similar vein, the assistance of Agnes Mill in the preparation of excellent TEM specimens also warrants my deep gratitude. To her, Dr. Lotnyk and Dr. David Poppitz I must also extend thanks for the pleasant working environment in our offices. If I had buried myself in a problem, you helped me catch my breath, and David Poppitz in particular was always open to bounce my less-well refined thoughts off of.

Numerous others deserve mention and thanks, not least of which: Dr. Jürgen Gerlach and co-workers at the IOM, in particular Christoph Grüner and Martin Erhardt for their assistance in annealing and laser irradiation experiments, Xinxing Sun and Isom Hilmi who carry on the excellent deposition and characterization work; my, albeit temporary, office colleagues Sabine Bernütz and Ron Hildebrandt, for tolerating my occasional frustrations; and Torben Dankwort for providing another informal communication partner at the CAU Kiel.

As I am a product of my alma mater, at this point I also need to extend my gratitude to Prof. Dr. Wolfgang Jäger and Prof. Dr. Erdmann Spiecker, who awakened and fostered my interest in the topics at hand in the first place, as well as Dr. Dietrich Häußler who introduced me to the practical aspects of microscopy work.

As one fact of life is that high-ranking research is not always cheap, at this point I would also like to extend my thanks for the funding support of the European Union and the Free State of Saxony (Projekt LenA, Projekt Nr 100.074.065).

Last but not least, I need to thank my friends and family. My cohabitants for their tolerance, my former fellow students for staying in, admittedly due to my failings sporadic, contact, and above all my sisters and parents for their unending and unquestioning support. I am what you made me, and I hope that will always be a source of pride to you.

Selbstständigkeitserklärung

Hiermit versichere ich dass die vorliegende Abhandlung mit dem Titel „Structural investigation of Ge-Sb-Te thin films by aberration-corrected scanning transmission microscopy“ nach Inhalt und Form selbstständig und ohne unzulässige fremde Hilfe erstellt wurde.

Ich versichere ebenfalls dass die vorliegende Arbeit weder ganz noch in Teilen bereits Inhalt eines Prüfungsverfahrens war, veröffentlicht worden ist, oder zur Veröffentlichung vorgelegt wurde.

Weiterhin versichere ich dass die Arbeit unter Einhaltung der Regeln zur guten wissenschaftlichen Praxis der Deutschen Forschungsgemeinschaft entstanden ist.

Leipzig, 07. November 2017

Ulrich Roß